UCLA
UCLA Electronic Theses and Dissertations

Title

Clumped Isotopes and Cryptic Cycling of Methane: Tracking the Microbial Footprint

Permalink

https://escholarship.org/uc/item/82k2w00g

Author

Krause, Sebastian Jian Ernst

Publication Date

2022

Peer reviewed|Thesis/dissertation

UNIVERSITY OF CALIFORNIA

Los Angeles

Clumped Isotopes and Cryptic Cycling of Methane:

Tracking the Microbial Footprint

A dissertation submitted in partial satisfaction of the

requirements for the degree Doctor of Philosophy

in Geochemistry

by

Sebastian Jian Ernst Krause

2022

ABSTRACT OF THE DISSERTATION

Methane Clumped Isotopologues and Cryptic Cycling of Methane:

Tracking the Microbial Footprint

by

Sebastian Jian Ernst Krause

Doctor of Philosophy in Geochemistry

University of California, Los Angeles, 2022

Professor Tina Treude, Chair

Methane is the simplest form of organic matter on Earth, the most abundant organic molecule in the atmosphere where it is a potent greenhouse gas, an important source of energy, and considered to be a signature of life on other worlds. Methane's genesis and its fate can occur abiotically and biotically in various atmospheric, geologic, and geographic settings. Investigations into the porewater and solid phase geochemistry, metabolic ex-situ activity and stable isotope compositions have brought considerable insight into distinguishing and tracking the microbial footprints of methane production and consumption. However, questions remain pertaining to, for example, 1) the potential for geomicrobiological communities to simultaneously produce and consume methane in sedimentary environments and, 2) the biological signatures of rare methane clumped isotopologues that indicate whether methane has been altered by oxidation.

The first question will be addressed in this dissertation, using a newly adapted radiotracer method to show the cryptic, simultaneous methane production and consumption by biological activity in coastal wetland and marine sediment. Radiotracer analysis of the sediment from within the top 15-20 cm, collected from a coastal wetland and a marine environment revealed the cryptic, simultaneous methane production and consumption by biological activity. The findings strongly suggest that this cryptic methane cycling was overlooked by previous studies and must be considered in sediment within other wetland and marine settings.

The second issue will be addressed by using the latest technological advancements in high resolution mass spectrometry to elucidate the rare methane isotopologue signatures of microbial methane oxidation in bacterial pure cultures, enzyme extracts, in environmental methane-bearing natural fluids, and in sediment slurries. Laboratory experiments that induced methane oxidation by biological activity revealed that the residual methane have distinct methane clumped isotopologue signatures in a two-dimensional space. The experimental data were applied to open and closed system models, which not only revealed that methane clumped isotopologue signatures of various microbial methane oxidation pathways are distinct from each other but also distinct from methane sources. The findings have furthered the utility of the methane clumped isotopologues in a two-dimensional space to distinguish source and process.

The dissertation of Sebastian Jian Ernst Krause is approved.

Edward D. Young

James William Schopf

David K. Jacobs

Tina Treude, Committee Chair

University of California, Los Angeles

2022

Dedication Page

I dedicate this dissertation to my family; my mother Cynthia, my father Robert, and my younger

brother Anselm, whose love and support throughout this journey, made it possible to produce

this work.

Table of Contents

List of Figures

List of Tables

List of Acronyms

°C – Degrees Celsius

ANME – Anaerobic Methotrophs

AOM-CH$_4$ – Anaerobic Oxidation of Methane determined directly from ^{14}C-methane

AOM-MMA – Anaerobic Oxidation of Methane determined from ^{14}C-methane via ^{14}C-mono-methylamine

AOM – Anaerobic Oxidation of Methane

ATP – Adenosine Triphosphate

AUV – Automated Underwater Vehicle

BES – 2-Bromoethylsulfonate

CaCl$_2$ – Calcium Chloride

CaCO$_3$ – Calcium Carbonate

CH$_3$COO$^-$ – Acetate

CH$_3$NH$_2$ – Mono-methylamine

CH$_3$OH – Methanol

CH$_4$ – Methane

cm – Centimeter

cm^{-3} – Centimeter Cubed

CO$_2$ – Carbon Dioxide

CoB – Coenzyme B

CoM – Coenzyme M

CORK – Circulation Obviation Retrofit Kit

CPM – Counts Per Minute

CSMR – Carpinteria Salt Marsh Reserve

D – Deuterium

d – Days

d^{-1} – Per Day

Da – Damkholer Number

DCO – Deep Carbon Observatory

DIC – Dissolved Inorganic Carbon

DOI – Digital Online Identifier

DSS – 2,2-dimethyl-2-silapentane-5-sulfonate-d6

EIE – Equilibrium Isotope Effects

ESRL – Earth System Research Laboratories

Fe(III) – Iron (III)

g – Grams

GBq – Giga Becquerel

GC –Gas Chromatography

GML – Global Monitoring Laboratory

H – Hydrogen

h – Hours

H^+ – Proton

H_2O – Water

HCO_3^- – Bicarbonate

HEPA – High Efficiency Particulate Air

HPD – Hyperdolphin Dives

HS^- – Hydrogen Sulfide

i.d. – Inner Diameter

k – Rate Constant

K – Kelvin

KBq – Kilo Becquerel

KIE – Kinetic Isotope Effects

K_m – Michaelis Menten Constant

KNO_3 – Potassium Nitrate

kPa – Kilo Pascals

L – Liter

M – Molar

m – Meters

m^{-2} – Meters Squared

Mcr – Methyl-Coenzyme Reductase

MetOH – Methanol

MG-MMA – Methanogenesis from Mono-methylamine

$MgSO_4$ – Magnesium Sulfate

mL – Milliliter

mM – Millimolar

MMA – Mono-methylamine

Mn (IV) – Manganese (IV)

mol – Moles

MOx – Aerobic Oxidation of Methane

MUC – Multicorer

N_2 – Dinitrogen

NaOH – Sodium Hydroxide

NDRO – Northern Depositional Radial Origin

NDT – Northern Depositional Transect

NH_4^+ – Ammonium

nmol – Nano Moles

NMR – Nuclear Magnetic Resonance

NMS – Nitrate Mineral Salts

NO_3^- – Nitrate

NOAA – National Oceanic and Atmospheric Administration

NSF – National Science Foundation

O_2 – Oxygen

OD – Outer Diameter

ODP – Ocean Drilling Project

OMZ – Oxygen Minimum Zones

PCR – Polymerase Chain Reaction

pH_2 – Partial Pressure of Hydrogen

PO_4 – Phosphate

PPMV – Parts Per Million Per Volume

P_{SED} – Sediment Porosity

PSU – Practical Salinity Unit

R/V – Research Vessel

RF – Recovery Factor

RGM – Rule of Geometric Mean

ROV – Remote Operated Vehicle

RuMP – Ribulose Monophosphate Pathway

S/N – Signal to Noise

SBB – Santa Barbara Basin

SDRO – Southern Depositional Radial Origin

SMTZ – Sulfate Methane Transition Zone

SO_4^{2-} – Sulfate

SR – Sulfate Reduction

t – Time

TBq – Tera Becquerel

TCD – Thermal Conductivity Detector

Tg – Tera-grams

TIC – Total Inorganic Carbon

TRIS – Total Reduced Inorganic Sulfur

USA – United States of America

UV – Ultraviolet

wk – Week

Yr^{-1} – Per Year

μL – Micro Liters

μM – Micro Molar

μmol – Micro Moles

Acknowledgements

The work presented in this dissertation could not have been completed without the support of many mentors and friends. I would like to first acknowledge my Ph.D. advisor and mentor, Prof. Tina Treude, who welcomed me into this great scientific community, provided guidance, resources, and importantly the intellectual space to produce this work. I would also like to acknowledge my gratitude to the Ph.D. committee, Prof. Edward D. Young, Prof. J. William Schopf, and Prof. David Jacobs of UCLA, all of whom dedicated their expertise, time, and resources to benefit me and the research presented here in this dissertation. I feel that my interactions with them, have made me a better scientist and person, and learned many valuable lessons that I will take with me for the rest of my scientific career and personal life.

I would like to acknowledge those who also helped advise, mentor or provide technical advice of this research: Dr. Jeana Drake, Dr. Stefan Krause, Dr. Ingeborg Bussmann, Dr. Guanchao Zhuang, Dr. Jabrane Labidi, Dr. Haolan Tang, Adjunct Assistant Prof. Benjamin Knowles, Stephanie A. Connon, Dr. Victoria Orphan, Troy Gunderson, Yubin Raut, Dr. Michael Morando, Dr. Douglas Capone, Dr. David Hoyt, Dr. Scott D. Wankel, Prof. David Valentine, and Prof. Peter Girguis. I would also like to thank the UCLA Earth, Planetary and Space Sciences Department, past and present staff, especially Lauri Holbrook, Carlene Brown, Richard Fort, Kelli Yang, Michelle Pang, Roderic O'Connor, Eric Wessenauer, Henry Gonzalez, Bill Harris, Emmanuel Masongsong, Jim Nakatsuka, and Hsiao-Tzu Chou.

I feel particularly privileged to have made new and maintained old friendships which has been essential to the completion of my dissertation. To my life partner, Lisa Y. Mesrop, who has provided unconditional love and support towards me perusing my research aspirations. To all of the close friends I have made at UCLA and from other institutions, I want to especially

Vita/Biographical Sketch

Sebastian Jian Ernst Krause

Education

University of California, Los Angeles   2018

     M.S., Geochemistry

University of California, Santa Cruz   2014

     B.S., Marine Biology

Publications

Krause S. J. E and Treude T. (2021) Deciphering cryptic methane cycling: Coupling of methylotrophic methanogenesis and anaerobic oxidation of methane in hypersaline coastal wetland sediment. *Geochimica et Cosmochimica Acta* **302**, 160-174.

Krause S. J. E, Liu J., Young E. D. and Treude T. (2022) $\Delta13CH3D$ and $\Delta12CH2D2$ signatures of methane aerobically oxidized by Methylosinus trichosporium with implications for deciphering the provenance of methane gases. *Earth and Planetary Science Letters* **593**, 117681.

Beulig, F., Schubert, F., Adhikari, R.R., Glombitza, C., Heuer, V.B., Hinrichs, K.U., Homola, K.L., Inagaki, F., Jørgensen, B.B., Kallmeyer, J., **Krause, S.J.E**, Morono, Y., Sauvage, A. J., and Treude, T,. (2022). Rapid metabolism fosters microbial survival in the deep, hot subseafloor biosphere. *Nature communications*, *13*(1), pp.1-9.

Previous appointments

2016 - present Ph.D Candidate, University of California, Los Angeles, Los Angeles, CA

2015 - 2016 Research Specialist, University of Southern California, Los Angeles, CA

2014 - 2014 Junior Research Specialist, University of California, Santa Cruz, Santa Cruz, CA

2012 - 2012 Junior Research Specialist, Southern California Coastal Research Project, Costa

  Mesa, CA

Selected Awards

UCLA EPSS Departmental Teaching Award   2020

UCLA EPSS Departmental Fellowship   2016-2019

NASA travel funds to attend the AbGradCon   2018

<center>**Chapter 1**</center>

Part I. Introduction to methane

Methane is the most reduced form of carbon and the most abundant organic molecule on Earth (Whiticar, 1999; Whiticar, 2020). It is the most simple of the *n*-alkanes and its high molecular stability is attributed to the strong bonds between the carbon and hydrogen, resulting in high dissociation energies (+439 kJ mol^{-1}) (Thauer and Shima, 2008; Whiticar, 2020). Although not named as "methane" until 1865 by (Von Hofmann), the molecule was first identified to be a component of "inflammable air" in various environmental settings (Priestley, 1776) and in marsh environments (Volta et al., 1777). Methane is also considered to be a signature of life outside of planet Earth (Westall and Cockell, 2016).

Methane originates from biotic and abiotic mechanisms from both anthropogenic activities and natural environments, as discussed below. Interest in methane has sparked extensive efforts of research for several key reasons. It is colloquially referred to as a natural gas that is used as a daily energy resource for industry and day-to-day living (Sun et al., 2020). In the atmosphere, methane is the most abundant organic molecule and inflicts a global warming potential that is ~28 and 84 times more potent than CO_2 as a greenhouse gas, over 100 and 20-year intervals, respectively (Whiticar, 2020).

Global methane budget: sources and sinks

Atmospheric methane concentrations reported in 2018 (~1850 ppb), have more than doubled since the year 1750 (722 ppb) (Nisbet et al., 2019; Saunois et al., 2020). These atmospheric methane concentrations continue to increase (Fig. 1-1). The large increase in

<center>1</center>

atmospheric methane concentrations within this time frame is mostly a result of anthropogenic (human derived) activities although there exist natural sources that also contribute to the buildup of methane in the Earth's atmosphere (Saunois et al., 2016; Saunois et al., 2020). Prior to the 1970's, atmospheric methane concentrations were reconstructed from ice core data. Direct measurements of atmospheric methane did not occur until the late 1970's. Moreover, global atmospheric methane concentration measurements were not available until the early 1980's. However, atmospheric methane concentration measurements collected over several decades has allowed assessments of global atmospheric methane budgets. These budgets are informed by top-down and bottom-up estimates. Top-down estimates are derived from atmospheric inverse-modeling studies, while bottom-up estimates combine process data about surface emissions, the atmospheric chemistry, and anthropogenic and natural emissions. Methane
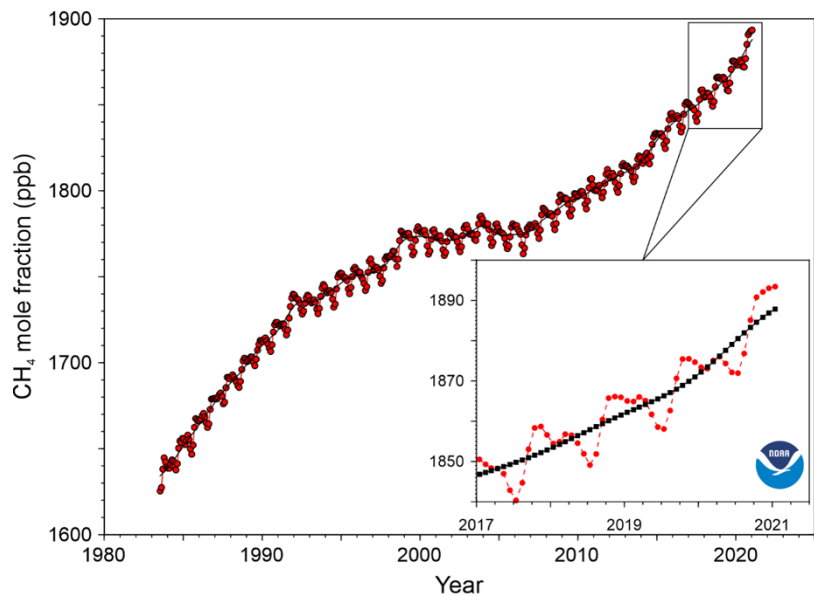
Figure 1-1. NOAA/ESRL atmospheric methane concentrations over time. Red circles are monthly averaged mixing ratios from marine surface sites dry mole fraction. Black squares are the global 12-month running mean from 1983 to present. The enhanced box shows the period from 2017-2021 in greater detail. Adapted from Ed Dlugokencky, NOAA/GML (www.esrl.noaa.gov/gmd/ccgg/trends_ch4/).

can be originated from either anthropogenic or from naturally occurring sources. These sources can be further characterized by their emission types which include, biogenic, thermogenic, pyrogenic and abiotic processes (Saunois et al., 2020). Biogenic methane mostly refers to methane produced by methanogenic archaea in anoxic environments such as marine sediments, freshwater

lake sediments, wetlands, rice paddies, wastewater treatment plants, and within digestive tracks of ruminants. Thermogenic methane is sourced from organic matter buried deeper within the Earth's crust that is broken down by heat and pressure over geological periods. Methane produced during the incomplete combustion of organic material, such as fossil fuels, biomass burning during deforestation, peat fires, and wildfires is considered pyrogenically derived. Methane that is formed during water-rock chemical reactions, without the degradation of organic matter or biological activity falls into the abiotic category (Etiope and Sherwood Lollar, 2013). Lastly, methane gases from different source types can also mix. This will be discussed further in part II of this chapter.

Figure 1-2. shows the global methane budget during the 2008–2017-decade. Total global methane emissions were found to be 576 Tg CH_4 yr^{-1} from top-down estimates and 737 Tg CH_4 yr^{-1} from bottom-up estimates (Saunois et al., 2020). During this decade, anthropogenic sources
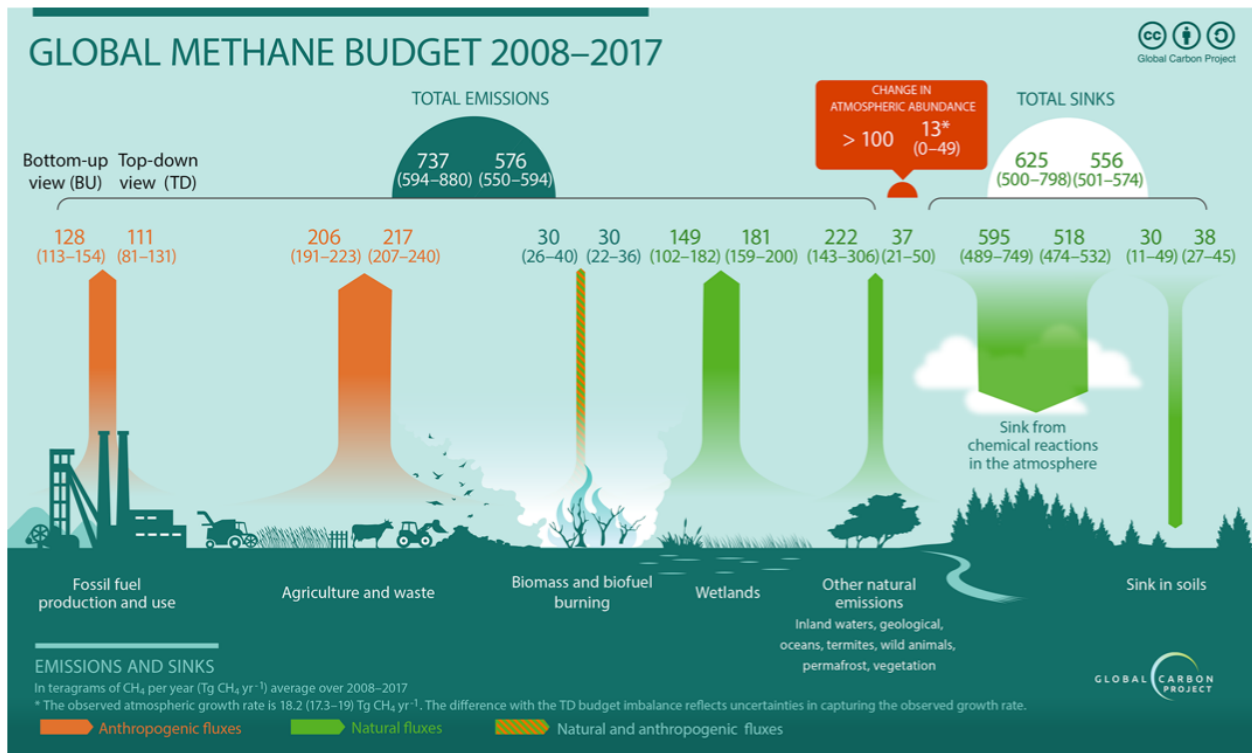
Figure 1-2. Depiction of the global methane budget for the 2008-2017 decade. Estimates of both bottom-up (right) and top-down (left) are provided in Tg CH_4 yr^{-1} for total methane emission and total methane sink, as well as each emission and sink category. Figure was generated for Saunois et al., (2020) by the Global Carbon Project.

(including biomass burning) contributed 359 Tg CH$_4$ yr^{-1} and 366 Tg CH$_4$ yr^{-1} according to top-down and bottom-up emission estimates, respectively. This equates to about 60% to the total global methane emission. Of these anthropogenic sources, agriculture contributed by far the highest (217 Tg CH$_4$ yr^{-1} and 206 Tg CH$_4$ yr^{-1}, respectively). Fossil fuel production and combustion were found to contribute 11 Tg CH$_4$ yr^{-1} and 128 Tg CH$_4$ yr^{-1}, respectively.

Naturally occurring methane sources cumulatively emit 218 Tg CH$_4$ yr^{-1} and 371 Tg CH$_4$ yr^{-1}, respectively. Out of all the natural sources, natural wetlands contribute the highest methane emissions (between 181 Tg CH$_4$ yr^{-1} and 149 Tg CH$_4$ yr^{-1}, respectively). Other naturally occurring methane sources, which include marine, freshwater and terrestrial environments cumulatively contribute methane emissions of 37 Tg CH$_4$ yr^{-1} and 222 Tg CH$_4$ yr^{-1}, respectively (Saunois et al., 2020).

Figure 1-2 also illustrates that the atmospheric methane emissions are greatly imbalanced by chemical reactions in the atmosphere and by soil uptake (Reeburgh, 2007; Saunois et al., 2020). During the 2008-2017 decade, the total methane sink amounted to 556 Tg CH$_4$ yr^{-1} and 625 Tg CH$_4$ yr^{-1} according to top-down and bottom-up estimates, respectively. Chemical loss in the atmosphere by hydroxyl and chloride radicals sink between 518 Tg CH$_4$ yr^{-1} and 595 Tg CH$_4$ yr^{-1}, respectively. Soil uptake of methane is minor in comparison ranging between 13 Tg CH$_4$ yr^{-1} and 112 Tg CH$_4$ yr^{-1}, respectively (Saunois et al., 2020).

Naturally occurring methane sources and sinks are more difficult to constrain with uncertainties ranging from 50-100%, whereas, emissions from anthropogenic sources are better constrained (20-25%) in specific sectors (Saunois et al., 2020). This means the methane budget is still not complete and our understanding of the true amount of methane on Earth is currently unknown (Whiticar, 2020). A substantial portion of this dissertation is focused primarily on the

4

biogenic methane that is produced and consumed naturally in sedimentary environments. The next sections will introduce the natural environments where naturally occurring methane can be sourced from and consumed within.

Methane in various aquatic environments

Marine cold seeps

Cold seeps occur where methane and other hydrocarbon fluids derived from the lithosphere move into the hydro - and (potentially) atmosphere (Leifer et al., 2010). Cold seeps on average contribute 45 Tg CH_4 yr^{-1} to the atmosphere, according to bottom-up methane emission estimates (Saunois et al., 2020). Hydrocarbon flow rates from cold seeps are much slower than those from hydrothermal vents and occur at ambient temperatures as the name implies (Suess, 2010; Suess, 2014). Located on the sea floor, cold seeps typically originate from groundwater effluent that exits its host aquifer at variable bathymetric depths ranging from several dozen meters below the continental shelves to several dozen kilometers within deep ocean fore-arc basins (Suess, 2014).

The best studied marine cold seeps occur at continent-convergent tectonic plate boundaries where a dense oceanic plate, overlain by thick, organic-rich sediments subducts underneath a less dense continental plate (oceanic-continental convergent margin). This tectonic process results in lateral compression and concurrent dewatering of the organic-rich sediments riding on the oceanic plate. Compression and dewatering of the sediments lead to groundwater expulsion via cold seeps at a regional scale. Hydrocarbons including methane within the groundwater, derived from the organic-rich sediments, exit the lithosphere via cold seeps, which then are released into the hydrosphere (Suess, 2014). Cold seeps also exist at oceanic-oceanic convergent plate boundaries. In this tectonic setting, older portions of the subducted plate are dewatered due to high

temperatures and pressures. At both convergent plate boudies, the fluids liberated from the plate, ascend to react with olivine- and pyroxene- rich bedrock within the overlying plate. These hydrocarbons, including methane, are generated through the geochemical alteration of bedrock by the ascending fluids, a process called serpentinization. Methane, other hydrocarbons, and excess fluids are carried upward to where they seep from serpentinite mud volcanos (Etiope and Sherwood Lollar, 2013; Etiope and Schoell, 2014; Suess, 2010; Suess, 2014).

At tectonically passive boundaries, as opposed to active boundaries, there is no subduction and destruction of a dense tectonic plate. Cold seepage at passive boundaries can occur across several different geological features including mud volcanoes, pockmarks, and thick organic-rich sedimentary rocks containing brines, gas hydrates, hydrocarbon reservoirs or buried evaporites. Release of fluids containing hydrocarbons at passive margins can occur from changes in permeability of the strata containing the hydrocarbon rich fluids. These permeability changes in the host rock for hydrocarbon passage can be caused by changes in sediment loading, variable subsurface overburden pressures, and facies changes (Suess, 2014).

At extensional transform boundaries, that maybe adjacent to spreading ridges or along strike-slip faults, extensive faulting and fracturing can cut through seafloor regions with thick organic-rich sediments. These faults and fractures can allow hydrocarbons including methane to seep through the marine sediments towards the ocean floor as cold seeps (Moretti, 1998; Smeraglia et al., 2022; Suess, 2010).

Finally, cold seeps can be found along continental margins where thick sequences of organic-rich sediments have accumulated. Such sediment accumulations are associated with coastal upwelling generating high biomass production, at or near the ocean surface, followed by sinking of the dead biomass ultimately to be converted to methane. This methane can diffuse

upward through the sediment column where methane can become a hydrate at specific depths, pressures, and temperatures. Or alternatively enter the water column (Suess, 2014).

Continental shelves

Methane is also found in sediments at shallower continental shelves, which are transition zones that connect coastal intertidal zones to the open ocean (Laruelle et al., 2013). Notable continental shelf locations, where large inventories of methane can be found, include, for example, the North Sea (Hovland and Judd, 1988), Chesapeake Bay (Hagen and Vogt, 1999), Black Sea (Knab et al., 2009), Baltic Sea (Dale et al., 2019; Piker et al., 1998; Wever et al., 2006) and East China Sea (Zhang et al., 2004). Continental shelves are important when discussing methane because up to ~80% of the organic carbon from primary production is buried within the shelf sediments (Bauer et al., 2013). However, the amount of organic carbon that reaches the sediment decreases with increasing water column depth (Pastor et al., 2011). This organic carbon within these sediment is then degraded following the microbial pathways shown in Figure 1-4 and 1-5 to ultimately form methane (Jørgensen, 2000), which will be discussed further in following sections. Approximately 75% of the marine methane emissions come from methane produced within continental shelves (Anderson et al., 2010; Bange et al., 1994). However, methane emission rates from continental shelves specifically are low ranging between 0.3 to 1.0 Tg CH_4 yr^{-1}(Weber et al., 2019). The reason why methane emissions from marine environments are relatively low, despite the burial of considerable volumes of organic matter, is largely because of microbial consumption through the anaerobic oxidation of methane (AOM) and the aerobic oxidation of methane (MOx) occurring primarily in sediment and in the water column, respectively (Reeburgh, 2007) (Fig. 1-4). These two methane sinks will be introduced further in upcoming sections of this chapter.

Inland freshwater lakes and ponds

Lakes and ponds contribute between 117-212 Tg CH_4 y^{-1}, which is approximately 10-20% of the global methane emissions (Saunois et al., 2016; 2020), even though they are covering only about 3.7% of all land globally (Verpoorter et al., 2014). In anoxic sediments of freshwater environments, methanogenesis is the dominant metabolic pathway for organic matter degradation. Thus, anoxic sediments in freshwater environments tend to emit more methane than marine anoxic sediments (4 to 10 Tg CH_4 yr^{-1}) (Saunois et al., 2020). This is because sulfate concentrations in freshwater lake sediments are usually considerably lower than in the marine environment. Sulfate concentrations do have an impact on methanogenesis and AOM activity which will be discussed in greater detail in the following sections.

Lakes are very sensitive to climate change (Adrian et al., 2009). Climate change is predicted to effect precipitation and evaporation, which controls the delivery or export of freshwater to and from lakes (Carpenter et al., 1992). Climate change is also predicted to shift macrofauna communities, which have been shown to greatly influence methane production in freshwater lakes (Emilson et al., 2018). Climate change is further projected to cause enhanced eutrophication in freshwater lakes. Enhanced eutrophication can lead to deoxygenation and elevated organic matter loading in the underlying sediments, stimulating more methane production (Bastviken et al., 2008; Bastviken et al., 2011; Moss et al., 2011). Furthermore, warming can influence organic matter turnover by microbial activity, which can lead to lower carbon storage in sediments, which could in turn release more methane from freshwater lakes (Moss et al., 2011; Walter et al., 2006). Although freshwater lakes appear to be geographical features that contributes to atmospheric methane emissions, it is certainly not the largest.

Wetlands

Globally, natural wetlands represent the largest natural source of methane to the atmosphere on Earth, emitting 181 Tg CH_4 yr^{-1} and 149 Tg CH_4 yr^{-1} according to top-down and bottom-up estimates, respectively (Saunois et al., 2020), despite covering only ~6% of all land surfaces globally (Reddy and DeLaune, 2008). Wetlands can be defined as the transitional land between terrestrial and aquatic landforms, where the groundwater surface is at, or near, the topographic ground surface (Reddy and DeLaune, 2008). Wetlands are extremely productive ecosystems and contain large inventories of inorganic and organic matter (Al-Haj and Fulweiler, 2020; Reddy and DeLaune, 2008). They represent inundated land that is covered with a shallow water column, which can be categorized into two general groups, coastal and freshwater wetlands (Reddy and DeLaune, 2008).

Coastal wetlands occupy the geographic transition between terrestrial and marine environments and thus their methane emissions are governed by salinity (Reddy and DeLaune, 2008). Consequently, coastal wetlands tend to be exposed to high concentrations of sulfate from the marine environment, which leads to less atmospheric emissions. This is largely because of the reduced methanogenesis activity in sulfate-rich sediment and also the strong AOM activity (Poffenbarger et al., 2011), which will be discussed in upcoming sections.

Freshwater wetlands, in contrast to their coastal counterparts, are characterized by high rates of methanogenesis and thus contribute the most methane emissions out of all natural sources (Segarra et al., 2015). Although freshwater wetlands contain large inventories of methane, AOM has also been detected (Segarra et al., 2013a; Segarra et al., 2015) and is estimated to reduce methane emissions by about 50% (Segarra et al., 2015).

9

Within the 20th century, 64% of all wetlands have been lost globally and are expected to experience further damage by climate change (Gardner et al., 2015; Segarra et al., 2015). Warming on a global scale could lead to sea level rise impacting coastal wetlands with seawater inundation, delivering sulfate and organic matter. Vizza et al., (2017) performed experiments that simulated seawater intrusion and enhanced organic matter input to wetland sediments. Their study showed that wetlands are sensitive to enhanced additions of organic matter due to sea level rise and could enhanced methane production (Vizza et al., 2017). In freshwater wetlands, warmer temperatures from climate change could enhance organic matter degradation and CO_2 emissions (Desta et al., 2012; Reddy and DeLaune, 2008).

In this introductory chapter we have so far discussed the global methane budget and geographical locations where methane can be commonly found. In the next sections I will discuss how organic matter is degraded leading to methane production and consumption in sedimentary and aquatic systems.

Organic matter remineralization in aquatic sediment

In sediment, organic matter is degraded by biological activity following basic laws of thermodynamics (Jørgensen, 2000; Kristensen, 2000). Eukaryotes and prokaryotic microorganisms use enzymes to catalyze reduction-oxidation (Redox) chemical reactions, to transfer electrons from donors (which can be organic matter) to electron acceptors (O_2, NO_3^-, Mn (VI), Fe(III), SO_4^{2-}, CO_2). These redox reactions generate a proton motive gradient between the inside and outside of the cell. Proton reentry into the cell ultimately conserves energy by generating adenosine triphosphate (ATP). This stored energy is then used by the cell to perform a variety of biological functions such as growth and cell division, movement, macromolecule synthesis,

transport of molecules in and out of the cell membrane etc. (Jørgensen, 2000). The order at which a particular electron acceptor is utilized by microorganisms is primarily dictated by the free energy yield of the redox reaction and the availability of electron donor and acceptor. Thus, the electron acceptor that yields highest Gibbs free energy is preferentially utilized first (Jørgensen, 2000). Equation 1 shows the standard Gibbs free energy (ΔG^o) equation in kJ mol^{-1},

$$\Delta G^o = -RT(\ln K) \tag{1}$$

Where R represents the ideal gas constant (Joules per temperature, in Kelvin, per mol), T is temperature in Kelvin, and K is the equilibrium constant of the reaction. Please note that ΔG^o here is the free energy yield at standard conditions (25°C, pH 7, 1 bar pressure, and 1 mol/L concentration of reactants and products). These standard conditions, however, are rarely met in the environment, and actual environmental conditions have to be determined before free-energy yield can be is quantified. Table 1-1 provides ΔG^o of the typical redox reactions that can occur in sediment. Oxygen yields the highest ΔG^o, and in oxygenated sediment, aerobic chemoheterotrophic microbes breakdown complex organic matter, such as glucose, to smaller units and CO_2 through aerobic respiration (Conrad, 2020). Below the O_2 penetration depth, metabolisms switch to anaerobic metabolic pathways. This is done by groups of facultative and/or obligate anaerobic chemoheterotrophic microorganisms, which through fermentation, continue to break down sugars, amino acids, and long chain fatty acids to lower molecular weight molecules such as lactate, butyrate, propionate, acetate, alcohols, methylated amines, hydrogen and CO_2 (Fenchel and Jørgensen, 1977; Jørgensen, 2000; Whiticar, 2020). The products of fermentation listed above are further consumed by chemoheterotrophs and chemoautotrophs using terminal electron acceptors (NO_3^-, Mn (VI), Fe(III), SO_4^{2-}, CO_2) following the thermodynamic order as mentioned above. This process classically imparts unique geochemical profiles and zonation's in

aquatic sediment (Jørgensen, 2000; Kristensen, 2000). After O_2, NO_3^-, Mn^{4+}, and Fe^{3+} are consumed, and before methanogenesis occurs, sulfate reduction is the dominant metabolic pathway, where chemoheterotrophic sulfate-reducing bacteria consume hydrogen and organic material such as acetate (Canfield, 1989; Jørgensen, 1977; Jørgensen, 2021). Sulfate is an important component of seawater, with concentrations of ~28 mM, which has major effects on methane production, as discussed below.

Pathway and stoichiometry of reaction	ΔG^0 (kJ mol-1)
Oxic respiration:	
$CH_2O + O_2 \rightarrow CO_2 + H_2O$	-479
Denitrification:	
$5CH_2O + 4NO_3^- \rightarrow 2N_2 + 4HCO_3^- + CO_2 + 3H_2O$	-453
Mn(IV) reduction:	
$CH_2O + 3CO_2 + H_2O + 2MnO_2 \rightarrow 2Mn^{2+} + 4HCO_3^-$	-349
Fe(III) reduction:	
$CH_2O + 7CO_2 + 4Fe(OH)_3 \rightarrow 4Fe^{2+} + 8HCO_3^- + 3H_2O$	-114
Sulfate reduction:	
$2CH_2O + SO_4^{2-} \rightarrow H_2S + 2HCO_3^-$	-77
$4H_2 + SO_4^{2-} + H^+ \rightarrow HS^- + 4H_2O$	-152
$CH_3COO^- + SO_4^{2-} + 2H^+ \rightarrow 2CO_2 + HS^- + 2H_2O$	-41
Methane production:	
$4H_2 + HCO_3^- + H^+ \rightarrow CH_4 + 3H_2O$	-136
$CH_3COO^- + H^+ \rightarrow CH_4 + CO_2$	-28
Acetogenesis:	
$4H_2 + 2CO_3^- + H^+ \rightarrow CH_3COO^- + 4H_2O$	-105
Fermentation:	
$CH_3CH_2OH + H_2O \rightarrow CH_3COO^- + 2H_2 + H^+$	10
$CH_3CH_2COO^- + 3H_2O \rightarrow CH_3COO^- + HCO_3^- + 3H_2 + H^+$	77

Table 1-1. Degradation pathways with various electron acceptors and associated standard Gibbs free energy (ΔG^o) published within Jørgensen, (2000) . Free energy values for the (Jørgensen, 2000) publication are from Thauer, (1977), Conrad et al., (1986) and Fenchel et al., (1998).

Microbial methanogenesis

In anoxic sediment, methane is known to be formed through three metabolic pathways (Table 1-2). Most microbially produced methane is generated in deeper sulfate-free sediment, either with hydrogen and CO_2 (hydrogenotrophic) or with acetate (acetoclastic). Hydrogenotrophic

and acetoclastic methanogenesis are often termed as "competitive methanogenesis" because these types of methanogenesis compete with sulfate reduction for hydrogen and acetate as electron donors. The reason for the competitive nature between methanogenesis and sulfate reduction is that more free energy is obtained from the redox reaction of hydrogen and/or acetate with sufficient availability of sulfate (Table 1-1). Thus, sulfate reduction tends to suppress methanogenesis (Oremland and Polcin 1982, Schönheit et al., 1982, King, Klug, and Lovely 1983, Reeburgh, 2007). However, the third methanogenesis pathway, known as methylotrophic methanogenesis, is often referred to as non-competitive methanogenesis because it can co-occur with sulfate-reduction. This type of methanogenesis utilizes non-competitive substrates, such as methionine, methanol, and methylated amines (Table 2) that are typically not consumed by other organisms (Oremland and Polcin 1982, King, Klug, and Lovely 1983, Capone and Keine 1988, and Maltby et al., 2016).

Pathway Name	Representative Reactions	ΔG^o (KJ mol^{-1})
Hydrogenotrophic	$CO_2 + H_2 \rightarrow CH_4 + 2H_2O$	-131
Acetoclastic	$CH_3COO^- + H^+ \rightarrow CH_4 + CO_2$	-36
Methylotrophic (Methylsulfide)	$2(CH_3)_2S + 2H_2O \rightarrow 3CH_4 + CO_2 + H_2S$	-74
Methylotrophic (Methanol)	$4CH_3OH \rightarrow 3CH_4 + CO_2 + 2H_2O$	-105
Methylotrophic (Mono-methylamine)	$4CH_3NH_3^+ + 2H_2O \rightarrow 3CH_4 + CO_2 + 4NH_4^+$	-75
Methylotrophic (Di-methylamine)	$2(CH_3)_2NH_2^+ + 2H_2O \rightarrow 3CH_4 + CO_2 + 2NH_4^+$	-73
Methylotrophic (Tri-methylamine)	$4(CH_3)_3NH^+ + 6H_2O \rightarrow 9CH_4 + 3CO_2 + 4NH_4^+$	-74

Table 1-2. Main microbial methanogenesis pathways by methanogenic archaea and associated standard Gibbs free energy (ΔG^o). Free energy values are from Whiticar, (2020).

Methanogenic archaea are obligate anaerobes responsible for the last step of organic matter degradation (Thauer, 1998). Groups of methanogens generally fall within the *Euryarchaeota, Crenarchaeota, Halobacterota* and *Thermoplasmatota* phyla (Fig. 1-3) (Lyu et al., 2018). Groups

of methanogens that perform hydrogenotrophic methanogenesis are considered chemolithoautotrophs because they fix CO_2 with hydrogen without light as the energy source. In contrast, groups of methanogens that perform acetoclastic and methylotrophic methanogenesis fall into the category of chemoheterotrophs. All methanogenic archaea use the methyl – coenzyme M reductase (Mcr), which is the key enzyme and the last step in the methanogenetic pathway where methane is ultimately produced (Lyu et al., 2018; Thauer, 1998).

Figure 1-3. Phylogenetic schematic of archaea across 10 phyla originally generated and published by Lyu et al., (2018). Methanogens are found within the bolded phyla *Euryarchaeota, Crenarchaeota, Halobacterota,* and *Thermoplasmatota.* Parentheticals next to the names of methanogen groups in purple signify the trophic types for each methanogen; Hydrogenotrophic (H_2), Acetoclastic (Ac), and Methylotrophic (Me).

Microbial methanogenesis is not necessarily exclusive to anoxic environments. Aerobic methanogenesis activity has been detected in marine and freshwater environments (Bižić et al., 2020). In the ocean water column, methane is typically undersaturated compared to the methane concentrations in the atmosphere. However, methanogenesis can occur under oxic conditions in the water column which has been termed the 'oceanic methane paradox'(Karl et al., 2008; Kiene, 1991; Reeburgh, 2007). In this scenario, methane is produced through the utilization of methylphosphonate, which is a

constituent in marine phytoplankton biomass and particulate and dissolved organic carbon in the seawater (Kittredge et al., 1969; Kittredge and Roberts, 1969; Kolowith et al., 2001). Bacteria, including mixotrophic cyanobacteria, in the water column use these methylphosphonates as a phosphorus source which is assimilated into the biomass, while methane is released into the seawater where it can also equilibrate with the atmosphere (Bižić et al., 2020; Daughton et al., 1979; Karl et al., 2008; Teikari et al., 2018). Cyanobacteria have also been implicated in in-vitro co-culture studies where a hydrogenase-deficient cyanobacteria strain was found to supply hydrogen to hydrogenotrophic methanogens when being subjected to increasing light intensities (Berg et al., 2014).

In addition, fungi have also been found to play a role in indirect and direct methane production. Fungi found within abandoned coal mines have been shown to release substrates from the degradation of coal that are then converted into methane by methanogenesis (Beckmann et al., 2011). Fungi that degrade wood have been shown to be accompanied by methanogens, where the fungi perform aerobic respiration while the methanogens produce methane from the biproducts of the fungal respiration (Mukhin and Voronin, 2007, 2008). White and brown rot fungus have been shown to directly produce methane anaerobically without the presence of methanogenic archaea (Lenhart et al., 2012). Furthermore, these fungi have been found to exhibit similar bulk carbon stable isotope signatures to those of methane producing archaea (Schroll et al., 2020).

Microbial methane oxidation

Methane production in sediment is balanced by microbial methane oxidation. As previously discussed, atmospheric methane is primarily oxidized abiotically by hydroxyl and chlorine radicals (Reeburgh, 2007; Saunois et al., 2020). However, before methane is emitted into

the
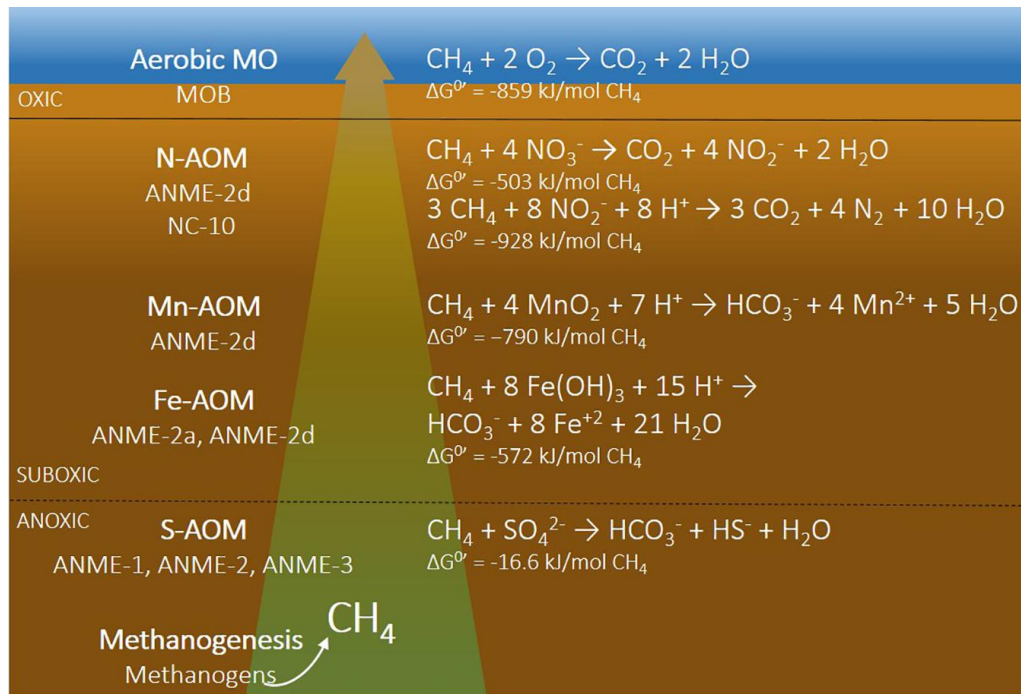
Figure 1-4. Schematic of microbial oxidation of methane pathways and the associated standard Gibbs free energy (ΔG^o). From Wallenius et al., (2021).

atmosphere, there exist several biological filters that oxidize methane to gain energy and produce inorganic carbon. To date the literature provides extensive evidence of methane oxidation by both aerobic and anaerobic chemoheterotrophic microorganisms, utilizing a variety of electron acceptors (Knittel and Boetius, 2009; Wallenius et al., 2021 and references therein). Figure 1-4 illustrates the various metabolic pathways of methane oxidation together with their associated Gibbs free energy yield and their relative position in the sediment column.

Aerobic oxidation of methane

Aerobic oxidation of methane (MOx) is mediated by two main types of aerobic methane-oxidizing bacteria (Type I and II) (*Pseudomonadota* phylum). The difference between the two types is the pathway to fix formaldehyde into the biomass, i.e., Ribulose Monophosphate (RuMP) pathway for Type I and the Serine pathway for Type II (Hanson and Hanson, 1996). Before formaldehyde is produced, the main enzyme that is responsible for oxidizing methane to methanol is the methane monooxygenase, which can either be in soluble or in particulate form (Hanson and

Hanson, 1996; Murrell, 2010). Aerobic methane-oxidizing bacteria are ubiquitously found in nature and responsible for oxidizing methane in a wide range of oxygenated environments (Murrell, 2010; Wallenius et al., 2021). MOx has been detected in oxygenated environments like soils (Henckel et al., 2000), freshwater lakes (Guggenheim et al., 2020) marine water columns above cold seeps (Boetius and Wenzhöfer, 2013; Steinle et al., 2015; Valentine et al., 2001), hypoxic coastal environments (Steinle et al., 2017), and marine sediments (Steinle et al., 2016).
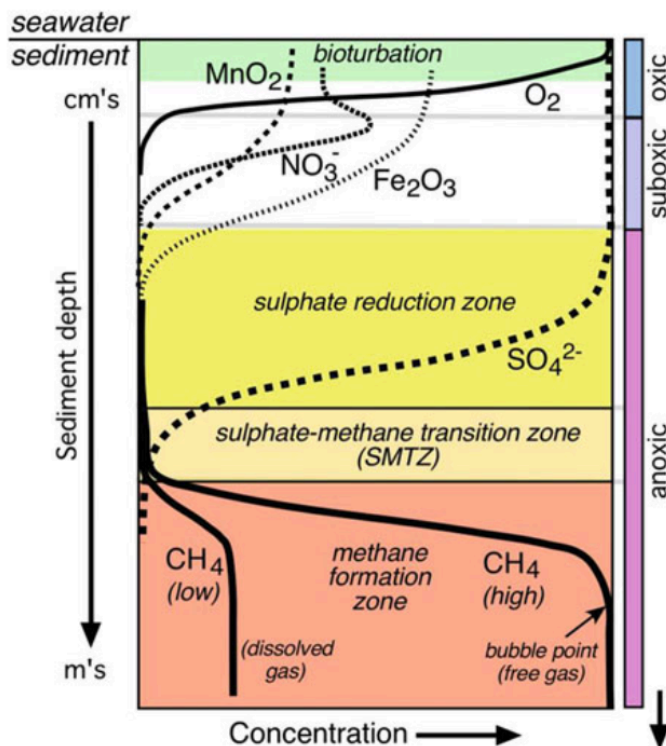
Figure 1-5. Schematic representing a sediment depth profile showing geochemical trends of inorganic and organic molecules and geochemical redox zonation's originally published in Whiticar, (2020)

Sulfate-dependent anaerobic oxidation of methane

In anoxic sediment, methane produced from methanogenesis in the deeper sulfate-free sediment diffuses upwards through the sediment column. Before this methane reaches the water column, sulfate-dependent AOM efficiently consumes a majority of methane that diffuses through the sulfate reduction zone (Knittel and Boetius, 2009). During the sulfate-dependent AOM, methane is oxidized to inorganic carbon and is coupled to sulfate reduction where sulfate acts as the terminal electron acceptor for the reaction (Fig. 1-4) (Knittel and Boetius 2009). This simultaneous consumption of sulfate and methane imparts a unique geochemical signature within

17

the sediment column, the sulfate-methane transition zone (SMTZ), where both the methane and sulfate concentrations intersect (Fig. 1-5) (Iversen and Jørgensen, 1985; Knittel and Boetius, 2009).

AOM activity is also a feature in sediment within freshwater environments (Knittel and Boetius, 2009; Wallenius et al., 2021). However, sulfate is not the dominant electron acceptor for AOM, in freshwater sediments, because sulfate concentrations in freshwater environments are typically much lower (100-200 μM) than in marine environments (28-29 mM). Thus, AOM activity in freshwater sediment is typically coupled to alternative electron acceptors present in freshwater systems, which will be discussed in upcoming sections (Martinez-Cruz et al., 2018; Reeburgh, 2007; Zehnder and Brock, 1980).

The majority of AOM pathways are reverse methanogenesis, because they use the same enzymatic steps in reverse, where Mcr is the key enzyme for consuming methane (Hallam et al., 2004; Timmers et al., 2017). The reversal of the Mcr enzyme in AOM is endergonic at standard conditions. To overcome this energy hurdle, the electrons from methane are shuttled to an electron acceptor, e.g., sulfate, which allows sulfate-dependent AOM to be exergonic (Timmers et al., 2017). In sediment that where sulfate is limiting (e.g. the lower boundaries of the SMTZ) AOM has been shown to "back-flux" inorganic carbon to methane (Yoshinaga et al., 2014), further highlighting the reversibility of the methanogenesis/methanotrophy enzymatic pathway.

Sulfate-dependent AOM is performed by anaerobic methanotrophic archaea (ANME) either independently or in a consortium with Deltaproteobacteria (Knittel and Boetius, 2009; McGlynn et al., 2015; Milucka et al., 2012; Orphan et al., 2001b; Wegener et al., 2015). There are three distinct groups of ANME: ANME-1 (a and b subclusters), ANME-2 (a, b, and c subclusters), and ANME-3, which have all been shown to have bacterial partnerships with sulfate reducers

(Knittel and Boetius, 2009; Timmers et al., 2017). ANME-1 and ANME-2 are typically associated with the sulfate-reducing bacteria *Desulfosarcina* and *Desulfococcus* (Boetius et al., 2000; Knittel et al., 2005; Knittel et al., 2003; Michaelis et al., 2002; Orphan et al., 2002; Orphan et al., 2001b; Reitner et al., 2005; Treude et al., 2007), while ANME-3 has been found associated with *Desulfobulbus* (Lösekann et al., 2007). ANME-1 are typically found as rectangular cells, individually or in chains surrounded by sulfate-reducing bacteria (Reitner et al., 2005). In contrast, ANME-2 and 3 typically form aggregates with sulfate-reducing bacteria (Lösekann et al., 2007; Niemann et al., 2006; Orphan et al., 2002; Treude et al., 2007). However, on occasion, ANME-2 and ANME-3 can be found in single cells (Omoregie et al., 2008; Treude et al., 2005).

Metal-dependent AOM

AOM has also been shown to be coupled to manganese- and iron-bearing minerals (Beal et al., 2009) and to oxidized metal analogues (Scheller et al., 2016). Beal et al. (2009) showed that the free energy gain from birnessite and ferrihydrite was 10 and 2 times more, respectively, than the free energy gain provided by sulfate as the electron acceptor for AOM. Metal-dependent AOM has been linked to methane consumption in a variety of marine (Beal et al., 2009; Egger et al., 2017; Riedinger et al., 2014; Rooze et al., 2016; Wankel et al., 2012) and brackish sediments (Egger et al., 2015). Metal-dependent AOM has also been detected in freshwater lake (Crowe et al., 2011; Norði et al., 2013; Su et al., 2020) and wetland systems (Segarra et al., 2013a; Valenzuela et al., 2019).

The microbial players involved with metal-dependent AOM are poorly understood (Timmers et al., 2017; Wallenius et al., 2021). However, it has been speculated that *Methanohalobium and Methanococcoides*/ANME-3 could be responsible for iron and manganese-

dependent AOM, respectively (Gupta et al., 2013; Oni et al., 2015). ANME-2 a and c have been suggested to oxidize methane with humic substances and soluble metal oxide minerals as electron acceptors (Scheller et al., 2016). ANME-2d is speculated to use extracellular structures to transfer electrons from methane to solid-phase iron (Egger et al., 2015; Kletzin et al., 2015).

Metal oxides as an electron acceptor for AOM are hypothesized to become more important with enhanced effects from climate change (Egger et al., 2015). Climate change effects such as enhanced eutrophication of the marine environment could lead to greater amounts of organic matter being loaded into the sediment. Such increased sediment loading with organic constituents could shift SMTZ's upwards within the sediment column as sulfate becomes more depleted from the enhanced sulfate reduction of the excess organic matter. As sulfate becomes more deplete, iron oxides buried below the SMTZ could then be coupled to AOM (Rooze et al., 2016; Wallenius et al., 2021). Anthropogenic activities that change natural landscapes or regional climates (or both) could also lead to enhanced input of organic matter and iron into sediment (Jickells et al., 2005; Lenstra et al., 2018). Such increased amounts of organic matter and iron could in turn trigger iron-dependent AOM (Wallenius et al., 2021).

Nitrate and nitrite dependent AOM

Nitrate and nitrite, when coupled to AOM, have reportedly yielded ~45 and ~24 times more free energy, respectively, as an electron acceptor than sulfate (Wallenius et al., 2021) (Fig. 1-4). Several investigation demonstrated that both bacteria and archaea are responsible for coupling nitrate and nitrite reduction to AOM in a wide range of environments, including: coastal marine sediments (Shen et al., 2016; Wang et al., 2018), oxygen minimum zones (Padilla et al., 2016; Thamdrup et al., 2019), wetlands (Hu et al., 2014; Wang et al., 2022; Zhang et al., 2022) and

freshwater lake sediments (Deutzmann et al., 2014; Luesken et al., 2011; Raghoebarsing et al., 2006; Shen et al., 2015).

Candidatus 'Methylomirabilis oxyfera' is the bacterium known to couple nitrite reduction with AOM. In doing so they utilize the oxygen biproduct from denitrification within the cell, which subsequently proceeds to oxidize methane using the methane monooxygenase from the aerobic oxidation of methane pathway (Allen and Van Niel, 1952; Ettwig et al., 2010; Guerrero-Cruz et al., 2018; Versantvoort et al., 2018). In contrast, ANME-2d within the ANME-2 clade of the Methanoperedenaceae are known to couple nitrate reduction to AOM (Guerrero-Cruz et al., 2018; Haroon et al., 2013; Timmers et al., 2017). The bacteria and archaea groups responsible for nitrate- and nitrite-dependent AOM are not typically part of a consortium, nor are they in syntropy with another microbial partner (Guerrero-Cruz et al., 2018; Wallenius et al., 2021).

Despite recent efforts, nitrate- and nitrite-dependent AOM is one of the least understood pathways for methane oxidation in terms of rate limitations, abundance of bacteria and archaea, and their impact on methane consumption in the environment (Wallenius et al., 2021; Welte et al., 2016). However, nitrate- and nitrite-dependent AOM are hypothesized to become increasingly important for methane removal. This is especially important in light of enhanced eutrophication, driven by anthropogenic activities and/or climate change, resulting in greater loading of organic matter and increased nitrate and nitrite concentrations from the decomposition of biomass from primary producers (Kraft et al., 2014; Wallenius et al., 2021).

Cryptic methane cycling

Recent studies reported methylotrophic methanogenesis activity in the sulfate-reducing zone off the coast of Peru (Maltby et al., 2018a) and in the Baltic Sea (Maltby et al., 2016). In this

context, Maltby et al. postulated that methane from methylotrophic methanogenesis could be directly oxidized by sulfate-dependent AOM as part of a cryptic methane cycle that has been previously overlooked. Since the coining of the cryptic methane cycle, a few studies directly detected this activity. Xiao et al. (2017) and (2018a) provided the first evidence of this cryptic methane cycle within anoxic organic-rich sediment from Aarhus Bay, Denmark. In these studies, sediment was incubated with ^{13}C-methane and the evolution of the ^{13}C signal was monitored over time. Results from the incubation were applied to an isotope dilution model, which showed the change in the ^{13}C-methane and ^{13}C-CO$_2$ mass balance as a result of concurrent methane production from indigenous carbon sources and AOM.

In another study, Bhattacharya et al. (2021) detected groups of methanogens, ANME and sulfate-reducing bacteria together in organic rich sediment collected near the sediment-water interface within the Arabian sea through metagenomic and metatranscriptomic analysis. Bhattacharya et al. (2021) concluded that the lack of detectable methane in the upper sulfidic sediment could be caused by an active cryptic methane cycle as indicated by the tandem abundance of both ANME and methanogens in their molecular analysis.

Hypothesis for cryptic methane cycling

This dissertation will present original research to test the original postulations by Maltby et al. (2016; 2018) and compare with the cryptic methane cycling results reported by Xiao et al. (2017; 2018). **The general hypothesis for this dissertation is that methane produced from methylotrophic methanogenesis is directly shuttled to AOM within the sulfate-reducing zone, in coastal wetland and marine sediments.** The significance of the findings from testing this hypothesis will help investigators determine whether repeated observations of

characteristically low methane concentrations within the sulfate-reduction zone could be appropriately explained by the cryptic methane cycle. In other words, if cryptic methane cycling is indeed responsible for a dramatic reduction of methane concentrations within the sulfate-reduction zone near the sediment-water interface, then cryptic methane cycling would need to be significantly more emphasized during the development of future methane budgets because the current methane budget is missing this process that is simultaneously producing and consuming methane. Moreover, properly and accurately defining the role of cryptic methane cycling should greatly improve evaluations of global warming and climate change, as it relates to the introduction of methane into Earth's atmosphere through emanations from marine and other aqueous environments.

Part II: Introduction to isotopic signatures of methane sources and sinks

Methane bulk stable isotope signatures and their applications

In part one of the introduction to this dissertation, it was mentioned that methane can be categorized as originating from biogenic, thermogenic, and abiotic sources. Stable carbon ($^{13}C/^{12}C$) and hydrogen (D/H) isotope ratios of methane have been used extensively to map out methane source regimes for decades (Fig. 1-6) (Etiope and Schoell, 2014; Schoell, 1980; Schoell, 1988; Whiticar, 1993, 1999; Whiticar, 2020). These bulk stable isotope ratios are expressed in the standard delta notation (δ) and reported as ‰ values. Values are referenced against international standards, i.e., Vienna PeeDee Belemnite (VPDB) for $\delta^{13}C$ and Vienna Standard Mean Ocean Water (VSMOW) for δD. The bulk stable isotope signatures for biotic methane sources, which have the lowest numerical signatures, can range between approximately −40 and −120‰ and −450 and −150‰ for $\delta^{13}C$ and δD, respectively. For thermogenic sources bulk isotope values can range between −20 and −57‰ and −300 and −100‰, respectively. Abiotic methane has by far the highest stable isotope signatures, and ranges between 0 and −50‰ and ~ −50 to −450‰, respectively.
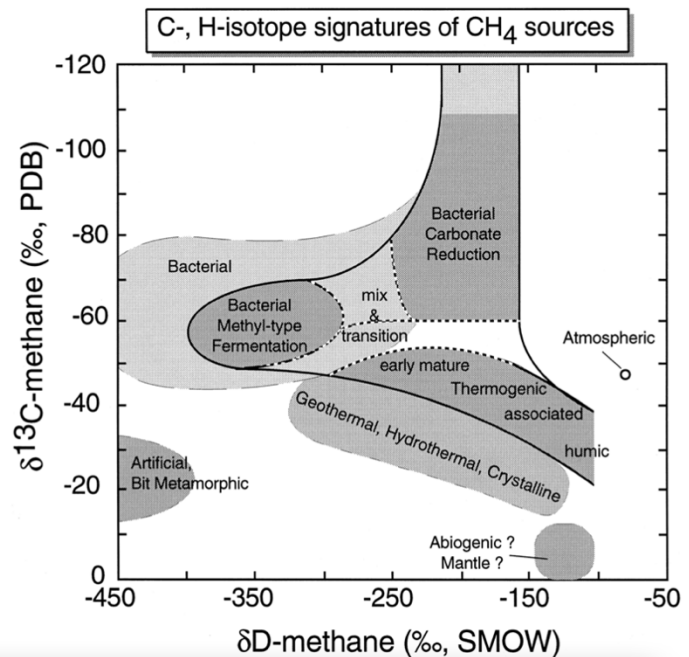
Figure 1-6. Diagram indicating methane source regimes of biogenic, thermogenic and abiotic based on the $\delta^{13}C$ versus δD values of each methane source, originally published in Whiticar, (1999).

As mentioned in Part I of this introduction chapter, methane can be oxidized in the environment by biological sinks (aerobic and anaerobic oxidation of methane) and abiotically in the atmosphere by primarily hydroxyl radicals (Reeburgh, 2007). Generally, microbial methane oxidation results in more positive values of the residual $\delta^{13}C$-CH4 (approximately −60 to −20‰) and δD-CH4 (approximately −350 to −70‰) with progressing methane consumption (Fig. 1-7).
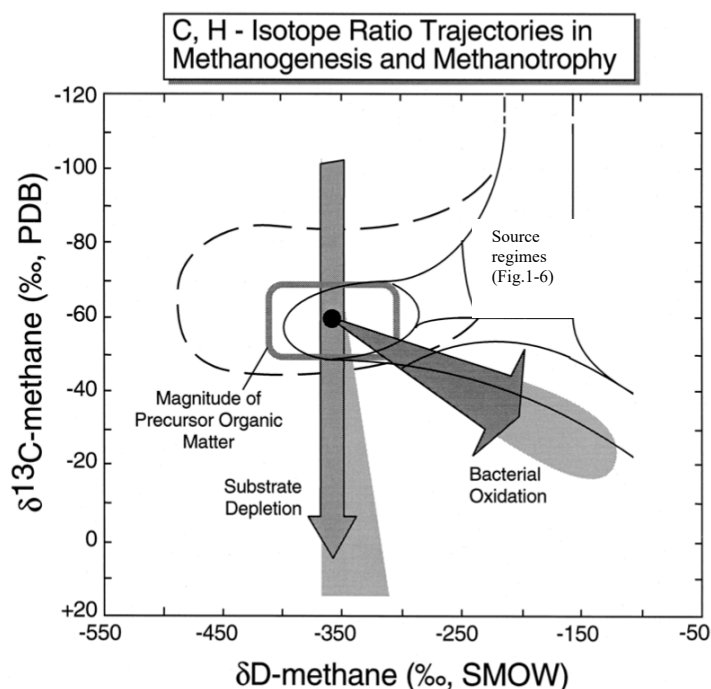
Figure 1-7. Diagram representing theoretical shift in the residual methane isotopic composition values ($\delta^{13}C$ and δD) due to substrate depletion and methane oxidation in relation to the methane source regime (dashed and solid lines with no fill) in Figure 1-6, originally published in Whiticar, (1999).

The differences in the $\delta^{13}C$ and δD of methane signatures that distinguish biotic sources from all other sources and from methane oxidation are largely controlled by 1) the isotopic composition of the source material from which methane is derived, and 2) kinetic isotope effects. Compounds from which methane can be derived that have a lower isotopic mass (e.g., $^{12}CO_2$ versus $^{13}CO_2$) generally react faster kinetically in biochemical reactions resulting in preferential conversion of various lighter ^{12}C-substrates to produce ^{12}C-methane, (Fig. 1-8) (Hayes, 2004; Whiticar, 1999; Whiticar, 2020).
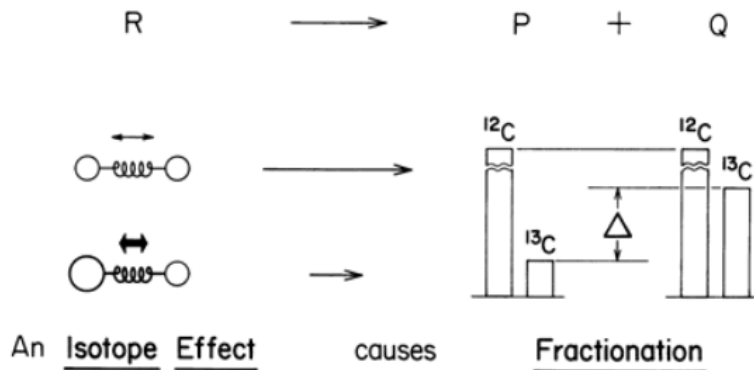
Figure. 1-8 Diagram showing the relationship between kinetic isotope effects of isotopically lighter versus heavier molecules and the difference in the quantitative isotope fractionation caused by kinetic isotope effects, originally published in Hayes, (2004)

A major challenge posed in traditional bulk isotope signatures of methane is that there is considerable overlap between the various methane sources (Fig. 1-6) and between methane sources and sinks (Fig.1-7). It is very difficult to determine whether the bulk isotopic composition of a carbon pool of interest (methane in this case) is reflecting the isotopic fractionation from a source with a different composition, or when two reservoirs that are isotopically distinct from each other combine to form a pool that is isotopically mixed (Eiler, 2007)

Clumped isotopologues (doubly-substituted isotopologues)

Eiler (2007) provides a comprehensive review on the study of naturally-occurring, clumped isotopologues. Note that in the literature clumped isotopologues, doubly – substituted isotopologues, and multiply-substituted isotopologues are used interchangeably. For simplicity in this introductory chapter, clumped isotopologues will be the preferred terminology. Clumped isotopologues, refers to compounds that contain more than one isotopically heavier element(s) in a molecule (Eiler, 2007). Clumped isotopologues are much more diverse than their single substituted counterparts since there exist multiple combinations of element arrangements within a

26

molecule. However, in any of Earth's environments, they are extremely rare in abundance on the order of 10's of parts per million.

Clumped isotopologues are denoted using Δ, which is the difference (given in ‰), between the measured abundance of the isotopologue of interest and the abundance of the isotopologue expected for the stochastic distribution for the sample. The stochastic distribution, in the context of clumped isotopologues, refers to the random distribution of all stable isotopes in a population of molecules among all possible variations of the isotopologues. It is important to note that as the bulk isotope composition varies, so does the absolute abundance of the clumped isotopologue species. However, the Δ value of clumped isotopologues is not influenced by the bulk isotope composition, instead the Δ measures the tendency of rarer isotopes to form clumped isotopologues either more or less than what would occur randomly through probability and statistics (Eiler, 2007).

Methane clumped isotopologues

Figures 1-6 and 1-7 show that the traditional use of bulk isotope compositions can help investigators determine a methane source provenance and the tendency of bulk isotope compositions to shift in the residual methane pool with greater methane oxidation. However, those diagrams also show overlap between methane source provenances. Moreover, bulk isotopic compositions of residual methane can mimic isotope compositions from a source (Whiticar, 1999; Whiticar, 2020). To help resolve these ambiguities caused by the overlapping within methane provenances in bulk isotope space, recent technological advancements enabled the application of two clumped isotopologues of methane, $^{13}CH_3D$ (Ono et al., 2014) and $^{12}CH_2D_2$ (Young et al., 2017; Young et al., 2016).

Generally, clumped isotopologues have been used as intramolecular geothermometers to determine formation temperature ranges for methane sources (Eiler, 2007). This application is useful because the abundance of methane clumped isotopologues is dependent on temperature, which is theoretically determined by quantum chemistry and statistics (Liu and Liu, 2016; Webb and Miller III, 2014) and validated by methane samples with known formation temperatures (Young et al., 2017).

To see the relationship between the abundance of methane clumped isotopologues and temperature, one must focus on the fractional abundances of heavy stable isotopes of carbon (^{13}C) and hydrogen (D) as seen in Equations 1 and 2,

$$X(^{13}C) = \frac{^{13}C}{^{13}C + ^{12}C} \tag{1}$$

$$X(D) = \frac{D}{D+H} \tag{2}$$

To then derive the random distribution of isotopologues, the fractional abundances are treated as probabilities, for example

$$X(^{12}CH_4) = X(^{12}C)(X(H))^4 \tag{3}$$

$$X(^{13}CH_4) = X(^{13}C)(X(H))^4$$

$$X(^{12}CH_3D) = 4X(^{12}C)(X(H))^3 X(D)$$

$$X(^{13}CH_3D) = 4X(^{13}C)(X(H))^3 X(D)$$

where the exponents are the multiplicity of isotopic isomer abundances. Equations 4 and 5 shows the exchange reactions that occurs between isotopologues for $^{13}CH_3D$ and $^{12}CH_2D_2$, respectively.

$$^{13}CH_4 + {}^{12}CH_3D \leftrightarrow {}^{12}CH_4 + {}^{13}CH_3D \tag{4}$$

$$2\,^{12}CH_3D \leftrightarrow\ ^{12}CH_2D_2 +\ ^{12}CH_4 \tag{5}$$
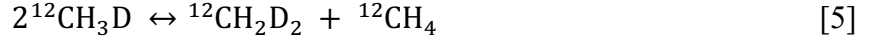
Equations 6 and 7 are the respective equilibrium constants for the above exchange reactions seen in Equations 4 and 5,

$$k_{Eq,^{13}CH_3D} = \frac{[^{13}CH_3D][^{12}CH_4]}{[^{13}CH_4][^{12}CH_3D]} \tag{6}$$

$$k_{Eq,^{12}CH_2D_2} = \frac{[^{12}CH_2D_2][^{12}CH_4]}{[^{12}CH_3D]^2} \tag{7}$$

where k_{Eq} is the equilibrium constant for each methane isotopologue and the square brackets represent the concentrations of the fractional abundances of the isotopologues. At higher temperatures (>1000°C) the intermolecular bond strength is unstable and distribution of all isotopologues are stochastic. The fractional concentrations in Equations 6 and 7 can be substituted with the probabilities in Equation 3, such that,

$$k_{Eq,^{13}CH_3D} = \frac{4X(^{13}C)(X(H))^3 X(D)X(^{12}C)(X(H))^4}{4X(^{12}C)(X(H))^3 X(D)X(^{13}C)(X(H))^4} = 1 \tag{8}$$

$$k_{Eq,^{12}CH_2D_2} = \frac{6X(^{12}C)(X(H))^2 X(D)^2 (X(H))^4}{\left[4X(^{12}C)(X(H))^3 X(D)\right]^2} = \frac{3}{8} \tag{9}$$

The relative abundances of methane clumped isotopologues differs from the stochastic distribution at lower temperatures due to the enhanced thermodynamic stability of bonds involving the heavier isotopes. Equations 10 and 11 show how ‰ shifts of $^{13}CH_3D$ and $^{12}CH_2D_2$ away from the stochastic unity is quantified using delta notation,

$$\Delta_{^{13}CH_3D} = 10^3 \left(\frac{X(^{13}CH_3D)}{X(^{12}CH_2D)_{stochastic}} - 1 \right) \tag{10}$$

$$\Delta_{^{12}CH_2D_2} = 10^3 \left(\frac{X(^{12}CH_2D_2)}{X(^{12}CH_2D_2)_{stochastic}} - 1 \right) \tag{11}$$

The relationship between $\Delta^{13}CH_3D$ and $\Delta^{12}CH_2D_2$ and temperature have been calculated (Liu and Liu, 2016; Ma et al., 2008; Webb and Miller III, 2014). When $\Delta^{13}CH_3D$ and $\Delta^{12}CH_2D_2$ are plotted together, the intersection of the two isotopologues at thermodynamic equilibrium provide a useful reference curve (Young et al., 2017) (Fig. 1-9). Sample measurements that plot on the equilibrium curve would apparently represent thermodynamic equilibrium at the temperatures the methane clumped isotopologues record intramolecularly. However, kinetics has been identified to explain how data can plot away from the thermodynamic equilibrium curve, which will be discussed next.
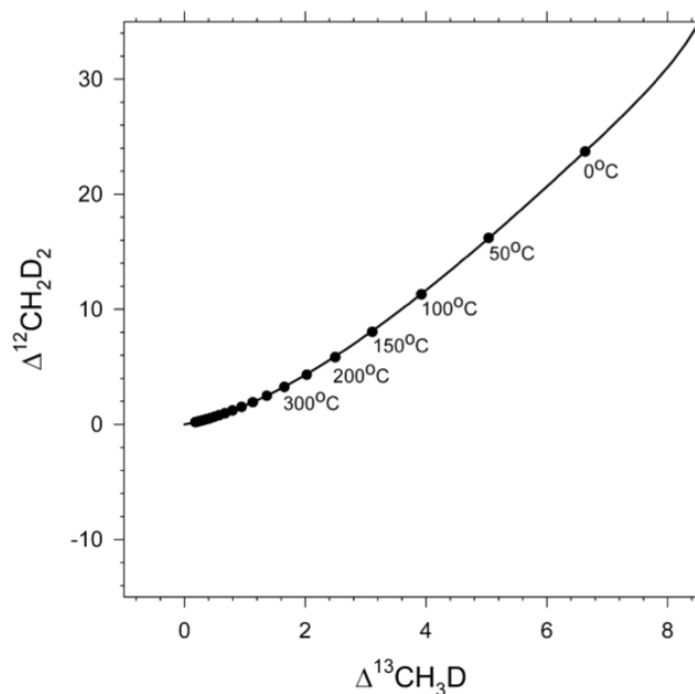
Figure 1-9. $\Delta^{13}CH_3D$ and $\Delta^{12}CH_2D_2$ plot in ‰ with the theoretical thermodynamic equilibrium curve.

Methane clumped isotope signatures of microbial methanogenesis

Mechanisms for departures from thermodynamic equilibrium include, but are not limited to, kinetic isotope effects. Severe departures from equilibrium have been observed in methane produced in axenic methanogen cultures (Giunta et al., 2019; Young et al., 2017). Methane in these

experiments was generated by various species of methanogenic archaea and resulted in isotopically light methane (-32 to -57‰ for $\delta^{13}C$ and -328 to $-394‰$ in δD). Similarly, the $\Delta^{13}CH_3D$ and $\Delta^{12}CH_2D_2$ became more negative or anti-clumped (~3.80 to $-3.88‰$ for $\Delta^{13}CH_3D$ and~ -16 to $-55‰$ for $\Delta^{12}CH_2D_2$) due to microbial methanogenesis (Giunta et al., 2019; Young et al., 2017). This trend suggests that microbially-produced methane is generated in disequilibrium due to kinetics. Importantly, it appears that the utilization of methane clumped isotopologues has the strong potential to disentangling biogenic sources from other sources that formed at equilibrium or disequilibrium (Fig.1-10) (Young, 2019).
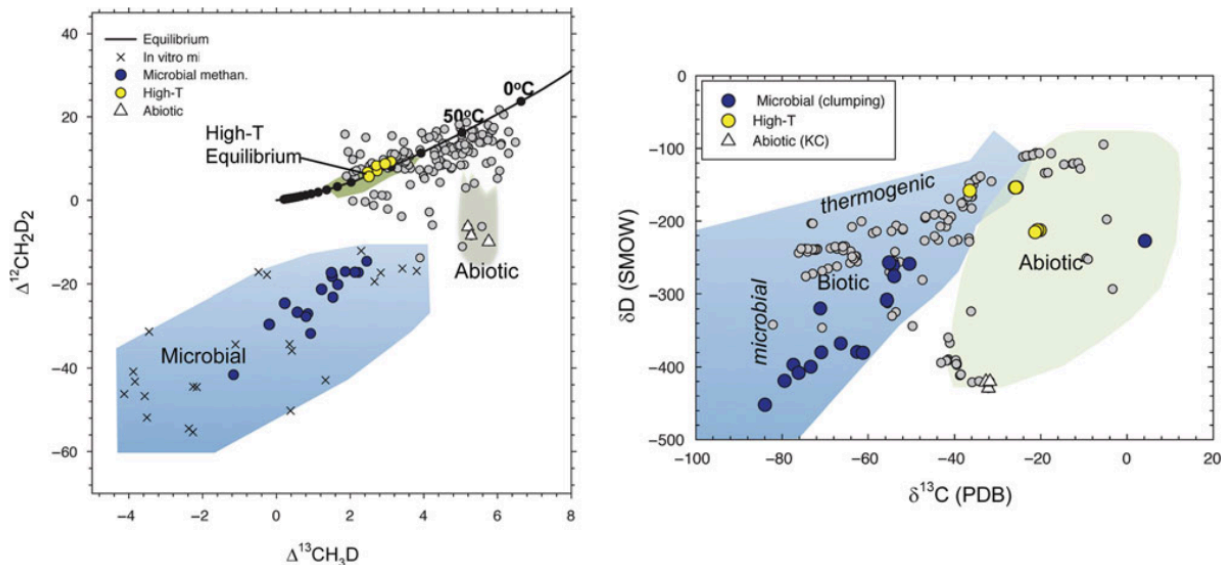
Figure 1-10. $\Delta^{13}CH_3D$ and $\Delta^{12}CH_2D_2$ signatures by process (left panel) compared to the process positions in the bulk isotope "Schoell" plot (right panel) originally published in Young, (2019).

Methane clumped isotopologue signatures of microbial methane oxidation

The other kinetic process that has received more recent attention, leading to shifts in the abundances of $\Delta^{13}CH_3D$ and $\Delta^{12}CH_2D_2$ is methane oxidation. Young et al., (2017) questioned whether the isotopic bond order equilibration can occur when minor alterations are made to the bulk $\delta^{13}C$ and δD within a given methane pool caused by methane oxidation (e.g. microbial AOM or MOx). In theory, within a closed system, steady-state could be achieved when methane

production is balanced by methane oxidation. The residual methane in this case could then resemble the original isotopic composition of the methane source. Young et al., (2017) proposed that in this kind of closed-system steady-state condition with simultaneous methane production and consumption, microbial methanogenesis may cause bond reordering, which would ultimately result in equilibrium or near equilibrium signatures at potentially lower temperature formations.

A recent study used *ab initio* calculations to calculate fractionation factors (α's) of $\Delta^{13}CH_3D$ and $\Delta^{12}CH_2D_2$ when methane is oxidized abiotically by hydroxyl and chloride radicals in the atmosphere (Haghnegahdar et al., 2017). When applying the α's to a time-dependent closed system steady-state model, moderate shifts in the $\Delta^{13}CH_3D$ and large shifts in the $\Delta^{12}CH_2D_2$ were found. Haghnegahdar et al., (2017) concluded that although $\Delta^{13}CH_3D$ is useful to trace methane sources, the $\Delta^{12}CH_2D_2$ is more sensitive at probing both methane sources and sinks in the atmosphere.

Wang et al., (2016) investigated methane isotopologue signatures of microbial aerobic methane oxidation. In this study, pure cultures of *Methylococcus capsulatus* (Bath) were incubated in liquid medium at two temperatures (30 and 37 °C) and the abundances of $^{12}CH_4$, $^{13}CH_4$, $^{12}CH_3D$ and $^{13}CH_3D$ were measured over time. The study showed that, while methane and oxygen concentrations decreased and carbon dioxide concentrations increased, the carbon ($^{13}C/^{12}C$) and hydrogen (D/H) isotope ratios became more positive, indicating that isotopically light methane was preferentially oxidized. Conversely, the $\Delta^{13}CH_3D$ signatures became more negative in both temperature incubations over time. The data were used by Wang et al., to calculate fractionation factors (α) for $^{12}CH_4$, $^{13}CH_4$, $^{12}CH_3D$ and $^{13}CH_3D$ and to introduce the gamma value (γ). The γ value is described as the ratio of the methane clumped isotopologue fractionation factors (α's) to the product of the bulk carbon and hydrogen α's. If γ is equal to 1 then the methane clumped

isotopologue fractionation is considered ideal and follows the rule of the geometric mean (RGM) (Bigeleisen, 1955). The study applied the calculated γ's and α's to a simple open-system model attributed to Hayes (2001a), which simulates a system where methane flows in passing through a sink (methane oxidation) and then exits the system. Steady state is achieved when the rates of inflow, outflow, and the sink are balanced. The model illustrated that the evolution of the $\Delta^{13}CH_3D$ did not change between fully advective (no oxidation) and fully oxidative. The study also demonstrated that the fractionation of $\Delta^{13}CH_3D$ is sensitive to the RGM, where deviations from unity by a factor ±0.002 does shift the modeled trajectory of the $\Delta^{13}CH_3D$. Although the (Wang et al., 2016) study was the first to obtain $\Delta^{13}CH_3D$ signatures from MOx, the α and γ factor for the $\Delta^{12}CH_2D_2$ was not obtained.

AOM has been hypothesized to yield isotopologue signatures that reflect thermodynamic equilibrium (Stolper et al., 2015). Ash et al., (2019) investigated $\Delta^{13}CH_3D$ and $\Delta^{12}CH_2D_2$ trends when methane gas was altered by AOM within the SMTZ within the Baltic Sea. They showed that the $\Delta^{13}CH_3D$ and $\Delta^{12}CH_2D_2$ signatures both increased with increasing sediment depth and were the highest within the deep SMTZ. In the two-dimensional methane isotopologue space, the $\Delta^{13}CH_3D$ and $\Delta^{12}CH_2D_2$ signatures in the residual methane appear to be at thermodynamic equilibrium. Ash et al., (2019) suggested the mechanism behind this trend is attributed to partial reversibility of the enzymatic pathway for AOM known as back flux, under sulfate-limiting conditions (Yoshinaga et al., 2014). In a separate study, Ono et al., (2021), used sediment-free cultures of ANME-1, under non-limiting sulfate conditions (28 mM), to observe the $\Delta^{13}CH_3D$ signatures (not $\Delta^{12}CH_2D_2$) of AOM. Their results revealed near-equilibrium $\Delta^{13}CH_3D$ values due to the kinetics of AOM that were ~ 3‰ higher than what was reported by Ash et al., (2019) in natural settings. Importantly, the study from Ono et al. demonstrated that the $\Delta^{13}CH_3D$ signatures

are distinguishable from aerobic oxidation of methane, but this work did not include the $\Delta^{12}CH_2D_2$ signatures. Therefore, it is crucial to investigate if aerobic and anaerobic oxidation of methane are distinguishable from each other in the $\Delta^{13}CH_3D/\Delta^{12}CH_2D_2$ space.

Hypothesis for the methane clumped isotopologue signatures of methane oxidation

A major challenge of using bulk isotopes of $\delta^{13}C$ and δD to distinguish between methane sources from methane sinks is residual methane altered by methane oxidation can mimic bulk isotope compositions of methane gases derived from a different source (Fig. 1-7). This dissertation will present original research following up on the findings of earlier investigations that suggested methane clumped isotopologue signatures are a promising tool to separate methane sources from methane that has been altered by methane oxidation. **The general hypothesis in this dissertation is that $\Delta^{13}CH_3D$ and $\Delta^{12}CH_2D_2$ signatures of aerobic and anaerobic methane oxidation are distinct from each other and from those of methane sources such as microbial methanogenesis. I further hypothesize that $\Delta^{13}CH_3D$ and $\Delta^{12}CH_2D_2$ are robust tools to distinguish methane altered by oxidation in open and closed systems.**

Part III. Dissertation outlook

This dissertation contains a total of four separate manuscripts and a conclusion chapter following this introductory chapter. These individual manuscripts represent original research reports that are either published or in preparation for submission to scientific journals for publication. Chapter 2, which was recently published in *Geochimica et Cosmochimica Acta* (Krause and Treude, 2021), presents a newly developed radiotracer method for the study of cryptic methane cycling, as it was applied to the analysis of hypersaline salt marsh sediments within the Carpinteria Salt Marsh Reserve. Chapter 3 is in its final stages of preparation for submission to *Biogeosciences*. This manuscript reports on how the adapted radiotracer method detailed in Chapter 2 of this dissertation was applied to find evidence of cryptic methane cycling within the sulfate-reducing zone in the Santa Barbara Basin. Chapters 4 and 5 of this dissertation present $\Delta^{13}CH_3D$ and $\Delta^{12}CH_2D_2$ signatures representative of both aerobic and anaerobic oxidation of methane, respectively. Chapter 4 was most recently published, in *Earth and Planetary Science Letters* (Krause et al., 2022). Chapter 5 (Liu et al., in prep) is not first authored by myself but contains a dataset on AOM-related changes in methane isotopologues I collected from Santa Barbara methane seep samples and is now incorporated into the manuscript with other datasets. Chapter 5 is currently in preparation for submission for peer review in *Geochimica et Cosmochimica Acta*. The last chapter in this dissertation serves to summarize the key findings and conclusions of these original research papers. Furthermore, the last chapter places the impacts of the dissertation's results and interpretations into broader context within the fields of biogeochemistry, geomicrobiology, stable isotope geochemistry and astrobiology.

References

Adrian R., O'Reilly C. M., Zagarese H., Baines S. B., Hessen D. O., Keller W., Livingstone D. M., Sommaruga R., Straile D. and Van Donk E. (2009) Lakes as sentinels of climate change. *Limnology and oceanography* **54**, 2283-2297.

Allen M. and Van Niel C. (1952) Experiments on bacterial denitrification. *Journal of bacteriology* **64**, 397-412.

Al-Haj A. N. and Fulweiler R. W. (2020) A synthesis of methane emissions from shallow vegetated coastal ecosystems. *Global Change Biology* **26**, 2988-3005.

Anderson B., Bartlett K. B., Frolking S., Hayhoe K., Jenkins J. C. and Salas W. A. (2010) Methane and nitrous oxide emissions from natural sources.

Ash J., Egger M., Treude T., Kohl I., Cragg B., Parkes R. J., Slomp C., Sherwood Lollar B. and Young E. D. (2019) Exchange catalysis during anaerobic methanotrophy revealed by 12CH2D2 and 13CH3D in methane. *Geochemical Perspective Letters* **10**, 26-30.

Bange H. W., Bartell U., Rapsomanikis S. and Andreae M. O. (1994) Methane in the Baltic and North Seas and a reassessment of the marine emissions of methane. *Global biogeochemical cycles* **8**, 465-480.

Bastviken D., Cole J. J., Pace M. L. and Van de Bogert M. C. (2008) Fates of methane from different lake habitats: Connecting whole-lake budgets and CH4 emissions. *Journal of Geophysical Research: Biogeosciences* **113**.

Bastviken D., Tranvik L. J., Downing J. A., Crill P. M. and Enrich-Prast A. (2011) Freshwater methane emissions offset the continental carbon sink. *Science* **331**, 50-50.

Bauer J. E., Cai W.-J., Raymond P. A., Bianchi T. S., Hopkinson C. S. and Regnier P. A. (2013) The changing carbon cycle of the coastal ocean. *Nature* **504**, 61-70.

Beal E. J., House C. H. and Orphan V. J. (2009) Manganese- and iron-dependent marine methane oxidation. *Science* **325**, 184-187.

Beckmann S., Krüger M., Engelen B., Gorbushina A. A. and Cypionka H. (2011) Role of bacteria, archaea and fungi involved in methane release in abandoned coal mines. *Geomicrobiology Journal* **28**, 347-358.

Berg A., Lindblad P. and Svensson B. H. (2014) Cyanobacteria as a source of hydrogen for methane formation. *World Journal of Microbiology and Biotechnology* **30**, 539-545.

Bhattacharya S., Mapder T., Fernandes S., Roy C., Sarkar J., Rameez M. J., Mandal S., Sar A., Chakraborty A. K. and Mondal N. (2021) Sedimentation rate and organic matter dynamics shape microbiomes across a continental margin. *Biogeosciences* **18**, 5203-5222.

Bigeleisen J. (1955) Statistical mechanics of isotopic systems with small quantum corrections. I. General considerations and the rule of the geometric mean. *The Journal of Chemical Physics* **23**, 2264-2267.

Bižić M., Klintzsch T., Ionescu D., Hindiyeh M., Günthel M., Muro-Pastor A. M., Eckert W., Urich T., Keppler F. and Grossart H.-P. (2020) Aquatic and terrestrial cyanobacteria produce methane. *Science advances* **6**, eaax5343.

Boetius A. and Wenzhöfer F. (2013) Seafloor oxygen consumption fuelled by methane from cold seeps. *Nature Geoscience* **6**, 725-734.

Boetius A., Ravenschlag K., Schubert C. J., Rickert D., Widdel F., Giesecke A., Amann R., Jørgensen B. B., Witte U. and Pfannkuche O. (2000) A marine microbial consortium apparently mediating anaerobic oxidation of methane. *Nature* **407**, 623-626.

Canfield D. E. (1989) Sulfate reduction and oxic respiration in marine sediments: implications for organic carbon preservation in euxinic environments. *Deep-Sea Res.* **36**, 121-138.

Carpenter S. R., Fisher S. G., Grimm N. B. and Kitchell J. F. (1992) Global change and freshwater ecosystems. *Annual review of ecology and systematics*, 119-139.

Conrad R. (2020) Importance of hydrogenotrophic, aceticlastic and methylotrophic methanogenesis for methane production in terrestrial, aquatic and other anoxic environments: a mini review. *Pedosphere* **30**, 25-39.

Conrad R., Schink B. and Phelps T. J. (1986) Thermodynamics of H2-consuming and H2-producing metabolic reactions in diverse methanogenic environments under in situ conditions. *FEMS Microbiology Ecology* **2**, 353-360.

Crowe S., Katsev S., Leslie K., Sturm A., Magen C., Nomosatryo S., Pack M., Kessler J., Reeburgh W. and Roberts J. (2011) The methane cycle in ferruginous Lake Matano. *Geobiology* **9**, 61-78.

Dale A. W., Flury S., Fossing H., Regnier P., Røy H., Scholze C. and Jørgensen B. (2019) Kinetics of organic carbon mineralization and methane formation in marine sediments (Aarhus Bay, Denmark). *Geochimica et Cosmochimica Acta* **252**, 159-178.

Daughton C., Cook A. and Alexander M. (1979) Biodegradation of phosphonate toxicants yields methane or ethane on cleavage of the CP bond. *FEMS Microbiology Letters* **5**, 91-93.

Desta H., Lemma B. and Fetene A. (2012) Aspects of climate change and its associated impacts on wetland ecosystem functions: A review. *J Am Sci* **8**, 582-596.

Deutzmann J. S., Stief P., Brandes J. and Schink B. (2014) Anaerobic methane oxidation coupled to denitrification is the dominant methane sink in a deep lake. *Proceedings of the National Academy of Sciences* **111**, 18273-18278.

Egger M., Rasigraf O., Sapart C. J., Jilbert T., Jetten M. S., Rockmann T., Van der Veen C., Banda N., Kartal B. and Ettwig K. F. (2015) Iron-mediated anaerobic oxidation of methane in brackish coastal sediments. *Environmental Science & Technology* **49**, 277-283.

Egger M., Hagens M., Sapart C. J., Dijkstra N., van Helmond N. A., Mogollón J. M., Risgaard-Petersen N., van der Veen C., Kasten S. and Riedinger N. (2017) Iron oxide reduction in methane-rich deep Baltic Sea sediments. *Geochimica et Cosmochimica Acta* **207**, 256-276.

Eiler J. M. (2007) "Clumped-isotope" geochemistry—The study of naturally-occurring, multiply-substituted isotopologues. *Earth and Planetary Science Letters* **262**, 309-327.

Emilson E. J., Carson M. A., Yakimovich K. M., Osterholz H., Dittmar T., Gunn J., Mykytczuk N., Basiliko N. and Tanentzap A. (2018) Climate-driven shifts in sediment chemistry enhance methane production in northern lakes. *Nature communications* **9**, 1-6.

Etiope G. and Sherwood Lollar B. (2013) Abiotic methane on Earth. *Reviews of Geophysics* **51**, 276-299.

Etiope G. and Schoell M. (2014) Abiotic gas: atypical, but not rare. *Elements* **10**, 291-296.

Ettwig K. F., Butler M. K., Le Paslier D., Pelletier E., Mangenot S., Kuypers M. M. M., Schreiber F., Dutilh B. E., Zedelius J., De Beer D., Gloerich J., Wessels H. J. C. T., Alen T. v., Luesken F., Wu M. L., Pas-Schoonen v. d., K.T., Op den Camp H. J. M., Janssen-Megens E. M., Francoijs K.-J., Stunnenberg H., Weissembach J., Jetten M. S. M. and Strous M. (2010) Nitrite-driven anaerobic methane oxdation by oxygenic bacteria. *Nature* **464**, 544-550.

Fenchel T., King G. and Blackburn T. (1998) Bacterial biogeochemistry: The ecophysiology of mineral cycling. Academic Press, London. *Bacterial biogeochemistry: The ecophysiology of mineral cycling. 2nd ed. Academic Press, London.*, -.

Fenchel T. M. and Jørgensen B. B. (1977) Detritus food chains of aquatic ecosystems: the role of bacteria. *Advances in microbial ecology*, 1-58.

Gardner R. C., Barchiesi S., Beltrame C., Finlayson C., Galewski T., Harrison I., Paganini M., Perennou C., Pritchard D. and Rosenqvist A. (2015) State of the world's wetlands and their services to people: a compilation of recent analyses.

Giunta T., Young E. D., Warr O., Kohl I., Ash J. L., Martini A., Mundle S. O., Rumble D., Pérez-Rodríguez I. and Wasley M. (2019) Methane sources and sinks in continental sedimentary systems: New insights from paired clumped isotopologues 13CH3D and 12CH2D2. *Geochimica et Cosmochimica Acta* **245**, 327-351.

Guerrero-Cruz S., Cremers G., van Alen T. A., Op den Camp H. J., Jetten M. S., Rasigraf O. and Vaksmaa A. (2018) Response of the anaerobic methanotroph "Candidatus Methanoperedens nitroreducens" to oxygen stress. *Applied and environmental microbiology* **84**, e01832-01818.

Guggenheim C., Freimann R., Mayr M. J., Beck K., Wehrli B. and Bürgmann H. (2020) Environmental and microbial interactions shape methane-oxidizing bacterial communities in a stratified lake. *Frontiers in microbiology* **11**, 2374.

Gupta V., Smemo K. A., Yavitt J. B., Fowle D., Branfireun B. and Basiliko N. (2013) Stable isotopes reveal widespread anaerobic methane oxidation across latitude and peatland type. *Environmental Science & Technology* **47**, 8273-8279.

Hagen R. A. and Vogt P. R. (1999) Seasonal variability of shallow biogenic gas in Chesapeake

    Bay. *Marine Geology* **158**, 75-88.

Haghnegahdar M. A., Schauble E. A. and Young E. D. (2017) A model for 12CH2D2 and

    13CH3D as complementary tracers for the budget of atmospheric CH4. *Global*

    Biogeochemical Cycles **31**, 1387-1407.

Hallam S. J., Putnam N., Preston C. M., Detter J. C., Rokhsar D., Richardson P. M. and DeLong

    E. F. (2004) Reverse methanognesis: testing the hypothesis with environmental

    genomics. *Science* **305**, 1457-1462.

Hanson R. S. and Hanson T. E. (1996) Methanotrophic bacteria. *Microbiol. Rev.* **60**, 439-471.

Haroon M. F., Hu S., Shi Y., Imelfort M., Keller J., Hugenholtz P., Yuan Z. and Tyson G. W.

    (2013) Anaerobic oxidation of methane coupled to nitrate reduction in a novel archaeal

    lineage. *Nature* **500**, 567 – 570.

Hayes J. M. (2001) Fractionation of Carbon and Hydrogen Isotopes in Biosynthetic Processes*.

    Reviews in Mineralogy and Geochemistry **43**, 225-277.

Hayes J. M. (2004) An introduction to isotopic calculations. *Woods Hole Oceanographic*

    Institution, Woods Hole, MA **2543**.

Henckel T., Jäckel U., Schnell S. and Conrad R. (2000) Molecular analyses of novel

    methanotrophic communities in forest soil that oxidize atmospheric methane. *Appl.*

    Environ. Microbiol. **66**, 1801-1808.

Hovland M. and Judd A. G. (1988) *Seabed pockmarks and seepages: impact on geology, biology*

    and the marine environment. Graham & Trotman London.

Hu B.-l., Shen L.-d., Lian X., Zhu Q., Liu S., Huang Q., He Z.-f., Geng S., Cheng D.-q. and Lou

    L.-p. (2014) Evidence for nitrite-dependent anaerobic methane oxidation as a previously

overlooked microbial methane sink in wetlands. *Proceedings of the National Academy of Sciences* **111**, 4495-4500.

Iversen N. and Jørgensen B. B. (1985) Anaerobic methane oxidation rates at the sulphate-methane transition in marine sediments from Kattegat and Skagerrak (Denmark). *Limnol. Oceanogr.* **30**, 944-955.

Jickells T., An Z., Andersen K. K., Baker A., Bergametti G., Brooks N., Cao J., Boyd P., Duce R. and Hunter K. (2005) Global iron connections between desert dust, ocean biogeochemistry, and climate. *science* **308**, 67-71.

Jørgensen B. B. (1977) Bacterial sulfate reduction within reduced microniches of oxidized marine sediments. *Mar. Biol.* **41**, 7-17.

Jørgensen B. B. (2000) Bacteria and marine biogeochemistry. In *Marine biogeochemistry* (eds. H. D. Schulz and M. Zabel). Springer Verlag, Berlin. pp. 173-201.

Jørgensen B. B. (2021) 3. SULFATE REDUCTION. *Geochemical Perspectives* **10**, 169-200.

Karl D. M., Beversdorf L., Björkman K. M., Church M. J., Martinez A. and Delong E. F. (2008) Aerobic production of methane in the sea. *Nature Geoscience* **1**, 473-478.

Kiene R. (1991) Microbial production and consumption of greenhouse gases: Methane, nitrogen oxides, and halomethanes. *American Society for Microbiology, Washington DC*, 111-146.

Kittredge J., Horiguchi M. and Williams P. (1969) Aminophosphonic acids: Biosynthesis by marine phytoplankton. *Comparative Biochemistry and Physiology* **29**, 859-863.

Kittredge J. S. and Roberts E. (1969) A Carbon-Phosphorus Bond in Nature: A spot on a chromatogram leads to a new field of phosphorus biochemistry. *Science* **164**, 37-42.

Kletzin A., Heimerl T., Flechsler J., van Niftrik L., Rachel R. and Klingl A. (2015) Cytochromes c in Archaea: distribution, maturation, cell architecture, and the special case of Ignicoccus hospitalis. *Frontiers in microbiology* **6**, 439.

Knab N. J., Cragg B. A., Hornibrook E. R., Holmquist L., Pancost R. D., Borowski W. S., Parkes R. J. and Jørgensen B. B. (2009) Regulation of anaerobic methane oxidation in sediments of the Black Sea. *Biogeosciences* **6**, 1505-1518.

Knittel K. and Boetius A. (2009) Anaerobic oxidation of methane: progress with an unknown process. *Annu. Rev. Microbiol.* **63**, 311-334.

Knittel K., Lösekann T., Boetius A., Kort R. and Amann R. (2005) Diversity and distribution of methanotrophic Archea (ANME) at cold seeps. *Appl. Environ. Microbiol.* **71**, 467-479.

Knittel K., Boetius A., Lemke A., Eilers H., Lochte K., Pfannkuche O. and Linke P. (2003) Activity, distribution, and diversity of sulfate reducers and other bacteria in sediments above gas hydrates (Cascadia Margin, Oregon). *Geomicrobiol. J.* **20**, 269-294.

Kolowith L. C., Ingall E. D. and Benner R. (2001) Composition and cycling of marine organic phosphorus. *Limnology and Oceanography* **46**, 309-320.

Kraft B., Tegetmeyer H. E., Sharma R., Klotz M. G., Ferdelman T. G., Hettich R. L., Geelhoed J. S. and Strous M. (2014) The environmental controls that govern the end product of bacterial nitrate respiration. *Science* **345**, 676-679.

Krause S. J. and Treude T. (2021) Deciphering cryptic methane cycling: Coupling of methylotrophic methanogenesis and anaerobic oxidation of methane in hypersaline coastal wetland sediment. *Geochimica et Cosmochimica Acta* **302**, 160-174.

Krause S. J., Liu J., Young E. D. and Treude T. (2022) Δ13CH3D and Δ12CH2D2 signatures of methane aerobically oxidized by Methylosinus trichosporium with implications for

deciphering the provenance of methane gases. *Earth and Planetary Science Letters* **593**, 117681.

Kristensen E. (2000) Organic matter diagenesis at the oxic/anoxic interface in coastal marine sediments, with emphasis on the role of burrowing animals. *Hydrobiologia* **426**, 1-24.

Laruelle G. G., Dürr H., Lauerwald R., Hartmann J., Slomp C., Goossens N. and Regnier P. (2013) Global multi-scale segmentation of continental and coastal waters from the watersheds to the continental margins. *Hydrology and Earth System Sciences* **17**, 2029-2051.

Leifer I., Kamerling M. J., Luyendyk B. P. and Wilson D. S. (2010) Geologic control of natural marine hydrocarbon seep emissions, Coal Oil Point seep field, California. *Geo-Marine Letters* **30**, 331-338.

Lenhart K., Bunge M., Ratering S., Neu T. R., Schüttmann I., Greule M., Kammann C., Schnell S., Müller C. and Zorn H. (2012) Evidence for methane production by saprotrophic fungi. *Nature communications* **3**, 1-8.

Lenstra W. K., Egger M., Van Helmond N. A., Kritzberg E., Conley D. J. and Slomp C. P. (2018) Large variations in iron input to an oligotrophic Baltic Sea estuary: impact on sedimentary phosphorus burial. *Biogeosciences* **15**, 6979-6996.

Liu Q. and Liu Y. (2016) Clumped-isotope signatures at equilibrium of CH4, NH3, H2O, H2S and SO2. *Geochim. Cosmochim. Acta* **175**, 252-270.

Lösekann T., Knittel K., Nadalig T., Fuchs B., Niemann H., Boetius A. and Amann R. (2007) Diversity and abundance of aerobic and anaerobic methane oxidizers at the Haakon Mosby Mud Volcano, Barents Sea. *Applied and environmental microbiology* **73**, 3348-3362.

Luesken F. A., van Alen T. A., van der Biezen E., Frijters C., Toonen G., Kampman C., Hendrickx T. L., Zeeman G., Temmink H. and Strous M. (2011) Diversity and enrichment of nitrite-dependent anaerobic methane oxidizing bacteria from wastewater sludge. *Applied microbiology and biotechnology* **92**, 845-854.

Lyu Z., Shao N., Akinyemi T. and Whitman W. B. (2018) Methanogenesis. *Current Biology* **28**, R727-R732.

Ma Q., Wu S. and Tang Y. (2008) Formation and abundance of doubly-substituted methane isotopologues (13CH3D) in natural gas systems. *Geochimica et Cosmochimica Acta* **72**, 5446-5456.

Maltby J., Sommer S., Dale A. W. and Treude T. (2016) Microbial methanogenesis in the sulfate-reducing zone of surface sediments traversing the Peruvian margin. *Biogeosciences* **13**, 283–299.

Maltby J., Steinle L., Löscher C. R., Bange H. W., Fischer M. A., Schmidt M. and Treude T. (2018) Microbial methanogenesis in the sulfate-reducing zone of sediments in the Eckernförde Bay, SW Baltic Sea. *Biogeosciences* **15**, 137– 157.

Martinez-Cruz K., Sepulveda-Jauregui A., Casper P., Anthony K. W., Smemo K. A. and Thalasso F. (2018) Ubiquitous and significant anaerobic oxidation of methane in freshwater lake sediments. *Water research* **144**, 332-340.

McGlynn S. E., Chadwick G. L., Kempes C. P. and Orphan V. J. (2015) Single cell activity reveals direct electron transfer in methanotrophic consortia. *Nature* **526**, 531-535.

Michaelis W., Seifert R., Nauhaus K., Treude T., Thiel V., Blumenberg M., Knittel K., Gieseke A., Peterknecht K., Pape T., Boetius A., Aman A., Jørgensen B. B., Widdel F., Peckmann

J., Pimenov N. V. and Gulin M. (2002) Microbial reefs in the Black Sea fueled by anaerobic oxidation of methane. *Science* **297**, 1013-1015.

Milucka J., Ferdelman T., Polerecky L., Franzke D., Wegener G., Schmid M., Lieberwirth I., Wagner M., Widdel F. and Kuypers M. M. M. (2012) Zero-valent sulphur is a key intermediate in marine methane oxidation. *Nature* **491**, 541-546.

Moretti I. (1998) The role of faults in hydrocarbon migration. *Petroleum Geoscience* **4**, 81-94.

Moss B., Kosten S., Meerhoff M., Battarbee R. W., Jeppesen E., Mazzeo N., Havens K., Lacerot G., Liu Z. and De Meester L. (2011) Allied attack: climate change and eutrophication. *Inland waters* **1**, 101-105.

Mukhin V. and Voronin P. Y. Methane emission during wood fungal decomposition. *Doklady Biological Sciences*. Springer Nature BV.

Mukhin V. and Voronin P. Y. (2008) A new source of methane in boreal forests. *Applied Biochemistry and Microbiology* **44**, 297-299.

Murrell J. (2010) The aerobic methane oxidizing bacteria (methanotrophs). *Handbook of hydrocarbon and lipid microbiology*, 1953-1966.

Niemann H., Lösekann T., De Beer D., Elvert M., Nadalig T., Knittel K., Aman A., Sauter E. J., Schlüter M., Klages M., Foucher J.-P. and Boetius A. (2006) Novel microbial communities of the Haakon Mosby mud volcano and their role as a methane sink. *Nature* **443**, 854-858.

Nisbet E. G., Manning M., Dlugokencky E., Fisher R., Lowry D., Michel S., Myhre C. L., Platt S. M., Allen G. and Bousquet P. (2019) Very strong atmospheric methane growth in the 4 years 2014–2017: Implications for the Paris Agreement. *Global Biogeochemical Cycles* **33**, 318-342.

Norði K. a., Thamdrup B. and Schubert C. J. (2013) Anaerobic oxidation of methane in an iron-rich Danish freshwater lake sediment. *Limnol. Ocenanogr.* **58**, 546-554.

Omoregie E. O., Mastalerz V., De Lange G., Straub K. L., Kappler A., Røy H., Stadnitskaia A., Foucher J.-P. and Boetius A. (2008) Biogeochemistry and community composition of iron-and sulfur-precipitating microbial mats at the Chefren mud volcano (Nile Deep Sea Fan, Eastern Mediterranean). *Applied and environmental microbiology* **74**, 3198-3215.

Oni O., Miyatake T., Kasten S., Richter-Heitmann T., Fischer D., Wagenknecht L., Kulkarni A., Blumers M., Shylin S. I. and Ksenofontov V. (2015) Distinct microbial populations are tightly linked to the profile of dissolved iron in the methanic sediments of the Helgoland mud area, North Sea. *Frontiers in Microbiology* **6**, 365.

Ono S., Rhim J. H., Gruen D. S., Taubner H., Kölling M. and Wegener G. (2021) Clumped isotopologue fractionation by microbial cultures performing the anaerobic oxidation of methane. *Geochimica et Cosmochimica Acta* **293**, 70-85.

Ono S., Wang D. T., Gruen D. S., Sherwood Lollar B., Zahniser M. S., McManus B. J. and Nelson D. D. (2014) Measurement of a doubly substituted methane isotopologue, 13CH3D, by tunable infrared laser direct absorption spectroscopy. *Analytical chemistry* **86**, 6487-6494.

Orphan V. J., House C. H., Hinrichs K.-U., McKeegan K. D. and DeLong E. F. (2002) Multiple archaeal groups mediate methane oxidation in anoxic cold seep sediments. *Proc. Acad. Nat. Sci. U.S.A* **99**, 7663-7668.

Orphan V. J., Hinrichs K.-U., Ussler III W., Paull C. K., Tayleor L. T., Sylva S. P., Hayes J. M. and DeLong E. F. (2001) Comparative analysis of methane-oxidizing archaea and

sulfate-reducing bacteria in anoxic marine sediments. *Appl. Environ. Microbiol.* **67**, 1922-1934.

Padilla C. C., Bristow L. A., Sarode N., Garcia-Robledo E., Gómez Ramírez E., Benson C. R., Bourbonnais A., Altabet M. A., Girguis P. R. and Thamdrup B. (2016) NC10 bacteria in marine oxygen minimum zones. *The ISME Journal* **10**, 2067-2071.

Pastor L., Deflandre B., Viollier E., Cathalot C., Metzger E., Rabouille C., Escoubeyrou K., Lloret E., Pruski A. M. and Vetion G. (2011) Influence of the organic matter composition on benthic oxygen demand in the Rhône River prodelta (NW Mediterranean Sea). *Continental Shelf Research* **31**, 1008-1019.

Piker L., Schmaljohann R. and Imhoff J. F. (1998) Dissimilatory sulfate reduction and methane production in Gotland Deep sediments (Baltic Sea) during a transition period from oxic to anoxic bottom water (1993-1996). *Aquatic Microbial Ecology* **14**, 183-193.

Poffenbarger H. J., Needelman B. A. and Megonigal J. P. (2011) Salinity Influence on Methane Emissions from Tidal Marshes. *Wetlands* **31**, 831-842.

Priestley J. (1776) *Experiments and observations on different kinds of air*. J. Johnson.

Raghoebarsing A. A., Pol A., Van de Pas-Schoonen K. T., Smolders A. J., Ettwig K. F., Rijpstra W. I. C., Schouten S., Damsté J. S. S., Op den Camp H. J. and Jetten M. S. (2006) A microbial consortium couples anaerobic methane oxidation to denitrification. *Nature* **440**, 918-921.

Reddy K. R. and DeLaune R. D. (2008) *Biogeochemistry of Wetlands*. CRC Press, Taylor & Francis Group, Boca Raton.

Reeburgh W. S. (2007) Oceanic methane biogeochemistry. *Chem. Rev.* **107**, 486-513.

Reitner J., Peckmann J., Blumenberg M., Michaelis W., Reimer A. and Thiel V. (2005) Concretionary methane-seep carbonates and associated microbial communities in Black Sea sediments. *Palaeogeography, Paleoclimatology, Palaeoecology* **227**, 18-30.

Riedinger N., Formolo M. J., Lyons T. W., Henkel S., Beck A. and Kasten S. (2014) An inorganic geochemical argument for coupled anaerobic oxidation of methane and iron reduction in marine sediments. *Geobiology* **12**, 172-181.

Rooze J., Egger M., Tsandev I. and Slomp C. P. (2016) Iron-dependent anaerobic oxidation of methane in coastal surface sediments: Potential controls and impact. *Limnology and Oceanography* **61**, S267-S282.

Saunois M., Bousquet P., Poulter B., Peregon A., Ciais P., Canadell J. G., Dlugokencky E. J., Etiope G., Bastviken D. and Houweling S. (2016) The global methane budget 2000–2012. *Earth System Science Data* **8**, 697-751.

Saunois M., Stavert A. R., Poulter B., Bousquet P., Canadell J. G., Jackson R. B., Raymond P. A., Dlugokencky E. J., Houweling S. and Patra P. K. (2020) The global methane budget 2000–2017. *Earth system science data* **12**, 1561-1623.

Scheller S., Yu H., Ghadwick G. L., McGlynn S. E. and Orphan V. J. (2016) Artificial electron acceptors decouple archaeal methane oxidation from sulfate reduction. *Science* **351**, 703-707.

Schoell M. (1980) The hydrogen and carbon isotopic composition of methane from natural gases of various origins. *Geochimica et Cosmochimica Acta* **44**, 649-661.

Schoell M. (1988) Multiple origins of methane in the earth. *Chem. Geol.* **71**, 1-10.

Schroll M., Keppler F., Greule M., Eckhardt C., Zorn H. and Lenhart K. (2020) The stable carbon isotope signature of methane produced by saprotrophic fungi. *Biogeosciences* **17**, 3891-3901.

Segarra K. E., Comerford C., Slaughter J. and Joye S. B. (2013) Impact of electron acceptor availability on the anaerobic oxidation of methane in coastal freshwater and brackish wetland sediments. *Geochimica et Cosmochimica Acta* **115**, 15-30.

Segarra K. E. A., Schubotz F., Samarkin V., Yoshinaga M. Y., Hinrichs K.-U. and Joye S. B. (2015) High rates of anaerobic methane oxidation in freshwater wetlands reduce potential atmospheric methane emissions. *Nature Comm.* **6**, DOI: 10.1038/ncomms8477.

Shen L.-d., Wu H.-s. and Gao Z.-q. (2015) Distribution and environmental significance of nitrite-dependent anaerobic methane-oxidising bacteria in natural ecosystems. *Applied microbiology and biotechnology* **99**, 133-142.

Shen L.-d., Hu B.-l., Liu S., Chai X.-p., He Z.-f., Ren H.-x., Liu Y., Geng S., Wang W. and Tang J.-l. (2016) Anaerobic methane oxidation coupled to nitrite reduction can be a potential methane sink in coastal environments. *Applied microbiology and biotechnology* **100**, 7171-7180.

Smeraglia L., Fabbi S., Billi A., Carminati E. and Cavinato G. P. (2022) How hydrocarbons move along faults: Evidence from microstructural observations of hydrocarbon-bearing carbonate fault rocks. *Earth and Planetary Science Letters* **584**, 117454.

Steinle L., Maltby J., Treude T., Kock A., Bange H. W., Engbersen N., Zopfi J., Lehmann M. F. and Niemann H. (2017) Effects of low oxygen concentrations on aerobic methane oxidation in seasonally hypoxic coastal waters. *Biogeosciences* **14**, 1631-1645.

Steinle L., Schmidt M., Bryant L., Haeckel M., Linke P., Sommer S., Zopfi J., Lehmann M. F.,
    Treude T. and Niemannn H. (2016) Linked sediment and water-column methanotrophy at
    a man-made gas blowout in the North Sea: Implications for methane budgeting in
    seasonally stratified shallow seas. *Limnology and Oceanography* **61**, S367-S386.

Steinle L., Graves C. A., Treude T., Ferré B., Biastoch A., Bussmann I., Berndt C., Krastel S.,
    James R. H., Behrens E., Böning C. W., Greinert J., Sapart C. J., Scheinert M., Sommer
    S., Lehmann M. F. and Niemann H. (2015) Water column methanotrophy controlled by a
    rapid oceanographic switch. *Nature Geosci.* **8**, 378.

Stolper D. A., Martini A. M., Clog M., Douglas P. M., Shusta S. S., Valentine D. L., Sessions A.
    L. and Eiler J. M. (2015) Distinguishing and understanding thermogenic and biogenic
    sources of methane using multiply substituted isotopologues. *Geochimica et
    Cosmochimica Acta* **161**, 219-247.

Su G., Zopfi J., Yao H., Steinle L., Niemann H. and Lehmann M. F. (2020) Manganese/iron-
    supported sulfate-dependent anaerobic oxidation of methane by archaea in lake
    sediments. *Limnology and Oceanography* **65**, 863-875.

Suess E. (2010) Marine cold seeps. In *Handbook of hydrocarbon and lipid microbiology* (ed. K.
    N. Timmis). Springer-Verlag, Berlin Heidelberg. pp. 187-203.

Suess E. (2014) Marine cold seeps and their manifestations: geological control, biogeochemical
    criteria and environmental conditions. *International Journal of Earth Sciences* **103**, 1889-
    1916.

Sun L., Wang Y., Guan N. and Li L. (2020) Methane activation and utilization: Current status
    and future challenges. *Energy Technology* **8**, 1900826.

Teikari J. E., Fewer D. P., Shrestha R., Hou S., Leikoski N., Mäkelä M., Simojoki A., Hess W. R. and Sivonen K. (2018) Strains of the toxic and bloom-forming Nodularia spumigena (cyanobacteria) can degrade methylphosphonate and release methane. *The ISME journal* **12**, 1619-1630.

Thamdrup B., Steinsdóttir H. G., Bertagnolli A. D., Padilla C. C., Patin N. V., Garcia-Robledo E., Bristow L. A. and Stewart F. J. (2019) Anaerobic methane oxidation is an important sink for methane in the ocean's largest oxygen minimum zone. *Limnology and Oceanography* **64**, 2569-2585.

Thauer R. K. (1998) Biochemistry of methanogenesis: a tribute to Marjory Stephenson. *Microbiology* **144**, 2377-2406.

Thauer R. K. and Shima S. (2008) Methane as fuel for anaerobic microorganisms. *Annals of the New York Academy of Sciences* **1125**, 158-170.

Thauer R. K., Jungermann K. and Decker K. (1977) Energy conservation in chemotrophic anaerobic bacteria. *Bacteriol. Rev.* **41**, 100-180.

Timmers P. H. A., Welte C. U., Koehorst J. J., Plugge C. M., Jetten M. S. M. and Stams A. J. M. (2017) Reverse methanogenesis and respiration in methanotrophic archaea. *Archaea* **Article ID 1654237**.

Treude T., Orphan V., Knittel K., Giesecke A., House C. H. and Boetius A. (2007) Consumption of methane and CO2 by methanotrophic microbial mats from gas seeps of the anoxic Black Sea. *Appl. Environ. Microbiol.* **73**, 2271-2283.

Treude T., Krüger M., Boetius A. and Jørgensen B. B. (2005) Environmental control on anaerobic oxidation of methane in the gassy sediments of Eckernförde Bay (German Baltic). *Limnol. Oceanogr.* **50**, 1771-1786.

Valentine D. L., Blanton D. C., Reeburgh W. S. and Kastner M. (2001) Water column methane oxidation adjacent to an area of active gas hydrate dissociation, Eel River Basin. *Geochim. Cosmochim. Acta* **65**, 2633-2640.

Valenzuela E. I., Avendaño K. A., Balagurusamy N., Arriaga S., Nieto-Delgado C., Thalasso F. and Cervantes F. J. (2019) Electron shuttling mediated by humic substances fuels anaerobic methane oxidation and carbon burial in wetland sediments. *Science of The Total Environment* **650**, 2674-2684.

Verpoorter C., Kutser T., Seekell D. A. and Tranvik L. J. (2014) A global inventory of lakes based on high-resolution satellite imagery. *Geophysical Research Letters* **41**, 6396-6402.

Versantvoort W., Guerrero-Cruz S., Speth D. R., Frank J., Gambelli L., Cremers G., Van Alen T., Jetten M. S., Kartal B. and Op den Camp H. J. (2018) Comparative genomics of Candidatus Methylomirabilis species and description of Ca. Methylomirabilis lanthanidiphila. *Frontiers in microbiology* **9**, 1672.

Vizza C., West W. E., Jones S. E., Hart J. A. and Lamberti G. A. (2017) Regulators of coastal wetland methane production and responses to simulated global change. *Biogeosciences. 14 (2): 431-446.* **14**, 431-446.

Volta A., Castelli m. F. and Campi C. G. (1777) *Lettere: sull'aria infiammabile nativa delle paludi*. Giuseppe Marelli.

Von Hofmann A. W. (1865) *Introduction to Modern Chemistry, Experimental and Theoretic: Embodying Twelve Lectures Delivered in the Royal College of Chemistry, London.* Walton and Maberley.

Wallenius A. J., Dalcin Martins P., Slomp C. P. and Jetten M. S. (2021) Anthropogenic and environmental constraints on the microbial methane cycle in coastal sediments. *Frontiers in Microbiology* **12**, 631621.

Walter K. M., Zimov S., Chanton J. P., Verbyla D. and Chapin F. S. (2006) Methane bubbling from Siberian thaw lakes as a positive feedback to climate warming. *Nature* **443**, 71-75.

Wang D. T., Welander P. V. and Ono S. (2016) Fractionation of the methane isotopologues 13 CH 4, 12 CH 3 D, and 13 CH 3 D during aerobic oxidation of methane by Methylococcus capsulatus (Bath). *Geochimica et Cosmochimica Acta* **192**, 186-202.

Wang J., Yao X., Jia Z., Zhu L., Zheng P., Kartal B. and Hu B. (2022) Nitrogen input promotes denitrifying methanotrophs' abundance and contribution to methane emission reduction in coastal wetland and paddy soil. *Environmental Pollution* **302**, 119090.

Wang J., Cai C., Li Y., Hua M., Wang J., Yang H., Zheng P. and Hu B. (2018) Denitrifying anaerobic methane oxidation: a previously overlooked methane sink in intertidal zone. *Environmental science & technology* **53**, 203-212.

Wankel S. D., Adams M. M., Johnston D. T., Hansel C. M., Joye S. B. and Girguis P. R. (2012) Anaerobic methane oxidation in metalliferous hydrothermal sediments: influence on carbon flux and decoupling from sulfate reduction. *Environmental microbiology* **14**, 2726-2740.

Webb M. A. and Miller III T. F. (2014) Position-specific and clumped stable isotope studies: comparison of the Urey and path-integral approaches for carbon dioxide, nitrous oxide, methane, and propane. *The Journal of Physical Chemistry A* **118**, 467-474.

Weber T., Wiseman N. A. and Kock A. (2019) Global ocean methane emissions dominated by shallow coastal waters. *Nature communications* **10**, 1-10.

Wegener G., Krukenberg V., Riedel D., Tegetmeyer H. E. and Boetius A. (2015) Intercellular wiring enables electron transfer between methanotrophic archaea and bacteria. *Nature* **526**, 587-590.

Welte C. U., Rasigraf O., Vaksmaa A., Versantvoort W., Arshad A., Op den Camp H. J., Jetten M. S., Lüke C. and Reimann J. (2016) Nitrate-and nitrite-dependent anaerobic oxidation of methane. *Environmental Microbiology Reports* **8**, 941-955.

Westall F. and Cockell C. S. (2016) Biosignatures for astrobiology. *Origins of Life and Evolution of Biospheres* **46**, 105-106.

Wever T. F., Lühder R., Voβ H. and Knispel U. (2006) Potential environmental control of free shallow gas in the seafloor of Eckernförde Bay, Germany. *Marine geology* **225**, 1-4.

Whiticar M. J. (1993) Stable isotopes and global budgets. In *NATO ASI Series* (ed. M. A. K. Khalil). Springer Verlag, Berlin. pp. 138-167.

Whiticar M. J. (1999) Carbon and hydrogen isotope systematics of bacterial formation and oxidation of methane. *Chem. Geol.* **161**, 291-314.

Whiticar M. J. (2020) The Biogeochemical Methane Cycle. *Hydrocarbons, Oils and Lipids: Diversity, Origin, Chemistry and Fate*, 669-746.

Xiao K., Beulig F., Kjeldsen K., Jorgensen B. and Risgaard-Petersen N. (2017) Concurrent Methane Production and Oxidation in Surface Sediment from Aarhus Bay, Denmark. *Frontiers in Microbiology* **8**.

Xiao K., Beulig F., Roy H., Jorgensen B. and Risgaard-Petersen N. (2018) Methylotrophic methanogenesis fuels cryptic methane cycling in marine surface sediment. *Limnology and Oceanography* **63**, 1519-1527.

Yoshinaga M. Y., Holler T., Goldhammer T., Wegener G., Pohlman J. W., Brunner B., Kuypers M. M. M., Hinrichs K.-U. and Elvert M. (2014) Carbon isotope equilibration during sulphate-limited anaerobic oxidation of methane. *Nature Geoscience* **7**, 190.

Young E., Orcutt B., Daniel I. and Dasgupta R. (2019) A two-dimensional perspective on CH4 isotope clumping. *Deep Carbon* **1029**, 388-414.

Young E., Kohl I., Lollar B. S., Etiope G., Rumble D., Li S., Haghnegahdar M., Schauble E., McCain K. and Foustoukos D. (2017) The relative abundances of resolved l2 CH 2 D 2 and 13 CH 3 D and mechanisms controlling isotopic bond ordering in abiotic and biotic methane gases. *Geochimica et Cosmochimica Acta* **203**, 235-264.

Young E. D., Rumble D., Freedman P. and Mills M. (2016) A large-radius high-mass-resolution multiple-collector isotope ratio mass spectrometer for analysis of rare isotopologues of O 2, N 2, CH 4 and other gases. *International Journal of Mass Spectrometry* **401**, 1-10.

Young E.D. (2019) A Two-Dimensional Perspective on CH4 Isotope Clumping: Distinguishing Process from Source, in: Orcutt B.N., Daniel I., Dasgupta R. (Eds.), Deep Carbon: Past to Present. Cambridge University Press, Cambridge, pp. 388-414.

Zehnder A. J. B. and Brock T. D. (1980) Anaerobic methane oxidation: occurrence and ecology. *Appl. Environ. Microbiol.* **39**, 194-204.

Zhang G., Zhang J., Kang Y. and Liu S. (2004) Distributions and fluxes of methane in the East China Sea and the Yellow Sea in spring. *Journal of Geophysical Research: Oceans* **109**.

Zhang K., Wu X., Wang W., Chen J., Luo H., Chen W., Ma D., An X., Chen F. and Cheng L. (2022) Anaerobic oxidation of methane (AOM) driven by multiple electron acceptors in constructed wetland and the related mechanisms of carbon, nitrogen, sulfur cycles. *Chemical Engineering Journal* **433**, 133663.

Chapter 2

Deciphering cryptic methane cycling: Coupling of methylotrophic methanogenesis and anaerobic oxidation of methane in hypersaline coastal wetland sediment

Sebastian J.E. Krause[1] and Tina Treude[1,2,*]

[1]Department of Earth, Planetary and Space Sciences, University of California, Los Angeles, Los Angeles CA 90095, USA

[2]Department of Atmospheric and Oceanic Sciences, University of California, Los Angeles, Los Angeles CA 90095, USA

* Corresponding author, E-mail address: ttreude@g.ucla.edu

Abstract

Methanogenesis has recently been shown to fuel anaerobic oxidation of methane (AOM) within the sulfate-reducing zone of marine sediments, coining the term "cryptic methane cycle". Here we present research on the relationship between methanogenesis and AOM in a shallow hypersaline pool (~130 PSU) within a southern California coastal wetland. Sediment (top 20 cm) was subjected to geochemical analyses, in-vitro slurry experiments, and radiotracer incubations using ^{35}S-SO_4^{2-}, ^{14}C-mono-methylamine, and ^{14}C-CH_4, to study sulfate reduction, methylotrophic methanogenesis, and AOM. An adapted radioisotope method was used to follow cryptic methane cycling in ^{14}C-mono-methylamine labeling incubations with increasing incubation times (1 hour to three weeks). Results showed peaks in AOM (max 13 nmol cm^{-3} d^{-1}) and sulfate reduction activity (max 685 nmol cm^{-3} d^{-1}) within the top 6 cm. Below 6 cm, AOM activity continued (max 15 nmol cm^{-3} d^{-1}), while sulfate reduction was absent despite 67 mM sulfate, suggesting AOM was coupled to the reduction of iron. Methane concentrations were low (< 50 nM) throughout the sediment. Batch sediment slurry incubations with methylated substrates (mono-methylamine and methanol) stimulated methanogenesis, pointing to the presence of methylotrophic methanogens. Incubations with ^{14}C-mono-methylamine revealed the simultaneous activity of methanogenesis and coupled AOM through the stepwise transfer of ^{14}C from mono-methylamine to CO_2 via methane. Our results suggest that AOM is a crucial process in coastal wetland sediment to prevent the buildup of methane above the sulfate-methane transition zone. We propose that cryptic methane cycling has been largely overlooked in coastal wetlands resulting in incomplete understanding of carbon cycling in this environment.

1. Introduction

In the atmosphere, methane is a potent greenhouse gas that traps ~ 25 times more heat than CO_2 (IPCC, 2014). Atmospheric methane has doubled from 722 ppb in pre-industrial times to ~1850 ppb in 2017 (Dlugokencky, 2020; Nisbet et al., 2019; Saunois et al., 2020) and hence we urgently need to comprehend the mechanisms controlling its emission.

Natural wetlands are the largest contributor of methane into the atmosphere (IPCC, 2007; IPCC, 2014). They fall into two categories: coastal and freshwater. Both environments are characterized by high organic matter loading into sediments, which stimulates microbial methane production (Le Mer and Roger, 2001; Reddy and DeLaune, 2008; Segers, 1998). However, coastal wetlands emit far less methane (1.3g CH_4 m^{-2} yr^{-1}) into the atmosphere than freshwater wetlands (7.1g CH_4 m^{-2} yr^{-1}) (Bridgham et al., 2006; Bridgham et al., 2013). This discrepancy is due to the connection of coastal wetlands to the ocean, which supplies sulfate to fuel microbial sulfate reduction (SR) and sulfate-dependent anaerobic oxidation of methane (AOM) in anoxic sediment. Both processes suppress major releases of methane into the atmosphere (Le Mer and Roger, 2001; Reddy and DeLaune, 2008; Segers, 1998).

Microbial methanogenesis is the last step in carbon remineralization in water-logged sediment (Stephenson and Stickland, 1933; Thauer, 1998). The process generates methane from the following sources: hydrogen and carbon dioxide (hydrogenotrophic pathway) (Eq.1), acetate (acetolactic pathway) (Eq.2), and methylated substrates (methanol, methylamines and methylsulfides) (methylotrophic pathway) (Eq.3 and 4).

$$4H_2 + CO_2 \rightarrow CH_4 + 2H_2O \qquad [1]$$

$$CH_3COO^- + H^+ \rightarrow CO_2 + CH_4 \qquad [2]$$

$$4CH_3OH \rightarrow 3CH_4 + CO_2 + 2H_2O \qquad\qquad [3]$$

$$4CH_3NH_2 + 2H_2O \rightarrow 3CH_4 + CO_2 + 4NH_4 \qquad\qquad [4]$$
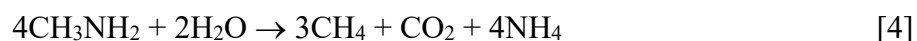
These pathways are facilitated by anaerobic archaea belonging to the Euryarchaeota Phyla. Hydrogen and acetate are competitive substrates, as they are also metabolized by sulfate-reducing bacteria, which tend to thermodynamically outcompete methanogens and thus suppress the production of methane in the presence of sulfate (Jørgensen, 2000; Kristjansson et al., 1982; Lovley and Klug, 1986; Winfrey and Ward, 1983). Consequently, methane builds up below the penetration depth of sulfate, i.e., in the absence of SR. In the zone where methane and sulfate overlap, methane can be consumed by AOM with sulfate as the terminal electron acceptor (Eq. 5). The process effectively removes roughly 90% of methane before reaching the water column (Hinrichs and Boetius, 2002; Knittel and Boetius, 2009; Reeburgh, 2007). AOM is mediated by a syntrophic consortium of anaerobic methanotrophic archaea (ANME) and sulfate-reducing bacteria (Boetius et al., 2000; Knittel and Boetius, 2009; Michaelis et al., 2002; Orphan et al., 2001a).

$$CH_4 + SO_4^{2-} \rightarrow HCO_3^- + HS^- + H_2O \qquad\qquad [5]$$

While hydrogenotrophic and acetoclastic methanogenesis is largely inhibited in the sulfate-reducing zone, methanogenesis can sustain their activity through a methylotrophic process. It is well established that methylated compounds (methanol, methylamine, methyl sulfides) are important non-competitive substrates for methanogenesis in sulfate-reducing sediment (Oremland and Polcin, 1982; Lovley and Klug, 1986; Maltby et al., 2016; Zhuang et al., 2016; Maltby et al.,

2018; Zhuang et al., 2018). Methanol sources include the degradation of lignin and pectin commonly found in terrestrial plant cell walls (Donnelly and Dagley, 1980; Schink and Zeikus, 1980). Methylamines and methyl sulfides are formed from the degradation of osmolytes such as glycine and betaine, and dimethylsulfoniopropinate, which are particularly abundant in saline and hypersaline environments (Oren, 1990; Zhuang et al., 2011; Zhuang et al., 2016). Methylotrophic methanogenesis has been detected in organic-rich, sulfate-reducing sediment of various aquatic environments such as intertidal estuaries and salt marshes (Oremland et al., 1982), river deltas (Zhuang et al., 2018), upwelling regions (Maltby et al., 2016), and eutrophic shelf sediment (Maltby et al., 2018b).

Despite strong evidences for methylotrophic methanogenesis in the sulfate-reducing zone, methane concentrations are considerably lower than in the deeper sulfate-free zone (Iversen and Jorgensen, 1985; Treude et al., 2005a; Treude et al., 2005b; Jorgensen and Kasten, 2006). Current research on the activity of methanogens in the sulfate-reducing zone of organic-rich sediment stimulated some speculation on the whereabouts of the produced methane and whether it could directly feed into AOM (Maltby et al., 2016; Maltby et al., 2018b; Zhuang et al., 2019a). Two recent studies using a combination of ^{13}C-CH$_4$ labeling and isotope dilution modeling provided the first evidence for a simultaneous production and consumption of methane and coined the 'cryptic methane cycle' (Xiao et al., 2017; Xiao et al., 2018). Experiments were conducted with anoxic organic-rich coastal sediment, which were spiked with ^{13}C-CH$_4$. The development of the ^{13}C-CH$_4$ signal was followed over time. The applied model presumed that the mole fraction of ^{13}C-CH$_4$ (^{13}C-CH$_4$ /(^{13}C-CH$_4$ + ^{12}C-CH$_4$)) changes through time as a result of production of methane from indigenous sources and consumption of methane due to AOM in the sediment. Community profiling revealed the presence of both hydrogenotrophic and methylotrophic methanogens among

61

the methanogenic archaea, while incubations with ^{14}C-labeled methanogenic substrates identified methylotrophic methanogenesis as the major pathway of methane production in the sediment.

Although it appears that AOM is the key to regulating methane in the sulfate-reducing zone, there are virtually no studies on the fate of methane produced from non-competitive methylotrophic methanogenesis in this environment. Notably, if AOM is active in the same zone as methanogenesis, the buildup and eventual emission of methane would be hampered, if not prevented. This would explain why only low levels of methane are detected in the sulfate-reducing zone, notwithstanding the presence of methanogenesis. Additionally, confirmation of a rapid turnover of methane would suggest that past gross methane budgets from wetlands were underestimated. Detection and quantification of this cryptic methane cycle is therefore essential to complement our understanding of carbon cycling in coastal wetlands.

With the application of an adapted radiotracer technique, this work will demonstrate the passage of carbon from a methylated substrate via methane to inorganic carbon within the sulfate-reducing zone of a coastal wetland. Our method shows that the methane source (i.e., methylotrophic methanogenesis) is spatially directly linked to its sink (AOM), hampering the buildup of methane in the sediment. This proof-of-concept study will provide an important step forward for the investigation of methane-related carbon cycling in coastal wetland sediment.

2. Methods

2.1 Study area and field sampling

The Carpinteria Salt Marsh Reserve (CSMR) is part of the University of California Natural Reserve System spanning a total of 230 acres of which 120 belong to the Natural Reserve System (Fig. 2-1A). Three major creeks run through and converge within the CSMR, and empty to the Pacific Ocean at its most southern end (Page et al., 1995). We selected a hypersaline pool within the CSMR (34°23'56.1"N 119°32'10.2"W) that exhibited black sulfidic sediment, indicative of a sulfate-reducing environment, and very little evidence of bioturbation, suggesting that sediment were largely anoxic (Fig. 2-1, B and C). During the sampling period, the pool had no visible supply of water from creeks, streams, or the ocean. However, salt crusts visible around the pool (Fig. 2-1B) and high salinity of the pool water (132 PSU, Fig. 2-2A) pointed towards past ocean influence.
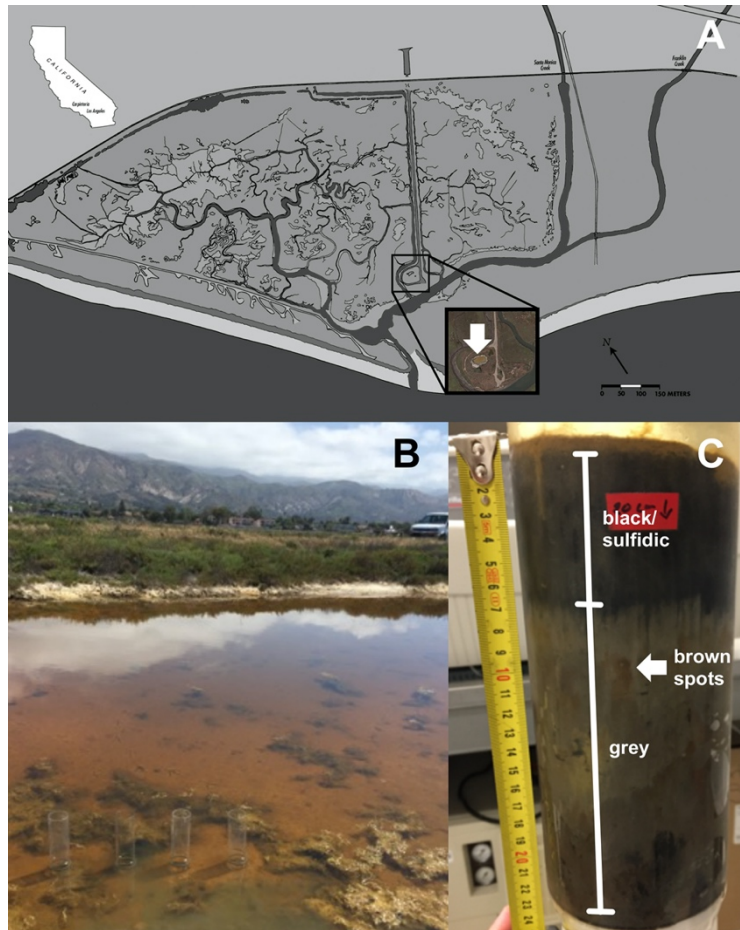
Figure 2-1. Study Site: (A) Map of the Carpinteria Salt Marsh Reserve and location of the hypersaline pool (white arrow); map courtesy of A. Brooks; satellite image from Google Maps. (B) Hypersaline pool with large push core liners placed for sampling. (C) Side view of a large sediment push core used for porewater extraction. Coloration of the sediment is labeled. For more details see text.

Sediment cores were collected in June 2018. The top ~20 cm of sediment was sampled by hand using large (10 cm i.d.) and small (2.6 cm i.d.) polycarbonate push core liners. Sediment were characterized by a brown surface (~0-1 cm), a distinct black (~1-8 cm) and grey/brown (>8 cm) layer. Water depth above the sampled sediment was approximately 10 cm. Liners were spaced at ~20 cm distance to facilitate sufficient space for extraction and closeness for comparability. Extraction of the sediment core was accomplished by careful removal of sediment around the liner and then placing a metal plate under the bottom of the liner for safe lifting. The air headspace remaining in the liner was carefully filled with water from the hypersaline pool and sealed bubble-free with rubber stoppers and electrical tape, to minimize disturbance of the surface sediment during transport. After same-day arrival at the home laboratory, all sediment cores were stored at 4 °C, in the dark, and processed within 1 d to 3 months of collection, depending on the type of analyses (for more details see below).

2.2 Porewater Geochemistry

For analyses of sediment porewater geochemistry, one large sediment push core was subsampled 1 d after collection. The core was sliced under a constant flow of argon to minimize oxidation of oxygen-sensitive solutes. The top sampled sediment layer, which had a high-water content, had a thickness of 1.5 cm. Below 1.5 cm, sediment were sliced evenly in 1 cm increments. All sediment layers were transferred into argon-flushed 50 mL conical centrifuge tubes and centrifuged at 4300 x g for 20 mins to separate porewater from sediment. Porewater was immediately analyzed for dissolved sulfide according to (Cline, 1969) and iron (II) according to (Grasshoff et al., 1999). Concentrations of the solutes were determined with a Shimadzu UV-Spectrophotometer (UV-1800). Remaining porewater was collected in plastic vials, stored at 4°C,

and later analyzed for sulfate and chloride concentrations using an ion chromatograph (Metrohm 761) according to (Dale et al., 2015). Salinity in the porewater was calculated from chlorinity using Knudsen's equation (Knudsen, 1901). Porosity of the sediment was determined by calculating the difference between sediment wet and dry weight divided by its volume. Sediment density was determined by dividing wet weight of the sediment by its volume.

2.3 In-vitro Methanogenesis

Two months after sample collection, one large push core was sliced into two layers (0-8 and 8-16 cm), distinguished by distinct black (1-8 cm) and grey/brown (8-16 cm) coloring, to study *in-vitro* methanogenesis after the addition of different substrates and inhibitors. Each layer was quickly subsampled using 3 mL cut-off plastic syringes under a steady flow of argon to minimize oxygen exposure. Ten mL of sediment were transferred into sterilized, argon-flushed 60 mL glass serum vials, sealed with blue butyl rubber stoppers (Bellco Glass Inc, 20 mm diameter) and crimped with aluminum crimps. Ten mL of artificial seawater medium, prepared according to (Widdel and Bak, 1992) and adjusted to sediment porewater salinity, was added to the sediment through the rubber stopper to make a 1:1 sediment/medium slurry. Medium was added to all sediment samples except a group of triplicates from each layer, which served as natural controls (see details below). Finally, the headspace of the sealed serum vials was flushed with argon for one minute to ensure anoxic conditions.

A total of 5 slurry amendments, each in triplicates per sediment layer, were prepared with: (1) 20 mM mono-methylamine (MMA), (2) 20 mM methanol, (3) 30 mM, sodium molybdate, (4) 60 mM, 2-bromoethanosulfonate (BES), (5) no addition (slurry control). In addition, triplicate vials per sediment layer containing undiluted sediment served as natural controls (6). Amendments

(1) and (2) served to study methane production from non-competitive methylated substrates. Amendments (3) and (4) served to evaluate methane production in the presence of a sulfate reducer (Oremland and Capone, 1988) and methanogen inhibitor (Hoehler et al., 1994), respectively. Controls (5) and (6) served to study the natural production of methane in diluted and undiluted sediment, respectively. Methane development in the headspace of the vials was monitored for a total of 3700 h.

Methane development in the headspace of the serum vials was tracked using a Shimadzu Gas Chromatograph (GC-2014) with a packed Haysep-D column and a flame ionization detector. The column temperature was 80 °C with helium as the carrier gas at 12 mL per min. Methane concentrations were calibrated against methane standards (Scotty Analyzed Gases) with a $\pm$ 5% precision.

2.4 Sulfate reduction

SR rates were determined by injecting radioactive, carrier-free ^{35}S-sulfate (^{35}S- SO_4^{2-}; dissolved in MilliQ water, injection volume 10 μL, activity 260 KBq, specific activity 1.59 TBq mg^{-1}) into a small whole-round push core at 1-cm increments according to (Jørgensen, 1978). The incubation started one month after core collection. Twenty-four hours prior to the injection of ^{35}S-SO_4^{2-}, the core was transferred from 4 °C storage to room temperature (in the dark). Radiotracer incubation was terminated after 24 h by slicing the cores in 1-cm increments into 50 mL centrifuge tubes filled with 20 mL 20% (w/w) zinc acetate solution. Each sample vial was shaken thoroughly to stop biological activity in the sediment and stored at -30°C until analyses. Control samples were prepared by slicing sediment from an additional small push core in 1-cm increments into tubes

with zinc acetate before radiotracer addition. Samples were analyzed using the cold-chromium distillation procedure and calculated according to (Kallmeyer et al., 2004).

2.5 Methanogenesis and AOM from ^{14}C-MMA

The main goal of this study was to follow (within the sulfate-rich zone) the conversion of a non-competitive substrate to methane by methanogenesis (MG-MMA), and the subsequent conversion of the produced methane to inorganic carbon by AOM (AOM-MMA). Tracking both processes simultaneously was accomplished by injecting whole round sediment cores with ^{14}C-labeled mono-methylamine (^{14}C-MMA) as representative methylated methanogen substrate. The concept of this method is that methanogens convert ^{14}C-MMA to ^{14}C-Methane (^{14}C-CH$_4$), which is then converted to ^{14}C-total inorganic carbon (^{14}C-TIC) via AOM. In the presence of both processes, we expect to find all three ^{14}C-compounds in the same sample after the incubation. With increasing incubation time, ^{14}C should move cumulatively from ^{14}C-MMA (via ^{14}C-CH$_4$) to ^{14}C-TIC. If AOM effectively removes methane at the rate of production, we expect to find no significant accumulation of ^{14}C-CH$_4$ in the sediment.

Twenty-four hours before sediment were injected with ^{14}C-MMA, six small sediment push cores were transferred to room temperature (in the dark) after storage for one month at 4 °C. Four of the push cores where injected with ^{14}C-MMA (^{14}C-mono-methylamine; dissolved in 1 mL water, injection volume 10 µL, activity 220 KBq, specific activity 1.85-2.22 GBq mmol^{-1}) and incubated for 1 h, 1 d, 1 wk and 3 wk, respectively, at room temperature, in the dark, to follow the step-wise conversion of ^{14}C-MMA via ^{14}C-CH$_4$ to ^{14}C-TIC. The incubations were terminated by slicing the cores at 1-cm increments into 50 mL wide-mouth crimp glass vials filled with 20 mL of 2.5% NaOH. Vials were sealed with butyl stoppers and aluminum crimps immediately and

67

shaken thoroughly to stop biological activity in the sediment and to separate ^{14}C-CH4 in the headspace from ^{14}C-MMA and ^{14}C-TIC in the liquid/solid phase of the sample. The 5th small push core was designated as the ^{14}C-MMA control core. The control core was sliced at 1-cm increments into vials with NaOH prior to radiotracer addition. Processing of the 6th core will be described under 2.5.3.

2.5.1 Determination of total CH$_4$ and ^{14}C-CH$_4$

Prior to the analyses of ^{14}C-CH$_4$ in the sample headspace, total CH$_4$ was determined by gas chromatography (Shimadzu GC-2014, see 2.3) from a small headspace sub-sample (100 µl). Analysis of ^{14}C-CH$_4$ was accomplished using a modified method by (Treude et al., 2005a), which was combined with a series of cold traps adapted from (Zhuang et al., 2017) to prevent potential contaminations with volatile ^{14}C-MMA or ^{14}C-CO$_2$. The full analytical setup is displayed in Fig. 2-2. In this adapted procedure, the headspace of the vial was purged with compressed air through a combustion oven (850°C) with copper (II) oxide to combust microbially produced ^{14}C-CH$_4$ to ^{14}C-CO$_2$. Additional traps were placed in line as follows, to prevent potential contaminations with other ^{14}C compounds: Impurities of volatilized ^{14}C-MMA were separated by passing the sample headspace through a 15 mL glass Hungate tube containing 10 mL of cold (0°C) 0.1 M citric acid buffer solution (19.3 g citric acid + 4g NaOH per liter of water, pH 4). Impurities of volatilized ^{14}C-CO$_2$ were separated by passing the gas headspace through a consecutive 15 mL Hungate tube, containing 10 mL of cold (0°C) 5% (w/w) sodium hydroxide. Both traps were held in a pre-frozen cryo safe cooler (Bel-Art, Junior 0°C). The purified headspace, containing CH$_4$ as the only ^{14}C-labelled compound, was then passed through a quartz column filled with granular copper (II) oxide placed in a combustion oven (850 °C) to oxidize ^{14}C-CH$_4$ to ^{14}C-CO$_2$. After exiting the oven, the

headspace with ^{14}C-CO_2 was then passed through a 20 mL scintillation vial containing 10 mL of citric acid buffer (pH 4, room temperature) to capture any water vapor, which could condense to tubing walls and collect ^{14}C-CO_2. Finally, the ^{14}C-CO_2 of the headspace was collected in two consecutive 20 mL scintillation vials filled with 10 mL of phenylethylamine and metoxyethanol (1:7 mixture, at room temperature). Oven timeseries tests conducted prior to sample analysis showed that >99% of ^{14}C-CH_4 is combusted to ^{14}C-CO_2 and collected in the CO_2 capture vials after 20 mins of headspace flushing. Radioactivity in both scintillation vials was determined by liquid scintillation counting after adding 10 ml scintillation cocktail (Ultima Gold XR, Perkin Elmer).

Prior to analyzing the first samples, the efficiency of all cold traps to capture ^{14}C-impurities was tested. Test samples were prepared by filling sample vials with 25 ml 5% NaOH to replicate the total volume of a sample containing sodium hydroxide (20 mL) and sediment (~5 mL). Added to the samples vials was either ^{14}C-MMA, ^{14}C -CH_4, ^{14}C-TIC (the latter in the form of ^{14}C-bicarbonate). Test samples were sealed and run through the combustion setup (see method above). Activity of all impurity traps and the final traps that captured the combusted ^{14}C-CH_4 was determined by liquid scintillation counting. Test samples with added ^{14}C-CH_4 showed that 97-99% of the analyzed ^{14}C was detected in the final methoxyethanol/phenylethylamine traps (CO_2 traps) (Fig. 2-2, #11). The remaining 1-3% of the ^{14}C was detected in the citric acid trap (Fig. 2-3, #10). Oven test samples with added ^{14}C-MMA showed that 99.97% of the ^{14}C remained in the sample vial, while <0.01% was detected in the cold citric acid (Fig. 2-2, #6), <0.01% in the cold NaOH cold trap (Fig. 2-2, #7) and <0.01% in the CO_2 traps (Fig. 2-2, #11). Oven test samples with added ^{14}C-TIC (in the form of ^{14}C-bicarbonate) showed that 99.97% of the ^{14}C remained in the sample

69

vial, while <0.01% was detected in the cold citric acid (Fig. 2-2, #6), <0.01% in the cold NaOH

cold trap (Fig. 2-2, #7) and <0.01% in the CO_2 traps (Fig. 2-2, #11).
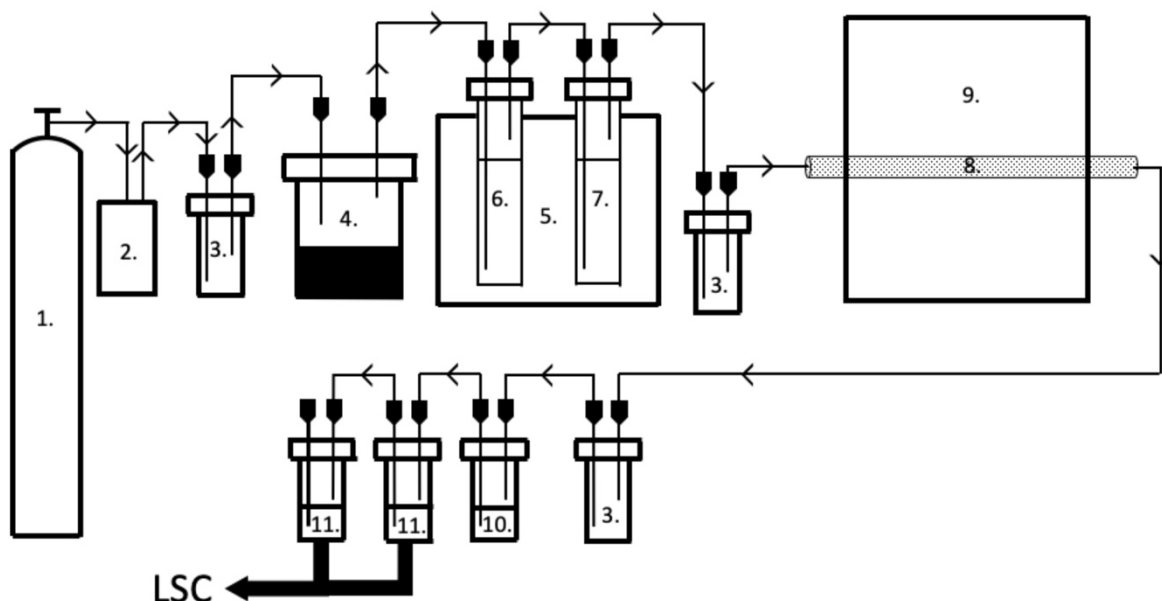
Figure 2-2. Schematic of the method used to purge, combust, and trap $^{14}C\text{-}CH_4$ from the sample vial headspace, while removing all potential volatile ^{14}C impurities ($^{14}C\text{-}MMA$ and $^{14}C\text{-}CO_2$) via intermediate traps. Narrow arrows indicate the direction of the gas flow. Labels: (1) compressed air tank, (2) mass flow controller (Analyt MTC), (3) safety vial: empty glass crimp vial (10 ml), (4) sample vial: glass crimp vial (50 ml) with sample and headspace, (5) cryo box, 0ºC (Bel Art), (6) $^{14}C\text{-}MMA$ trap: Hungate tube (15ml) filled with citric acid buffer (10 ml, pH 4, 0ºC), (7) $^{14}C\text{-}CO_2$ trap: Hungate tube filled with 5% w/w NaOH (10 ml, pH 14, 0ºC), (8) quartz column with granular copper (II) oxide, (9) combustion oven (850ºC), (10) H_2O trap: glass crimp vial (10 ml) filled with citric acid buffer (10 ml, pH 4), (11) $^{14}CO_2$-trap (for combusted $^{14}C\text{-}CH_4$): two consecutive scintillation vials (20 ml) filled with 10 ml phenylethylamine/methoxyethanol (1:7 mixture), (LSC) liquid scintillation counting. Tubing (in direction of flow): copper (between tank and controller), TYGON (between controller and the second safety trap), ISO-VERSINIC (before/after oven), TYGON (between the third safety trap and the second scintillation vial). Gas enters/exists vials from/into tubing via luer connectors/needles. Note that objects are not to scale. The method was adapted from Treude et al., (2005a) and Zhuang et al., (2017). For more details see text.

2.5.2 Determination of $^{14}C\text{-}MMA$ and $^{14}C\text{-}TIC$

Total ^{14}C activity in the liquid sample (i.e., the sum of residual $^{14}C\text{-}MMA$ and the dissolved

fraction of the produced $^{14}C\text{-}TIC$) was determined by subsampling 100 μL of clear supernatant

from the sample vial into a 6 ml scintillation vial, to which 1 mL ultrapure water and 3 mL

scintillation cocktail (Ultima Gold XR, Perkin Elmer) was added before liquid scintillation

70

counting. Note that this procedure does not capture potential ^{14}C-CaCO$_3$ precipitates in the solid phase of the sample. Any ^{14}C that was present in the solid phase as ^{14}C-CaCO$_3$ would lead to an overestimation of the rates, because it would underestimate the pool of ^{14}C injected at the start of the incubation. However, since microbially-induced carbonate precipitations can be expected to be a sluggish process even under optimized conditions (Krause, 2012), we expect no significant overestimation of rates for the applied incubation times.

The total produced ^{14}C-TIC (including potential ^{14}C-CaCO$_3$ precipitates) was determined by acidification according to (Joye et al., 2004). The sample vial was opened and weighed before and after the sample was transferred to a 250 mL Erlenmeyer flask to determine the sample weight. After transfer to the Erlenmeyer flask, a drop of antifoam agent (Antifoam B Silicon Emulsion) was added to prevent excessive foaming after acidification. The Erlenmeyer flask was then sealed with a butyl stopper, which was prepped with a metal wire threaded through the stopper and a plastic ring at the end of the wire. The ring was used to hold an open 6 mL scintillation vial filled with a mixture of 1 mL of phenylethylamine and 1 mL of 2.5% (w/w) NaOH, which served as a trap for ^{14}C-CO$_2$. The sample was acidified by injecting 6 mL of 6 M hydrochloric acid using a 10 mL syringe equipped with a long needle. The needle of the loaded syringe was held in place between the butyl stopper and the glass of the Erlenmeyer flask while acid was injected. After injection, the needle was removed quickly, and the stopper was fixed with a metal clip. The Erlenmeyer flask was then placed on a shaking table for 4 h to ensure all ^{14}C-TIC was converted to ^{14}C-CO$_2$, released into the headspace, and captured in the ^{14}C-CO$_2$ trap. The scintillation vial was then removed from the flask and radioactivity was determined by liquid scintillation (see above). The resulting value, which represents the total ^{14}C-TIC, was then subtracted from the total

[14]C activity in the liquid sample (see above) to determine the activity of the residual ^{14}C-MMA in the liquid phase.

Prior to sample analysis, test samples containing only NaOH solution and ^{14}C-MMA were sent through the same procedure to test if ^{14}C-MMA is accidently captured by the suspended ^{14}C-CO_2 trap. These samples showed that 99.99% of the ^{14}C remained in the NaOH supernatant and <0.01% was detected in the CO_2 trap. Vice versa, test samples containing only NaOH and ^{14}C-TIC (in the form of ^{14}C-bicarbonate) showed that 99.99% of the ^{14}C was captured in the CO_2 trap while <0.01% of the ^{14}C remained in the NaOH supernatant after acidification/shaking.

2.5.3 Determination of ^{14}C-MMA recovery from sediment

Methylated amines bind to sediment surfaces and therefore quantification of methylated amines from sediment porewaters underestimates the total amount present in the sediment (Wang and Lee, 1993, 1994; Xiao and Peacock, 2019). The recovery factor of ^{14}C-MMA from sediment was determined as follows: the top 5 cm of the 6th small push core from the hypersaline pool was sliced at 1-cm intervals, and each sediment slice was transferred to 250 ml Erlenmeyer flasks with NaOH similar to the above procedure (2.5.2) to produce a total of 5 killed sediment samples. An additional set of three 250 ml Erlenmeyer flasks containing only NaOH (no sediment) served for the determination of the total added ^{14}C-MMA. A magnetic stir bar was added to each Erlenmeyer flask, and each flask was placed on a magnetic stir plate. After the sediment was homogeneously mixed with the NaOH, ^{14}C-MMA (dissolved in water, 1 mL, 220 KBq, 1.85-2.22 GBq specific activity) was added to each flask (killed samples and NaOH samples) and stirred into the samples. The two setups were then shaken for 4 h. After shaking and resting, 100 μl of the clear supernatant

72

was subsampled from all flasks, and radioactivity was determined by liquid scintillation (see method above). The recovery factor was calculated as follows (Eq. 6):

$$RF = \left[\frac{a_{SED}}{a_{NaOH}}\right]$$
[6]

where RF is the recovery factor; a_{SED} is the averaged amount of radioactivity (CPM) recovered from the flasks containing NaOH and the sediment sample; a_{NaOH} is the averaged amount of radioactivity (CPM) recovered from the flasks containing only NaOH. The total amount of ^{14}C-MMA in samples was then determined by dividing the ^{14}C-MMA determined in 2.5.2 by the recovery factor (see Eq. 7).

The tested sediment samples showed a mean ^{14}C-MMA recovery of 46% after shaking and acidification compared to sediment-free controls. The standard deviation of CPM recovered from five test samples was 22.5%, while the standard deviation of CPM recovered from three controls was 3%. The determined recovery factor (0.46, Eq. 6) was applied to calculate the total CPM of ^{14}C-MMA.

2.5.4 Calculations of methanogenesis and AOM rates

Results from ^{14}C-MMA incubations were used to calculate metabolic rate of MG-MMA and coupled AOM-MMA. MG-MMA rate calculations take into consideration the natural porewater concentrations of MMA, residual ^{14}C-MMA, ^{14}C-CH$_4$, and ^{14}C-TIC (Eq. 7). The sum of all three ^{14}C-components represents the total amount of ^{14}C-MMA injected at t_0, while the sum of ^{14}C-CH$_4$ and ^{14}C-TIC represents the metabolic product of methanogenesis at the end of the incubation, assuming that ^{14}C-TIC was derived from ^{14}C-CH$_4$ after consumption by AOM. Natural

concentrations of MMA could not be determined for this study. Fitsimmons et al., 1997 reported MMA concentrations from salt marsh sediment pore water between 0-319 μM. Based on this knowledge, a high (100 μM) and a low (10 μM) MMA concentration was assumed to complete the rate calculations as follows (Eq. 7):

$$MG\text{-}MMA = \frac{a_{CH_4} + a_{TIC}}{a_{CH_4} + a_{TIC} + \left[\frac{a_{MMA}}{RF}\right]} * [MMA]_{LIT} * \frac{1}{t} \qquad [7]$$

where *MG-MMA* is the rate of methanogenesis from MMA (nmol cm^{-3} d^{-1}); a_{CH4} is the produced radioactive methane (CPM); a_{TIC} is the ^{14}C-TIC produced from methane (CPM); a_{MMA} the residual ^{14}C-MMA (CPM); RF is the recovery factor (Eq. 6); *[MMA]$_{LIT}$* is the assumed MMA porewater concentrations from (Fitzsimons et al., 1997) (nmol cm^{-3}); t is the incubation time (d). ^{14}C-CH$_4$ and ^{14}C-TIC sample activity was corrected by respective non-biological activity determined in controls.

Calculation of AOM-MMA rates based on methane produced from ^{14}C-MMA take into consideration the total methane measured from the headspace of the sample vial, ^{14}C-CH$_4$ produced by MG-MMA, and ^{14}C-TIC produced by AOM (Eq. 8). The sum of ^{14}C-CH$_4$ and ^{14}C-TIC represents the total amount of ^{14}C-CH$_4$ that was produced and available for AOM over the entire incubation, while ^{14}C-TIC represents the metabolic product of AOM at the end of the incubation. Note that concentrations of total methane should usually be taken at the start of an incubation (not at the end as done here). But since methane concentrations remained stable in controls of long-term incubations over the first weeks (see 3.2), we felt comfortable using the end concentrations for our calculations. It should be further highlighted that ^{14}C-labeled methane available for AOM was not present at t_0 but instead was produced over time. Hence, AOM rates

based on ^{14}C-CH$_4$ from ^{14}C-MMA represent an underestimation of the actual rate in this approach. AOM-MMA rates were calculated according to Eq. 8:

$$AOM - MMA = \frac{a_{TIC}}{a_{CH_4} + a_{TIC}} * [CH_4] * \frac{1}{t} \hspace{3cm} [8]$$

where *AOM-MMA* is the AOM rate based on methane produced from MMA (nmol cm^{-3}d^{-1}); a_{TIC} is the produced ^{14}C-TIC (CPM); a_{CH4} is the residual radioactive methane (CPM); *[CH$_4$]* is the methane concentration in the sample vial headspace (nmol cm^{-3}); t is the incubation time (d). ^{14}C-TIC activity was corrected by non-biological activity determined in controls.

2.6 AOM from ^{14}C-CH$_4$

AOM rates determined directly from ^{14}C-CH$_4$ (AOM-CH$_4$) were produced by injecting ^{14}C-CH$_4$ (^{14}C-CH$_4$ dissolved in anoxic MilliQ, injection volume 15 µL, activity 5 KBq, specific activity 1.85-2.22 GBq mmol^{-1}) into a small push core from the hypersaline pool at 1-cm increments similar to the injections procedures in 2.4 and 2.5. One month after storage at 4 °C, and 24 h prior to radiotracer injection, the core was transferred to room temperature (in the dark). After radiotracer injection, the core was incubated for 24 h at room temperature, in the dark. The incubation was terminated by slicing the core at 1-cm increments into 50 mL wide-mouth crimp glass vials filled with 20 mL of 2.5% NaOH. Vials were sealed with butyl stoppers and aluminum crimps immediately and shaken thoroughly to stop biological activity in the sediment. Control samples were prepared by slicing sediment from a separate small pushcore into vials with NaOH before tracer addition. Prior to ^{14}C analysis, total CH$_4$ concentrations within each vial was determined by extracting a 100 µL gas sample from the headspace of the AOM-CH$_4$ samples and analyzing it by gas chromatography (see 2.5). Residual ^{14}C-CH$_4$ in the headspace was determined

by liquid scintillation counting after combustion to ^{14}C-CO_2 and CO_2-capturing. ^{14}C-TIC produced as a result of AOM was determined by liquid scintillation counting after acidification and shaking. AOM-CH_4 rates were calculated according to Eq. 8.

3. Results

3.1 Biogeochemical characterization of the study site

Porewater salinity in the sediment core (0-20 cm) ranged between ~110-140 PSU characterizing the pool as hypersaline (Fig. 2-3A). Porewater sulfate concentrations (60 - 75 mM) were about three times above open ocean seawater concentrations and illustrated that samples were taken within the sulfate-rich zone (Fig. 2-3C). The highest sulfate concentration (74 mM) was measured at 1.5-2.5 cm. Sulfate gradually decreased with sediment depth displaying the lowest concentration (63 mM) at 16.5-17.5 cm. Microbial SR activity was only detected in the top 6 cm, showing a maximum rate of 728 nmol $cm^{-3}d^{-1}$ at 0-1 cm. Below 6 cm, SR was not detectable despite high concentration of sulfate throughout the core. Porewater sulfide concentrations varied throughout the sediment column (1-12 μM) with one maximum at 7.5-8.5 cm (12 μM) (Fig. 2-3D). Dissolved iron (II) was detected throughout the sediment column, reaching two maxima (~760 and 642 μM) between 0-2.5 cm and at 11.5-12.5 cm, respectively (Fig. 2-3D).

Methane concentrations determined in the AOM vials peaked (~40 nmol cm^{-3}) at 0-1cm (Fig. 2-3B). Between 1 and 4 cm, methane decreased to 16 nmol cm^{-3} before increasing again to 30 nmol cm^{-3} at 4-5 cm. Between 5 and 19 cm, methane concentrations varied between 13 and 35 nmol cm^{-3}. AOM activity determined from ^{14}C-CH_4 (AOM-CH_4) was detected within and below the sulfate-reducing zone. Within the sulfate-reducing zone (0-6 cm), a peak in AOM (13 nmol $cm^{-3}d^{-1}$) was detected at 0-1 cm, which aligned with the highest SR rates and a peak in methane. Below 1 cm, AOM declined along with SR and methane. Below the sulfate-reducing zone, AOM gradually increased again, reaching a broad second peak (4.5 to 15 nmol $cm^{-3}d^{-1}$) between 6 and 12 cm. These maxima roughly coincided with elevated iron (II) concentrations (Fig. 2-3D). Below 12 cm, AOM and iron (II) decreased with depth whereas methane concentrations varied between

22 and 36 nmol cm^{-3} through the rest of the core (Fig. 2-3B). An additional smaller AOM peak (6 nmol cm^{-3}d^{-1}) was detected at the bottom of the core.
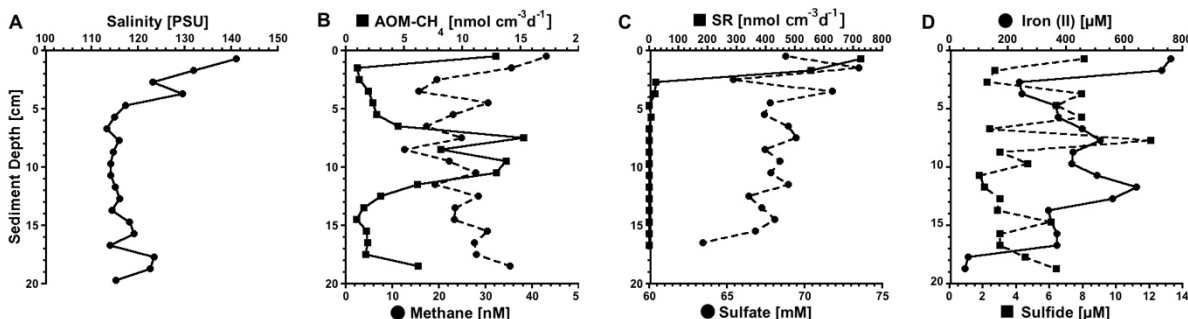
Figure 2-3. Depth profiles of biogeochemical parameters in sediment from the hypersaline pool in the CSMR: (A) salinity, (B) methane (determined in the AOM vial) and AOM-CH$_4$ (determined from the direct injection of ^{14}C-CH$_4$), (C) porewater sulfate and sulfate reduction (SR), (D) porewater sulfide and iron (II).

3.2 Response of methanogenesis to different additives

Fig. 2-4 shows results from the *in-vitro* time-series study of methanogenesis with sediment slurries from the 0-8 cm and 8-16 cm layers. Slurries contained either non-competitive methanogenesis substrates (MMA or MetOH), inhibitors of methanogenesis and SR (BES or molybdate, respectively), or no additives (slurry control). Undiluted sediment without additions served as natural controls.

Methane in the natural control increased only slightly from ca. 40 to 150 ppmv in both the 0-8 cm and 8-16 cm layers over 3700 h (Fig. 2-4F). The slurry control followed a similar trend (Fig. 2-4C). Different to the controls, all treatments with non-competitive methanogen substrates showed a steep increase in methane to >40000 ppmv after 320 h and reached a stationary phase starting at 420 h (Fig. 2-4A and D). Starting at 1000 h, a slight decrease in methane was observed. Sediment from the bottom 8-16 cm developed slightly higher methane maxima (49000 and 49500 ppmv) with MMA and methanol, respectively.

Methane in sediment slurries amended with BES varied without trend between 30 to 60 ppmv in both sediment layers, which was lower than the controls (Fig. 2-4E). Methane in sediment slurries from 0-8 cm amended with molybdate increased from 130 to 1340 ppmv after 400 h and remained between 1260 and 1950 ppmv for the remaining 3400 h (Fig. 2-4B). One replicate from the top 0-8 cm increased to 7284 ppmv at the end of the incubation. Molybdate-amended slurries from 8-16 cm (Fig. 2-4B) released methane an order of
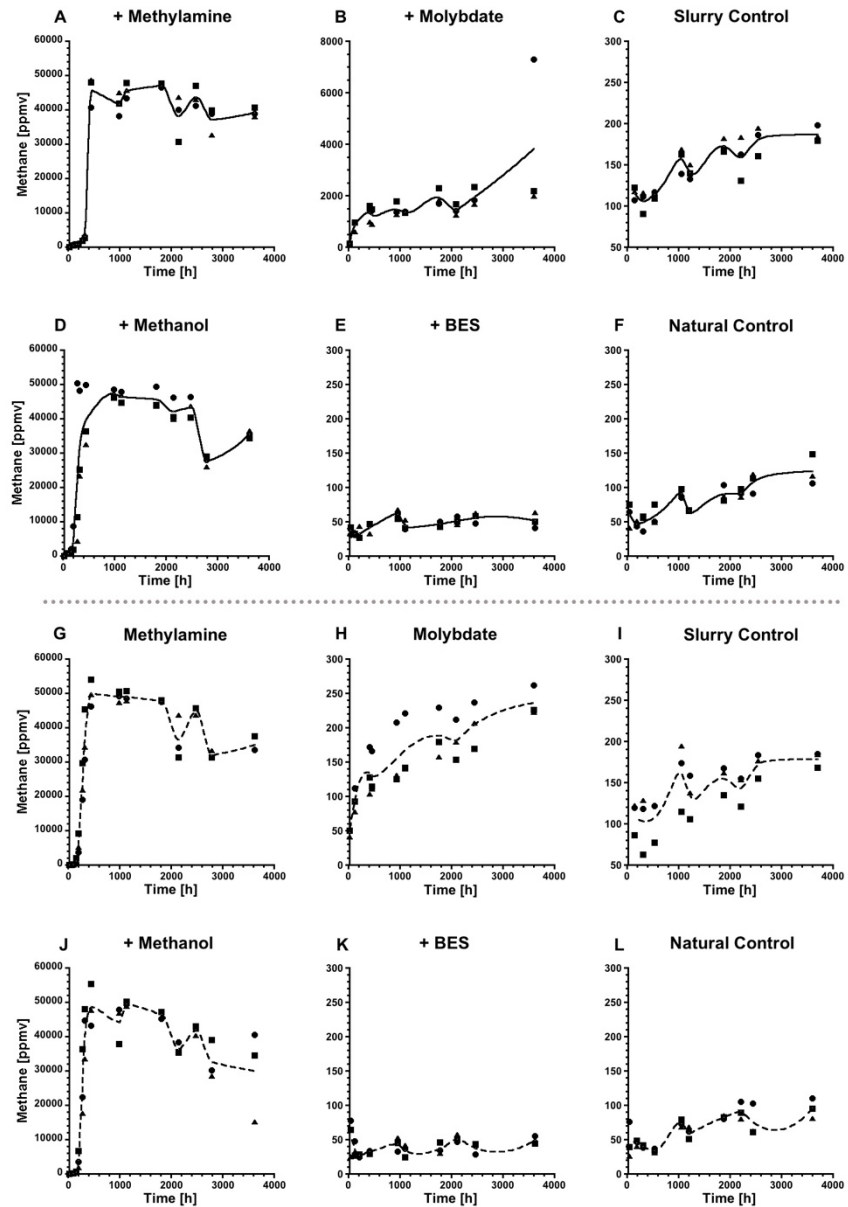
Figure 2-4. Temporal development of methane (ppmv) in the headspace of incubation vials containing sediment slurries from the 0-8 cm (solid line and filled symbols) and 8-16 cm (dashed line and open symbols) layer of the hypersaline pool. Slurries were treated with mono-methylamine (20 mM, A), methanol (20 mM, D), molybdate (30 mM, B), BES (60 mM, E). Slurries without additives (slurry control, C) and undiluted sediment (natural control, F) served as controls. Note the different scales on the y-axes.

79

magnitude lower than the respective slurries from 0-8 cm, which was closer to trends found in the slurry controls (Fig. 2-4C).

3.3 Coupled methanogenesis and AOM

3.3.1 ^{14}C-MMA time-series incubation with sediment cores

Methylotrophic methanogenesis supporting AOM (AOM-MMA) in the sulfate-rich zone was determined by ^{14}C-MMA injections into 4 separate push cores, which were incubated for 1 h, 1 d, 1 wk, and 3 wk, respectively. Fig. 2-5 shows the radioactivity distribution (percentage counts per minute = % CPM) between the residual ^{14}C-MMA, the produced ^{14}C-CH$_4$, and the produced ^{14}C-TIC for the four incubations.

After the 1-h incubation, the majority of radioactivity remained in the residual ^{14}C-MMA (96-99%) throughout the core, while smaller percentages of radioactivity were found in ^{14}C-CH$_4$ (0-0.06%) and ^{14}C-TIC (1-5%) (Fig. 2-5A).

After the 1-d incubation, the percentage of ^{14}C-MMA was lower in the top 4 cm, reaching as low as 58% at 1-2 cm (Fig. 2-5B). Below 5 cm, 94-98% of the radioactivity remained in the ^{14}C-MMA. Correspondingly, more ^{14}C-CH$_4$ was detected in the top 5 cm, with a maximum of 11% at 0-2 cm. These depths of elevated ^{14}C-CH$_4$ overlapped with depths of elevated AOM-CH$_4$ and SR in replicate cores (Fig. 2-3). Below 5 cm, ^{14}C-CH$_4$ remained low (0.05-0.6%) (Fig. 2-5B). Similarly, the percentage of ^{14}C-TIC was higher (10-32%) in the top 5 cm with a maximum at 1-2 cm. Below 5 cm, the percentage of ^{14}C-TIC decreased gradually with depth from 5 to 2%.

After the 1-wk incubation, radioactivity from ^{14}C-MMA was below detection at 1-3 and 4-5 cm, pointing to complete exhaustion of the labeled compound (Fig. 2-5C). At depths below 5 cm, between 40 and 80% of the radioactivity remained in the ^{14}C-MMA. Radioactivity from ^{14}C-

CH$_4$ was between 3 and 19% percent in the top 7 cm, with a maximum at 2-3 cm. Below 7 cm, 0.1 to 3% of radioactivity was found in ^{14}C-CH$_4$. Radioactivity from ^{14}C-TIC was 81 to 87% between 1-5 cm, indicating the majority of the label was completely turned over. Below 7 cm, radioactivity from ^{14}C-TIC decreased from 57 to 20% with depth. It is notable that the production of ^{14}C-TIC was weaker at 5-6 and 6-7 cm (14 and 27 %), while ^{14}C-CH$_4$ made up 14 and 8 % of the label, respectively.

After the 3-wk incubation, radioactivity from ^{14}C-MMA was below detection in the top 7 cm and at 12-13 cm (Fig. 2-5D). Between 7-12, and 13-15 cm, 2-17% of the radioactivity was found in the ^{14}C-MMA. Throughout the sediment core, a small fraction of radioactivity was detected in ^{14}C-CH$_4$ (0.05-10%), reaching a maximum at 9-10 cm. In the top 7 cm, most radioactivity was found in ^{14}C-TIC (94-99%). Below 7 cm, radioactivity of ^{14}C-TIC was more variable, ranging between 79-97%.

Note that radioactivity detected in the killed control samples was not subtracted from CPM results presented in Fig. 2-5, because we noticed after the analyses that microbial activity in the controls (and possibly also in the samples) was not immediately terminated after the addition of NaOH, likely due to insufficient homogenization (shaking). Since killed controls were produced from the top 5 cm of the sediment, which also showed the highest microbial activity (see Fig. 2-5), it was not advisable to use the average of these controls to make CPM corrections for the entire sediment core. Radioactivity detected in the killed controls relative to the samples was on average 26%, 0.5%, 0.2%, and 0.3% for ^{14}C-CH$_4$, as well as 107%, 65%, 16%, and 9% for ^{14}C-TIC in the 1-h, 1-d, 1-wk, and 3-wk incubation, respectively. The development of ^{14}C-TIC in the controls relative to the samples indicates that microbial activity was likely terminated after roughly 1 day.
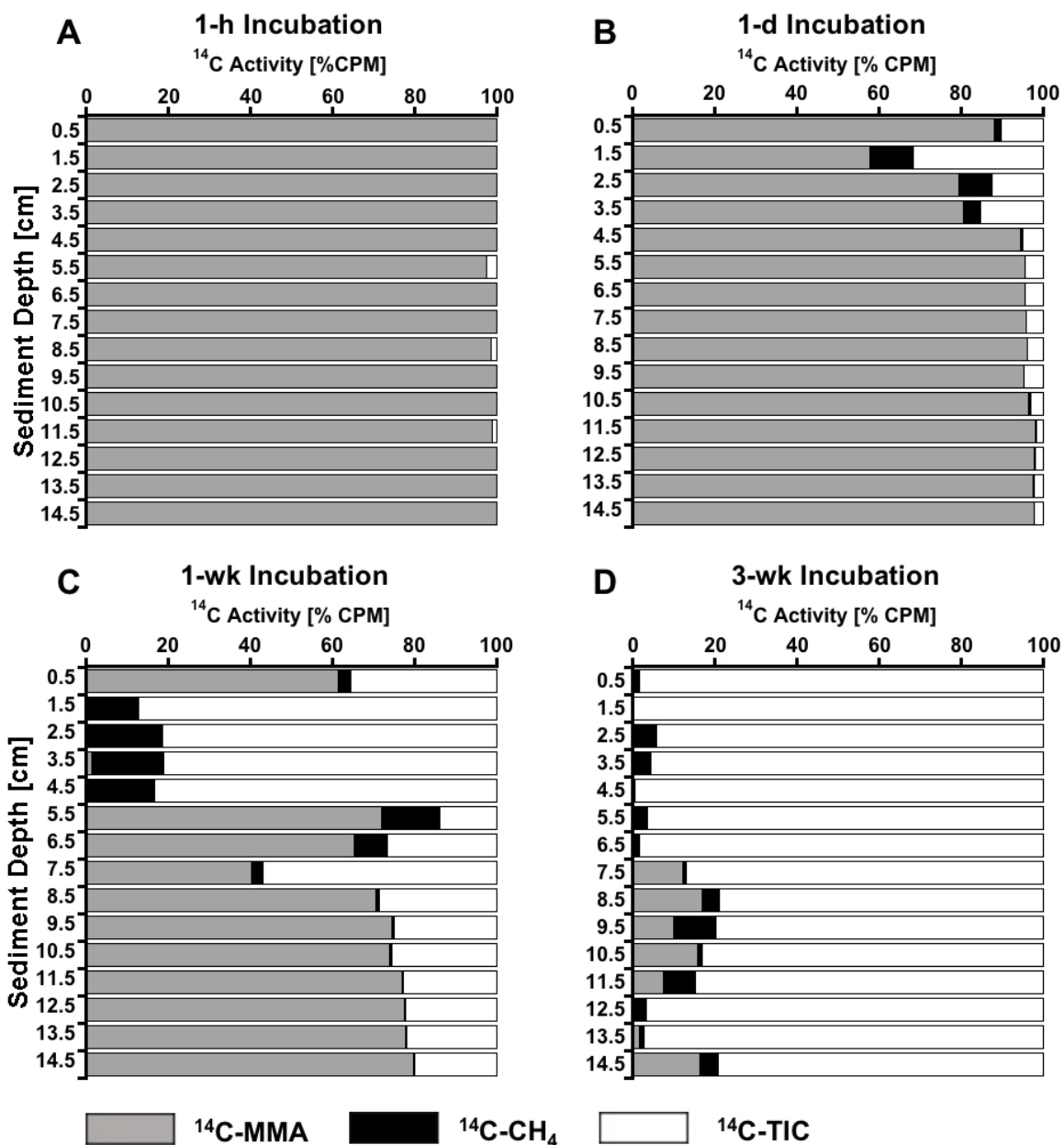
Figure 2-5. Sediment depth profiles of ^{14}C radioactivity (in counts per minute = CPM) from mono-methylamine (MMA), CH$_4$, and total inorganic carbon (TIC) expressed as the percentage of the sum of all [14]C. Shown are depth profiles for 1-h (A), 1-d (B), 1-wk (C) and 3-wk (D) incubations in replicate sediment cores.

3.3.2 Estimation of environmental turnover rates

Fig. 2-6 compares MG-MMA rates with rates of AOM-MMA and AOM-CH$_4$. The MG-MMA rates were calculated assuming min/max concentrations of MMA (10 and 100 µM) based

on a study by (Fitzsimons et al., 1997) (for details see 2.5.4). AOM rate calculations were based on methane concentrations determined in the headspace of the incubation vials (Fig. 2-6B). We selected the 1-d incubation from the ^{14}C-MMA time series incubation as the optimum incubation time for rate calculations (see 4.3.1). Note that for these calculations, the average radioactivity detected in controls of the MMA incubation was subtracted from the sample values, which likely resulted in an underestimation of the rates, as microbial activity continued for ~1 d past incubation termination (see 2.5.4).

Activity of MG-MMA and AOM-MMA overlapped between 0-10 and 15-17 cm (Fig. 2-6). AOM-MMA rates were highest between 4-10 cm, peaking at 4-5 cm (27 nmol cm^{-3}d^{-1}), while MG-MMA rates were highest between 0-4 cm, peaking at 2-3 cm (1.6 and 16 nmol cm^{-3}d^{-1} for the 10 and 100 μM MMA, respectively). AOM-MMA was below detection between 10 and 15 cm, as a result of the control correction, while MG-MMA was low (< 1 nmol cm^{-3}d^{-1}). AOM rates peaked between 15-17 cm (14 nmol cm^{-3}d^{-1}), while MG-MMA rates were low (0.1 and 1 nmol cm^{-3} d^{-1}, respectively).

In comparison, AOM-MMA and AOM-CH$_4$ reached similar maxima (10-30 nmol cm^{-3}d^{-1}), but slightly offset patterns in activity peaks (Fig. 2-6B). While AOM-MMA activity was separated between the top half and a lower section of the core, AOM-CH$_4$ showed three peaks: at 0-1 cm, between 7 and 12 cm, and at the bottom of the core.

Integrated rates (0-15 cm) of MG-MMA (based on 10/100 μM MMA), AOM-MMA, and AOM-CH$_4$ were 0.08/0.83, 1.74, and 0.88, respectively for the 1-d incubations.
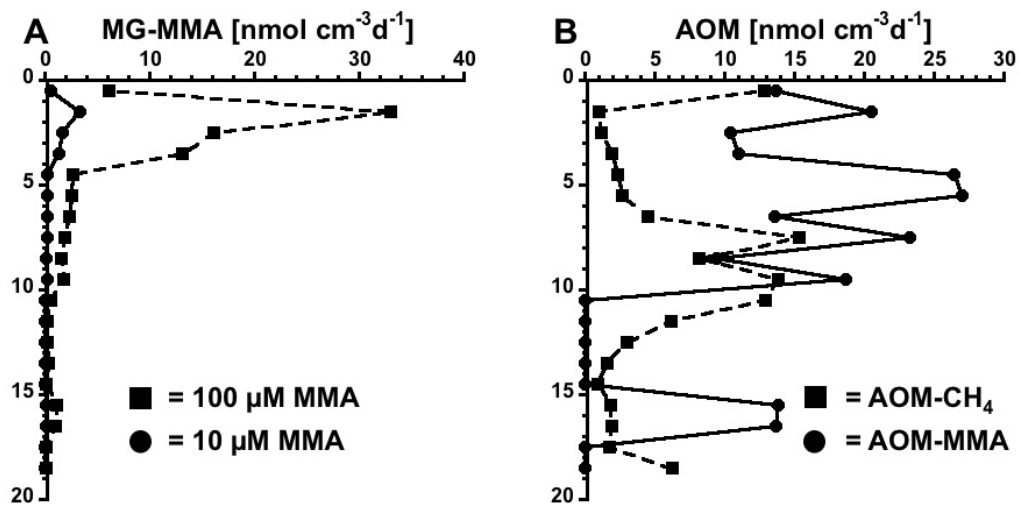
Figure 2-6. Depth profiles of (A) methanogenesis rates determined from ^{14}C-MMA incubations (MG-MMA) assuming natural mono-methylamine concentrations of 10 and 100 μM based on (Fitzsimons et al., 1997), and (B) AOM rates determined from ^{14}C-CH4 incubations (AOM-CH4) and ^{14}C-MMA incubations (AOM-MMA) in hypersaline sediment from the Carpinteria Salt Marsh Reserve.

4. Discussion

4.1 Vertical organization of electron acceptor utilization

SR rates determined by $^{35}S\text{-}SO_4^{2-}$ incubations were highest in the top 1 cm layer of sediment and restricted to the top 6 cm (Fig. 2-2C), illustrating a distinct sulfate-reducing environment. This finding is consistent with black coloration of the sediment in the top 1-8 cm, most likely due to precipitation of iron sulfides. Sulfate was never limiting (>63 mM) throughout the core, while salinity was found to be slightly higher ($\sim15\%$) in the sulfate-reducing environment. Lack of direct water supply makes the pool highly susceptible to evaporation, which likely explains high salinity and sulfate concentrations. The abrupt drop of SR below 4 cm despite the presence of high sulfate concentrations is surprising and unlikely to be correlated to a limitation in organic matter, since coastal salt marshes are known to be rich in organic matter substrates in the top 50 to 100 cm (Ouyang and Lee, 2014; Reddy and DeLaune, 2008; Schlesinger, 1977). An explanation could be the stimulation of halophilic-sulfate reducers in the more saline surface layers of the sediment. A weak positive correlation between salinity and SR was found in natural sediment from hypersaline and highly saline coastal pans in South Africa (Oren, 2015; Porter et al., 2007). *In-vitro* sediment slurry experiments with these sediment revealed optimum salinities for sulfate-reduction activity was between 272 to 311 in hypersaline pans and 134 to 244 in highly saline pans.

Below the zone of SR, the dominant electron acceptor for metabolic processes was likely iron (III), which is supported by the observation of brown spots (indicative for iron oxides, Fig. 2-1C) and the presence of dissolved iron (II) (Fig. 2-2D, product of iron reduction). Iron reduction activity could be an alternative reason for the absence of SR below 6 cm. In freshwater river sediment, SR was inhibited by 85-100% in the presences of iron reduction (Lovley and Phillips,

1987b). However, direct evidence of iron reduction in the hypersaline pool is not available for this study and needs future investigation.

It is notable that both iron (II) and sulfide were present throughout the entire sediment core, i.e., sulfide was detected below the zone of SR and iron (II) was present within the sulfate-reducing zone. This finding points to potential seasonal fluctuations of processes in the sediment. It is possible that halophilic SR is only facilitated during the dry season, when salinity in the surface layer is highest, and is likewise inhibited during the wet season, when salinity drops below the salinity optimum. Consequently, our study would only provide a snapshot of a highly dynamic system. Future studies should therefore test if halophilic-sulfate reducers are outcompeting iron reducers during the dry season owing to their hypersaline adaptation.

The reverse redox gradient makes this hypersaline environment unique and unconventional compared to the usual succession of heterotrophic processes in marine sediment (Jørgensen, 2000), and possibly plays a role for cryptic methane cycling. Following suggested vertical distribution of redox processes, AOM activity determined by ^{14}C-CH$_4$ incubations was likely coupled to SR within the top 6 cm, and to iron reduction at depths below (Fig. 2-2B-D). This hypothesis is supported by double maxima of AOM at the surface (in alignment with the SR peak) and between 7 and 12 cm (in alignment with an increase in iron (II)). Both sulfate and iron (III) are known electron acceptors used by AOM (Beal et al., 2009; Nauhaus et al., 2002; Segarra et al., 2013b; Treude et al., 2005b). It should be kept in mind, however, that aside from the availability of electron acceptors, also the distribution and magnitude of *in-situ* methane production plays an important role for the location of AOM hot spots in the sulfate-rich sediment.

4.2 Methanogenesis coupled to methylotrophic substrates

Considerable methane production was observed in sediment slurries, when either MMA or methanol was added (Fig. 2-4). Methanogenesis from MMA and methanol produced three orders of magnitude more methane than controls. The results suggest methylotrophic methanogens were present in the sediment and responded to the substrate addition. The spike in methane production after the 400 h (16 d) lag phase is likely a result of methanogen community expansion in response to excess availability of methylated substrates. This trend concurs with results of (Oremland and Polcin, 1982), who reported a spike in methane production in estuarian sediment after 10 d following the addition of trimethylamine, methanol and methyl-sulfides. Similarly, methanogenesis from methanol in sediment from Eckernförde Bay, SW Baltic Sea, observed a sharp methane increase after 16 d (Maltby et al., 2018b).

Sediment slurries treated with molybdate showed a low increase in methane production in sediment from the 0-8 cm layer, which contained the sulfate-reducing zone, suggesting that methanogens were utilizing competitive substrates (acetate and/or hydrogen) following the inhibition of SR by molybdate (Oremland and Taylor, 1978; Oremland and Capone, 1988). Additionally, simultaneous inhibition of sulfate-dependent AOM likely suspended methane consumption. Methane in the bottom 8-16 cm layer showed no build-up over time after molybdate was added, suggesting that it had no inhibitory affect below the sulfate-reducing zone. This observation supports our hypothesis that organoclastic iron reduction dominated sediment below SR activity, because it is not affected by molybdate addition (Jacobson, 1994). Similarly, AOM coupled to iron reduction is not expected to be inhibited by molybdate addition and would therefore continue to consume methane in this zone.

The methanogen inhibitor BES suppressed methane production in both experiments, while controls showed a slight increase in methane over time, supporting the idea that methane was produced from in-situ methanogenic communities.

4.3 Deciphering cryptic methane cycling in sulfate-rich sediment

4.3.1 Method discussion

In this study, we conducted a radiotracer time series incubation with ^{14}C-MMA to determine the optimum incubation time for tracking the cryptic methane cycle. Short (~1 h) incubation times for radiotracer incubations have been found to cause issues with initial disturbance of the sediment, while long incubations (>1 d) can cause a gradual change in metabolism and chemical stratification of the sediment (Jørgensen, 1978). In the present study, we selected the 1-d (24-h) incubation as the optimal incubation period, because within this time frame sufficient products from both methanogenesis (^{14}C-CH$_4$) and AOM (^{14}C-TIC) were detected without considerably depleting the injected ^{14}C-MMA. Since this method depends on the production of an intermediate (^{14}C-CH$_4$) to track two processes in parallel, sufficient time should be provided for the intermediate to build up, while ensuring conditions in the sediment remain relatively stable. It should be kept in mind that the total incubation time was likely >24 h due to the delay in incubation termination (see 3.3.1).

Tests of the radiotracer method demonstrated that each stage of the cryptic methane cycle (i.e., initial substrate: ^{14}C-MMA, intermediate substrate: ^{14}C-CH4, final product: ^{14}C-TIC) was successfully separated and quantified. Oven tests confirmed that only ^{14}C-CO$_2$ from combusted ^{14}C-CH4 was captured in the final trap. Similarly, the acidification/shaking tests confirmed that all

^{14}C-TIC was liberated as CO_2 and captured in the suspended CO_2 trap after shaking, while the ^{14}C-MMA remained in solution.

In section 2.5.3 we showed that on average only 46% of ^{14}C-MMA initially injected into killed sediment from the hypersaline pool was recovered in the sample supernatant. Methylamines are known to strongly adsorb to sediment through electrostatic and Van der Walls interactions (Wang and Lee, 1990, 1993; Fitzsimons et al., 2006; Zhuang et al., 2017, 2018). Applying a ^{14}C-MMA recovery factor of 0.46 to rate calculations (Eq. 7) resulted in lower methanogenesis rates, because the factor is accounting for ^{14}C-MMA not captured by our standard analyses and hence increased the total pool of ^{14}C-MMA potentially available for methanogenesis. However, whether adsorbed ^{14}C-MMA is available for biological processes is currently unknown and needs additional studies. Future work should test the adsorption behavior of MMA with respect to different sediment types, because adsorption was reported to change with salinity, organic carbon, and clay mineral content (Wang and Lee, 1990; Wang and Lee, 1993; Xiao and Peacock, 2019). In our study, we recognized variability (22.5%) of ^{14}C-MMA recovery in replicate samples from different sediment depths, which indicates that differences in the absorption behavior might even occur within the same sediment core.

4.3.2 Methane cycling in the hypersaline sediment

The ^{14}C-MMA experiments demonstrated, for the first time, that carbon is directly shuttled from a methylotrophic substrate to CO_2 via CH_4, linking methanogenesis and AOM. Through increasing incubations times, we were able to show that radioactivity gradually shifted from MMA via CH_4 to TIC (Fig. 2-5A-D). Radioactive methane was detected in all four incubation experiments, confirming methanogenesis from MMA in the hypersaline sediment at the CSMR.

Further, in all four incubations (from 1 h to 3 wk), the concentration of ^{14}C-CH$_4$ remained low. This observation matches with low natural methane concentrations found in the sediment (Fig. 2-2B) and with almost stationary concentration of methane in the headspace of natural control sediment in long-term incubations (Fig. 2-4F and L). Hence, the radiotracer method identified AOM as a powerful mechanism that keeps methane concentrations low within the sulfate-rich zone of the hypersaline sediment despite simultaneous methane production.

Determination of methylotrophic methanogenesis rates from the 1-d ^{14}C-MMA incubations, which assumed a natural MMA porewater concentration of 10 and 100 µM based on literature values (Fitzsimons et al., 1997), resulted in max rates of up to 3.3 and 33 nmol cm^{-3} d^{-1}, respectively, within the top 5 cm, i.e. within the sulfate-reducing zone (Fig. 2-6A). These maxima were 1-2 orders of magnitude higher compared to rates of total methanogenesis detected in the sulfate-reducing zone by (Xiao et al., 2017; Xiao et al., 2018b), while rates in deeper zones of the sediment were in the same order of magnitude. The studies by (Xiao et al., 2017; Xiao et al., 2018b) were conducted in sediment from Arhus Bay in the Baltic Sea, while our study was conducted in a hypersaline salt marsh. Salt marsh sediment are known for their richness in methylated substrates (Fitzsimons et al., 2005; Fitzsimons et al., 1997; Wang and Lee, 1994) and hence we believe that the estimated higher rates in our study are not unrealistic. However, determination of in-situ concentrations of MMA in sediment from the CSMR hypersaline pool are required to test this hypothesis.

AOM rates determined directly from ^{14}C-CH$_4$ and via ^{14}C-MMA injections (1 d incubation) ranged within the same order of magnitude (Fig. 2-6C). It should be kept in mind, however, that AOM rates determined from ^{14}C-MMA incubations likely underestimated the true AOM rate, since ^{14}C-CH$_4$ tracer was not added in one batch at t_0 but was instead produced from methanogenesis

over time. Similarly, AOM rates determined from ^{14}C- CH_4 incubations could be underestimated, because the labeled methane was likely diluted by the production of new, unlabeled methane during the incubation. Irrespective of these uncertainties, confirmation of AOM activity by two separate methods suggests that AOM plays an important role in keeping methane concentrations in this sediment low.

It is notable that MMA could also be utilized by denitrifying bacteria (Martineau et al., 2015), and there is an ongoing debate about the potential involvement of sulfate reducers in the degradation of methylamines (Zhuang et al., 2019a). However, to the best of our knowledge there is neither a confirmed case of denitrifying bacteria involved in MMA degradation in coastal wetland sediment, nor exists evidence for the metabolic capability of sulfate reducers to degrade MMA. Further work using methanogen and sulfate-reducer inhibitors in combination with ^{14}C-MMA incubations should be conducted to better elucidate the relationship between methylotrophic methanogens and sulfate-reducing bacteria in CSMR sediment.

4.4 Implications for methane budgeting in coastal wetlands

The present study demonstrated simultaneous production and consumption of methane in the sulfate-rich zone of a coastal wetland - a process that has to the best of our knowledge not been considered in previous coastal wetland studies. In combination, our results strongly indicate that methanogenesis was not able to build up significant concentrations of methane in the studied hypersaline sediment due to simultaneous activity of AOM. This finding could have important implications for our understanding of carbon cycling in coastal wetlands. While tremendous knowledge has been gained on methane production and emission from this type of environment (e.g., (Bridgham et al., 2013; Le Mer and Roger, 2001; Oremland and Polcin, 1982; Oremland et

al., 1982; Segers, 1998; Vizza et al., 2017), the underlying process that regulates emissions seems to be not fully understood. It is therefore necessary to consider cryptic methane cycling in coastal wetlands to predict potential future shifts in methane emission linked to the availability of electron acceptors for AOM. Environmental factors that could change electron acceptor availability in coastal wetland sediment include sea-level rise, droughts, increase in precipitation, and river run-offs, which are all likely to affect coastal wetlands in the near future (Junk et al., 2013; Mitsch and Hernandez, 2013; Mitsch et al., 2013; O'Connor et al., 2010).

5. Conclusion

In the present study, we investigated the relationship between SR, iron reduction, methylotrophic methanogenesis, and AOM in hypersaline sediment of the CSMR. Sediment slurry incubations with non-competitive substrates (MMA and methanol) indicated the presence of a methylotrophic methanogenic community. Our adapted radiotracer method successfully demonstrated that carbon is shuttled from MMA to TIC via CH_4, linking methanogenesis and AOM. The production and consumption of radioactive methane was detected both in the sulfate- and (apparently) iron-reducing zone of the sediment suggesting that (1) MMA served as a non-competitive substrate for methanogens and (2) AOM was coupled to both sulfate and iron reduction. Radioactive methane generated by methylotrophic methanogenesis remained always at a low level in ^{14}C incubations ranging from 1 h to 3 wk, suggesting that AOM was keeping up with the rate of methane production. Constant low levels of methane in the sediment despite the presence of methanogenesis identifies AOM as a potential key sink for methane produced in sulfate-rich sediment from this environment. The relationship between methanogenesis and AOM needs to be considered in future studies to complete carbon cycling in coastal wetlands and to evaluate the sensitivity of this balance to environmental changes.

Acknowledgements

References

Beal E. J., House C. H. and Orphan V. J. (2009) Manganese- and iron-dependent marine methane oxidation. *Science* **325**, 184-187.

Boetius A., Ravenschlag K., Schubert C. J., Rickert D., Widdel F., Giesecke A., Amann R., Jørgensen B. B., Witte U. and Pfannkuche O. (2000) A marine microbial consortium apparently mediating anaerobic oxidation of methane. *Nature* **407**, 623-626.

Bridgham S. D., Cadillo-Quiroz H., Keller J. K. and Zhuang Q. (2013) Methane emissions from wetlands: biogeochemical, microbial, and modeling perspectives from local to global scales. *Glob. Change Biol.* **19**, 1325-1346.

Cline J. D. (1969) Spectrophometric determination of hydrogen sulfide in natural waters. *Limnol. Oceanogr.* **14**, 454-458.

Dale A. W., Sommer S., Lomnitz U., Montes I., Treude T., Liebetrau V., Gier J., Hensen C., Dengler M., Stolpovsky K., Bryant L. D. and Wallmann K. (2015) Organic carbon production, mineralisation and preservation on the Peruvian margin. *Biogeosciences* **12**, 1537-1559.

Dlugokencky E. (2020) *NOAA/GML (www.esrl.noaa.gov/gmd/ccgg/trends_ch4/)*. *www.esrl.noaa.gov/gmd/ccgg/trends_ch4/*.

Fitzsimons M., Dawit M., Revitt D. and Rocha C. (2005) Effects of early tidal inundation on the cycling of methylamines in inter-tidal sediments. *Marine Ecology Progress Series* **294**, 51-61.

Fitzsimons M. F., Jemmett A. W. and Wolff G. A. (1997) A preliminary study of the geochemistry of methylamines in a salt marsh. *Organic geochemistry* **27**, 15-24.

Grasshoff K., Ehrhardt M. and Kremling K. (1999) *Methods of seawater analysis*. Wiley-VCH Verlag GmbH, Weinheim.

Hinrichs K.-U. and Boetius A. (2002) The anaerobic oxidation of methane: new insights in microbial ecology and biogeochemistry. In *Ocean Margin Systems* (eds. G. Wefer, D. Billett, D. Hebbeln, B. B. Jørgensen, M. Schlüter and T. Van Weering). Springer-Verlag, Berlin. pp. 457-477.

Hoehler T. M., Alperin M. J., Albert D. B. and Martens C. S. (1994) Field and laboratory studies of methane oxidation in an anoxic marine sediments: evidence for methanogen-sulphate reducer consortium. *Global Biochem. Cycles* **8**, 451-463.

IPCC (2007) The scientific basis. Contribution of Working Group I to the Fourth Assessment Report of the Intergovernmental Panel on Climate Change (IPCC). In. Cambridge University Press, Cambridge, MA.

IPCC C. C. (2014) Mitigation of climate change. *Contribution of working group III to the fifth assessment report of the intergovernmental panel on climate change*.

Jacobson M. (1994) Chemical and biological mobilization of Fe (III) in marsh sediments. *Biogeochemistry* **25**, 41-60.

Joye S. B., Boetius A., Orcutt B. N., Montoya J. P., Schulz H. N., Erickson M. J. and Logo S. K. (2004) The anaerobic oxidation of methane and sulfate reduction in sediments from Gulf of Mexico cold seeps. *Chem. Geol.* **205**, 219-238.

Junk W. J., An S., Finlayson C., Gopal B., Kvĕt J., Mitchell S. A., Mitsch W. J. and Robarts R. D. (2013) Current state of knowledge regarding the world's wetlands and their future under global climate change: a synthesis. *Aquatic sciences* **75**, 151-167.

Jørgensen B. B. (1978) A comparison of methods for the quantification of bacterial sulphate reduction in coastal marine sediments: I. Measurements with radiotracer techniques. *Geomicrobiol. J.* **1**, 11-27.

Jørgensen B. B. (2000) Bacteria and marine biogeochemistry. In *Marine biogeochemistry* (eds. H. D. Schulz and M. Zabel). Springer Verlag, Berlin. pp. 173-201.

Kallmeyer J., Ferdelman T. G., Weber A., Fossing H. and Jørgensen B. B. (2004) A cold chromium distillation procedure for radiolabeled sulfide applied to sulfate reduction measurements. *Limnol. Oceanogr. Methods* **2**, 171-180.

Knittel K. and Boetius A. (2009) Anaerobic oxidation of methane: progress with an unknown process. *Annu. Rev. Microbiol.* **63**, 311-334.

Knudsen M. (1901) *Hydrographical Tables According to the Measurings of Carl Forch...[et Al.] and with Assistance of Björn-Andersen...[et Al.]*. GEC Gad.

Krause S. (2012) Effects of microbial activity on marine carbonates.

Kristjansson J. K., Schönheit P. and Thauer R. K. (1982) Different Ks values for hydrogen of methanogenic bacteria and sulfate reducing bacteria: an explanation for the apparent inhibition of methanogenesis by sulfate. *Arch. Microbiol.* **131**, 278-282.

Le Mer J. and Roger P. (2001) Production, oxidation, emission and consumption of methane by soils: a review. *European journal of soil biology* **37**, 25-50.

Lovley D. R. and Klug M. J. (1986) Model for the distribution of sulfate reduction and methanogenesis in freshwater sediments. *Geochim. Cosmochim. Acta* **50**, 11-18.

Lovley D. R. and Phillips E. J. (1987) Competitive mechanisms for inhibition of sulfate reduction and methane production in the zone of ferric iron reduction in sediments. *Appl. Environ. Microbiol.* **53**, 2636-2641.

Maltby J., Sommer S., Dale A. W. and Treude T. (2016) Microbial methanogenesis in the
sulfate-reducing zone of surface sediments traversing the Peruvian margin.
Biogeosciences **13**, 283–299.

Maltby J., Steinle L., Loscher C., Bange H., Fischer M., Schmidt M. and Treude T. (2018)
Microbial methanogenesis in the sulfate-reducing zone of sediments in the Eckernforde
Bay, SW Baltic Sea. *Biogeosciences* **15**, 137-157.

Martineau C., Mauffrey F. and Villemur R. (2015) Comparative analysis of denitrifying
activities of Hyphomicrobium nitrativorans, Hyphomicrobium denitrificans, and
Hyphomicrobium zavarzinii. *Appl. Environ. Microbiol.* **81**, 5003-5014.

Michaelis W., Seifert R., Nauhaus K., Treude T., Thiel V., Blumenberg M., Knittel K., Gieseke
A., Peterknecht K., Pape T., Boetius A., Aman A., Jørgensen B. B., Widdel F., Peckmann
J., Pimenov N. V. and Gulin M. (2002) Microbial reefs in the Black Sea fueled by
anaerobic oxidation of methane. *Science* **297**, 1013-1015.

Mitsch W. J. and Hernandez M. E. (2013) Landscape and climate change threats to wetlands of
North and Central America. *Aquatic Sciences* **75**, 133-149.

Mitsch W. J., Bernal B., Nahlik A. M., Mander Ü., Zhang L., Anderson C. J., Jørgensen S. E.
and Brix H. (2013) Wetlands, carbon, and climate change. *Landscape Ecology* **28**, 583-
597.

Nauhaus K., Boetius A., Krüger M. and Widdel F. (2002) In vitro demonstration of anaerobic
oxidation of methane coupled to sulphate reduction in sediment from marine gas hydrate
area. *Environ. Microbiol.* **4**, 298-305.

Nisbet E. G., Manning M., Dlugokencky E., Fisher R., Lowry D., Michel S., Myhre C. L., Platt
S. M., Allen G. and Bousquet P. (2019) Very strong atmospheric methane growth in the 4

years 2014–2017: Implications for the Paris Agreement. *Global Biogeochemical Cycles* **33**, 318-342.

O'Connor F. M., Boucher O., Gedney N., Jones C., Folberth G., Coppell R., Friedlingstein P., Collins W., Chappellaz J. and Ridley J. (2010) Possible role of wetlands, permafrost, and methane hydrates in the methane cycle under future climate change: A review. *Reviews of Geophysics* **48**.

Oremland R. S. and Taylor B. F. (1978) Sulfate reduction and methanogenesis in marine sediments. *Geochimica et Cosmochimica Acta* **42**, 209-214.

Oremland R. S. and Polcin S. (1982) Methanogenesis and sulfate reduction: competitive and noncompetitive substrates in estuarine sediments. *Appl. Environ. Microbiol.* **44**, 1270-1276.

Oremland R. S. and Capone D. G. (1988) Use of specific inhibitors in biogeochemistry and microbial ecology. In *Advances in microbial ecology* (ed. K. C. Marshall). Pleneum Press, New York. pp. 285-383.

Oremland R. S., Marsh L. M. and Polcin S. (1982) Methane production and simultaneous sulphate reduction in anoxic, salt marsh sediments. *Nature* **296**, 143-145.

Oren A. (1990) Formation and breakdown of glycine betaine and trimethylamine in hypersaline environments. *Antonie van Leeuwenhoek* **58**, 291-298.

Oren A. (2015) Halophilic microbial communities and their environments. *Current opinion in biotechnology* **33**, 119-124.

Orphan V. J., House C. H., Hinrichs K.-U., McKeegan K. D. and De Long E. F. (2001) Methane-consuming Archaea revealed by directly coupled isotopic and phylogenetic analysis. *Science* **293**, 484-487.

Ouyang X. and Lee S. (2014) Updated estimates of carbon accumulation rates in coastal marsh sediments. *Biogeosciences*, 5057.

Page H. M., Petty R. L. and Meade D. E. (1995) Influence of watershed runoff on nutrient dynamics in a southern California salt marsh. *Estuar. Coast. Shelf Sci.* **41**, 163-180.

Porter D., Roychoudhury A. N. and Cowan D. (2007) Dissimilatory sulfate reduction in hypersaline coastal pans: activity across a salinity gradient. *Geochimica et Cosmochimica Acta* **71**, 5102-5116.

Reddy K. R. and DeLaune R. D. (2008) *Biogeochemistry of Wetlands*. CRC Press, Taylor & Francis Group, Boca Raton.

Reeburgh W. S. (2007) Oceanic methane biogeochemistry. *Chem. Rev.* **107**, 486-513.

Saunois M., Stavert A. R., Poulter B., Bousquet P., Canadell J. G., Jackson R. B., Raymond P. A., Dlugokencky E. J., Houweling S. and Patra P. K. (2020) The global methane budget 2000–2017. *Earth System Science Data* **12**, 1561-1623.

Schlesinger W. H. (1977) Carbon balance in terrestrial detritus. *Annual review of ecology and systematics* **8**, 51-81.

Segarra K. E. A., Comerford C., Slaughter J. and Joye S. B. (2013) Impact of electron acceptor availability on the anaerobic oxidation of methane in coastal freshwater and brackish wetland sediments. *Geochim. Cosmochim. Acta* **115**, 15-30.

Segers R. (1998) Methane production and methane consumption: a review of processes underlying wetland methane fluxes. *Biogeochemistry* **41**, 23-51.

Stephenson M. and Stickland L. H. (1933) CCVII. Hydrogenase. III. The bacterial formation of methane by the reduction of one-carbon compounds by molecular hydrogen. *Biochem. J.* **27**, 1517–1527.

Thauer R. K. (1998) Biochemistry of methanogenesis: a tribute to Marjory Stephenson. *Microbiology* **144**, 2377-2406.

Treude T., Krüger M., Boetius A. and Jørgensen B. B. (2005a) Environmental control on anaerobic oxidation of methane in the gassy sediments of Eckernförde Bay (German Baltic). *Limnol. Oceanogr.* **50**, 1771-1786.

Treude T., Niggemann J., Kallmeyer J., Wintersteller P., Schubert C. J., Boetius A. and Jørgensen B. B. (2005b) Anaerobic oxidation of methane in the sulfate-methane transition along the Chilean continental margin. *Geochim. Cosmochim. Acta* **69**, 2767-2779.

Vizza C., West W. E., Jones S. E., Hart J. A. and Lamberti G. A. (2017) Regulators of coastal wetland methane production and responses to simulated global change. *Biogeosciences. 14 (2): 431-446.* **14**, 431-446.

Wang X.-c. and Lee C. (1990) The distribution and adsorption behavior of aliphatic amines in marine and lacustrine sediments. *Geochimica et Cosmochimica Acta* **54**, 2759-2774.

Wang X.-C. and Lee C. (1993) Adsorption and desorption of aliphatic amines, amino acids and acetate by clay minerals and marine sediments. *Marine Chemistry* **44**, 1-23.

Wang X.-C. and Lee C. (1994) Sources and distribution of aliphatic amines in salt marsh sediment. *Organic Geochemistry* **22**, 1005-1021.

Widdel F. and Bak F. (1992) Gram-negative mesophilic sulfate-reducing bacteria. In *The Prokaryotes* (eds. A. Balows, H. G. Trüper, M. Dworking, W. Harder and K. H. Schleifer). Springer, New York. pp. 3352-3378.

Winfrey M. R. and Ward D. M. (1983) Substrates for sulfate reduction and methane p roduction in i ntertidal sediments. *Appl. Environm. Microbiol* **45**, 193-199.

Xiao K., Beulig F., Kjeldsen K., Jorgensen B. and Risgaard-Petersen N. (2017) Concurrent Methane Production and Oxidation in Surface Sediment from Aarhus Bay, Denmark. *Frontiers in Microbiology* **8**.

Xiao K.-Q. and Peacock C. (2019) The Role of Minerals in Cryptic Methane Cycling in Marine Surface Sediment.

Xiao K. Q., Beulig F., Røy H., Jørgensen B. B. and Risgaard-Petersen N. (2018) Methylotrophic methanogenesis fuels cryptic methane cycling in marine surface sediment. *Limnol. Oceanogr.* **63**, 1519-1527.

Zhuang G.-C., Montgomery A. and Joye S. B. (2019) Heterotrophic metabolism of C1 and C2 low molecular weight compounds in northern Gulf of Mexico sediments: Controlling factors and implications for organic carbon degradation. *Geochimica et Cosmochimica Acta* **247**, 243-260.

Zhuang G.-C., Yang G., Yu J. and Gao Y. (2011) Production of DMS and DMSP in different physiological stages and salinity conditions in two marine algae. *Chinese J. Oceanol. Limnol.* **29**, 369-377.

Zhuang G.-C., Elling F. J., Nigro L. M., Samarkin V., Joye S. B., Teske A. and Hinrichs K.-U. (2016) Multiple evidence for methylotrophic methanogenesis as the dominant methanogenic pathway in hypersaline sediments from the Orca Basin, Gulf of Mexico. *Geochim. Cosmochim. Acta* **187**, 1-20.

Zhuang G.-C., Lin Y.-S., Bowles M. W., Heuer V. B., Lever M. A., Elvert M. and Hinrichs K.-U. (2017) Distribution and isotopic composition of trimethylamine, dimethylsulfide and dimethylsulfoniopropionate in marine sediments. *Mar. Chem.* **196**, 35-46.

Zhuang G.-C., Heuer V. B., Lazar C. S., Goldhammer T., Wendt J., Samarkin V. A., Elvert M., Teske A. P., Joye S. B. and Hinrichs K.-U. (2018) Relative importance of methylotrophic methanogenesis in sediments of the Western Mediterranean Sea. *Geochim. Cosmochim. Acta* **224**.

Chapter 3

Evidence of cryptic methane cycling in the sulfate-reducing zone of sediment in the Santa Barbara Basin, California

Sebastian J.E. Krause[1]*, Jiarui Liu[1], DJ. Yousavich[1], DeMarcus Robinson[2], David W. Hoyt[3], David L. Valentine[4], and Tina Treude[1,2]*

[1]Department of Earth Planetary and Space Sciences, University of California, Los Angeles, CA 90095, USA

[2]Department of Atmospheric and Ocean Sciences, University of California, Los Angeles, CA 90095, USA

[3]Pacific Northwest National Laboratory Environmental and Molecular Sciences Division, Richland, WA 99352, USA

[4]Department of Earth Science, University of California Santa Barbara, Santa Barbara, CA 93106, USA

*Correspondence: Sebastian Krause (sjkrause@ucla.edu), Tina Treude (ttreude@g.ucla.edu)
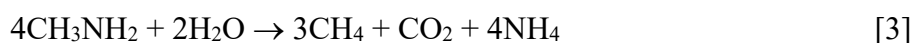
Abstract

Methylotrophic methanogenesis has been recently coupled to anaerobic oxidation of methane (AOM) in the sulfate reducing zones of marine and wetland sediments, which is now termed as the cryptic methane cycle. Here we present evidence of cryptic methane cycling activity within the upper regions of the sulfate reducing zone, along a depth transect within the Santa Barbara Basin, off the coast of California, USA. Sediment samples (top 15 cm) were subjected to porewater geochemical analyses and radiotracer incubations using ^{35}S-SO_4^{2-}, ^{14}C-mono-methylamine, and ^{14}C-CH_4 to find evidence of cryptic methane cycling. Methane concentrations were consistently low across the depth transect (~3 to ~16 µM), despite increasing AOM rates, determined directly with ^{14}C-CH_4, with decreasing water column depth (~0.007 – 0.050 nmol cm^{-3} d^{-1} at the deepest station to ~0.500 – 1.800 nmol cm^{-3} d^{-1} at the shallowest station). Porewater sulfate concentrations remained high (~23mM to ~29 mM), despite the detection of sulfate reduction ranging from as low as ~14 nmol cm^{-3} d^{-1} and as high as 134 nmol cm^{-3} d^{-1}. Metabolomic analysis showed that substrates for methanogenesis (i.e. acetate, methanol and methylamines) were mostly below the detection limits but some porewater in the 1-2 cm interval showed non-quantifiable evidence of these substrates, indicating a fast turnover of these substrates by biological activity. Methanogenesis from mono-methylamine, with an assumed porewater mono-methylamine concentrations of 3 µM, were as low as ~0.2 nmol cm^{-3} d^{-1} and as high as ~0.5 nmol cm^{-3} d^{-1}. AOM rates derived from the methane produced from mono-methylamine were 1 to 2 orders of magnitude higher than methanogenesis and AOM directly from ^{14}C-CH_4. The results suggest that the present but low methane concentrations are a result of cryptic methane cycling activity in the sulfate rich sediment. Rate constant calculations of methanogenesis from mono-methylamine, AOM from methane derived from mono-methylamine and AOM from methane

directly, show that there is a separate biological process, concurrently active with the cryptic methane cycle, directly consuming mono-methylamine to CO_2 causing the discrepancy in the AOM and methanogenesis rates. We conclude that the results presented in this work show strong evidence of cryptic methane cycling occurring in the Santa Barbara Basin and that this currently overlooked process is keeping methane concentrations present but low close to the sediment-water interface. We also conclude that methylamine turnover in the Santa Barbara Basin samples is not exclusive to methanogenesis. We hypothesize that sulfate reduction is responsible for the methylamine turnover, which needs further testing.

1. Introduction

In anoxic marine sediment, methane is produced by microbial methanogenesis in the last step of organic carbon remineralization (Reeburgh, 2007; Stephenson and Stickland, 1933; Thauer, 1998). This methane is produced by groups of obligate anaerobic methanogenic archaea across the Euryarchyota, Crenarchaeota, Halobacterota , and Thermoplasmatota phyla (Lyu et al., 2018). Methanogens can produce methane through a few metabolic pathways using CO_2 and hydrogen (hydrogenotrophic) (Eq. 1), acetate (acetoclastic) (Eq. 2) and methylated substrates such as, methyl sulfides, methanol, and methylamines (methylotrophic) (e.g., Eq. 3).

$$4H_2 + CO_2 \rightarrow CH_4 + 2H_2O \qquad [1]$$

$$CH_3COO^- + H^+ \rightarrow CO_2 + CH_4 \qquad [2]$$

$$4CH_3NH_2 + 2H_2O \rightarrow 3CH_4 + CO_2 + 4NH_4 \qquad [3]$$

Classically, hydrogenotrophic and acetoclastic methanogenesis are dominant in deeper sediment below the depth of sulfate penetration. This distinct sediment redox zonation is due to the higher free energy gain by sulfate-reducing bacteria coupling sulfate reduction with hydrogen and acetate in sulfate-rich sediment. Thus, sulfate-reducing bacteria tend to outcompete methanogenic archaea for hydrogen and acetate (Jørgensen, 2000; Kristjansson et al., 1982; Lovley and Klug, 1986; Winfrey and Ward, 1983). However, methylotrophic methanogenesis is less susceptible to competition by sulfate-reducing bacteria because methylated substrates, such as methylamines, are not known to be carbon sources for sulfate-reducing bacteria (Krause and Treude, 2021; Lovley and Klug, 1986; Maltby et al., 2016; 2018a; Oremland and Taylor, 1978; Zhuang et al., 2016; 2018). Methylotrophic methanogenesis activity in the sulfate-reducing zone has been detected in a wide range of aquatic environments such as; coastal wetlands (Krause and Treude, 2021; Oremland and Polcin, 1982; Oremland et al., 1982), upwelling regions (Maltby et

al., 2016), eutrophic shelf sediment (Maltby et al., 2018a). Despite methylotrophic activity in the upper sulfate-reducing zone, methane concentrations are several orders of magnitude lower than in deeper sulfate-poor sediment e.g., (Barnes and Goldberg, 1976; Beulig et al., 2018; Dale et al., 2008b; Wehrmann et al., 2011).

Recent studies detected methylotrophic methanogenesis activity in the sulfate-reducing zone off the coast of Peru (Maltby et al., 2018a) and in the Baltic Sea (Maltby et al., 2016), had first postulated that methane from methylotrophic methanogenesis could be directly oxidized by sulfate-dependent Anaerobic Oxidation of Methane (AOM). In anoxic marine sediment, AOM is an important methane sink that is typically coupled to sulfate reduction (Eq. 4) and mediated by a consortium of anaerobic methane oxidizing archaea (ANME) and sulfate-reducing bacteria (Boetius et al., 2000; Hinrichs and Boetius, 2002; Knittel and Boetius, 2009; Michaelis et al., 2002; Orphan et al., 2001b; Reeburgh, 2007). AOM occurring in the sulfate-reducing zone is fueled by concurrent methylotrophic methanogenesis activity, which is now known as the cryptic methane cycle, could be the reason why methane concentrations are consistently low in sulfidic sediment.

$$CH_4 + SO_4^{2-} \rightarrow HCO_3^- + HS^- + H_2O \qquad [4]$$
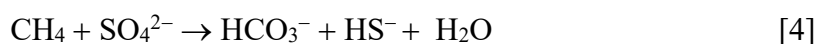
Since the first postulation of the cryptic methane cycle, there are few recent studies that utilized stable isotope (Xiao et al., 2017) (2018a) and radiotracer incubations (Krause and Treude, 2021), and metagenomic and metatranscriptomic analysis (Bhattacharya et al., 2021) to elucidate cryptic methane cycling activity. These first studies highlight the importance of cryptic methane cycling has on the global methane budget. But the extent of our knowledge of cryptic methane cycle is restricted to a few aquatic environments. Thus, it is crucial to investigate and understand the cryptic methane cycling process in other systems.

In shallower coastal, thermally stratified, geographically enclosed basins, oxygen minimum zones (OMZ) can occur. In this case, high oxygen demand is required to degrade enhanced organic matter loading, derived from excessive phytoplankton growth within the euphtic zone due to coastal upwelling. In poorly ventilated water bodies, such as thermally stratified basins, the enhanced aerobic respiration is faster than oxygen replenishment, results in strong seasonal or continuous low oxygen conditions (Helly and Levin, 2004; Levin et al., 2009; Wright et al., 2012; Wyrtki, 1962). Organic matter content in sediment that lie beneath the OMZ, with shallower water column depths, are thus typically quite high (Levin, 2003; Rullkötter, 2006) resulting in anoxic conditions supporting sulfate reduction and methanogenesis as the dominant metabolic pathways consuming organic matter in the sediment (Fernandes et al., 2022). Thus, OMZ are likely to have large inventories of methane in the sediment of which the origins and the fate of methane in these systems still need to be constrained (Chronopoulou et al., 2017; Pack et al., 2015; Wright et al., 2012).

Carbon sources such as methylamine, for methylotrophic methanogenesis, are apparently ubiquitous in the coastal marine environments (Oren, 1990; Zhuang et al., 2016; Zhuang et al., 2018) where OMZ's exist (Ferdelman et al., 1997; Gibb et al., 1999) and are derived from osmolytes, such as glycine betaine commonly synthesized in phytoplankton biomass (Oren, 1990). However, the abundance of methylamines and how they may be driving cryptic methane cycling in anoxic sediment within OMZ's are virtually unknown.

Located within the Pacific Ocean between the Channel Islands and the mainland of Santa Barbara, California, USA, the Santa Barbara Basin (SBB) is a thermally stratified, silled coastal marine basin (Arndt et al., 1990; Reimers et al., 1996; Sholkovitz, 1973; Soutar and Crill, 1977). Low oxygen concentrations (<10 µM) are found in the bottom waters below the sill depth (~475

m) of the SBB (Reimers et al., 1996; Sholkovitz, 1973) due to high aerobic respiration rates of organic matter derived from high surface ocean primary productivity supported by seasonal coastal upwelling (Sholkovitz, 1973). The relatively shallow water column and low bottom water oxygen concentrations means the sediment in the SBB can have total organic matter content as high as 4% (Schimmelmann and Kastner, 1993). These low oxygen conditions and high organic matter loading within the SBB sediment may favor methylotrophic methanogenesis in the sulfate reduction zone of the sediment (Chronopoulou et al., 2017; Oremland and Taylor, 1978; Warford et al., 1979). In fact, it has been long proposed by Warford et al., (1979) that the present but low methane concentrations within the first two meters within the SBB sediment could be a result of methane production balanced with oxidation. However, despite extensive investigation of methane dynamics in the SBB, the fate of methane from methylotrophic methanogenesis in the sulfate reduction zone near the sediment water interface is poorly constrained. Particularly, if cryptic methane cycling is active in the upper anoxic sediment, gross production and consumption of methane have likely been underestimated. Therefore, finding evidence for the cryptic methane cycle in the SBB is a necessary step towards understanding how carbon is cycled through the sediment of the SBB and other OMZs.

In the present study we report biogeochemical evidence of cryptic methane cycling in surface sediment (top ~15 cm) collected across a depth transect located within the SBB. We applied a newly adapted radiotracer method from Krause and Treude, (2021) to trace the production of methane from mono-methylamine, followed by the anaerobic oxidation of methane to CO_2. We combined this approach with standard radiotracer methods for the detection of AOM and sulfate reduction as well as with analyses of sediment porewater geochemistry. Our results indicate that 1) methylotrophic methanogenesis is directly fueling AOM in the sulfate reduction

zone of the SBB sediment, 2) mono-methylamine is also consumed by an additional, currently unknown process.

2. Methods.

2.1. Study site and sediment sampling

Sediment samples were collected during the R/V *Atlantis* expedition AT42-19 in fall 2019. Collection was achieved with polycarbonate push cores (~30 cm long, 6 cm i.d.), which were deployed by the ROV *JASON* along a depth transect through the Santa Barbara Basin. The depth transect selected for this particular study was the Northern Deposition Transect 3 (NDT3), with three stations (NDT3-A, -C and -D), as well as the Northern Depositional Radial Origin (NDRO), and the Southern Depositional Radial Origin (SDRO) station, located in the deepest part of the basin. For depths and locations of the stations see Table 3-1.

After collection push cores were returned to the surface by an elevator platform. Upon retrieval onboard the R/V *Atlantis,* sediment samples were transported to an onboard cold-room set to 6°C for further processing of biogeochemical parameters within 3-6 hours (see details below).

Station	SDRO	NDRO	NDT3-A	NDT3-C	NDT3-D
Depth (m)	586	580	572	498	447
Bottom water Oxygen (µM)	10	19	24	26	27

Table 3-1. Depth transect stations with associated water column depth and bottom water oxygen concentrations in µM.

2.2. Sediment porewater sampling and analysis

For porewater analyses, two sediment push cores from each station were sliced in 1-cm increments in the top 10 cm of sediment, followed by 2-cm increments below. During sediment sampling, ultra-high pure argon was flushed over the sediment to minimize oxidation of oxygen sensitive molecules. The sliced sediment layers were quickly transferred to pre-argon flushed 50 mL plastic centrifuge vials and centrifuged at 2300 X g for 20 mins to extract the porewater. Subsequently, two ml porewater was subsampled from the supernatant and frozen at -20 °C for

shore-based sulfate analysis by ion chromatography (Metrohm 761) following (Dale et al., 2015). Porewater from push cores was additionally subsampled for the determination of natural methylamine and other metabolic substrates (see section 2.4).

2.3. Methane

Methane was determined in sediment from a separate pushcore at each station. Sediments were sliced at 1-cm intervals in the top 10 cm, followed by 2-cm increments below. Sediment was quickly transferred to 12 ml glass serum vials filled with 5 ml of 5% (w/w) NaOH solution. The vials were sealed immediately with a grey butyl rubber stopper and aluminum crimps, shaken thoroughly, and stored upside down at 4 °C. Methane concentrations in the headspace were determined shore-based using a Shimadzu gas chromatograph (Shimadzu GC-2015) equipped with a packed Haysep-D column and flame ionization detector. The column was filled with helium as a carrier gas, flowing at 12 ml per minute and heated to 80 °C. Methane concentrations in the environmental samples were calibrated against methane standards (Scotty Analyzed Gases) with a $\pm$ 5% precision.

2.4. Porewater metabolomics

To obtain porewater concentrations of substrates that are known to be utilized by methanogens, 1 mL of porewater extracted from sediment intervals at 1-2 cm and 9-10 cm at each station was syringe filtered (0.2 µm) into pre-combusted (350 °C for 3 hrs) amber vials (1.8 mL) equipped with a PTFE septa and frozen at -80 °C. Note no porewater from the gravity core was analyzed for mono-methylamine concentrations. Samples were sent to the Pacific Northwest National Laboratory, Environment and Molecular Sciences Division for metabolite analysis using

proton nuclear magnetic resonance (NMR). Prior to analysis porewater samples were diluted by 10% (v/v) with an internal standard 5 mM 2,2-dimethyl-2-silapentane-5-sulfonate-d6 (DSS). All NMR spectra were collected using a 800 MHz Bruker Avance Neo (Tava), TCl 800/54 H&F/C/N-D-05 Z XT extended temperature range CryoProbe . The 1D 1H NMR spectra of all samples were processed, assigned, and analyzed by using Chenomx NMR Suite 8.6 with quantification based on spectral intensities relative to the internal standard. Candidate metabolites present in each of the complex mixture were determined by matching the chemical shift, J-coupling, and intensity information of experimental NMR signals against the NMR signals of standard metabolites in the Chenomx library. The 1D 1H spectra were collected following standard Chenomx data collection guidelines, employing a 1D NOESY presaturation experiment (noesypr1d) with 65536 complex points and at least 4096 scans at 298 K. Signal to noise ratios (S/N) were measured using MestReNova 14 with the limit of quantification equal to a S/N of 10 and the limit of detection equal to a S/N of 3. The 90° ^{1}H pulse was calibrated prior to the measurement of each sample with a spectral width of 12 ppm and 1024 transients. The NOESY mixing time was 100 ms and the acquisition time was 4 s followed by a relaxation delay of 1.5 s during which presaturation of the water signal was applied. Time domain free induction decays (72114 total points) were zero-filled to 131072 total points prior to Fourier transform.

2.5. Radiotracer incubations

The main goal of this study was to elucidate any evidence metabolic activity of cryptic methane cycling. For this a separate sediment pushcore from each station was selected for radiotracer incubations using a variety of radiotracers. Sulfate reduction was determined with ^{35}S-labeled sulfate. ^{14}C-labeled mono-methylamine (^{14}C-MMA) was used to determine the conversion

of ^{14}C-MMA to ^{14}C-methane (^{14}C-CH$_4$) by methanogenesis (MG-MMA) and the subsequent oxidation of ^{14}C-CH$_4$ by AOM (AOM-MMA). AOM (not derived from methane from MMA) was determined directly using ^{14}C-CH$_4$ (AOM-CH$_4$).

Prior to radiotracer injections, 3 smaller polycarbonate sub-pushcores (~20 cm long, 2.6 cm i.d.) were inserted vertically into the larger push core leaving some supernatant seawater overlying the sediment. To minimize compression of the soft sediment layers while sub-coring, a hollowed rubber stopper equipped with tygon tubing running through the rubber stopper attached to a 60 mL plastic syringe was placed onto the exposed opening of the sub-pushcore. As the sub-pushcore was inserted into the sediment, the 60 mL syringe plunger was lifted to maintain a level sediment horizon. The sub-pushcore were then extracted and sealed with butyl rubber stoppers such that no headspace was left in the above supernatant seawater. The sub-pushcore were then injected with radiotracers within 3 hours of collection. Additional sediment from each larger push core was collected for killed controls.

2.5.1. Sulfate reduction (^{35}S-Sulfate)

Within the same day of collection, one sediment sub-pushcore from each station was used to determine sulfate-reduction rates. Radioactive carrier-free ^{35}S-sulfate (^{35}S-SO$_4^{2-}$; dissolved in MilliQ water, injection volume 10 µL, activity 260 KBq, specific activity 1.59 TBq mg^{-1}) was injected into the sub-pushcores at 1-cm increments and incubated at 6 °C in the dark following (Jørgensen, 1978). Injected sediment samples were stored vertically in racks and incubated at 6 °C and in the dark. The incubations for the sub-pushcore samples were stopped after approximately 6 hours by slicing the sediment in 1-cm increments into 50 mL plastic centrifuge tubes containing 20 mL 20% (w/w) zinc acetate solution. Each sediment sample was sealed and shaken thoroughly

and stored at -20 °C to halt metabolic activity. Killed control samples were prepared in triplicate by transferring approximately 5 ml of extra sediment from each station into a 50 mL centrifuge vial with zinc acetate solution, followed by radiotracer injection. The injected dead controlled samples were shaken and stored similarly to the live sediment above. At the home laboratory, samples were analyzed using the cold-chromium distillation method and ex situ rates were calculated according (Kallmeyer et al., 2004). The sulfate reduction rates were calculated according to Eq. 5.

$$SRR = P_{SED} * [SO_4^{2-}] * \frac{a_{TRIS}}{a_{Total}} * \frac{1}{t} * \alpha * 1000 \qquad [5]$$

Where SRR is the sulfate reduction rate (nmol cm^{-3} d^{-1}); P_{SED} is the sediment porosity (v/v); [SO_4^{2-}] is the porewater sulfate concentration (mmol L^{-1}); a_{TRIS} is the radioactivity of the total reduced inorganic sulfur TRIS (counts per minute (CPM)); a_{Total} is the total radioactivity in the sample (CPM); t is the incubation time (d); α is the expected isotopic fractionation factor (1.06); 1000 is the factor to convert mmol L^{-1} to nmol cm^{-3}.

2.5.2. Methanogenesis and AOM from ^{14}C-Mono-Methylamine

Ultimately, this study aimed to determine the activity of MG-MMA and the subsequent oxidation of methane from MG-MMA to inorganic carbon by AOM-MMA. To accomplish this goal, a sub-pushcore from each station was injected with radiolabeled ^{14}C-mono-methylamine (^{14}C-MMA) (^{14}C-mono-methylamine dissolved in 1 mL water, injection volume 10 µL, activity 220 KBq, specific activity 1.85-2.22 GBq mmol^{-1}) at 1-cm increments according to (Jørgensen, 1978) and incubated at 6 °C and in the dark. After 24 hrs, the incubation was terminated by slicing

116

the sediment at 1-cm increments into 50 mL wide mouth glass vials filled with 20 mL of 5% NaOH. Five killed control samples were prepared by transferring approximately 5 ml of extra sediment from each station into 50 mL wide mouth vials filled with 20 mL of 5% NaOH prior to radiotracer addition. Sample vials and killed controls were immediately sealed with butyl rubber stoppers and aluminum crimps, and shaken thoroughly for 1 min to ensure complete biological inactivity. Vials were stored upside down at room temperature until further processing.

In the home laboratory, methane production from ^{14}C-MMA by methanogenesis and subsequent oxidation of the produced ^{14}C-methane (^{14}C-CH$_4$) by AOM was determined according to the radiotracer method outlined in (Krause and Treude, 2021). Briefly, ^{14}C-CH$_4$ in the headspace of the sample vial was flushed through a series of cold-traps designed to remove any ^{14}C that was not associated with CH$_4$ before ^{14}C-CH$_4$ was combusted to ^{14}C-labeled carbon dioxide (^{14}C -CO$_2$) and captured in CO$_2$ traps. Radioactivity in the CO$_2$ traps was analyzed by liquid scintillation counting after adding 10 mL of scintillation cocktail (Ultima Gold XR, Perkin Elmer). After the headspace of the sample vials was combusted a 100 µL supernatant subsample was analyzed by liquid scintillation counting for total sum of ^{14}C-MMA and ^{14}C-labeled total inorganic carbon (^{14}C-TIC) radioactivity in the supernatant. Sediment samples were then analyzed for ^{14}C-TIC by acidification and shaking and the ^{14}C-TIC captured in the CO$_2$ trap was analyzed by liquid scintillation counting. The ^{14}C-TIC activity was then subtracted from the total ^{14}C activity in the supernatant (^{14}C-MMA + ^{14}C-TIC) to obtain the ^{14}C-MMA.

It is known that methylated amines have the tendency to bind to sediment surfaces and are therefore not detected in the liquid phase, which leads to the underestimation of the total amount of MMA in the sediment (Wang and Lee, 1993, 1994; Xiao et al., 2022). To account for ^{14}C-MMA bound to mineral surfaces, we determined the recovery factor (RF) of the studied sediment

according to Krause and Treude, (2021) (Eq. 6). Briefly, a total of 5 sediment samples were pooled from different depth sections from the NDT3-C, D and NDRO stations separately. These pooled sediment samples were previously incubated with ^{14}C-CH$_4$ and processed by oven combustion and acidification and shaking back at the home laboratory (see section 2.4). The acidified sediment samples were transferred into 50 mL centrifuge vials and then centrifuged at (2300 X g for 20 mins) to separate out the solid phase from the residual liquid from the acidification and shaking analysis, which was discarded. The pooled sediment samples were then repetitively cleaned to ensure no radioactivity remained from the ^{14}C-CH$_4$ incubations. This was done by resuspending the sediment with 20 mL of 5% (w/w) NaOH followed by centrifugation (2300 X g for 20 mins). The separated 5% (w/w) NaOH supernatant was then decanted. This cleaning step was repeated 3 times before adding a final 20 mL of 5% NaOH followed by the addition of the ^{14}C-MMA tracer similar to injection procedure of dead controls described above. Sediment free controls were prepared by adding 20 mL of 5% NaOH to 50 mL centrifuge vials followed by the addition of the ^{14}C-MMA tracer. The prepared sediment samples and sediment free controls were mixed thoroughly by vortex and stored in the dark at 4 °C for 2 weeks. After 2 weeks both the sediment and sediment-free samples were mixed and centrifuged (2300 X g for 20 mins). Then a 100 µL 5% NaOH supernatant subsample was collected from each sediment and sediment free sample. The radioactivity of the residual ^{14}C-MMA in the 5% NaOH was analyzed by liquid scintillation counting. The RF was calculated as follows (Eq. 6):

$$\text{RF} = \left[\frac{a_{SED}}{a_{NaOH}} \right] \tag{6}$$

where *RF* is the recovery factor; a_{SED} is the averaged amount of radioactivity (CPM) recovered from the centrifuge tubes containing 5% NaOH and the sediment sample; a_{NaOH} is the averaged amount of radioactivity (CPM) recovered from the centrifuge tubes containing only 5% NaOH.

Metabolic rates of MG-MMA and AOM-MMA were calculated according to Eq. 7. Note that natural concentrations of mono-methylamine in the Santa Barbara Basin sediment porewater were either below detection or detectable, but below the quantification limit (<10 nmol cm^{-3}) (Table 3-1). Therefore, MMA concentrations were assumed to be 3 nmol cm^{-3} to calculate the ex-situ rate of MG-MMA (Eq. 7).

$$MG\text{-}MMA = \frac{a_{CH_4} + a_{TIC}}{a_{CH_4} + a_{TIC} + \left[\frac{a_{MMA}}{RF}\right]} * [MMA] * \frac{1}{t} \tag{7}$$

where *MG-MMA* is the rate of methanogenesis from mono-methylamine (nmol cm^{-3} d^{-1}); a_{CH4} is the radioactive methane produced from methanogenesis (CPM); a_{TIC} is the radioactive total inorganic carbon produced from the oxidation of methane (CPM); a_{MMA} the residual radioactive mono-methylamine (CPM); RF is the recovery factor (Eq. 6); *[MMA]* is the assumed mono-methylamine concentrations in the sediment (nmol cm^{-3}); *t* is the incubation time (d). ^{14}C-CH$_4$ and ^{14}C-TIC sample activity was corrected by respective abiotic activity determined in killed controls.

Results from the ^{14}C-MMA incubations were also used to estimate the AOM-MMA rates according to Eq. 8,

$$AOM - MMA = \frac{a_{TIC}}{a_{CH_4} + a_{TIC}} * [CH_4] * \frac{1}{t} \tag{8}$$

where *AOM-MMA* is the rate of anaerobic oxidation of methane based on methane produced from mono-methylamine (nmol cm^{-3}d^{-1}); a_{TIC} is the produced radioactive total inorganic carbon (CPM);

a_{CH4} is the residual radioactive methane (CPM); *[CH4]* is the sediment methane concentration (nmol cm^{-3}); t is the incubation time (d). ^{14}C-TIC activity was corrected by abiotic activity determined by replicate dead controls.

2.5.3 Anaerobic oxidation of methane from ^{14}C-CH4

AOM rates from ^{14}C-CH$_4$ (AOM-CH$_4$) were determined by injecting radiolabeled ^{14}C-CH$_4$ (^{14}C-CH$_4$ dissolved in anoxic MilliQ, injection volume 10 µL, activity 5 KBq, Specific activity 1.85-2.22 GBq mmol^{-1}) into one sub-pushcore from each station at 1-cm increments similar to section 2.5.1. Incubations of the sub-pushcore samples were stopped after approximately 24, similar to section 2.5.1. Sediment samples were stored on board at room temperature until further processing at the home laboratory. In the laboratory, AOM-CH$_4$ was analyzed using oven combustion (Treude et al., 2005a) and acidification/shaking (Joye et al., 2004). The radioactivity was determined by liquid scintillation counting. AOM-CH$_4$ rates were calculated according to Eq. 8.

2.5.4 Rate constants for AOM-CH4, MG-MMA, and AOM-MMA

Metabolic rate constants (k) for AOM-CH$_4$, MG-MMA and AOM-MMA were calculated using the experimental data determined by sections 2.5.2 and 2.5.3. The rate constants consider the metabolic reaction products, divided by the sum of reaction reactants and products. The metabolic rate constants for AOM-CH$_4$, MG-MMA and AOM-MMA were calculated according to Eq 9,

$$k = \frac{a_{products}}{a_{products} + a_{reactants}} * \frac{1}{t} \qquad [9]$$

where k is the metabolic rate constant (day^{-1}); $a_{products}$ is the radioactivity (CPM) of the metabolic reaction products; $a_{reactants}$ is the radioactivity (CPM) of the metabolic reaction reactants; t is time in days.

3. Results

3.1. Sediment geochemistry

Fig. 3-1A, E, I, M, and Q shows profiles of sediment methane and porewater sulfate concentrations in push cores. At SDRO, methane concentrations varied slightly with depth ranging from ~5 µM to ~11 µM between 0 and 8 cm (Fig. 3-1A). At NDRO, methane ranged between ~3.5 and ~12 µM at 0-13 cm, followed by an increase to ~16 µM at 14-15 cm (Fig. 3-1E). At NDT3-A, methane decreased slightly from ~8 µM to 4 µM between 0-4 cm (Fig. 3-1I). Below 4 cm, methane varied with no pattern between ~3 and ~8 µM. At NDT3-C, a small peak in methane were seen between 2-4 (~5 µM to 9 µM) and 8-9 cm (~8 µM to 11 µM). Otherwise, concentrations ranged between 6 to 9 µM (Fig. 1M). At NDT3-D, methane ranged from ~9 to 13 µM without clear pattern (Fig. 3-1Q).

Sulfate concentrations at SDRO decreased very slightly with increasing sediment depth from ~27 to ~25 mM between 0-8 cm (Fig. 3-1A). At NDRO, sulfate varied between ~23 and ~29 mM without clear trend (Fig. 3-1E). At NDT3-A sulfate decreased slightly from ~28 mM to ~25 mM between 0-12 cm (Fig. 3-1I). At NDT3-C sulfate showed small variations in the top 3 cm but otherwise remained relatively stable around ~26 mM throughout the core (Fig. 3-1M). At NDT3-D, sulfate varied between ~23 and 30 mM with no clear trend (Fig. 3-1Q).

Table 3-2. shows the porewater concentrations of carbon sources known to support methanogenesis from the metabolomic analysis by NMR. Methylamine concentrations were detected but below the quantification limits at SDRO and NDT3-A at 1-2 cm. Otherwise methylamine was below detection for the rest of the samples. Methanol was detected but below quantification only at NDT3-A, 1-2 cm, otherwise methanol was below detection. Acetate reached

as high as 21 µM at NDT3-A, 1-2 cm, otherwise acetate was either below detection or detected

but below quantification.

STATION, SEDIMENT DEPTH (CM)	ACETATE (µM)	METHANOL (µM)	METHYLAMINE (µM)
SDRO, 1-2 CM	BQ	BD	BQ
SDRO, 9-10 CM	BD	BD	BD
NDRO, 1-2 CM	BQ	BD	BD
NDRO, 9-10 CM	BD	BD	BD
NDT3-A, 1-2 CM	21	BQ	BQ
NDT3-A, 9-10 CM	BD	BD	BD
NDT3-C, 1-2 CM	BD	BD	BD
NDT3-C, 9-10 CM	BD	BD	BD
NDT3-D, 1-2 CM	BD	BD	BD
NDT3-D, 9-10 CM	BD	BD	BD

Table 3-2. Porewater metabolite results analyzed by NMR. BQ signifies concentrations were detectable but below the quantification limit (10 µM). BD signifies concentrations were below the detection limit.

3.2 AOM from ^{14}C-methane and sulfate reduction from ^{35}S-sulfate

Fig. 1B, F, J, N, and R depicts rates of AOM-CH$_4$ and sulfate reduction from the radiotracer

incubations with ^{14}C-methane and ^{35}S-sulfate in sub-pushcores, respectively. AOM-CH$_4$ in the top

~5 cm of the sediment showed a tendency to increase with decreasing water depth (from ~0.007 –

0.050 nmol cm^{-3} d^{-1} at NDRO to ~0.500 – 1.800 nmol cm^{-3} d^{-1} at NDT3-D), while rates were either

at or close to zero (SDRO, NDRO, NDT3-A) or varying between ~0.050 and 4.525 nmol cm^{-3} d^{-1}

(NDT3-C, NDT3-D) in depths >5 cm. Where peaks in AOM were present (SDRO, NDT3-C, NDT3-D) they were always located at the top 0-1 cm sediment layer.

Sulfate reduction activity was detected throughout all sediment cores with peaks mostly located at the top 0-1 cm sediment layer. The highest individual sulfate reduction peaks were found at NDRO, NDT3-A, and NDT3-C (~120, ~85 and~134 nmol cm^{-3} d^{-1}). NDT3-D did not show a clear trend in sulfate reduction rates, varying between ~14 and ~45 nmol cm^{-3} d^{-1} throughout the core. Note that sulfate reduction data are missing for 0-5 cm at SDRO.

3.3 Methanogenesis and AOM from ^{14}C-mono-methylamine

3.3.1 ^{14}C-MMA recovery from sediment

In section 2.5.2, we used additional sediment from NDRO, NDT3-C and D stations to determine the RF values (Eq. 6) to correct MG-MMA rates at each station of the study (Eq. 7). The corresponding RF values were 0.93, 0.84, and 0.75, respectively. Note that no RF values were determined for SDRO or the NDT3-A. We applied RF values from NDRO and NDT3-C, respectively, instead.

3.3.2 MG-MMA and AOM-MMA

Fig. 3-1C, G, K, O, S shows ex situ rates of MG-MMA and AOM-MMA, assuming a natural MMA concentration of 3 µM (see section 2.5.2). At SDRO, MG-MMA ranged between ~0.3 and 0.5 nmol cm^{-3} d^{-1} between 0 -5 cm. Below 5 cm MG-MMA was stable ~0.3 nmol cm^{-3} d^{-1} (Fig. 3-1C). MG-MMA at NDRO peaked at 0-1cm and at 4-5 cm reaching ~0.4 nmol cm^{-3} d^{-1} otherwise MG-MMA decreased with depth below 5 cm from ~0.4 nmol cm^{-3} d^{-1} to ~0.2 nmol cm^{-3} d^{-1} (Fig. 3-1G). At NDT3-A, MG-MMA generally decreased from ~0.45 nmol cm^{-3} d^{-1} at 0-1cm

to ~0.25 nmol cm^{-3} d^{-1} at 14-15 cm. MG-MMA at NDT3-C varied with no pattern ranging between 0.007 nmol cm^{-3} d^{-1} and 0.3 nmol cm^{-3} d^{-1} (Fig. 3-1O). At NDT3-D, MG-MMA sharply increased from 0.05 nmol cm^{-3} d^{-1} at 0-1cm, to ~0.34 nmol cm^{-3} d^{-1} at 1-2 cm. MG-MMA then decreased slightly to ~0.2 nmol cm^{-3} d^{-1} between 2 and 9 cm, before increasing to ~0.5 nmol cm^{-3} d^{-1} at the bottom of the core (Fig. 3-1S).

AOM-MMA on the other hand was 1 to 2 orders of magnitude higher than MG-MMA and 1 to 4 orders of magnitude higher than AOM-CH$_4$ (Fig. 3-1C, G, K, O, S). At SDRO, AOM-MMA rates varied between 0-3 cm and 4-8 cm ranging between ~6 to ~10 nmol cm^{-3} d^{-1}. Between 10-14 cm, at SDRO, AOM-MMA was around ~9 nmol cm^{-3} d^{-1} (Fig. 3-1C). At NDRO, AOM-MMA rates were ~5 nmol cm^{-3} d^{-1} at 0-1cm, and ~7.5-8 nmol cm^{-3} d^{-1} between 5-7 cm (Fig. 3-1G). At NDT3-A, AOM-MMA rates varied with no pattern with increasing sediment depth ranging ~2 nmol cm^{-3} d^{-1} and ~8 nmol cm^{-3} d^{-1} (Fig. 3-1K). At NDT3-C, AOM-MMA rates varied with no trend ranging between ~4 nmol cm^{-3} d^{-1} and ~9 nmol cm^{-3} d^{-1} (Fig. 3-1O). At NDT3-D, AOM-MMA rates decreased with depth starting at ~16 nmol cm^{-3} d^{-1} at 1-2 cm to 9 nmol cm^{-3} d^{-1} 11-12 cm (Fig. 3-1S).

3.4 Rate constants for MG-MMA, AOM-MMA and AOM-CH$_4$

Fig. 3-1D, H, L, P, and T show the rate constant (k) for MG-MMA, AOM-MMA and AOM-CH$_4$ to compare relative radiotracer turnover between the processes and methods. At all stations, MG-MMA rate constants were almost always higher than and AOM-CH$_4$ rate constants. MG-MMA rate constants were consistent across the depth transect ranging between ~0.01 to 0.15 d^{-1} . AOM-CH$_4$ rate constants were also consistent across the depth transect ranging between ~0.0009 d^{-1} and ~0.3 d^{-1} (Fig. 3-1 D, H, L, P and T). Rate constants for AOM-MMA on the other

hand, was considerably higher with values consistently ~0.9 d^{-1} (Fig. 3-1 D and H) at SDRO and

NDRO, between ~0.7 and 0.8 d^{-1} at NDT3-A and NDT3-C (Fig. 3-1L and P), and ~0.9-1.2 d^{-1} At
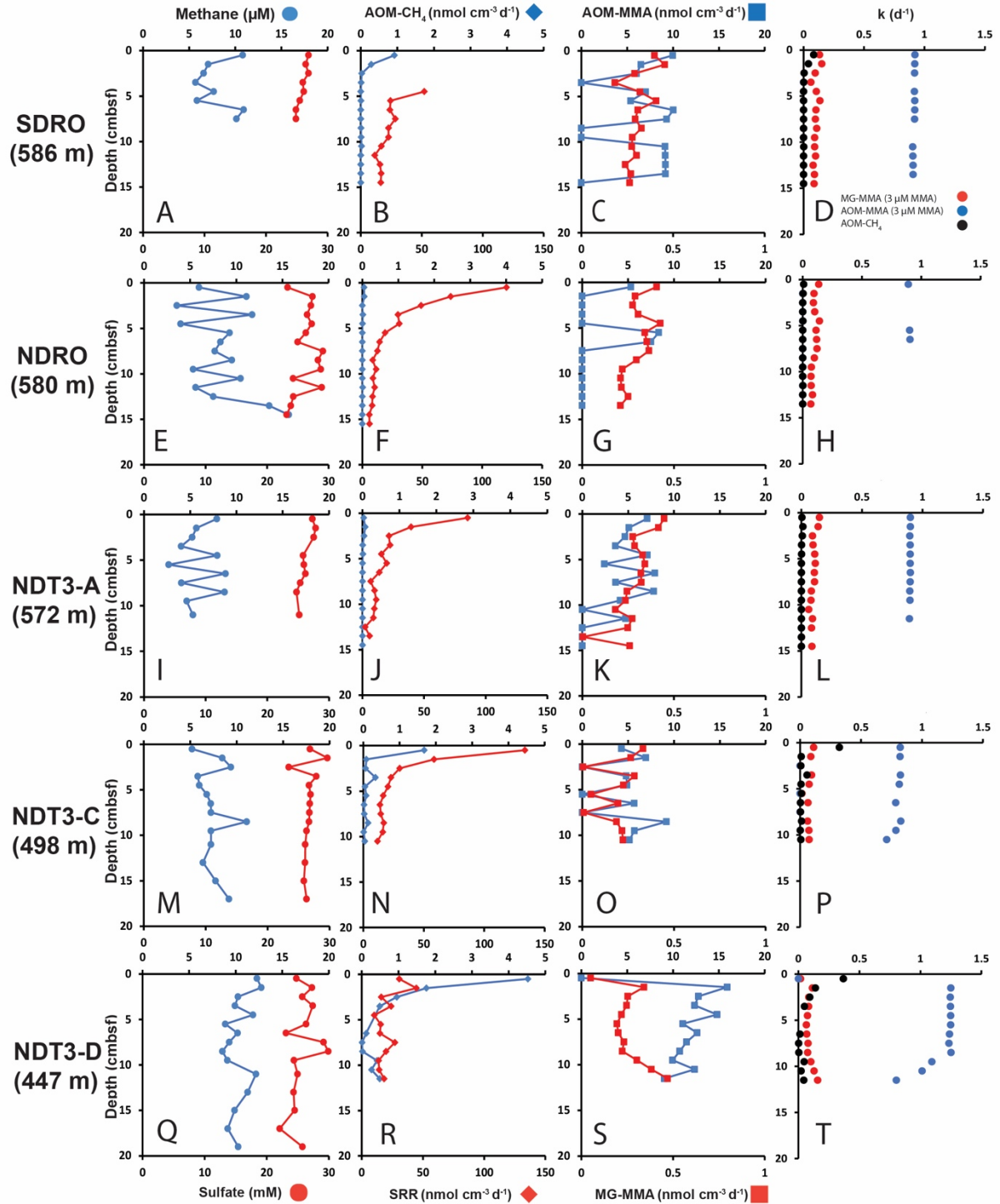
NDT3-D (Fig. 3-1T).

Figure 3-1. Depth profiles of biogeochemical parameters in sediment across the depth transect of the SBB; (A, E, I, M, and Q) sediment methane and porewater sulfate, (B, F, J, N, and R) AOM-CH$_4$ and sulfate reduction (determined from direct injection of ^{14}C-CH$_4$ and ^{35}S-Sulfate, respectively), (C, G, K, O, and S) AOM-MMA and MG-MMA (determined from direct injection of ^{14}C-MMA), (D, H, L, P, and T) rate constants for AOM-CH$_4$, MG-MMA and AOM-MMA.

4. Discussion

4.1 Vertical substrate availability

Methane concentrations within the top ~15 cm across all transect stations were similarly low to what has been reported in previous studies from the SBB (Fig. 3-1A, E, I, M, Q) (Barnes and Goldberg, 1976; Warford et al., 1979). The methane reported here are also similar to low methane concentrations found in the sulfate-reducing zone off the coast of Peru, within similar water column depths (70 m to 770 m) (Maltby et al., 2016) and within Eckenfoerde Bay (Maltby et al., 2018a).

Methane concentrations are expected to be low in the upper sediment layers where sulfate is plentiful and sulfate reduction is active. The methane detected in the upper sulfate-rich sediment could be derived from methylotrophic methanogenesis producing methane from non-competitive substrates within the sulfate-reducing zone (King et al., 1983; Maltby et al., 2016; Maltby et al., 2018a; Oremland and Taylor, 1978). The production and fate of this methane will be discussed in detail in section 4.3.

4.2 Metabolite concentration and turnover

Natural methylamine concentrations were mostly below detection (<3 µM); however, in porewater close to the sediment-water interface of SDRO and NDT3-A, methylamine was detected but below the quantification limit (<10 µM) (Table 3-2). This observation at a minimum suggests that methylamines are present but are either rapidly turned over by biological activity (Anthony, 1982; Chistoserdova, 2015) or locked in the solid phase (not determined in this study)(Wang and Lee, 1990; Wang and Lee, 1993; Xiao et al., 2022). Similarly, methanol was below detection, except for one sample, where it was not quantifiable [NDT3-A, 1-2 cm]. In the marine

128

environment, methanol is known to be a non-competitive substrate for methanogenesis (King et al., 1983; Oremland and Taylor, 1978). However, methanol is a carbon source for a wide variety of metabolisms, including sulfate-reducing and denitrifying bacteria, as well as aerobic and anaerobic methylotrophs (Fischer et al., 2021), which could all be present in the SBB sediments keeping methanol concentrations low. Acetate was also detected in the metabolomic analysis but mostly below quantification [NDT3-A, 1-2 cm]. Acetate is formed through fermentation reactions of complex organic matter or through acetogenesis (Jørgensen, 2000; Ragsdale and Pierce, 2008). It is classically known to be a favorable food source for many bacteria and archaea such as sulfate reducers and methanogens (Conrad, 2020; Jørgensen, 2000), which would explain its low abundance in the SBB sediments. It appears that the methanogenic potential in surface sediment of the SBB is substantial. Low concentrations of these metabolites are likely signatures of rapid metabolic turnover, similar to what has been described for microbial utilization of hydrogen in sediment (Conrad 1999). In this situation, metabolites would be kept at a steady-state concentration close to the thermodynamic equilibrium of the respective consumers. The same is likely true in the relationship between methanogens and methanotrophs, where we would expect methane concentration to be kept at the thermodynamic equilibrium of the methanotrophs. If we assumed that all metabolites (i.e., methylamine, methanol, acetate, methane) are at thermodynamic equilibrium, it would allow us to use the equilibrium constant K to calculate the threshold partial pressures for the processes consuming them (Conrad 1999).

4.4. Bioavailability of methylamine vs. adsorption to minerals

MMA is known to be a carbon source for some groups of bacteria (Chistoserdova, 2015) and methanogenic archaea (Thauer, 1998; Winfrey and Ward, 1983), which we will discuss further

(see section 4.6). It is worth discussing here that methylamines have the tendency to adsorb to mineral surfaces through electrostatic and Van der Walls interactions (Krause and Treude, 2021; Wang and Lee, 1993, 1994; Xiao et al., 2022; Zhuang et al., 2017; Zhuang et al., 2018). The methylamine adsorption is dependent on salinity, organic carbon content, and mineral clay content (Wang and Lee, 1993, 1994; Xiao and Peacock, 2019). The result of this mineral molecule interaction could be a reduction in methane production, which could impact cryptic methane cycling in sediment (Xiao et al., 2022). In the present study we assumed the natural MMA concentration that is bioavailable in the porewater to be 3 µM MMA. To constrain the MMA bound to the sediment we correct using the ^{14}C-MMA RF values calculated in Eq. 6 which is applied to the MG-MMA rate equation (Eq. 7). Thus, the methanogenesis rates presented here maybe slightly inflated, because the RF values increase the MMA pool leading to an overestimation of the methanogenesis rate (Eq. 7).

Krause and Treude, (2021) recommended to assess the methylamine adsorption in different sediment types and sediment depth intervals. The recovery factors (RF) calculated in section 3.3.1 indicate that adsorption of methylamine to minerals varies spatially in the SBB. Sediment collected from the depocenter of the SBB (SDRO and NDRO) seem to adsorb MMA the least. Whereas sediment collected at the shallowest station (NDT3-D), adsorbed the most. This pattern could potentially be explained by the close proximity of NDT3-D to the mainland, which could supply the sediment with more terrestrial input (Jickells et al., 2005) and therefore contain more clays that increase methylamine adsorption (Wang and Lee, 1993, 1994; Xiao and Peacock, 2019; Xiao et al., 2022). Fine grain brownish sediment was observed during sediment subsampling from the NDT3-D station, suggesting the sediment at this station may be comprised of clay, but direct mineralogical analysis of the sediment was not conducted for this study. The RF values determined

in this study (0.75-0.93, section 3.3.1) are higher than the RF value (0.46) reported for hypersaline salt marsh sediment in Krause and Treude (2021). This comparison further reinforces the interpretation that methylamine adsorption changes with sediment type and environmental settings and future studies must elucidate the methylamine adsorption potential in different environmental settings.

4.5. Evidence of cryptic methane cycling

4.5.1 Concurrent sulfate reduction and methylotrophic methanogenesis

To obtain evidence of cryptic methane cycling in the SBB, sediment from each station were incubated with different radioactive substrates. SBB sediment were incubated with radioactive ^{35}S -sulfate and ^{14}C-MMA to show that concurrent sulfate reduction and MG-MMA, respectively, were active in the SBB sediment. Except for station NDT3-D, sulfate reduction and MG-MMA rates were the highest near the sediment-water interface (Fig. 3-1B, F, J, N and R), most likely because of fresh organic matter availability and low bottom water oxygen concentrations (Table 3-1). However, note a small portion of the sulfate reduction detected is likely also coupled to AOM.

One explanation for lower sulfate reduction rates at NDT3-D could be attributed to the presence of iron oxides, which would thermodynamically favor iron over sulfate reduction (Jørgensen, 2000) (Lovley and Phillips, 1987a). The station was closest to the mainland, where terrestrial input from weathering and erosion could bring in iron-bearing minerals into marine sediment (Jickells et al., 2005). The presence of iron oxides is supported by visible brown-orange, fine-grained clay sediment observed during sampling (not shown). However, sulfate reduction and MG-MMA activity was still detected. Contrary to Lovley and Phillips, (1987a), simultaneous

131

iron reduction, sulfate reduction, and methylotrophic methanogenesis is commonly observed in marine sediment (Li et al., 2020). This simultaneous activity depends on the environmental pH and type of iron oxide mineral available (Postma and Jakobsen, 1996). Iron reduction activity was not directly determined in this study however, future work should elucidate the role iron reduction may have on cryptic methane cycling, because iron reduction can suppress or promote methanogenesis (Baek et al., 2019) and can be linked to AOM (Beal et al., 2009).

An alternative or concurrent cause for decreased sulfate reduction in surface sediment of NDT3-D could be the presence of bioturbation and bioirrigation by macrofauna. At this station, oxygen concentrations in the bottom water were ~27 µM allowing benthic animals to inhabit the sediment, as indicated by burrows and lack of lamination in the sediment (not shown). Introduction of oxygen into sediment would push anaerobic processes into deeper sediment layers and reduce the amount of carbon delivered to them (Jørgensen et al. 2022). The presence of oxygen would explain the strongly reduced activity of sulfate reduction and MG-MMA (and coupled AOM-MMA; Fig. 3-1R and S) in the 0-1 cm sediment layer and suggests that the peak in supposed AOM-CH_4 (Fig. 3-1D) is instead linked to aerobic oxidation of methane.

Rates of methylotrophic methanogenesis coupled to mono-methylamine (MG-MMA) detected in SBB sediment were similar to bulk methanogenesis reported from the sulfate-reducing zone in sediment in the oxygen minimum zone off Peru (Maltby et al., 2016) and deep-sea sediment of the South China Sea (Zhuang et al., 2019b). Despite the methanogenic activity in the sulfate-reducing zone, methane did not buildup in the sediment as indicated by relatively low methane concentrations (< 15 µM) (Fig. 3-1A, E, I, M, Q). Most of this activity was detected close to the sediment-water interface, so it is conceivable that some methane could diffuse out of the sediment where it may be oxidized in the water column by aerobic oxidation of methane before

emitting into the atmosphere (Reeburgh, 2007). During the fall, oxygen concentrations are extremely low in the SBB (Valentine et al., 2016), which could still support aerobic oxidation of methane at pretty high rates when seawater oxygen concentrations are submicromolar (Steinle et al., 2017). But benthic chamber incubations at the SBB stations did not indicate a release of methane into the water column (cite Q. Qin, unpul. data) despite the SBB contains a prolific network of cold seeps where methane is major constituent (Boles et al., 2004; Hornafius et al., 1999; Leifer et al., 2010). At stations where bottom waters may still contain dissolved oxygen (e.g., NDT3-D), may also help explain why methane is low. The presence of oxygen could support aerobic oxidation of methane in the sediments which would keep methane concentrations low. However, the ^{14}C tracer incubations do not differential between aerobic and anaerobic oxidation of methane in the sediment. Though direct measurements of aerobic oxidation of methane could be could be a useful parameter for future work to better constrain the fate of methane from SBB sediment, as it has been proposed that aerobic-methane oxidizing bacteria could persist on nM concentrations of oxygen within the sediment (Vigderovich et al., 2022). We suggest, however that AOM, as part of the cryptic methane cycle, is mainly responsible for keeping methane concentrations low in the sulfate-reducing zone, which we will be discussed next.

4.5.2 Methylotrophic methanogenesis coupled to AOM

To assess the coupling of methanogenesis from monomethylamine with AOM, sediment samples from the SBB were incubated with either ^{14}C-CH$_4$ or ^{14}C-MMA at each station. Generally, AOM determined by direct injection of ^{14}C-CH$_4$ were consistent with AOM rates determined in other organic-rich coastal surface sediment (Beulig et al., 2018; Knittel and Boetius, 2009; Treude et al., 2005b). AOM-CH$_4$ rates further showed a tendency to increase with decreasing water depth,

while methane concentrations remained basically the same regardless of station and sediment depth. This provides evidence that there is more fresh organic matter reaching sediment at shallower stations which can be converted to methane (Krüger et al., 2005). It also suggests that the threshold partial pressure of methane (respectively, the Michaelis constant K_m) of AOM remained the same at thermodynamic equilibrium between AOM and methanogenesis (compare, e.g., with Conrad 1999). Importantly, this pattern strongly indicates that AOM is keeping methane concentrations in the upper sulfate-reducing zone low (Fig. 3-1).

AOM determined by direct injection of ^{14}C-CH_4 and methanogenesis from ^{14}C-MMA were concurrently active within the same order of magnitude in the top 5 cm of the sulfate-reducing zone at all stations, which suggests cryptic methane cycling is real. However, the mismatch between AOM determined directly from ^{14}C-CH_4 vs AOM determined via ^{14}C-MMA (AOM-CH_4 is roughly 1-2 orders of magnitude lower than AOM-MMA) indicates that AOM rates determined via ^{14}C-MMA were overestimated. We hypothesize that this mismatch was caused by the conversion of ^{14}C-MMA directly to ^{14}C-TIC by processes other than AOM coupled to MG-MMA. Any process converting ^{14}C-MMA directly to ^{14}C-TIC would inflate the rate constant slightly for MG-MMA, but dramatically for AOM-MMA (see Eq. 7 and 8).

Accordingly, the rate constant for AOM-MMA differs by 1 to 2 orders of magnitude compared to AOM-CH_4 and MG-MMA (Fig. 3-1D, H, L, P, T). This trend strongly suggests that the ^{14}C-TIC detected from our analysis must be the sum of ^{14}C-TIC produced from AOM in the cryptic methane cycle and ^{14}C-TIC produced from direct methylamine oxidation by a different anaerobic methylotrophic metabolism that could not be disambiguated using the adapted radiotracer method. In fact a recent study Zhuang et al., (2019a) investigated heterotrophic metabolisms of C1 and C2 low molecular weight compounds in anoxic sediment collected in the

Gulf of Mexico. Similar to the present study, sediment was incubated with a variety of ^{14}C radiotracers to elucidate the metabolic turnover of low molecular weight compounds, including ^{14}C-labeled trimethylamine. Their results showed clearly that although methylamines did stimulate methane production, methylamines were simultaneously oxidized by non-methanogenic microorganisms. The data presented in this study strongly indicate that in addition to cryptic methane cycling, the buildup of the excess ^{14}C-TIC in the SBB sediment could be linked to a non-methanogenic metabolism occurring concurrently with the cryptic methane cycle in the SBB sediment. Turnover of ^{14}C-MMA by microbial groups other than methanogens was not directly tested in this study. However, we discuss current literature on methylamine turnover and examples of microbial groups involved in-vivo and in marine sediment in the following section.

4.6 Methylamine turnover by non-methanogenic pathways

Methylamines are the simplest alkylated amine derived from the degradation of choline and betaine found in plant and phytoplankton biomass (Oren, 1990; Taubert et al., 2017). The molecules are ubiquitously found in saline and hypersaline conditions in the marine environment (Mausz and Chen, 2019; Zhuang et al., 2016; Zhuang et al., 2017). The importance of methylamine as a nitrogen and carbon source for microbes to build biomass has been well documented (Anthony, 1975; Capone et al., 2008; Mausz and Chen, 2019; Taubert et al., 2017). Methylamines can be metabolized by aerobic methylotrophic bacteria (Chistoserdova, 2015; Hanson and Hanson, 1996; Taubert et al., 2017) and by methylotrophic methanogens anaerobically (Chistoserdova, 2015; Thauer, 1998). Here we hypothesize that, in addition to methylotrophic methanogenesis, sulfate reduction was involved in MMA consumption in surface sediment of the SBB. To the best of our knowledge there is virtually no literature that found direct evidence of methylamine

oxidation to CO_2 by sulfate-reducing bacteria. However, there appears to be a growing paradigm shift in the understanding of how non-competitive substrates in anoxic sediment are utilized by sulfate-reducing bacteria and methylotrophic methanogens. For example, methanol, classically known to be a non-competitive substrate for methylotrophic methanogenesis in natural settings (King et al., 1983; Oremland et al., 1982), has been shown to be a carbon source for bacterium that perform denitrification (Martineau et al., 2015). Methanol has also been shown to be a carbon source for thermophilic sulfate-reducing bacteria that perform sulfate reduction (Fischer et al., 2021; Sousa et al., 2018). Furthermore, methanol can be converted to acetate with CO_2 by acetogens (Fischer et al., 2021).

Current literature does implicate anaerobic methylamine oxidation by sulfate reduction. For example, Cadena et al., (2018) performed in vitro incubations with microbial mats collected from a hypersaline environment with various competitive and non-competitive substrates including tri-methylamine. Microbial mats incubated with trimethylamine stimulated considerable methane production, but after 20 days, H_2S began to accumulate and plateau after 40 days, suggesting that trimethylamine is not exclusively shuttled to methylotrophic methanogenesis. The molecular data reported in Cadena et al., (2018), however, could not identify a particular group of sulfate-reducing bacteria that proliferated by the addition of trimethylamine. Instead, their molecular data suggested other microbial processes to be responsible for trimethylamine turnover, which we will expand on in the next section. The accumulation of H_2S in Cadena et al., (2018) could also have been derived from sulfate-dependent AOM, which is supported by their molecular data, but was not quantified.

Radiotracer incubations using ^{14}C-labled methylamine reported in Zhuang et al., (2019a) showed direct oxidation to ^{14}C-CO_2, suggesting that substrates like methylamine could be

competitive between methanogens and sulfate-reducing bacteria; however, their study did not directly show the consumption of methylamine to be directly linked to sulfate reduction. A more compelling study implicating sulfate-reducing bacteria in methylamine consumption was shown in Kivenson et al., (2021). Their study discovered dual genetic code expansion in Deltaproteobacteria, which allows them to metabolize trimethylamine in sediment within a deep-sea industrial waste dumpsite in the San Pedro Basin, off the coast of California, USA. The authors expanded their study to revisit metagenomic and metatranscriptomic data collected from the Baltic Sea and in the Columbia River Estuary and found expression of trimethylamine methyltransferase in Deltaproteobacteria. Their result suggested that a trimethylamine metabolism does exist in Deltaproteobacteria, which was enabled by the utilization of genetic code expansion. Furthermore, the results also suggest that trimethylamine could be competitively utilized by both Deltaproteobacteria and methylotrophic methanogens.

Although the evidence of sulfate-reducing bacteria playing a larger role in methylamine utilization is growing, there are other methylotrophic microorganisms in anaerobic settings that could also be responsible to degrading methylamines. De Anda et al., (2021) discovered and classified a new phylum called Brockarchaeota. The study reconstructed archaeal metagenome-assembled genomes from sediment near hydrothermal vent systems in the Guaymas Basin, Gulf of California, Mexico. Their findings showed that some Brockarchaeota, were capable of assimilating trimethylamines, byway of the tetrahydrofolate methyl branch of the Wood-Ljunghal pathway and the reductive glycine pathway, bypassing methane production in anoxic sediment.

Farag et al., (2021) found genomic evidence of a novel Asgard Phylum called *Sifarchaeota* in deep marine sediment off the coast of Coasta Rica. The study used comparative genomics to show a cluster, *Candidatus* Odinarchaeota within the *Sifarchaeota* Phylum, which contains genes

encoding for an incomplete methanogenesis pathway that is coupled to the carbonyl branch of the Wood-Ljunghal pathway. The results suggest that this cluster could be involved with utilizing methylamines. The *Sifarchaeota* metagenome-assembled genomes results found genes for nitrite reductase and sulfate adenylyltransferase and phosphoadenosine phosphosulfate reductase, indicating *Sifarchaeota* could perform nitrite and sulfate reduction. But their study did not directly linked nitrite and sulfate reduction to the utilization of methylamines by *Sifarchaeota*.

Molecular analysis was not performed in the present study, therefore we are unable to directly link sulfate-reducing or other heterotrophic bacteria to the direct oxidation of methylamine in the SBB. Future work should combine available geochemical and molecular tools to piece together the complexity of metabolisms involved with methylamine turnover and how it may affect the cryptic methane cycle.

4.7 Implications for cryptic methane cycling in SBB and other OMZ's

The SBB is known to have a network of hydrocarbon cold seeps, where methane and other hydrocarbons are released from the lithosphere into the hydro and atmosphere either perennially or continuously (Boles et al., 2004; Hornafius et al., 1999; Leifer et al., 2010). The migration of methane and other hydrocarbons vertically into the hydrosphere occur along channels that are focused and permeable, such as fault lines and fractures (Moretti, 1998; Smeraglia et al., 2022). Local tectonics and earthquakes could create new fault lines or fractures that reshape or redisperse less permeable sediment, which may open or close migration pathways for hydrocarbons, including methane (Smeraglia et al., 2022). In fact it has been shown that hydrocarbons move much more efficiently through faults when the region in question is seismically active on time scales <100.000 yrs (Moretti, 1998). Given the current and historical seismic activity

(Probabilities, 1995) and faulting (Boles et al., 2004) within and surrounding the SBB, it is conceivable that hydrocarbon seep patterns and seepage pathways could also shift over time. A potential consequence of this shifting in the SBB is that methane seepage could spontaneously flow through prior non-seep surface sediment. The fate of this methane would then fall on the methanotrophic communities that are part of the cryptic methane cycle. However, it is not well understood how quickly anaerobic methanotrophs could handle this shift due to their extremely slow growth rates (Dale et al., 2008a; Knittel and Boetius, 2009; Nauhaus et al., 2007; Wilfert et al., 2015). After gaining a better understanding of cryptic methane cycling in the SBB presented in this study, a hypothesis worth testing in future studies is whether this process primes surface sediment to respond faster to increases in methane transport through the sediment.

On a much more immediate timescale, accelerated anthropogenic eutrophication and climate change threaten the overall health of coastal marine environments (Seidel et al., 2021). Eutrophication is amplified in shallow coastal marine environments, due to the close proximity to land where anthropogenic activities produce more reactive carbon, nitrogen and phosphorus, which can be discharged to the marine environment by artificial run-off and rivers. The loading of carbon, nitrogen and phosphorus will ultimately generate more organic matter through the stimulation of primary productivity in the euphotic zone. This increase in productivity will amplify anoxic conditions and supply more organic matter to deeper oceans and into sediment (Rabalais et al., 2009; Seidel et al., 2021). Hence, eutrophication in the SBB could supply more competitive and non-competitive substrates to support methane production and the cryptic methane cycle. Thus, the already established cryptic methane cycle could cycle more methane and limit methane emission.

Global oceanic oxygen concentrations are projected to decrease with warming due to climate change, and thus OMZ's are also projected to expand (Stramma et al., 2010). The evidence of cryptic methane cycling in the SBB suggests that other, much larger OMZ's, may also have cryptic methane cycling in the sediment. OMZ's are thought to contain large reservoirs of methane but many OMZ's are not normally known to be large sources of methane into the atmosphere (Chronopoulou et al., 2017; Wright et al., 2012). With the evidence in the study in hand, the cryptic methane cycle could be playing a much more important role in reducing the amount of methane release from marine sediments where OMZ's are located globally, and future investigations must elucidate this possibility.

The SBB is a particularly interesting case as it is a thermally stratified, silled basin (Arndt et al., 1990; Reimers et al., 1996; Sholkovitz, 1973; Soutar and Crill, 1977) which offers very low oxygen concentrations in the bottom waters most of the time (Valentine et al., 2016). Other OMZ's may get oxygenated during upwelling events which can help restore oxygen concentrations into the water column and at the surface of sediments (Levin et al., 2009). It is then conceivable that the flushing of OMZ's with oxygenated water could negatively impact anaerobic metabolisms such as the cryptic methane cycle in the sediments near the sediment water interface, which has not been investigated. Future investigations should consider whether the cryptic methane cycle can adapt or recover in the event of flushing from upwelling events within OMZ's.

5. Conclusions

In the present study, we set about to find evidence of cryptic methane cycling in anoxic sediment along a depth transect of the SBB using a variety of geochemical analytics including a adapted radiotracer method from Krause and Treude, (2021). Geochemical analysis showed, within the top 15 cm, low methane concentrations were present within sulfate-rich sediment. The low methane concentrations were attributed to the balance between methylotrophic methanogenesis and subsequent consumption by AOM in intervals within the top 15 cm. Our results provide strong evidence of cryptic methane cycling in the SBB. We conclude that this process is an important, yet overlooked, process maintaining low methane concentrations in surface sediments of OMZ's and future work should consider cryptic methane cycling in other OMZ's to better constrain carbon cycling in these expanding marine environments.

Our radiotracer analyses also indicated microbial activity that oxidizes monomethylamine directly to CO_2 thereby bypassing methane production. Based off the sulfate reduction activity and methylamine consumption to CO_2 detected in this study and the metagenomic clues presented in the literature, we hypothesize that sulfate reduction may also be supported by methylamines. Our study highlights the metabolic complexity and versatility of anoxic marine sediment near the sediment-water interface within the SBB. Future work should consider how methylamines are utilized by different groups of bacteria and archaea, how methylamine utility by other anaerobic methylotrophs affects the cryptic methane cycle and evaluate if potential environmental changes affect the cryptic methane cycle activity.

References

Anthony C. (1975) The biochemistry of methylotrophic micro-organisms. *Science Progress (1933-)*, 167-206.

Anthony C. (1982) The biochemistry of methylotrophs.

Arndt S., Lange C. B. and Berger W. H. (1990) Climatically controlled marker layers in Santa Barbara Basin sediments and fine-scale core-to-core correlation. *Limnology and Oceanography* **35**, 165-173.

Baek G., Kim J. and Lee C. (2019) A review of the effects of iron compounds on methanogenesis in anaerobic environments. *Renewable and Sustainable Energy Reviews* **113**, 109282.

Barnes R. and Goldberg E. (1976) Methane production and consumption in anoxic marine sediments. *Geology* **4**, 297-300.

Beal E. J., House C. H. and Orphan V. J. (2009) Manganese- and iron-dependent marine methane oxidation. *Science* **325**, 184-187.

Beulig F., Røy H., McGlynn S. E. and Jørgensen B. B. (2018) Cryptic CH4 cycling in the sulfate-methane transition of marine sediments apparently mediated by ANME-1 archaea. *The ISME journal*, https://doi.org/10.1038/s41396-41018-40273-z.

Bhattacharya S., Mapder T., Fernandes S., Roy C., Sarkar J., Rameez M. J., Mandal S., Sar A., Chakraborty A. K. and Mondal N. (2021) Sedimentation rate and organic matter dynamics shape microbiomes across a continental margin. *Biogeosciences* **18**, 5203-5222.

Boetius A., Ravenschlag K., Schubert C. J., Rickert D., Widdel F., Giesecke A., Amann R., Jørgensen B. B., Witte U. and Pfannkuche O. (2000) A marine microbial consortium apparently mediating anaerobic oxidation of methane. *Nature* **407**, 623-626.

Boles J. R., Eichhubl P., Garven G. and Chen J. (2004) Evolution of a hydrocarbon migration pathway along basin-bounding faults: Evidence from fault cement. *AAPG bulletin* **88**, 947-970.

Cadena S., García-Maldonado J. Q., López-Lozano N. E. and Cervantes F. J. (2018) Methanogenic and sulfate-reducing activities in a hypersaline microbial mat and associated microbial diversity. *Microbial ecology* **75**, 930-940.

Capone D. G., Bronk D. A., Mulholland M. R. and Carpenter E. J. (2008) *Nitrogen in the marine environment*. Elsevier.

Chistoserdova L. (2015) Methylotrophs in natural habitats: current insights through metagenomics. *Applied microbiology and biotechnology* **99**, 5763-5779.

Chronopoulou P.-M., Shelley F., Pritchard W. J., Maanoja S. T. and Trimmer M. (2017) Origin and fate of methane in the Eastern Tropical North Pacific oxygen minimum zone. *The ISME journal* **11**, 1386-1399.

Conrad R. (2020) Importance of hydrogenotrophic, aceticlastic and methylotrophic methanogenesis for methane production in terrestrial, aquatic and other anoxic environments: a mini review. *Pedosphere* **30**, 25-39.

Dale A. W., Van Cappellen P., Aguilera D. and Regnier P. (2008a) Methane efflux from marine sediments in passive and active margins: Estimations from bioenergetic reaction– transport simulations. *Earth and Planetary Science Letters* **265**, 329-344.

Dale A. W., Regnier P., Knab N. J., Jørgensen B. B. and Van Cappellen P. (2008b) Anaerobic oxidation of methane (AOM) in marine sediments from the Skagerrak (Denmark): II. Reaction-transport modeling. *Geochim. Cosmochim. Acta* **72**, 2880-2894.

Dale A. W., Sommer S., Lomnitz U., Montes I., Treude T., Liebetrau V., Gier J., Hensen C., Dengler M., Stolpovsky K., Bryant L. D. and Wallmann K. (2015) Organic carbon production, mineralisation and preservation on the Peruvian margin. *Biogeosciences* **12**, 1537-1559.

De Anda V., Chen L.-X., Dombrowski N., Hua Z.-S., Jiang H.-C., Banfield J. F., Li W.-J. and Baker B. J. (2021) Brockarchaeota, a novel archaeal phylum with unique and versatile carbon cycling pathways. *Nature communications* **12**, 1-12.

Farag I. F., Zhao R. and Biddle J. F. (2021) "Sifarchaeota," a Novel Asgard Phylum from Costa Rican Sediment Capable of Polysaccharide Degradation and Anaerobic Methylotrophy. *Applied and environmental microbiology* **87**, e02584-02520.

Ferdelman T. G., Lee C., Pantoja S., Harder J., Bebout B. M. and Fossing H. (1997) Sulfate reduction and methanogenesis in a Thioploca-dominated sediment off the coast of Chile. *Geochimica et Cosmochimica Acta* **61**, 3065-3079.

Fernandes S., Mandal S., Sivan K., Peketi A. and Mazumdar A. (2022) Biogeochemistry of Marine Oxygen Minimum Zones with Special Emphasis on the Northern Indian Ocean. *Systems Biogeochemistry of Major Marine Biomes*, 1-25.

Fischer P. Q., Sánchez-Andrea I., Stams A. J., Villanueva L. and Sousa D. Z. (2021) Anaerobic microbial methanol conversion in marine sediments. *Environmental microbiology* **23**, 1348-1362.

Gibb S. W., Mantoura R. F. C., Liss P. S. and Barlow R. G. (1999) Distributions and biogeochemistries of methylamines and ammonium in the Arabian Sea. *Deep Sea Research Part II: Topical Studies in Oceanography* **46**, 593-615.

Hanson R. S. and Hanson T. E. (1996) Methanotrophic bacteria. *Microbiol. Rev.* **60**, 439-471.

Helly J. J. and Levin L. A. (2004) Global distribution of naturally occurring marine hypoxia on continental margins. *Deep Sea Research Part I: Oceanographic Research Papers* **51**, 1159-1168.

Hinrichs K.-U. and Boetius A. (2002) The anaerobic oxidation of methane: new insights in microbial ecology and biogeochemistry. In *Ocean Margin Systems* (eds. G. Wefer, D. Billett, D. Hebbeln, B. B. Jørgensen, M. Schlüter and T. Van Weering). Springer-Verlag, Berlin. pp. 457-477.

Hornafius J. S., Quigley D. and Luyendyk B. P. (1999) The world's most spectacular marine hydrocarbon seeps (Coal Oil Point, Santa Barbara Channel, California): Quantification of emissions. *Journal of Geophysical Research: Oceans* **104**, 20703-20711.

Jickells T., An Z., Andersen K. K., Baker A., Bergametti G., Brooks N., Cao J., Boyd P., Duce R. and Hunter K. (2005) Global iron connections between desert dust, ocean biogeochemistry, and climate. *science* **308**, 67-71.

Joye S. B., Boetius A., Orcutt B. N., Montoya J. P., Schulz H. N., Erickson M. J. and Logo S. K. (2004) The anaerobic oxidation of methane and sulfate reduction in sediments from Gulf of Mexico cold seeps. *Chem. Geol.* **205**, 219-238.

Jørgensen B. B. (1978) A comparison of methods for the quantification of bacterial sulphate reduction in coastal marine sediments: I. Measurements with radiotracer techniques. *Geomicrobiol. J.* **1**, 11-27.

Jørgensen B. B. (2000) Bacteria and marine biogeochemistry. In *Marine biogeochemistry* (eds. H. D. Schulz and M. Zabel). Springer Verlag, Berlin. pp. 173-201.

Kallmeyer J., Ferdelman T. G., Weber A., Fossing H. and Jørgensen B. B. (2004) A cold chromium distillation procedure for radiolabeled sulfide applied to sulfate reduction measurements. *Limnol. Oceanogr. Methods* **2**, 171-180.

King G., Klug M. J. and Lovley D. R. (1983) Metabolism of acetate, methanol, and methylated amines in intertidal sediments of Lowes Cove, Maine. **45**, 1848-1853.

Kivenson V., Paul B. G. and Valentine D. L. (2021) An ecological basis for dual genetic code expansion in marine deltaproteobacteria. *Frontiers in microbiology*, 1545.

Knittel K. and Boetius A. (2009) Anaerobic oxidation of methane: progress with an unknown process. *Annu. Rev. Microbiol.* **63**, 311-334.

Krause S. J. and Treude T. (2021) Deciphering cryptic methane cycling: Coupling of methylotrophic methanogenesis and anaerobic oxidation of methane in hypersaline coastal wetland sediment. *Geochimica et Cosmochimica Acta* **302**, 160-174.

Kristjansson J. K., Schönheit P. and Thauer R. K. (1982) Different Ks values for hydrogen of methanogenic bacteria and sulfate reducing bacteria: an explanation for the apparent inhibition of methanogenesis by sulfate. *Arch. Microbiol.* **131**, 278-282.

Krüger M., Treude T., Wolters H., Nauhaus K. and Boetius A. (2005) Microbial methane turnover in different marine habitats. *Palaeogeography, Paleoclimatology, Palaeoecology* **227**, 6-17.

Lee C. and Olson B. L. (1984) Dissolved, exchangeable and bound aliphatic amines in marine sediments: initial results. *Organic Geochemistry* **6**, 259-263.

Leifer I., Kamerling M. J., Luyendyk B. P. and Wilson D. S. (2010) Geologic control of natural marine hydrocarbon seep emissions, Coal Oil Point seep field, California. *Geo-Marine Letters* **30**, 331-338.

Levin L. (2003) Oxygen minimum zone benthos: Adaptation and community response to hypoxia. *Oceanogr. Mar. Biol. Ann. Rev.* **41**, 1-45.

Levin L. A. E., W., Gooday A. J., Jorissen F., Middelburg J. J., Naqvi S. W. A., Neira C. and Rabalais N. N. Z., J. (2009) Effects of natural and human-induced hypoxia on coastal benthos. *Biogeosciences* **6**, 2063–2098.

Li H., Yang Q. and Zhou H. (2020) Niche differentiation of sulfate-and iron-dependent anaerobic methane oxidation and methylotrophic methanogenesis in deep sea methane seeps. *Frontiers in microbiology* **11**, 1409.

Lovley D. R. and Klug M. J. (1986) Model for the distribution of sulfate reduction and methanogenesis in freshwater sediments. *Geochim. Cosmochim. Acta* **50**, 11-18.

Lovley D. R. and Phillips E. J. (1987) Competitive mechanisms for inhibition of sulfate reduction and methane production in the zone of ferric iron reduction in sediments. *Applied and Environmental Microbiology* **53**, 2636-2641.

Lyu Z., Shao N., Akinyemi T. and Whitman W. B. (2018) Methanogenesis. *Current Biology* **28**, R727-R732.

Maltby J., Sommer S., Dale A. W. and Treude T. (2016) Microbial methanogenesis in the sulfate-reducing zone of surface sediments traversing the Peruvian margin. *Biogeosciences* **13**, 283–299.

Maltby J., Steinle L., Löscher C. R., Bange H. W., Fischer M. A., Schmidt M. and Treude T. (2018) Microbial methanogenesis in the sulfate-reducing zone of sediments in the Eckernförde Bay, SW Baltic Sea. *Biogeosciences* **15**, 137– 157.

Martineau C., Mauffrey F. and Villemur R. (2015) Comparative analysis of denitrifying activities of Hyphomicrobium nitrativorans, Hyphomicrobium denitrificans, and Hyphomicrobium zavarzinii. *Appl. Environ. Microbiol.* **81**, 5003-5014.

Mausz M. A. and Chen Y. (2019) Microbiology and ecology of methylated amine metabolism in marine ecosystems. *Current Issues in Molecular Biology* **33**, 133-148.

Michaelis W., Seifert R., Nauhaus K., Treude T., Thiel V., Blumenberg M., Knittel K., Gieseke A., Peterknecht K., Pape T., Boetius A., Aman A., Jørgensen B. B., Widdel F., Peckmann J., Pimenov N. V. and Gulin M. (2002) Microbial reefs in the Black Sea fueled by anaerobic oxidation of methane. *Science* **297**, 1013-1015.

Moretti I. (1998) The role of faults in hydrocarbon migration. *Petroleum Geoscience* **4**, 81-94.

Nauhaus K., Albrecht M., Elvert M., Boetius A. and Widdel F. (2007) In vitro cell growth of marine archaeal-bacterial consortia during anaerobic oxidation of methane with sulfate. *Environ. Microbiol.* **9**, 187-196.

Oremland R. S. and Taylor B. F. (1978) Sulfate reduction and methanogenesis in marine sediments. *Geochimica et Cosmochimica Acta* **42**, 209-214.

Oremland R. S. and Polcin S. (1982) Methanogenesis and sulfate reduction: competitive and noncompetitive substrates in estuarine sediments. *Appl. Environ. Microbiol.* **44**, 1270-1276.

Oremland R. S., Marsh L. M. and Polcin S. (1982) Methane production and simultaneous sulphate reduction in anoxic, salt marsh sediments. *Nature* **296**, 143-145.

148

Oren A. (1990) Formation and breakdown of glycine betaine and trimethylamine in hypersaline environments. *Antonie van Leeuwenhoek* **58**, 291-298.

Orphan V. J., Hinrichs K.-U., Ussler III W., Paull C. K., Tayleor L. T., Sylva S. P., Hayes J. M. and DeLong E. F. (2001) Comparative analysis of methane-oxidizing archaea and sulfate-reducing bacteria in anoxic marine sediments. *Appl. Environ. Microbiol.* **67**, 1922-1934.

Pack M. A., Heintz M. B., Reeburgh W. S., Trumbore S. E., Valentine D. L., Xu X. and Druffel E. R. (2015) Methane oxidation in the eastern tropical North Pacific Ocean water column. *Journal of Geophysical Research: Biogeosciences* **120**, 1078-1092.

Postma D. and Jakobsen R. (1996) Redox zonation: equilibrium constraints on the Fe (III)/SO4-reduction interface. *Geochimica et Cosmochimica Acta* **60**, 3169-3175.

Probabilities W. G. o. C. E. (1995) Seismic hazards in southern California: probable earthquakes, 1994 to 2024. *Bulletin of the Seismological Society of America* **85**, 379-439.

Qin Q., Kinnaman F. S., Gosselin K. M., Liu N., Treude T., Valentine D. L. (2022) *Seasonality of water column methane oxidation and deoxygenation in a dynamic marine environment* Unpublished

Rabalais N. N., Turner R. E., Díaz R. J. and Justić D. (2009) Global change and eutrophication of coastal waters. *ICES Journal of Marine Science* **66**, 1528-1537.

Ragsdale S. W. and Pierce E. (2008) Acetogenesis and the Wood–Ljungdahl pathway of CO2 fixation. *Biochimica et Biophysica Acta (BBA)-Proteins and Proteomics* **1784**, 1873-1898.

Reeburgh W. S. (2007) Oceanic methane biogeochemistry. *Chem. Rev.* **107**, 486-513.

Reimers C. E., Ruttenberg K. C., Canfield D. E., Christiansen M. B. and Martin J. B. (1996) Porewater pH and authigenic phases formed in the uppermost sediments of Santa Barbara Basin. *Geochim. Cosmochim. Acta* **60**, 4037-4057.

Rullkötter J. (2006) Organic matter: the driving force for early diagenesis. In *Marine geochemistry*. Springer. pp. 125-168.

Schimmelmann A. and Kastner M. (1993) Evolutionary changes over the last 1000 years of reduced sulfur phases and organic carbon in varved sediments of the Santa Barbara Basin, California. *Geochimica et Cosmochimica Acta* **57**, 67-78.

Seidel L., Broman E., Turner S., Ståhle M. and Dopson M. (2021) Interplay between eutrophication and climate warming on bacterial communities in coastal sediments differs depending on water depth and oxygen history. *Scientific reports* **11**, 1-12.

Sholkovitz E. (1973) Interstitial water chemistry of the Santa Barbara Basin sediments. *Geochimica et Cosmochimica Acta* **37**, 2043-2073.

Smeraglia L., Fabbi S., Billi A., Carminati E. and Cavinato G. P. (2022) How hydrocarbons move along faults: Evidence from microstructural observations of hydrocarbon-bearing carbonate fault rocks. *Earth and Planetary Science Letters* **584**, 117454.

Sousa D. Z., Visser M., Van Gelder A. H., Boeren S., Pieterse M. M., Pinkse M. W., Verhaert P. D., Vogt C., Franke S. and Kümmel S. (2018) The deep-subsurface sulfate reducer Desulfotomaculum kuznetsovii employs two methanol-degrading pathways. *Nature communications* **9**, 1-9.

Soutar A. and Crill P. A. (1977) Sedimentation and climatic patterns in the Santa Barbara Basin during the 19th and 20th centuries. *Geological Society of America Bulletin* **88**, 1161-1172.

Steinle L., Maltby J., Treude T., Kock A., Bange H. W., Engbersen N., Zopfi J., Lehmann M. F. and Niemann H. (2017) Effects of low oxygen concentrations on aerobic methane oxidation in seasonally hypoxic coastal waters. *Biogeosciences* **14**, 1631-1645.

Stephenson M. and Stickland L. H. (1933) CCVII. Hydrogenase. III. The bacterial formation of methane by the reduction of one-carbon compounds by molecular hydrogen. *Biochem. J.* **27**, 1517–1527.

Stramma L., Schmidtko S., Levin L. A. and Johnson G. C. (2010) Ocean oxygen minima expansions and their biological impacts. *Deep-Sea Research I* **57**, 587-595.

Taubert M., Grob C., Howat A. M., Burns O. J., Pratscher J., Jehmlich N., von Bergen M., Richnow H. H., Chen Y. and Murrell J. C. (2017) Methylamine as a nitrogen source for microorganisms from a coastal marine environment. *Environmental microbiology* **19**, 2246-2257.

Thauer R. K. (1998) Biochemistry of methanogenesis: a tribute to Marjory Stephenson. *Microbiology* **144**, 2377-2406.

Treude T., Krüger M., Boetius A. and Jørgensen B. B. (2005a) Environmental control on anaerobic oxidation of methane in the gassy sediments of Eckernförde Bay (German Baltic). *Limnol. Oceanogr.* **50**, 1771-1786.

Treude T., Niggemann J., Kallmeyer J., Wintersteller P., Schubert C. J., Boetius A. and Jørgensen B. B. (2005b) Anaerobic oxidation of methane in the sulfate-methane transition along the Chilean continental margin. *Geochim. Cosmochim. Acta* **69**, 2767-2779.

Valentine D. L., Fisher G. B., Pizarro O., Kaiser C. L., Yoerger D., Breier J. A. and Tarn J. (2016) Autonomous marine robotic technology reveals an expansive benthic bacterial

community relevant to regional nitrogen biogeochemistry. *Environmental Science & Technology* **50**, 11057-11065.

Vigderovich H., Eckert W., Elul M., Rubin-Blum M., Elvert M. and Sivan O. (2022) Long-term incubations provide insight into the mechanisms of anaerobic oxidation of methane in methanogenic lake sediments. *Biogeosciences* **19**, 2313-2331.

Wang X.-c. and Lee C. (1990) The distribution and adsorption behavior of aliphatic amines in marine and lacustrine sediments. *Geochimica et Cosmochimica Acta* **54**, 2759-2774.

Wang X.-C. and Lee C. (1993) Adsorption and desorption of aliphatic amines, amino acids and acetate by clay minerals and marine sediments. *Marine Chemistry* **44**, 1-23.

Wang X.-C. and Lee C. (1994) Sources and distribution of aliphatic amines in salt marsh sediment. *Organic Geochemistry* **22**, 1005-1021.

Warford A. L., Kosiur D. R. and Doose P. R. (1979) Methane production in Santa Barbara basin sediments. *Geomicrobiology Journal* **1**, 117-137.

Wehrmann L. M., Risgaard-Petersen N., Schrum H. N., Walsh E. A., Huh Y., Ikehara M., Pierre C., D'Hondt S., Ferdelman T. G. and Ravelo A. C. (2011) Coupled organic and inorganic carbon cycling in the deep subseafloor sediment of the northeastern Bering Sea Slope (IODP Exp. 323). *Chemical Geology* **284**, 251-261.

Wilfert P., Krause S., Liebetrau V., Schönfeld J., Haeckel M., Linke P. and Treude T. (2015) Response of anaerobic methanotrophs and benthic foraminifera to 20 years of methane emission from a gas blowout in the North Sea. *Marine and Petroleum Geology* **68**, 731-742.

Winfrey M. R. and Ward D. M. (1983) Substrates for sulfate reduction and methane p roduction in i ntertidal sediments. *Appl. Environm. Microbiol* **45**, 193-199.

Wright J. J., Konwar K. M. and Hallam S. J. (2012) Microbial ecology of expanding oxygen minimum zones. *Nature Reviews Microbiology* **10**, 381-394.

Wyrtki K. The oxygen minima in relation to ocean circulation. *Deep Sea Research and Oceanographic Abstracts*. Elsevier.

Xiao K., Beulig F., Kjeldsen K., Jorgensen B. and Risgaard-Petersen N. (2017) Concurrent Methane Production and Oxidation in Surface Sediment from Aarhus Bay, Denmark. *Frontiers in Microbiology* **8**.

Xiao K., Beulig F., Roy H., Jorgensen B. and Risgaard-Petersen N. (2018) Methylotrophic methanogenesis fuels cryptic methane cycling in marine surface sediment. *Limnology and Oceanography* **63**, 1519-1527.

Xiao K.-Q. and Peacock C. (2019) The Role of Minerals in Cryptic Methane Cycling in Marine Surface Sediment.

Xiao K.-Q., Moore O. W., Babakhani P., Curti L. and Peacock C. L. (2022) Mineralogical control on methylotrophic methanogenesis and implications for cryptic methane cycling in marine surface sediment. *Nature Communications* **13**, 1-9.

Zhuang G.-C., Montgomery A. and Joye S. B. (2019a) Heterotrophic metabolism of C1 and C2 low molecular weight compounds in northern Gulf of Mexico sediments: Controlling factors and implications for organic carbon degradation. *Geochimica et Cosmochimica Acta* **247**, 243-260.

Zhuang G.-C., Elling F. J., Nigro L. M., Samarkin V., Joye S. B., Teske A. and Hinrichs K.-U. (2016) Multiple evidence for methylotrophic methanogenesis as the dominant methanogenic pathway in hypersaline sediments from the Orca Basin, Gulf of Mexico. *Geochim. Cosmochim. Acta* **187**, 1-20.

Zhuang G.-C., Lin Y.-S., Bowles M. W., Heuer V. B., Lever M. A., Elvert M. and Hinrichs K.-U. (2017) Distribution and isotopic composition of trimethylamine, dimethylsulfide and dimethylsulfoniopropionate in marine sediments. *Mar. Chem.* **196**, 35-46.

Zhuang G.-C., Heuer V. B., Lazar C. S., Goldhammer T., Wendt J., Samarkin V. A., Elvert M., Teske A. P., Joye S. B. and Hinrichs K.-U. (2018) Relative importance of methylotrophic methanogenesis in sediments of the Western Mediterranean Sea. *Geochim. Cosmochim. Acta* **224**.

Zhuang G. C., Xu L., Liang Q., Fan X., Xia Z., Joye S. B. and Wang F. (2019b) Biogeochemistry, microbial activity, and diversity in surface and subsurface deep-sea sediments of South China Sea. *Limnology and Oceanography* **64**, 2252-2270.

Chapter 4

$\Delta^{13}CH_3D$ and $\Delta^{12}CH_2D_2$ signatures of methane aerobically oxidized by *Methylosinus trichosporium* with implications for deciphering the provenance of methane gases

Sebastian J. E. Krause[1*], Jiarui Liu[1], Edward D. Young[1], Tina Treude[1,2*]

[1]Department of Earth, Planetary and Space Sciences, University of California, Los Angeles, Los Angeles CA 90095, USA

[2]Department of Atmospheric and Oceanic Sciences, University of California, Los Angeles, Los Angeles CA 90095, USA

* Corresponding author, E-mail address: sjkrause@g.ucla.edu and ttreude@g.ucla.edu

Abstract

Aerobic oxidation of methane (MOx) is an important biologically mediated process that consumes methane in a wide range of environments. Here we report results of culture experiments with the aerobic methane-oxidizing bacterium *Methylosinus trichosporium* (OB3b) that are used to characterize the mass-18 istopologue ($\Delta^{13}CH_3D$ and $\Delta^{12}CH_2D_2$) signatures of MOx in residual methane gases. MOx activity was confirmed by simultaneous decrease of methane and oxygen in the bulk gas headspace. Bulk carbon ($^{13}C/^{12}C$) and hydrogen (D/H) isotope ratios of the methane gas increased while both $\Delta^{13}CH_3D$ and $\Delta^{12}CH_2D_2$ decreased as the oxidation proceeded. The corresponding fractionation factors (α) calculated from our experimental results are 0.98485 ± 0.00006 for $^{13}C/^{12}C$, 0.7265 ± 0.0010 for D/H, 0.7141 ± 0.0011 for $^{13}CH_3D/^{12}CH_4$, and 0.4757 ± 0.0023 for $^{12}CH_2D_2/^{12}CH_4$. Deviations of the mass-18 fractionation factors from the Rule of the Geometric Mean (RGM) expressed as γ values are 0.9981 ± 0.0017 for $^{13}CH_3D/^{12}CH_4$ and 0.9013 ± 0.0045 for $^{12}CH_2D_2/^{12}CH_4$. Our α and γ values suggest that while MOx fractionates $^{13}CH_3D$ within error of the RGM, the $\Delta^{13}CH_3D$ and $\Delta^{12}CH_2D_2$ trajectories are very sensitive to even small deviations in $^{13}CH_3D/^{12}CH_4$ from the RGM. Fractionation of $^{12}CH_2D_2$ deviates considerably from RGM, and this causes dramatic and robust effects on the trajectories of residual methane in $\Delta^{13}CH_3D$ vs. $\Delta^{12}CH_2D_2$ space. Our models suggest that $\Delta^{13}CH_3D$ and $\Delta^{12}CH_2D_2$ could potentially mimic microbial methanogenesis signatures in an environment that exhibits a strong Rayleigh Distillation process with little to no replenishment of methane during oxidation. However, in closed or open systems where oxidation is attended by simultaneous methane production, we find that modest increases in $\Delta^{13}CH_3D$ and dramatic increases in $\Delta^{12}CH_2D_2$ are to be expected, thus resulting in isotopologue signatures distinct from

microbial methanogenesis. The overall trend in these conditions suggest that methane altered by

MOx is distinguishable from other methane sources in $\Delta^{13}CH_3D$ and $\Delta^{12}CH_2D_2$ space.

1. Introduction

Understanding the sources and sinks of methane gas has relevance for many research areas. Methane is an important energy source (Demirbas, 2006), a promising extraterrestrial biosignature (Bouquet et al., 2015; Yung et al., 2018), and a potent greenhouse gas with increasing atmospheric concentrations (Saunois et al., 2016).

Methane sources are either microbial, thermogenic, or abiotic. Microbial methane is produced anaerobically from organic matter by archaea (Whiticar, 1999), aerobically from methylphosphonate by cyanobacteria (Karl et al., 2008), and by groups of fungi (Lenhart et al., 2012). Thermogenic methane is derived from thermal cracking of organic matter (Schoell, 1980), and references therein). Abiotic methane is formed through water-rock interactions (Etiope and Sherwood Lollar, 2013; Etiope and Schoell, 2014).

In the atmosphere, methane is oxidized to CO_2 by hydroxyl radicals (90%) (Reeburgh, 2007). Before emission into the atmosphere, methane can be consumed by microbial aerobic (MOx) or anaerobic oxidation of methane (AOM). MOx, the focus of this study, consumes methane with oxygen according to:

$$CH_4 + 2O_2 \rightarrow CO_2 + 2H_2O. \qquad (1)$$
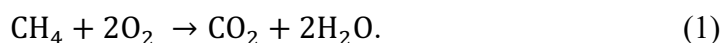
MOx is an important methane sink in a wide range of environments, including soils (Henckel et al., 2000), freshwater lakes (Guggenheim et al., 2020), and oceanic waters overlying cold seeps (Boetius and Wenzhöfer, 2013; Steinle et al., 2015; Valentine et al., 2001). It is mediated by different groups of aerobic methane-oxidizing bacteria, which use methane as their carbon source (Hanson and Hanson, 1996; Murrell, 2010).

Isotope ratios of carbon ($^{13}C/^{12}C$) and hydrogen (D/H) have been used to distinguish methane source pathways (Etiope and Sherwood Lollar, 2013; Schoell, 1988; Whiticar, 1999;

Whiticar, 2020), as well as sink mechanisms (Barker and Fritz, 1981; Coleman et al., 1981; Whiticar, 1999; Whiticar, 2020). Microbially-produced methane is strongly depleted in the heavy carbon and hydrogen isotopes (Claypool and Kaplan, 1974; Rayleigh, 1896; Whiticar, 2020). By virtue of the same principles, methane oxidation preferentially consumes the isotopically lighter methane, leaving behind the isotopically heavier methane in the residual pool. This heavy isotope signature of oxidation has been demonstrated in environmental (Barker and Fritz, 1981; Coleman et al., 1981) and pure culture studies with aerobic methane-oxidizing bacteria (Feisthauer et al., 2011; Templeton et al., 2006; Wang et al., 2016). While carbon and hydrogen isotopes have proved useful for unraveling the formation and subsequent processing of methane gases, substantial overlap in the bulk isotope signatures has led to ambiguity surrounding methane sources and sinks (Whiticar, 1999; Whiticar, 2020).

Recent technological advancements enabled application of two mass-18 doubly-substituted isotopologues of methane, $^{13}CH_3D$ (Ono et al., 2014) and $^{12}CH_2D_2$ measured separately (Young et al., 2017; Young et al., 2016) or together ($^{13}CH_3D + ^{12}CH_2D_2$) (Stolper et al., 2014), to help resolve some of these ambiguities arising from the use of bulk isotope ratios alone. The potential utility of these rare isotopologues as tracers of methane formation and destruction is evidenced in a recent study of methane in serpentinites of the Samail Ophiolite in Oman (Nothaft et al., 2021). In the study, bulk isotope ratios ($\delta^{13}C$ and δD) suggest that some methane is abiotic in origin, while mass-18 isotopologue measurements indicate that it is microbial (Nothaft et al., 2021; Young et al., 2019). However, this conclusion is tempered by the need to understand more thoroughly the effects of oxidation on rare isotopologue abundances.

Multiply-substituted isotopologues have been used as intramolecular geothermometers to determine CH_4 formation temperatures, because their abundances are dependent on temperature.

This dependence is well known on the basis of theory (Liu and Liu, 2016; Webb and Miller III, 2014) and has been validated by measurements (Ono et al., 2014; Wang et al., 2020; Young et al., 2017) . The temperature dependence is expressed in the form of the exchange reactions between isotopologues, yielding the two doubly-substituted isotopologues by the reactions

$$^{13}CH_4 + {}^{12}CH_3D \leftrightarrow {}^{12}CH_4 + {}^{13}CH_3D \tag{2}$$

and

$$2\,{}^{12}CH_3D \leftrightarrow {}^{12}CH_2D_2 + {}^{12}CH_4. \tag{3}$$
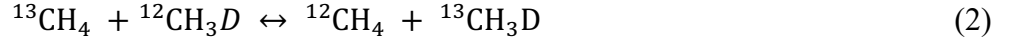
The equilibrium constants for these exchange reactions in the limit of high temperature are (e.g., (Young et al., 2017)

$$k_{Eq,{}^{13}CH_3D} = \frac{4X({}^{13}C)(X(H))^3 X(D) X({}^{12}C)(X(H))^4}{4X({}^{12}C)(X(H))^3 X(D) X({}^{13}C)(X(H))^4} = 1 \tag{4}$$

and

$$k_{Eq,{}^{12}CH_2D_2} = \frac{6X({}^{12}C)(X(H))^2 X(D)^2 (X(H))^4}{\left[4X({}^{12}C)(X(H))^3 X(D)\right]^2} = \frac{3}{8}, \tag{5}$$

where X(*i*) are the atomic fractions of the indicated isotopes *i* comprising the methane isotopologues (e.g., $X({}^{13}C) = {}^{13}C/({}^{12}C+{}^{13}C)$ and $X(D) = D/(H+D)$, etc.) and the factor of 3/8 is a reflection of the different symmetry numbers of the isotopologues in reaction 3. As temperatures decrease, the lower energies of the intramolecular bonds involving the heavier isotopes become more important, resulting in higher relative abundances of the clumped species and departures from this purely statistical distribution of isotopes. The deviations in the relative abundances of the rare, mass-18 isotopologues relative to the high-temperature limit are expressed using the notation

$$\Delta_{{}^{13}CH_3D} = 10^3 \left(\frac{X({}^{13}CH_3D)}{X({}^{13}CH_3D)_{stochastic}} - 1\right) \tag{6}$$

and,

$$\Delta_{^{12}CH_2D_2} = 10^3 \left(\frac{X(^{12}CH_2D_2)}{X(^{12}CH_2D_2)_{stochastic}} - 1 \right), \tag{7}$$

where $X(^{13}CH_3D)$ represents the molecular fraction of $^{13}CH_3D$ in the methane gas, and so forth, and where stochastic abundances are obtained by treating the relative concentrations of the isotopic species as probabilities, as in Equations (4) and (5), yielding

$$x(^{13}CH_3D)_{stochastic} = 4x(^{13}C)x(D)x(H)^3 \tag{8}$$

and

$$x(^{12}CH_2D_2)_{stochastic} = 6x(^{12}C)x(H)^2x(D)^2. \tag{9}$$

The relationship between $\Delta^{13}CH_3D$, $\Delta^{12}CH_2D_2$, and temperature (Liu and Liu, 2016; Ma et al., 2008; Webb and Miller III, 2014) provides a useful reference curve in $\Delta^{13}CH_3D$ vs. $\Delta^{12}CH_2D_2$ space that depicts thermodynamic equilibrium (Young et al., 2017). Sample measurements plotted on the equilibrium curve are evidently in thermodynamic equilibrium. However, most methane gas samples lie off the curve, with isotopologue abundances reflecting kinetic effects (Ash et al., 2019; Giunta et al., 2021; Giunta et al., 2019; Labidi et al., 2020; Young et al., 2019; Young et al., 2017). The $\Delta^{13}CH_3D$ and $\Delta^{12}CH_2D_2$ values for methane produced by the microbial methanogenesis incubations should be largely independent of substrate effects and are distinctive, with $\Delta^{13}CH_3D \sim +2.5$ to $-4.0‰$ and $\Delta^{12}CH_2D_2 \sim -20$ to $-45‰$, respectively. These negative values have been attributed to either a "combinatorial" effect in the case of $\Delta^{12}CH_2D_2$ (Taenzer et al., 2020) or classical and/or quantum kinetic effects that could affect both values (Young et al., 2017).

Here, we are concerned with the effects of aerobic oxidation of methane on $\Delta^{13}CH_3D$ and $\Delta^{12}CH_2D_2$ values in methane gases and how these effects might be observable in natural settings. Recognition of the effects of oxidation may be critical to using $\Delta^{13}CH_3D$ and $\Delta^{12}CH_2D_2$ values as

tracers of the provenance of methane gases.

   Methylosinus trichosporium (OB3b) is a obligate aerobic methanotrophic bacterium belonging to the alpha proteobacteria class that oxidize methane to CO_2 according to Equation 1 (Hanson and Hanson, 1996). It is one of few aerobic methanotrophs with both soluble and particulate methane monooxygenase, which are the main enzymes that facilitate the oxidation of methane (Hanson and Hanson, 1996; Murrell, 2010). *M. trichosporium* is one of the best characterized aerobic methanotrophic bacterium and an excellent candidate for isotope studies because it has been studied in a wide variety of environments and in pure cultures (Murrell, 2010). However, methane isotopologue signatures of *M. trichosporium* consuming methane sources are non-existent.

2. Previous Work

Wang et al. (2016), the only other study on the effect of MOx on methane isotopologue signatures we are aware of, investigated pure cultures of *Methylococcus capsulatus* (Bath), in liquid medium, at two temperatures in the presence of methane and oxygen. The abundances of head-space methane isotopologues, including $^{12}CH_4$, $^{13}CH_4$, $^{12}CH_3D$ and $^{13}CH_3D$ were measured over time while methane was consumed with oxygen. Methane carbon ($^{13}C/^{12}C$) and hydrogen (D/H) isotope ratios became progressively higher with time, consistent with a classical kinetic isotope effect, in which isotopically light methane was preferentially oxidized by the aerobic methane-oxidizing bacteria. The $\Delta^{13}CH_3D$ signatures became progressively lower in both temperature incubations, a trend that is also consistent with classical kinetic effects. These measurements allowed Wang et al. to calculate fractionation factors (α) for $^{13}CH_4$, $^{12}CH_3D$ and $^{13}CH_3D$ relative to $^{12}CH_4$, where the fractionation factors are defined as, for example, α_{13CH3D} =$(^{13}CH_3D/^{12}CH_4)/(^{13}CH_3D/^{12}CH_4)_o$ where the subscript zero signifies the ratio prior to reaction. The study introduced the gamma factor (γ) to describe deviations from the Rule of the Geometric Mean, or RGM (Bigeleisen, 1955). The RGM articulates the zero-order expectation that the fractionation factor for a multiply-substituted isotopologue will be approximately equal to the product of the fractionation factors for the constituent singly-substituted species. For example, one might predict that the fractionation factor for $^{13}CH_3D/^{12}CH_4$ would be the product of the fractionation factor for $^{13}CH_4/^{12}CH_4$ and that for $^{12}CH_3D/^{12}CH_4$, i.e., $\alpha_{13CH3D} = \alpha_{13CH4} \, \alpha_{12CH3D}$. By defining the γ parameters as the ratio of observed α to the α predicted by the RGM (Equations 10 and 11), the deviations from this simple expectation are quantified; if γ is equal to 1 then the mass-18 isotopologue fractionation is ideal in that it follows the expectations from the RGM:

$$^{13D}\gamma = \frac{^{13D}\alpha}{^{13}\alpha \cdot {}^{D}\alpha} \tag{10}$$

163

$$^{D2}\gamma = \frac{^{D2}\alpha}{^{D}\alpha \cdot ^{D}\alpha} \tag{11}$$

Deviations from the RGM imply complexities involving the isotopes of interest due to the "clumping" of the heavy isotopes on bonds. Wang et al. applied their γ's and α's to a simple open system model attributed to Hayes (2001b), which depicts a flow system where methane flows through the system as it is removed by oxidation. Steady state in this case is achieved because of a constant flux into the system, a constant reaction rate, and a constant flux out of the system.

Using this simple calculation, the authors demonstrated that the degree, and even the sign, of fractionation of $\Delta^{13}CH_3D$ is critically sensitive to γ, with deviations from unity by a factor ±0.002 resulting in differences in $\Delta^{13}CH_3D$ of several per mil with progressive oxidation. Although Wang et al. (2016) was the first study to obtain $\Delta^{13}CH_3D$ signatures from MOx, the α and γ factor for the $\Delta^{12}CH_2D_2$ were not obtained.

Haghnegahdar et al. (2017) used ab initio calculations to calculate fractionation factors for $\Delta^{13}CH_3D$ and $\Delta^{12}CH_2D_2$ associated with abiotic oxidation of methane by hydroxyl and chlorine radicals in the atmosphere. They found that at steady state, atmospheric CH_4 should have exceptionally high $\Delta^{12}CH_2D_2$ values of order +100 ‰ relative to the sources because of relatively low γ values for this species. They concluded that $\Delta^{12}CH_2D_2$ values may prove to be sensitive tracers of methane sources and sinks in the atmosphere (Haghnegahdar et al., 2017). Such strikingly positive $\Delta^{12}CH_2D_2$ values that contrast with expectations from simple kinetics, and result from deviations in γ values from unity, underscore the need to characterize the effects of oxidation on $\Delta^{13}CH_3D$ and $\Delta^{12}CH_2D_2$. Ab initio calculations for microbially-mediated oxidation are challenging. However, laboratory experiments provide a more direct means of assessing these effects.

In the present study we use pure cultures of *Methylosinus trichosporium* (OB3b) to characterize the isotopologue effects of methane consumption during MOx. Our goals are four-fold: 1) observe the $\Delta^{13}CH_3D$ and $\Delta^{12}CH_2D_2$ signatures from MOx in closed system pure culture experiments; 2) calculate α's and the γ's that affect $\Delta^{13}CH_3D$ and $\Delta^{12}CH_2D_2$ values due to MOx operating in closed systems; 3) apply the derived α's and γ's to determine the trajectories of oxidation in $\Delta^{13}CH_3D$ vs. $\Delta^{12}CH_2D_2$ space for Rayleigh distillation in closed systems, production and oxidation in closed systems leading to a steady state, and oxidation where methane flows through systems and 4) characterize the effects of oxidation in terms of the resulting trajectories in mass-18 methane isotopologue space.

3. Materials and Methods

3.1. Pure culture cultivation

Cells from a dense contamination-free culture of *Methylosinus trichosporium* (OB3b) in liquid Nitrate Mineral Salts medium (NMS) were transferred to an NMS agar in sterile petri dishes (Fig. 4-1). Prior to inoculation, NMS agar was prepared with basal salts containing 0.93 g/L MgSO$_4$•6 H$_2$O, 10 g/L KNO$_3$, 1.22 g /L CaCl$_2$, 0.15 ml/L of 1 M PO$_4$ solution, 5 ml/L of 2 M HEPES buffer and 15 g/L agarose modified from Whittenbury et al., (1970). One ml/L trace element solution and 1 ml/L vitamin solution according to Widdel and Pfenning, (1981) was added to the NMS agar medium. The medium was autoclaved, and pH was adjusted to 7. While

Figure 4-1. Three-liter glass flange flask containing *Methylosinus trichosporium* colonies on NMS agar plates. Agar plates are placed into shelves of a custom-built stainless-steel rack. Close up picture shows example of *M. trichosporium* colonies on an

medium was dispensed to the petri dishes, 5 mL of Cycloheximide (1%) was added to the NMS agar to avoid contamination by fungal eukaryotes. In a sterile (UVC light sterilization) clean bench (VWR PCR workstation Pro HEPA), equipped with a HEPA filter for providing germfree airflow, a total of 6 NMS agar plates were inoculated with the culture of *M. trichosporium* (OB3b) by dipping a sterile metal culture loop into the liquid culture and then spreading the loop over the surface of the NMS agar plate. The inoculated plates were then placed without lids into the shelves of a custom made sterile stainless-steel rack (Fig. 4-1). While still in the clean bench, the stainless-

166

steel rack with inoculated NMS agar plates was carefully placed into a sterile 3-liter glass flange flask (Glasgerätebau Ochs, Germany), and closed air-tight (via an O-ring connection and quick release clamp) at atmospheric pressure with a glass flange lid equipped with four butyl stopper-sealed openings (one GL 45, one GL 25, and two N20) (Fig. 4-1). Outside the clean bench, 1.2 liters of Ultra-high pure methane (Airgas) was injected into the sealed flange flask through the butyl rubber stopper in one of the N20 openings using a sterile 60 mL plastic syringe equipped with a 0.2 µm syringe sterile filter and a needle, raising the internal pressure by ~1.4 times atmospheric pressure. The headspace was then mixed by repetitive plunging of the 60 mL plastic syringe >10 times to ensure that the air and methane were properly mixed. The sealed flange flask with inoculated agar plates was stored in the dark at room temperature for incubation.

3.2 Incubation parameters

We conducted two time series incubations at room temperature with the same *M. trichosporium* (OB3b) inoculum inside the flange flask as described in section 3.1. The first time series lasted a total of 30 days, during which the headspace was sampled at 0, 12, 15, and 30 days (Table 4-1). The second time-series lasted a total of 9 days, where methane headspace was sampled at 0, 1, 3, 4, 7 and 9 days (Table 4-1). The second incubation provided a higher temporal resolution during the first nine days after methane addition. Between incubations, the headspace in the glass flange flask was completely exchanged by opening the flange flask inside the clean bench and flushing with HEPA-filtered air for 30 min. After flushing, the flange flask was sealed and supplied with new methane gas (see section 3.1.). Over the course of both incubations, the *M. trichosporium* (OB3b) inoculum developed rich, macroscopic colonies on the NMS agar (Fig. 4-1).

3.3 Methane isotopologue measurements

3.3.1 Headspace subsampling and methane purification

Abundances of the singly and doubly-substituted methane isotopologues $^{12}CH_4$, $^{13}CH_4$, $^{12}CH_3D$, $^{13}CH_3D$ and $^{12}CH_2D_2$ in this study were measured on the Panorama mass spectrometer (Nu Instruments) located at the University of California, Los Angeles. Prior to mass spectrometric measurements, the headspace of the glass flange flask containing the *M. trichosporium* colonies was subsampled at each time point (see 3.1.) by inserting the needle of a 5 mL gas-tight glass syringe through a butyl rubber stopper in one of the N20 openings. Total subsample volumes for each time point can be found in Table 4-1. Subsample volumes were aliquoted into 5 mL portions, until the 60-100 µmol CH_4 threshold required for methane analyses on the Panorama mass spectrometer was met. The methane fraction within the subsampled gas was purified from the remaining air fraction according to methods described by Young et al. (2017). Briefly, the gas aliquots were injected into a vacuum line interfaced to a gas chromatograph. Water vapor and carbon dioxide were separated from the gas sample in a liquid nitrogen trap for 10 mins. The remaining gas sample was then captured by freezing methane onto silica gel within a second trap with liquid nitrogen for 30 mins. The frozen silica gel trap was then flushed with helium gas and then warmed to ~ 40°C to transfer the sample to the GC. Methane was purified using two GC columns in series. The first is a 5 A molecular sieve packed column used to separate oxygen and nitrogen from CH_4. The second is a packed HayeSep D column used to separate methane from other hydrocarbons in the gas sample. A passive thermal conductivity detector (TCD) was used to identify peaks. The area of peaks for oxygen, nitrogen and methane were recorded. Retention time of methane gas was approximately 17 minutes with a carrier He flow rate of 20 ml/minute.

Upon exiting the TCD, the purified methane was captured by freezing a trap filled with

168

silica gel with liquid nitrogen for 30 mins. After collection, helium was pumped away, and the frozen silica gel with methane was then heated (~40 °C) and the effusing methane was captured in a separate glass vial filled with silica gel at liquid nitrogen temperature for 30 mins. The sealed glass vial with the purified methane was removed from the vacuum line and attached to the dual inlet located on the mass spectrometer where it was then concentrated into a "cold finger" filled with silica gel at liquid nitrogen temperature. The gas was then released to the variable volume of the dual inlet of the instrument by heating the silica gel to 30 °C

3.3.2 Mass spectrometer measurements

The Panorama instrument is described by Young et al. (2016). Briefly, the instrument operates at a mass resolving power ($m/\Delta m$) of ~ 40,000, which enables measurements of $^{12}CH_4^+$, $^{13}CH_4^+$, $^{12}CH_3D^+$, $^{13}CH_3D^+$, and $^{12}CH_2D_2^+$ ion currents in the same gas sample with no significant mass interferences. The abundances of both $^{13}CH_3D$ and $^{12}CH_2D_2$ are measured using an electron multiplier. Measurements were made with two magnet mass settings. The magnet was first adjusted to measure $^{12}CH_2D_2^+$ (18.04385 amu) in the ion counter. The $^{12}CH_2D_2^+/^{12}CH_4^+$ and $^{12}CH_3D^+/^{12}CH_4^+$ ratios were used to determine the $\Delta^{12}CH_2D_2$ and δD values, where $\delta D = 10^3(^DR/^DR_{VSMOW}-1)$, ^DR is the D/H ratio, and VSMOW refers to the international reference value. Measurements of these ratios consisted of 40 blocks of alternating sample/standard measurements of 30 s each. The ratios $^{13}CH_4^+/^{12}CH_4^+$ and $^{13}CH_3D^+/^{12}CH_4^+$ in the same gas sample were obtained with the magnet set at 18.04090 amu for the axial collector. Twenty blocks were obtained for these measurements. These ratios combined with those from the previous mass setting were used to calculate $\Delta^{13}CH_3D$ and $\delta^{13}C$ values, where $\delta^{13}C = 10^3(^{13}R/^{13}R_{PDB}-1)$, ^{13}R is the $^{13}C/^{12}C$ ratio, and PDB refers to the international reference value. Typical external reproducibility as determined by

multiple measurements of shale gas for δD, $\Delta^{12}CH_2D_2$, $\delta^{13}C$ and $\Delta^{13}CH_3D$ are 0.2, 0.6, 0.1, and 0.2 ‰, respectively, at the 1 σ level, based on replicate samples (Young et al., 2017). We also report $\delta^{13}CH_3D$ and $\delta^{12}CH_2D_2$ values relative to the laboratory reference gas for purposes of extracting fractionation factors.

3.3 Determination of Fractionation factors and gamma's

A key objective of this study was to determine fractionation factors (α) for the $^{13}CH_4$, $^{12}CH_3D$, $^{13}CH_3D$ and $^{12}CH_2D_2$ isotopologues relative to $^{12}CH_4$ during the MOx incubations. For this purpose, we made use of the Rayleigh fractionation equation that describes the isotopologue effects of uptake of methane from a well-mixed reservoir of gas.

To obtain the α values from our data, isotope ratios relative to the reference materials were obtained from delta values obtained by mass spectrometry using

$$\frac{R}{R_{std}} = \frac{\delta}{1000} + 1, \tag{12}$$

where R represents the isotope ratio of interest and subscript std is the standard used as the reference for the deltas. The ratio in Eq. 12 taken at time t was then divided by the same ratio at the time zero to then obtain a measure of the change in ratio with time:

$$\frac{\frac{R^t}{R_{std}}}{\frac{R^0}{R_{std}}} = \frac{R^t}{R^0} \tag{13}$$

This ratio in turn can be used in the Rayleigh equation for fractionation from a well-mixed reservoir, in our case the methane comprising the head-space gas, using

$$\frac{\frac{\delta}{1000}+1}{\frac{\delta^0}{1000}+1} = \left(\frac{^{12}CH_4}{^{12}CH_4^o}\right)^{\alpha-1}, \tag{14}$$

170

where α is the fractionation factor for the methane isotopologues, and $^{12}CH_4/^{12}CH_4^o$ is the fraction of methane remaining in the head space, often referred to as F (and closely approximated by the ratio of the major isotopologues to the initial value).Applying the natural logarithm of both sides in Eq. 14, we have

$$ln\left(\frac{R}{R^0}\right) = (1 - \alpha)(-lnF). \qquad (15)$$

The form of Equation (15) is useful as the slope for $\ln(R/R^o)$ vs. $-\ln(F)$ yields the fractionation factors, α ,we seek. The ratios of methane to nitrogen GC areas were used to obtain values for F. Standard error propagation (with 1 σ error) was used (York et al., 2004) to propagate errors in both $\ln(R/R^o)$ from the isotope ratio measurements themselves, and in $-\ln(F)$ to uncertainties in the derived fractionation factors (from errors in the regression slopes). Uncertainties in $-\ln(F)$ were obtained by replicate (n=5) samplings of head-space gas in the absence of microbes, indicating methane concentration errors of 0.3% of the measured value.

4. Results

4.1 Methane isotopologue trends with time

Throughout the two-time series in this study, large cell colonies were visible on the NMS agar plates (Fig. 4-1). We observed buildup of water condensation on the walls of the glass flange flask and gas chromatography showed lower methane and oxygen concentrations with longer incubation periods (Table 4-1). By the 12th day of the first long incubations the fraction of methane remaining in the chamber (F) was ~0.52 and showed no further decrease up to day 30. In the second, shorter incubation, the fraction of methane (F) remaining was ~0.57 by day 9 (Table 4-1). We note that the measurement taken at day 7 was negatively affected by a software error in peak areas. A correction for the F value of the 7th day was calculated using the F values from the 4th and 9th days of the short incubation.

The initial bulk isotopic compositions for the long and short incubations were −39.93‰ and −37.41‰ for $\delta\,^{13}C$ and, −147.79‰ and −145.01‰ for δD, respectively. With time, the $\delta\,^{13}C$ and δD values for the headspace methane became less negative in both time series. In the longer-duration incubation the methane $\delta^{13}C$ increased from −39.93‰ to −30.37‰ and the δD increased from -147.79‰ to 21.04‰ after 30 days (Table 4-1). In the shorter-duration incubation the $\delta\,^{13}C$ increased from −37.41‰ to −31.15‰ and δD increased from −145.01‰ to−2.14‰ after 9 days (Table 4-1). The initial mass-18 compositions on day 0 for the long and short incubations were 2.27‰ and 3.08‰ for $\Delta^{13}CH_3D$ and 6.11‰ and 6.42‰ for $\Delta^{12}CH_2D_2$, respectively. There was a 0.8‰ difference in $\Delta^{13}CH_3D$ and a 0.3‰ difference in $\Delta^{12}CH_2D_2$ between starting compositions in each incubation, evidently from the result of analytical uncertainties and/or small fractionations imparted by the gas loading procedure. The $\Delta^{13}CH_3D$ and $\Delta^{12}CH_2D_2$ values in both incubations, became more negative as the incubations progressed. In the longer incubation the $\Delta^{13}CH_3D$

172

decreased from 2.27‰ to 1.46‰ while $\Delta^{12}CH_2D_2$ decreased from 6.11‰ to −5.79‰ after 30 days (Table 4-1). In the shorter incubation, the $\Delta^{13}CH_3D$ values decreased from 3.08‰ to 1.40‰ while $\Delta^{12}CH_2D_2$ decreased from 6.42‰ to −6.65‰ after 9 days (Table 4-1).

Incubation Time (d)	Volume of gas analyzed (mL)	F $((CH_4/N_2)/(CH_4/N_2)_{initial})$	O_2/N_2 Area	$\delta^{13}C$ (1 se)(‰)	δD (1 se)(‰)	$\delta^{13}CH_3D$ (1 se) (‰)	$\Delta^{13}CH_3D$ (1 se) (‰)	$\delta^{12}CH_2D_2$ (1 se) (‰)	$\Delta^{12}CH_2D_2$ (1 se) (‰)
0	10	1.000	0.2377	-39.93 (0.006)	-147.79 (0.038)	-95.28 (0.19)	2.27 (0.22)	-173.88 (0.83)	6.11 (1.00)
12	10	0.5168	0.0152	-30.11 (0.004)	21.37 (0.028)	94.11 (0.16)	1.10 (0.15)	172.17 (0.89)	-6.14 (0.77)
15	10	0.5196	0.0014	-30.07 (0.006)	21.31 (0.029)	94.09 (0.16)	1.10 (0.15)	174.23 (1.15)	-4.28 (0.98)
30	15	0.5156	0.0145	-30.37 (0.014)	21.04 (0.020)	93.84 (0.43)	1.46 (0.40)	171.81 (0.65)	-5.79 (0.56)
0	10	1.000	0.2725	-37.41 (0.004)	-145.01 (0.021)	-89.22 (0.12)	3.08 (0.13)	-168.24 (0.58)	6.42 (0.70)
1	10	0.9688	0.2147	-36.47 (0.006)	-123.23 (0.021)	-65.81 (0.12)	2.33 (0.13)	-124.69 (0.67)	7.14 (0.76)
3	10	0.7356	0.1165	-34.59 (0.005)	-76.74 (0.025)	-14.71 (0.19)	1.97 (0.20)	-32.53 (0.86)	3.90 (0.89)
4	10	0.6733	0.078	-33.29 (0.005)	-51.79 (0.022)	12.97 (0.18)	1.67 (0.18)	19.06 (0.61)	2.53 (0.60)
7	15	0.6114	0.017	-31.22 (0.004)	-3.17 (0.021)	66.16 (0.13)	0.70 (0.12)	117.41 (0.75)	-5.35 (0.67)
9	15	0.5701	0.0144	-31.15 (0.004)	-2.14 (0.023)	68.10 (0.13)	1.40 (0.12)	118.25 (0.74)	-6.65 (0.67)

Table 4-1. Experimental details and methane isotopologues result from incubations of methane with *Methylosinus trichosporium* (OB3b).

4.2 Isotopologue fractionation factors departures from the RGM

Figure 4-2 shows the slopes defined by $1000\ln(R/R_o)$ and $-\ln(F)$ and the corresponding α values for the four methane isotopologues relative to $^{12}CH_4$. The derived slopes are 15.15 ± 0.06 for $^{13}C/^{12}C$, 273.5 ± 1.0 for D/H, 285.9 ± 1.1 for $^{13}CH_3D/^{12}CH_4$, and 524.3 ± 2.3 for $^{12}CH_2D_2/^{12}CH_4$. The corresponding fractionation factors, α's, are 0.98485 ± 0.00006 for $^{13}C/^{12}C$, 0.7265 ± 0.0010 for D/H, 0.7141 ± 0.0017 for $^{13}CH_3D/^{12}CH_4$, and 0.4757 ± 0.0023 for $^{12}CH_2D_2/^{12}CH_4$. The γ values from these α values are 0.9981 ± 0.0017 and 0.9013 ± 0.0045 for $^{13}CH_3D/^{12}CH_4$, and

$^{12}CH_2D_2/^{12}CH_4$, respectively.
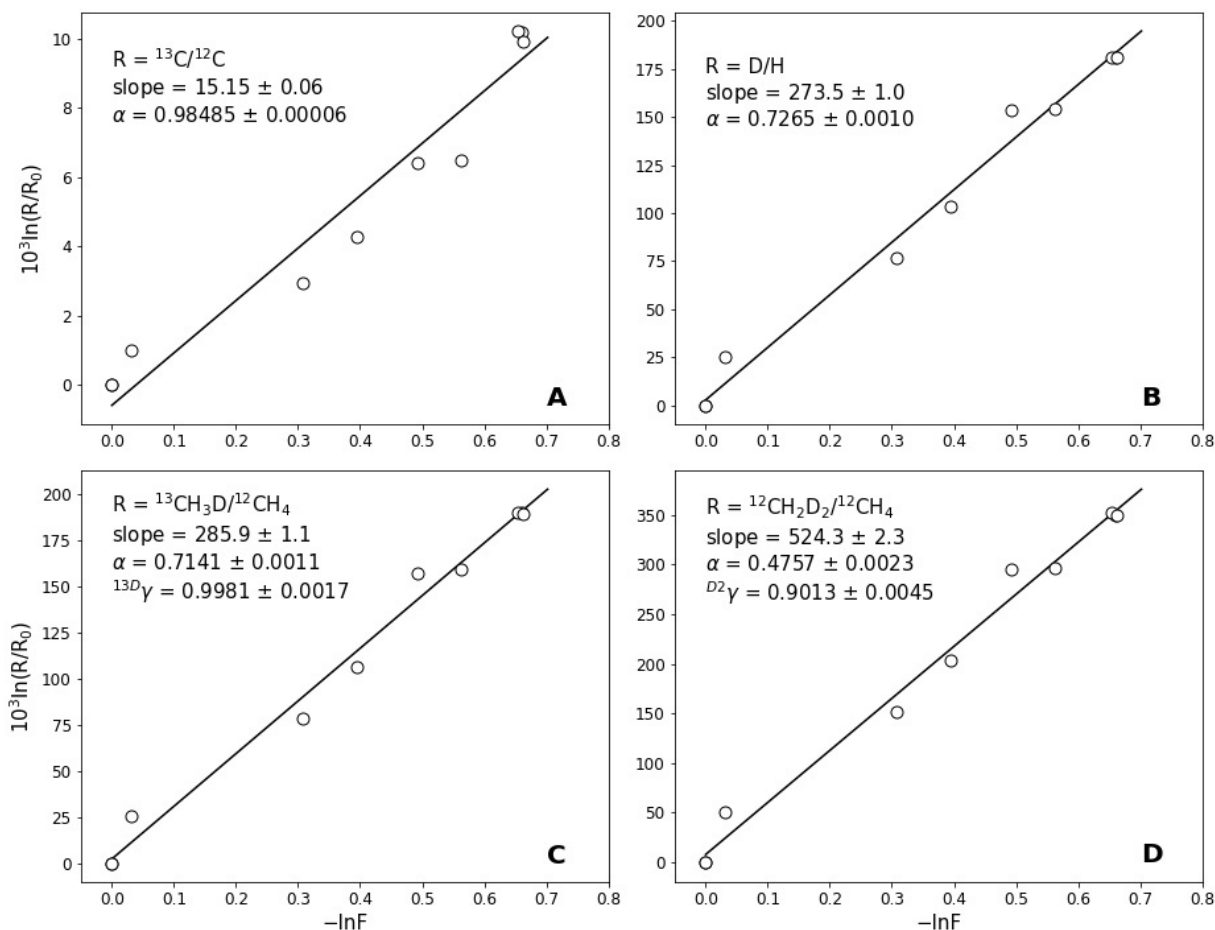

Figure 4-2. Derived fractionation factors (α's) and mass-18 isotopologue γ's (C and D) from linear regressions of MOx experimental data assuming Rayleigh fractionation for carbon (A), hydrogen (B), $\Delta^{13}CH_3D$ (C) and $\Delta^{12}CH_2D_2$. Dashed lines represent the standard propagation of error (1se).

5. Discussion

5.1 Fractionation of carbon, hydrogen, $^{13}CH_3D$ and $^{12}CH_2D_2$ during MOx

Higher bulk isotope ratios with progressive depletion of methane gas through uptake by a microbial community is expected in a closed system as a result of the kinetic advantages of the lighter species. Our derived fractionation factors can be used to calculate the enrichment factors for carbon and hydrogen, ε, where $\varepsilon = (\alpha-1) \ 1000$ for the species of interest. The resulting ε_c and ε_D in our study are -15.15 ± 0.06 ‰ and -273.5 ± 1.0‰, respectively. These MOx enrichment factors are within the range of those previously determined for MOx in laboratory pure and mixed cultures and environmental studies, where carbon enrichment factors range from (-3‰ to -38‰) and hydrogen enrichment factors (-38‰ to -320‰) (Barker and Fritz, 1981; Coleman et al., 1981; Feisthauer et al., 2011; Kinnaman et al., 2007; Templeton et al., 2006; Wang et al., 2016)

The calculated γ values, with a 1 σ error, for $^{13}CH_3D/^{12}CH_4$ using the average $^{13}C/^{12}C$ and D/H α's from both incubations of 0.9981 ($\pm$ 0.0017) could be considered "ideal", in that fractionation is within error of the RGM. In other words, the fractionation of $^{13}CH_3D$ relative to $^{12}CH_4$ is approximately the product of the fractionation factors for bulk carbon and hydrogen isotopes. This result is consistent with the $^{13}CH_3D$ γ's calculated by Wang et al., (2016) who reported weighted averages $^{13}CH_3D$ γ's of 1.0005 ($\pm$ 0.0003) and 1.0000 ($\pm$ 0.0007) in their 30 and 37 °C incubations, respectively.

To the best of our knowledge, we here report the first $\Delta^{12}CH_2D_2$ values of methane involved in MOx, obtained from pure bacterial cultures. Unlike the "ideal" $^{13}CH_3D$ γ values, the $^{12}CH_2D_2$ γ values, with a 1 σ error, are distinctly lower than ideal, with a value of 0.9013 ($\pm$ 0.0045) (Fig. 4-2), showing that the $^{12}CH_2D_2$ fractionation does not follow the RGM during MOx.

It is instructive to compare our MOx results to α's and γ's predicted for $^{12}CH_2D_2$ resulting

from abiotic methane oxidation by hydroxyl radicals. The α's in our study for D/H and $^{12}CH_2D_2$ of 0.7265 ($\pm$ 0.0010) and 0.4757 ($\pm$ 0.0023), respectively, are similar to the fractionation factors for D/H and $^{12}CH_2D_2$, of 0.757 and 0.521 for OH oxidation of methane, respectively, obtained from ab initio calculations by Haghnegahdar et al. (2017) . The value for the $^{12}CH_2D_2$ γ from our MOx pure culture experiments of 0.9013 $\pm$ 0.0045 is similar to the $^{12}CH_2D_2$ γ of 0.906 for oxidation by OH radicals implied by the results from e.g. Haghnegahdar et al., (2017).

The mechanism behind the low γ value for $^{12}CH_2D_2$ remains poorly understood. Ono et al., (2021), conducted experiments to elucidate the $\Delta^{13}CH_3D$ (not $\Delta^{12}CH_2D_2$) and singly-substituted isotopologue signatures during AOM and found the γ values for $^{13}CH_3D$ obtained in their study were unexpectedly lower than unity ($\gamma < 1$). In that work, the phenomenon was explained in terms of difference in zero-point energies from reactant-like to product-like transition states of the enzyme structure during the oxidation reaction. In this context, any solution involving zero-point energies will lead to larger effects where D substitutions for H are involved, as shown by the ab initio calculations by Haghnegahdar et al, (2017). In any case, it appears that deviations from RGM could indicate alteration of a methane source by oxidation. The transition states of the monooxygenase enzymatic in our study were not determined, and further research into the relationship of deviations of the RGM to enzyme transition state causing isotopologue effects should be conducted. Nevertheless, the low γ value for $^{12}CH_2D_2$ exerts a significant influence over the trajectories in mass-18 isotopologue space followed by methane affected by MOx, as discussed next.

5.2 Trajectories of $\Delta^{13}CH_3D$ and $\Delta^{12}CH_2D_2$ in open and closed systems

Our results allow us to characterize the trajectories followed by methane in $\Delta^{13}CH_3D$ vs. $\Delta^{12}CH_2D_2$ space as it is consumed by MOx in either open or closed systems. We find that these

trajectories are controlled by the precise values for γ's. In order to illustrate the effects of γ's, we consider three cases, oxidation in the absence of production in a closed system (the case for our incubations), oxidation with production in closed systems, and the steady-state case where transport (flow) is balanced against oxidation.

5.2.1 Rayleigh Distillation in closed systems

We first consider the closed system case where methane is consumed by a Rayleigh distillation process in which only aerobic oxidation of methane is occurring, and no new methane is being supplied to the system. Figure 4-3 shows the calculated trajectories of residual methane gas in $\Delta^{13}CH_3D$ vs. $\Delta^{12}CH_2D_2$ space based on our measured MOx fractionation factors. The overall trend shows decreases in both $\Delta^{13}CH_3D$ and $\Delta^{12}CH_2D_2$. For comparison, we also show calculated trajectories in $\Delta^{13}CH_3D$ vs. $\Delta^{12}CH_2D_2$ space for a range in $^{13}CH_3D$ γ values at a fixed value for the $^{12}CH_2D_2$ γ that matches the value measured in our incubations (Fig. 4-3). Although the paths become steeper for $^{13}CH_3D$ γ less than 1, the paths are all similar in showing decreasing $\Delta^{12}CH_2D_2$
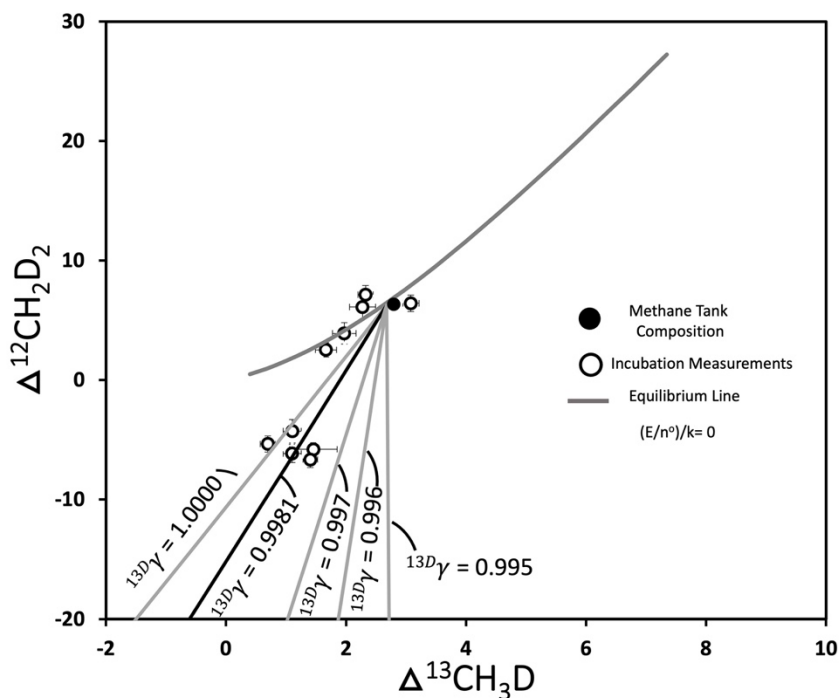
Figure 4-3. Mass-18 isotopologue plot showing trajectories of residual methane gas affected by uptake by MOx in a closed system Rayleigh distillation model. Paths for different $^{13}CH_3D$ γ values at our measured γ for CH_2D_2 are shown. Solid black line is the trajectory using measured γ's from the MOx experiments in this study. Solid grey lines are modeled trajectories with a range of different $^{13}CH_3D$ γ's. Open circles are the MOx data from this study. The closed black circle is the starting methane isotopologue composition. The dark grey curve represents thermodynamic equilibrium for comparison.

with more moderate changes in $\Delta^{13}CH_3D$ where only oxidation occurs (Fig. 4-3).

5.2.2 Time-dependent oxidation with production

Next we consider the case where there is a balance between methane production and consumption over time in a closed system (Haghnegahdar et al., 2017). Here, a constant rate of production is balanced against oxidation, where the oxidation is taken to be a first-order kinetic process with a fixed rate constant. The overall process is described by the ordinary differential equation,

$$\frac{dn_i}{dt} = E_i - k_i n_i, \tag{16}$$

where n_i is the time variant moles of the isotopologue of interest i, E_i is the methane source term for species i, and k_i is the rate constant for oxidation of i (yr^{-1}). The solution for the time-dependent variability in moles of isotopologue i is,

$$n_i(t) = n_i^o e^{-k_i t} + \frac{E_i}{k_i}(1 - e^{-k_i t}), \tag{17}$$

where n_i^o is the initial moles of i and t is time. The steady-state moles of the methane isotopologue species i are obtained by evaluating (17) where $t \to \infty$, and thus $e^{k_i t} \to 0$, yielding

$$n_i(t \sim \infty) = \frac{E_i}{k_i}. \tag{18}$$

The steady-state amount of methane is thus seen to be controlled by the ratio of the methane production rate and the methane oxidation rate constant. The steady-state ratio of two isotopologues is then,

$$\frac{n_i(t\sim\infty)}{n_j(t\sim\infty)} = \frac{k_i E_j}{E_j k_i}, \tag{19}$$

where n_i (n_j) is the amount of moles of isotopologue i (j), E_i (E_j) is the methane source term for i (j), and k_i (k_j) is the rate constant for oxidation of i (j). Figure 4-4 shows the calculated trajectories of methane gas in $\Delta^{13}CH_3D$ vs. $\Delta^{12}CH_2D_2$ space based on Equation (17) for $(E/n_o)/k$ of 1. We address the effects of different $(E/n_o)/k$ in greater detail below. Steady state will be achieved in several e-folding times for oxidation (i.e., where $t \gg 1/k_i$). For the α and γ values measured in our experiments, the path followed by methane begins with moderate decreases in $\Delta^{13}CH_3D$ and $\Delta^{12}CH_2D_2$ followed by modest increases in $\Delta^{13}CH_3D$ and, eventually, dramatic increases in $\Delta^{12}CH_2D_2$ with progressive oxidation. The precise path, however, is exceedingly sensitive to the γ value for $^{13}CH_3D$ (Fig. 4-4). While $\Delta^{12}CH_2D_2$ always increases dramatically, when γ for $^{12}CH_2D_2$ is less than 1, and we assume this to be true in all cases, the
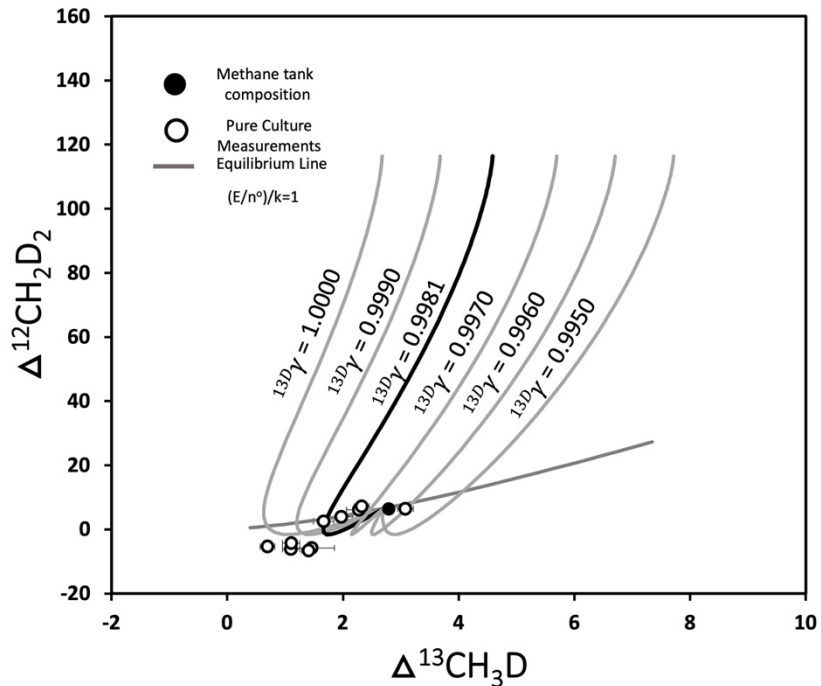
Figure 4-4. Mass-18 isotopologue plot showing trajectories of the mass-18 isotopologues in a closed-system time dependent model (e.g., Haghnegahdar et al., 2017) when production and oxidation rate constants are equivalent $((E/n^o)/k =1)$ and with varying $^{13}CH_3D$ γ. Solid black line is the trajectory using our measured γ's from the MOx experiments. Solid grey lines are modeled trajectories with varying $^{13}CH_3D$ γ's. Open circles are experimental data points to demonstrate the difference in mass-18 isotopologue signatures in our experiments to the mass-18 trajectories in the open system flow-through model. The closed black circle is the starting methane isotopologue composition to compare with the experimental data points and the mass-18 trajectories in the open flow-through system. The grey curved line is the thermodynamic equilibrium curve for reference.

179

magnitude, and even the sign of $\Delta^{13}CH_3D$ changes with even small differences in γ for $^{13}CH_3D$ of 0.001. Lowering the $^{13}CH_3D$ γ from 0.997 to 0.996, for example, is sufficient to cause a change in sign in the shift in $\Delta^{13}CH_3D$ with oxidation (Fig. 4-4).

5.2.3 Oxidation in open systems at steady state

Next, we consider the situation in which the supply of methane in the system is not from local biota, but from an outside flux of methane into the system, through the region of oxidation, after which methane exits again. The calculated α's from the experimental data were applied to an open system steady-state flow-through model (Hayes, 2001b). We first rearrange the mass balance equation to obtain for the steady state case,

$$R^o = (1 - \varphi)R + R\varphi\alpha, \tag{20}$$

where R^o is the initial isotopologue ratio, R is the steady state value, φ is the ratio of methane oxidation rate to residence time of the gas in the flow system, and α is the fractionation factor for the MOx reaction. Substitution of δ +1 for R yields the equation cited by Wang et al., (2016),

$$\delta = \frac{\delta^o + 1}{1 + \varphi(\alpha - 1)} - 1. \tag{21}$$

Figure 4-5 shows calculated $\Delta^{13}CH_3D$ and $\Delta^{12}CH_2D_2$ values in the steady-state flow-through open system scenario. Each point along the curve represents a steady state at different values for φ. While resembling the curves in Figure 4-5, these curves do not depict time evolution, but rather a series of possible steady-state compositions for methane affected by oxidation in the presence of flowing gas. The parameter φ in Equation (20) is a normalized version of the Dahmköhler number, Da, where Da = $\tau/(1/k)$, τ is the residence time of gas in the system and k is the rate constant for the reaction. Therefore, φ = Da/(1+Da). When k is large in comparison to τ, Da is large and φ goes to its maximum value of unity and the situation approaches that in the last

180

section where production is low compared with the rate of oxidation. Conversely, if k is lower than τ, φ goes to 0 and the methane in the system is unaffected by oxidation. Here again, the curves for cases in between are sensitive to small changes in γ for $^{13}CH_3D$. In all cases, the evolution of both $\Delta^{13}CH_3D$ and $\Delta^{12}CH_2D_2$ trajectories are above the thermodynamic equilibrium line when methane oxidation is dominant.
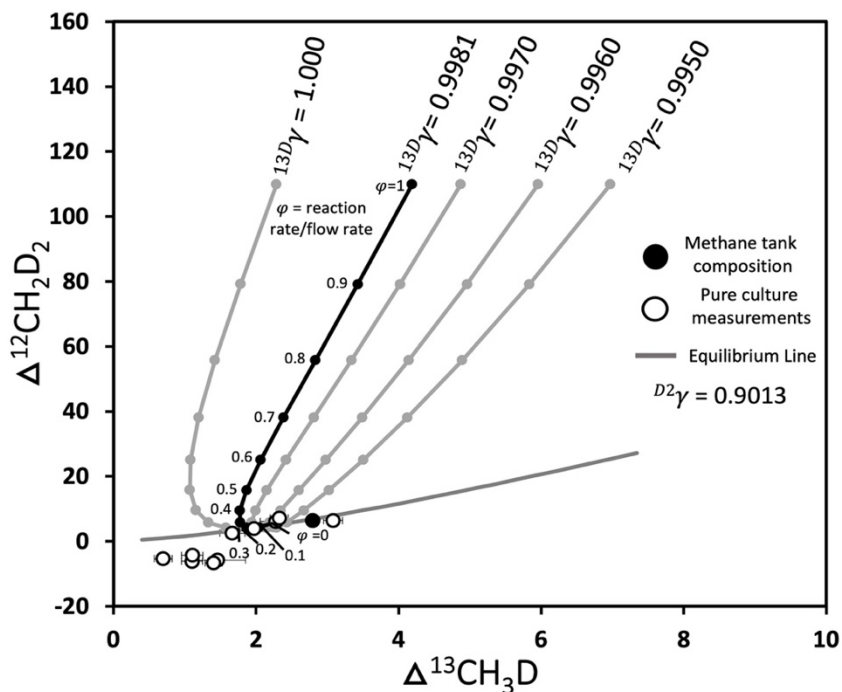

Figure 4-5. Mass-18 isotopologue plot showing different steady state methane compositions in an open flow-through system from Hayes (2001), with varying $^{13}CH_3D$ γ. The circles on the curves represent the steady state values for different relative rates of flow and oxidation (φ, see text). Solid black line is the trajectory defined by different steady-state values using the measured γ's from the MOx experiments. Solid grey lines are modeled trajectories with varying $^{13}CH_3D$ γ's. Open circles are experimental data points to demonstrate the difference in mass-18 isotopologue signatures in our experiments to the mass-18 trajectories in the open system flow-through model. The closed black circle is the starting methane isotopologue composition to compare with the experimental data points and the mass-18 trajectories in the open flow-through system. The grey curved line is the thermodynamic equilibrium line.

5.3. Implications

The analysis above shows that in a closed system, in the absence of introduction of fresh methane, oxidation will lower $\Delta^{12}CH_2D_2$ in the residual gas as oxidation progresses, and $\Delta^{13}CH_3D$

will decrease, stay the same, or even increase depending upon the precise γ values for $^{13}CH_3D$. In our analysis, we observe that $\Delta^{12}CH_2D_2$ is far removed from the RGM, and thus we have assumed that γ is always smaller than 1 for $\Delta^{12}CH_2D_2$ and that this is a robust feature of oxidation in all cases.

Where oxidation is balanced against production of methane, either in closed or open systems, one expects to find decreases in $\Delta^{12}CH_2D_2$ in the residual gas relative to the source where replenishment of the gas is negligible, but for production rates that are significant compared with rates of oxidation, the effect of oxidation is to raise $\Delta^{12}CH_2D_2$ values rather than lower them. This is a direct reflection of $^{12}CH_2D_2$ γ being smaller than 1. This proves to be a critically important observation for using mass-18 isotopologues as a means for determining the provenance and history of methane gases.

Recent work has determined the mass-18 isotopologue signatures of microbiologically produced methane in vitro and in vivo and the results suggest that $\Delta^{13}CH_3D$ and $\Delta^{12}CH_2D_2$ are markedly negative where methane is produced by microbial methanogenesis (e.g., -4 ‰ for $\Delta^{13}CH_3D$ and -43‰ for $\Delta^{12}CH_2D_2$) (Young et al., 2017). The question arises as to whether or not oxidation could mimic these mass-18 isotopologue signatures, thus adding confusion as to the origin of methane with low $\Delta^{12}CH_2D_2$ and low $\Delta^{13}CH_3D$ values. Our results suggest that in the absence of methane production, extreme degrees of oxidation (where a large fraction of the methane is consumed) could lead to low $\Delta^{12}CH_2D_2$ and $\Delta^{13}CH_3D$ values that might be confused with the signature of microbial methanogenesis. However, where production is simultaneous with oxidation, either in-situ (Fig. 4-4) or outside the region of oxidation where gas flows through the oxidation region (Fig. 4-5), the resulting $\Delta^{12}CH_2D_2$ and $\Delta^{13}CH_3D$ values do not resemble those produced by microbial methanogenesis (Fig. 4-6).

The precise positions of the gases in mass-18 isotopologue space will depend on the source, but if the source is microbial methanogenesis, then the residual gas will have either low $\Delta^{12}CH_2D_2$ (and $\Delta^{13}CH_3D$) or higher values with oxidation where the source persists. Indeed, the confusion that may arise where methane is added to a region of methane oxidation is that the microbial source of methane might be less evident because the $\Delta^{12}CH_2D_2$ values will be higher than expected.

From the preceding analysis it is clear that the ratio of production rate to consumption rate will influence the trajectory of residual methane during aerobic oxidation methane. We illustrate the impact of varying rate constants of methane production relative to methane oxidation $(E/n^o)/k$ in the Figure 4-6. Lowering $(E/n^o)/k$ to $\ll 1$ forces the $\Delta^{12}CH_2D_2$ and $\Delta^{13}CH_3D$ trajectory of the residual methane into the microbial methanogenesis field where more than 90% of the methane has been consumed (Fig. 4-6). Further oxidation results in an increase in $\Delta^{12}CH_2D_2$ above the thermodynamic equilibrium line as the residual methane is consumed by oxidation, but the fraction of methane remaining is exceedingly small by this stage (Fig. 4-6). We note that trajectories of residual methane in $\Delta^{12}CH_2D_2$ vs. $\Delta^{13}CH_3D$ space are almost indistinguishable for $(E/n^o)/k$ of 1, 10, 100, and 1000 (not shown). This finding illustrates explicitly that only where replenishment of methane is very low can MOx mimic microbial production in $\Delta^{12}CH_2D_2$ and $\Delta^{13}CH_3D$ space.

With this result in hand, we can return to the example of the methane in the Oman Ophiolite. We conclude that the low $\Delta^{12}CH_2D_2$ and $\Delta^{13}CH_3D$ values exhibited by some of the gas emanating from the ultramafic complex reported in Nothaft et al. (2021) are best interpreted as a microbial source of methane unless oxidation was acting on existing gas in the absence of any source of methane. The latter seems unlikely, bolstering the use of these mass-18 isotopologues as tracers of microbial methanogenesis.
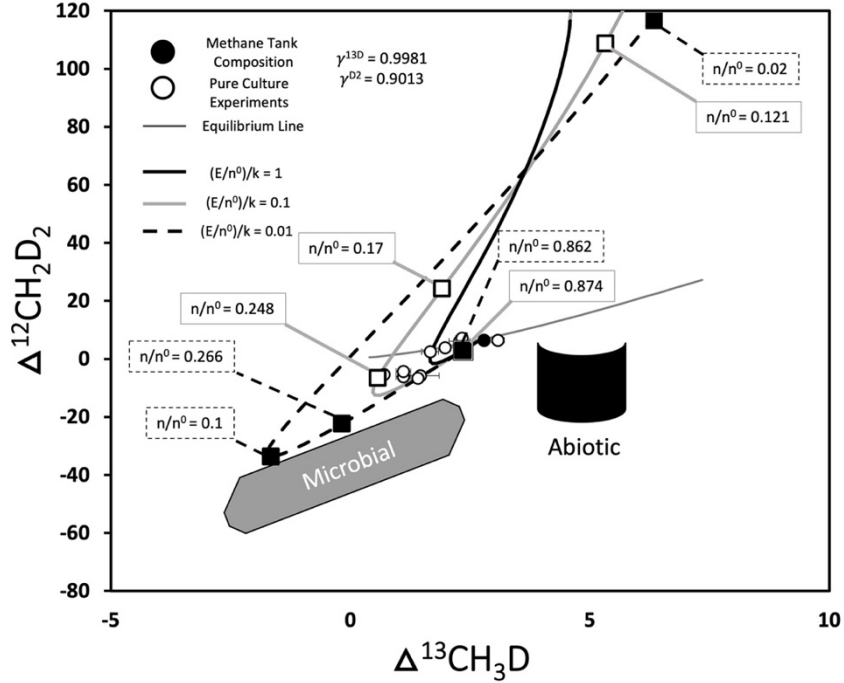
Figure 4-6. Mass-18 isotopologue plot showing trajectories of the mass-18 isotopologues in a closed-system time dependent model (e.g., Haghnegahdar et al., 2017), with varying $(E/n^o)/k$. Solid black line is the trajectory using our measured γ's from the MOx experiments where $(E/n^o)/k = 1$. The solid grey line is the modeled trajectory using the measured γ's from the MOx experiments when $(E/n^o)/k = 0.1$. The dashed black line corresponds to the measured γ's from the MOx experiments where $(E/n^o)/k = 0.01$. Open and closed squares represent the mole ratio as time proceeds when $(E/n^o)/k$ equals 0.1 and 0.01, respectively. Open circles are experimental data points from this study. The closed black circle is the starting methane isotopologue composition. The grey curved line is the thermodynamic equilibrium curve for reference. Grey solid polygon represents the microbial field. Black solid cylinder represents the abiotic field.

184

6. Conclusions

In the present study we observed the $\Delta^{12}CH_2D_2$ and $\Delta^{13}CH_3D$ signatures over time in a closed system chamber containing aerobic methane-oxidizing bacteria in pure cultures. The results were used to obtain α's and γ's for both $\Delta^{12}CH_2D_2$ and $\Delta^{13}CH_3D$. We conclude that MOx fractionates $^{13}CH_3D$ "ideally" with respect to RGM, which validates previous work. We report for the first time measured α's and γ's for $^{12}CH_2D_2$ from MOx (to the best of our knowledge). We conclude that the fractionation of $^{12}CH_2D_2$ exhibits marked departures from the RGM, which tends to drive residual methane to high $\Delta^{12}CH_2D_2$ values with progressive oxidation where a source of methane is present during oxidation. The trajectories of residual methane gases in $\Delta^{12}CH_2D_2$ vs. $\Delta^{13}CH_3D$ space are sensitive to small deviations in $^{13}CH_3D$ from the RGM. Our results indicate that in a closed system, where methane production is absent, or occurring at very low rates relative to oxidation, the mass-18 isotopologue signatures of residual methane could potentially mimic microbial methanogenesis signatures. However, in a closed system where methane production and oxidation are simultaneously occurring, the MOx mass-18 isotopologue signatures are not at risk of mimicking microbial methanogenesis. Furthermore, we show that in open systems, where methane production is balanced by oxidation and advection, oxidation results in a combination of $\Delta^{13}CH_3D$ and $\Delta^{12}CH_2D_2$ values distinct from microbial methanogenesis, suggesting methane oxidation in an open system is clearly distinguishable from gas produced by microbial methanogenesis.

CRediT author statement

Sebastian J. E. Krause: Conceptualization, Methodology, Formal Analysis, Investigation, Data Curation, Writing-Original Draft, Visualization; **Jiarui Liu:** Software, Validation, Formal Analysis, Investigation, Data Curation, Writing-Review and Editing; **Edward D. Young:** Conceptualization, Methodology, Formal Analysis, Resources, Data Curation, Writing-Review and Editing, Supervision, Project Administration, Funding Acquisition; **Tina Treude:** Conceptualization, Methodology, Resources, Writing-Review and Editing, Supervision, Project Administration, Funding Acquisition

References

Ash J., Egger M., Treude T., Kohl I., Cragg B., Parkes R. J., Slomp C., Sherwood Lollar B. and Young E. D. (2019) Exchange catalysis during anaerobic methanotrophy revealed by 12CH2D2 and 13CH3D in methane. *Geochemical Perspective Letters* **10**, 26-30.

Barker J. F. and Fritz P. (1981) Carbon isotope fractionation during microbial methane oxidation. *Nature* **293**, 289-291.

Bigeleisen J. (1955) Statistical mechanics of isotopic systems with small quantum corrections. I. General considerations and the rule of the geometric mean. *The Journal of Chemical Physics* **23**, 2264-2267.

Boetius A. and Wenzhöfer F. (2013) Seafloor oxygen consumption fuelled by methane from cold seeps. *Nature Geoscience* **6**, 725-734.

Bouquet A., Mousis O., Waite J. H. and Picaud S. (2015) Possible evidence for a methane source in Enceladus' ocean. *Geophysical Research Letters* **42**, 1334-1339.

Claypool G. E. and Kaplan I. R. (1974) The origin and distribution of methane in marine sediments. In *1. Marine sediments - Gas content - Congresses* (eds. I. Kaplan and R. Isaacs). Plenum Press, New York. pp. 99-139.

Coleman D. D., Risatti J. B. and Schoell M. (1981) Fractionation of carbon and hydrogen isotopes by methane-oxidizing bacteria. *Geochimica et Cosmochimica Acta* **45**, 1033-1037.

Demirbas A. (2006) The importance of natural gas as a world fuel. *Energy Sources, Part B* **1**, 413-420.

Etiope G. and Sherwood Lollar B. (2013) Abiotic methane on Earth. *Reviews of Geophysics* **51**, 276-299.

188

Etiope G. and Schoell M. (2014) Abiotic gas: atypical, but not rare. *Elements* **10**, 291-296.

Feisthauer S., Vogt C., Modrzynski J., Szlenkier M., Krüger M., Siegert M. and Richnow H.-H. (2011) Different types of methane monooxygenases produce similar carbon and hydrogen isotope fractionation patterns during methane oxidation. *Geochimica et Cosmochimica Acta* **75**, 1173-1184.

Giunta T., Labidi J., Kohl I., Ruffine L., Donval J.-P., Géli L., Çağatay M., Lu H. and Young E. (2021) Evidence for methane isotopic bond re-ordering in gas reservoirs sourcing cold seeps from the Sea of Marmara. *Earth and Planetary Science Letters* **553**, 116619.

Giunta T., Young E. D., Warr O., Kohl I., Ash J. L., Martini A., Mundle S. O., Rumble D., Pérez-Rodríguez I. and Wasley M. (2019) Methane sources and sinks in continental sedimentary systems: New insights from paired clumped isotopologues 13CH3D and 12CH2D2. *Geochimica et Cosmochimica Acta* **245**, 327-351.

Guggenheim C., Freimann R., Mayr M. J., Beck K., Wehrli B. and Bürgmann H. (2020) Environmental and microbial interactions shape methane-oxidizing bacterial communities in a stratified lake. *Frontiers in microbiology* **11**, 2374.

Haghnegahdar M. A., Schauble E. A. and Young E. D. (2017) A model for 12CH2D2 and 13CH3D as complementary tracers for the budget of atmospheric CH4. *Global Biogeochemical Cycles* **31**, 1387-1407.

Hanson R. S. and Hanson T. E. (1996) Methanotrophic bacteria. *Microbiol. Rev.* **60**, 439-471.

Hayes J. M. (2001) Fractionation of Carbon and Hydrogen Isotopes in Biosynthetic Processes. *Rev. Mineral Geochem.* **43**, 225-277.

Henckel T., Jäckel U., Schnell S. and Conrad R. (2000) Molecular analyses of novel methanotrophic communities in forest soil that oxidize atmospheric methane. *Appl. Environ. Microbiol.* **66**, 1801-1808.

Karl D. M., Beversdorf L., Björkman K. M., Church M. J., Martinez A. and Delong E. F. (2008) Aerobic production of methane in the sea. *Nature Geoscience* **1**, 473-478.

Kinnaman F. S., Valentine D. L. and Tyler S. C. (2007) Carbon and hydrogen isotope fractionation associated with the aerobic microbial oxidation of methane, ethane, propane and butane. *Geochimica et Cosmochimica Acta* **71**, 271-283.

Labidi J., Young E. D., Giunta T., Kohl I. E., Seewald J., Tang H., Lilley M. D. and Früh-Green G. L. (2020) Methane thermometry in deep-sea hydrothermal systems: evidence for re-ordering of doubly-substituted isotopologues during fluid cooling. *Geochimica et Cosmochimica Acta* **288**, 248-261.

Lenhart K., Bunge M., Ratering S., Neu T. R., Schüttmann I., Greule M., Kammann C., Schnell S., Müller C. and Zorn H. (2012) Evidence for methane production by saprotrophic fungi. *Nature communications* **3**, 1-8.

Liu Q. and Liu Y. (2016) Clumped-isotope signatures at equilibrium of CH4, NH3, H2O, H2S and SO2. *Geochim. Cosmochim. Acta* **175**, 252-270.

Ma Q., Wu S. and Tang Y. (2008) Formation and abundance of doubly-substituted methane isotopologues (13CH3D) in natural gas systems. *Geochimica et Cosmochimica Acta* **72**, 5446-5456.

Murrell J. (2010) The aerobic methane oxidizing bacteria (methanotrophs). *Handbook of hydrocarbon and lipid microbiology*, 1953-1966.

Nothaft D. B., Templeton A. S., Rhim J. H., Wang D. T., Labidi J., Miller H. M., Boyd E. S., Matter J. M., Ono S. and Young E. D. (2021) Geochemical, biological, and clumped isotopologue evidence for substantial microbial methane production under carbon limitation in serpentinites of the Samail Ophiolite, Oman. *Journal of Geophysical Research: Biogeosciences* **126**, e2020JG006025.

Ono S., Rhim J. H., Gruen D. S., Taubner H., Kölling M. and Wegener G. (2021) Clumped isotopologue fractionation by microbial cultures performing the anaerobic oxidation of methane. *Geochimica et Cosmochimica Acta* **293**, 70-85.

Ono S., Wang D. T., Gruen D. S., Sherwood Lollar B., Zahniser M. S., McManus B. J. and Nelson D. D. (2014) Measurement of a doubly substituted methane isotopologue, 13CH3D, by tunable infrared laser direct absorption spectroscopy. *Analytical chemistry* **86**, 6487-6494.

Rayleigh L. (1896) L. Theoretical considerations respecting the separation of gases by diffusion and similar processes. *The London, Edinburgh, and Dublin Philosophical Magazine and Journal of Science* **42**, 493-498.

Reeburgh W. S. (2007) Oceanic methane biogeochemistry. *Chem. Rev.* **107**, 486-513.

Saunois M., Bousquet P., Poulter B., Peregon A., Ciais P., Canadell J. G., Dlugokencky E. J., Etiope G., Bastviken D. and Houweling S. (2016) The global methane budget 2000–2012. *Earth System Science Data* **8**, 697-751.

Schoell M. (1980) The hydrogen and carbon isotopic composition of methane from natural gases of various origins. *Geochimica et Cosmochimica Acta* **44**, 649-661.

Schoell M. (1988) Multiple origins of methane in the earth. *Chem. Geol.* **71**, 1-10.

Steinle L., Graves C. A., Treude T., Ferré B., Biastoch A., Bussmann I., Berndt C., Krastel S., James R. H., Behrens E., Böning C. W., Greinert J., Sapart C. J., Scheinert M., Sommer S., Lehmann M. F. and Niemann H. (2015) Water column methanotrophy controlled by a rapid oceanographic switch. *Nature Geosci.* **8**, 378.

Stolper D. A., Sessions A. L., Ferreira A. A., Neto E. V. S., Schimmelmann A., Shusta S. S., Valentine D. L. and Eiler J. M. (2014) Combined 13C–D and D–D clumping in methane: methods and preliminary results. *Geochimica et Cosmochimica Acta* **126**, 169-191.

Taenzer L., Labidi J., Masterson A. L., Feng X., Rumble III D., Young E. D. and Leavitt W. D. (2020) Low Δ12CH2D2 values in microbialgenic methane result from combinatorial isotope effects. *Geochimica et Cosmochimica Acta* **285**, 225-236.

Templeton A. S., Chu K.-H., Alvarez-Cohen L. and Conrad M. E. (2006) Variable carbon isotope fractionation expressed by aerobic CH4-oxidizing bacteria. *Geochimica et Cosmochimica Acta* **70**, 1739-1752.

Valentine D. L., Blanton D. C., Reeburgh W. S. and Kastner M. (2001) Water column methane oxidation adjacent to an area of active gas hydrate dissociation, Eel River Basin. *Geochim. Cosmochim. Acta* **65**, 2633-2640.

Wang D. T., Welander P. V. and Ono S. (2016) Fractionation of the methane isotopologues 13 CH 4, 12 CH 3 D, and 13 CH 3 D during aerobic oxidation of methane by Methylococcus capsulatus (Bath). *Geochimica et Cosmochimica Acta* **192**, 186-202.

Wang D. T., Sattler A., Paccagnini M. and Chen F. G. (2020) Method for calibrating methane clumped isotope measurements via catalytic equilibration of methane isotopologues on γ-alumina. *Rapid Communications in Mass Spectrometry* **34**, e8555.

Webb M. A. and Miller III T. F. (2014) Position-specific and clumped stable isotope studies: comparison of the Urey and path-integral approaches for carbon dioxide, nitrous oxide, methane, and propane. *The Journal of Physical Chemistry A* **118**, 467-474.

Whiticar M. J. (1999) Carbon and hydrogen isotope systematics of bacterial formation and oxidation of methane. *Chem. Geol.* **161**, 291-314.

Whiticar M. J. (2020) The Biogeochemical Methane Cycle. *Hydrocarbons, Oils and Lipids: Diversity, Origin, Chemistry and Fate*, 669-746.

Whittenbury R., Phillips K. and Wilkinson J. (1970) Enrichment, isolation and some properties of methane-utilizing bacteria. *Microbiology* **61**, 205-218.

Widdel F. and Pfennig N. (1981) Studies on dissimilatory sulfate-reducing bacteria that decompose fatty acids. *Archives of microbiology* **129**, 395-400.

York D., Evensen N. M., Martınez M. L. and De Basabe Delgado J. (2004) Unified equations for the slope, intercept, and standard errors of the best straight line. *American Journal of Physics* **72**, 367-375.

Young E.D. (2019) A Two-Dimensional Perspective on CH4 Isotope Clumping: Distinguishing Process from Source, in: Orcutt B.N., Daniel I., Dasgupta R. (Eds.), Deep Carbon: Past to Present. Cambridge University Press, Cambridge, pp. 388-414.

Young E., Kohl I., Lollar B. S., Etiope G., Rumble D., Li S., Haghnegahdar M., Schauble E., McCain K. and Foustoukos D. (2017) The relative abundances of resolved l2 CH 2 D 2 and 13 CH 3 D and mechanisms controlling isotopic bond ordering in abiotic and biotic methane gases. *Geochimica et Cosmochimica Acta* **203**, 235-264.

Young E. D., Rumble D., Freedman P. and Mills M. (2016) A large-radius high-mass-resolution multiple-collector isotope ratio mass spectrometer for analysis of rare isotopologues of O 2, N 2, CH 4 and other gases. *International Journal of Mass Spectrometry* **401**, 1-10.

Yung Y. L., Chen P., Nealson K., Atreya S., Beckett P., Blank J. G., Ehlmann B., Eiler J., Etiope G. and Ferry J. G. (2018) Methane on Mars and habitability: challenges and responses. *Astrobiology* **18**, 1221-1242.

Chapter 5

Reversibility controls on extreme methane clumped isotope signatures from anaerobic oxidation of methane

Jiarui Liu [1, *], Rachel L. Harris [2], Jeanine L. Ash [3], James G. Ferry [4], **Sebastian J.E. Krause** [a], Jabrane Labidi [5], Divya Prakash [4], Barbara Sherwood Lollar [5, 6], Tina Treude [1, 7], Oliver Warr [6], Edward D. Young [1, *]

[1]Department of Earth, Planetary and Space Sciences, University of California, Los Angeles, CA, USA.

[2]Department of Organismic and Evolutionary Biology, Harvard University, Cambridge, MA, USA.

[3]Department of Earth, Environmental and Planetary Sciences, Rice University, Houston, TX, USA.

[4]Department of Biochemistry and Molecular Biology, Pennsylvania State University, University Park, PA, USA.

[5]Université de Paris, Institut de Physique du Globe de Paris, CNRS, Paris, France.

[6] Department of Earth Sciences, University of Toronto, Toronto, Ontario, Canada.

[7]Department of Atmospheric and Oceanic Sciences, University of California, Los Angeles, CA, USA.

* Corresponding author. Email: jiaruiliu@ucla.edu (J.L.); eyoung@epss.ucla.edu (E.D.Y.)

Abstract

Microbial anaerobic oxidation of methane (AOM) substantially mitigates atmospheric methane emissions on Earth and is a process to consider for astrobiological targets where methane has been detected. The measurement of doubly substituted, or "clumped", methane isotopes has proven useful in tracing processes of methane formation and oxidation. Both near-equilibrium and extreme disequilibrium methane clumped isotope signatures can be attributed to AOM, but, to date, understanding the mechanistic and environmental controls on those signatures have been lacking. We report measurements of methane clumped isotope ratios of residual methane in AOM-active microbial incubations using sediment slurries from Svalbard and Santa Barbara Channel methane seeps. Incubation experiments of Svalbard sediment slurries resulted in residual methane with very high $\Delta^{13}CH_3D$ and $\Delta^{12}CH_2D_2$ values up to 19.5‰ and 65.1‰, respectively. We found similarly high $\Delta^{13}CH_3D$ and $\Delta^{12}CH_2D_2$ values in fluid samples from the Chamorro Seamount, a serpentinite mud volcano in the Mariana forearc, suggesting that minimal reversibility of AOM intracellular reactions leads to kinetic fractionation of clumped isotopologues. When conditions were consistent with a low thermodynamic drive for AOM, however, methane isotopologues approached intra-species quasi-equilibrium. This was clearly observed in isotope exchange experiments with methyl-coenzyme M reductase (Mcr) and in microbial incubations of the Santa Barbara Channel sediment slurries. The near-equilibrium methane isotopologue signatures are generalized as a result of the Mcr-catalyzed intracellular isotope exchange operating under near threshold free energy conditions, as shown in the deep-biosphere incubations. Our results show that the reversibility of the Mcr-catalyzed reaction is central to understanding the meaning of methane isotopologue ratios affected by microbial production and oxidation.

1. Introduction

Methane, the simplest of all hydrocarbons, is a gas with economic, societal, and environmental relevance. It is the main component of natural gas, a key component of the global carbon cycle (Reeburgh, 2003), and a primary target for understanding the relative role of geologic processes and potential extinct/extant life elsewhere in the universe (e.g., Yung et al., 2018). As a potent greenhouse gas, methane contributes to climate change and its concentration in the atmosphere has been increasing since the beginning of industrialization (IPCC, 2021). The main "biological" processes forming methane are microbial degradation (microbialgenic) and pyrolysis (thermogenic) of organic matter (e.g., Reeburgh, 2003; Repeta et al., 2016). Abiotic methane can be formed through various types of water-rock interactions (Etiope and Sherwood Lollar, 2013 and references therein) under a range of both low temperature and high temperature conditions. Identifying the sources and processes of methane emission is vital for constraining fluxes from major reservoirs contributing to climate change, and more broadly, for understanding biogeochemical dynamics of the planet's critical zone. Traditionally, microbial and thermogenic methane gases are interpreted by their carbon ($\delta^{13}C$) and hydrogen (δD) isotopic compositions (e.g., Schoell, 1988; Whiticar, 1999). However, applying $\delta^{13}C$ and δD as a diagnostic framework alone has significant limitations, most notably circumstances in which isotopic signatures of methane sources are not sharply demarcated, exhibit some degree of overlap, and such empirical frameworks are inevitably redefined as additional experimental and field data come to light (Sherwood Lollar et al., 2006; Douglas et al., 2017). In addition, empirical fields in $\delta^{13}C$ vs. δD space are inherently linked to the isotopic signature of the source materials coupled with the formation processes, which in turn are strongly affected by mixing and secondary alteration processes (Etiope and Sherwood Lollar, 2013 and references therein).

Recently, sophisticated instrumentation has become available to precisely measure the abundances of doubly substituted, "clumped", isotopologues of methane gas, including $^{13}CH_3D$ (Ono et al., 2014; Stolper et al., 2014b) and $^{12}CH_2D_2$ (Young et al., 2016). The relative abundances of these two mass-18 methane isotopologues are expressed as $\Delta^{13}CH_3D$ and $\Delta^{12}CH_2D_2$ values, representing deviations from a stochastic standard in which distributions of isotopes across all isotopologues are effectively random. The latter is the expected state at sufficiently high temperatures (>1000 K). The relative abundances of doubly substituted methane isotopologues differs from the stochastic distribution at lower temperatures due to the enhanced thermodynamic stability of bonds involving the heavier isotopes (e.g., Ma et al., 2008; Webb and Miller, 2014; Liu and Liu, 2016). In principle, isotopic bond ordering, or clumping, is a tracer of the processes attending the formation of the molecules independent of source material, coupled with any consumption and/or re-equilibration processes, and therefore gives the potential for their application to discern processes of methane formation and oxidation both on Earth and beyond (Young, 2019). The utility of $\Delta^{13}CH_3D$ and $\Delta^{12}CH_2D_2$ lies in the fact that the values should be sensitive to process, but not substrate, and interpretations of their significance are not dependent upon long-lost isotope exchange partners (e.g., water). In practice, this appears to be true with some exceptions due to significantly different δD of hydrogen sources that contribute to the formation of methane molecules (Taenzer et al., 2020).

In some cases, $\Delta^{13}CH_3D$ has been used to reconstruct the formation temperatures of thermogenic methane (Stolper et al., 2014a) and the combination of $\Delta^{13}CH_3D$ and $\Delta^{12}CH_2D_2$ has been used to verify that the molecules record equilibrium at a given temperature (Young et al., 2017; Xie et al., 2021). The abundances of mass-18 isotopologues of microbial methane, on the other hand, have been shown to be inconsistent with thermodynamic equilibrium, meaning that

their distribution does not reflect the temperature at which the methane was formed (Stolper et al., 2015; Wang et al., 2015; Young et al., 2017; Ash et al., 2019; Giunta et al., 2019; Warr et al., 2021). The $\Delta^{13}CH_3D$ and $\Delta^{12}CH_2D_2$ of microbial methane can be modeled as the result of the combination of equilibrium and kinetic steps during the enzymatically facilitated formation of methane (Cao et al., 2019; Young, 2019; Gropp et al., 2021; Gropp et al., 2022; Ono et al., 2022). In particular, the extremely negative $\Delta^{12}CH_2D_2$ values are most likely due to the combinatorial effect of accessing multiple sources of hydrogen with significantly different hydrogen isotopic signatures during the formation of methane (Röckmann et al., 2016; Yeung, 2016; Young, 2019; Taenzer et al., 2020). Furthermore, abiotic methane and low-maturity thermogenic methane has been found with deficits in $^{12}CH_2D_2$ compared with equilibrium values in methane gas, but the true range of methane sources in $\Delta^{13}CH_3D$ vs. $\Delta^{12}CH_2D_2$ space remains poorly defined due to limited data (Douglas et al., 2017; Young et al., 2017; Dong et al., 2021; Warr et al., 2021; Xie et al., 2021).

While the ability to define a methane isotopologue signature related to microbial methanogenesis is promising, there are caveats. One is that abiotic or biotic consumption processes could potentially alter the relative abundances of the mass-18 isotopologues in ways that might mimic the putative microbial methanogenesis signature. Laboratory experiments and *ab initio* modeling indicate that methane oxidation in the atmosphere by OH or Cl radicals is accompanied by large shifts in methane clumping down to very negative $\Delta^{13}CH_3D$ and $\Delta^{12}CH_2D_2$ values due to Rayleigh distillation (Haghnegahdar et al., 2017; Whitehill et al., 2017; Young, 2019). Similarly, both $\Delta^{13}CH_3D$ and $\Delta^{12}CH_2D_2$ values of residual methane in microbial culture were observed to decrease during aerobic oxidation of methane (Wang et al., 2016; Krause et al., 2022).

Photocatalytic oxidation and aerobic microbial oxidation of methane occur in the atmosphere and oxygenated environments. Therefore, these processes are in principle separated spatially from microbial methanogenesis, which operates almost exclusively under anoxic, and thus reducing, conditions. Anaerobic oxidation of methane (AOM), however, is closely related to methanogenesis both spatially and metabolically. For example, concurrent methanogenesis and AOM have been found in near-surface sediment and at the sulfate–methane transition (Xiao et al., 2017; Beulig et al., 2019; Krause and Treude, 2021). Anaerobic methanotrophic (ANME) archaea are close relatives of methanogenic archaea and have the full enzymatic machinery of methanogenesis working in reverse (Timmers et al., 2017). The recent demonstration of methanogens belonging to *Methanosarcina* reversing key reactions of methanogenesis coupled to ferric iron reduction (Yan et al., 2018; Yu et al., 2022) and, vice versa, the prospect of a methanotroph (ANME-1) from natural sediment conducting methanogenesis (Beulig et al., 2019; Kevorkian et al., 2021) underscore the potential versatility of methanoarchaeal enzymes. Factors forcing these enzymes to operate in either direction need further investigation. However, even when operating in full AOM mode with the highest net turnover of methane, ANME archaea demonstrate some fraction (~4–15%) of net reversibility, defined as the ratio of the backward to forward fluxes (Treude et al., 2007; Holler et al., 2011; Wegener et al., 2021). Back flux of material during the enzymatic reactions of AOM has implications for isotope fractionation, leading to carbon isotope ($^{13}C/^{12}C$) equilibration between methane and intracellular metabolites, in particular when AOM is operating close to thermodynamic limitations where the methyl-coenzyme M reductase (Mcr)-catalyzed reaction is near equilibrium (Hoehler et al., 2000; Holler et al., 2011; Yoshinaga et al., 2014; Chuang et al., 2019; Wegener et al., 2021).

The precise mechanisms that are responsible for $\Delta^{13}CH_3D$ vs. $\Delta^{12}CH_2D_2$ effects of AOM are largely unknown, and further laboratory incubation experiments under different environmental conditions are required. The overarching goal is to develop these intra-methane isotopologue signals as tracers for the origin and processing of methane in general, and AOM in particular. One of the biggest challenges for understanding the isotopologue composition of natural samples is limited knowledge of how isotopic bond re-ordering caused by AOM can overwrite formation-process signatures. Given the high level of reversibility of Mcr-catalyzed reactions during AOM, Ash et al. (2019), Giunta et al. (2019), and Warr et al. (2021) suggested that AOM could be responsible for thermodynamic isotopic bond-order equilibrium in methane found in sulfate-depleted Baltic Sea sediment, sedimentary basins, and the deep subsurface, respectively. Recently, Ono et al. (2021) found that the methane clumped isotopologue $^{13}CH_3D$ exhibits kinetic fractionation in an ANME-1 sediment-free enrichment culture with a high sulfate concentration (28 mM), where $\Delta^{13}CH_3D$ values increased by up to 5.8‰. Importantly, Wegener et al. (2021) demonstrated a sulfate dependence of the net bulk isotopic fractionation by virtue of the thermodynamic drive of the intracellular reactions of AOM. Based on the earlier studies, therefore, it appears that the reversibility of intracellular reactions of AOM is responsible for the observed discrepancy between the kinetic isotopologue fractionation in a sulfate-replete culture (Ono et al., 2021) and the intra-species isotope equilibrium in sulfate-depleted settings (Ash et al., 2019; Giunta et al., 2019; Warr et al., 2021).

To document the range of effects that AOM may have on modifying methane isotopologue signatures, we collected a suite of marine sediments and fracture fluids from diverse marine and terrestrial settings that showed different degrees of ANME abundance and AOM activity (Fig. 1). We performed microbial incubations using these samples to evaluate the relationship between the

202

reversibility of intracellular reactions of AOM and the methane isotopologue fractionation/re-ordering, and to elucidate the unknown fractionation factors for $^{12}CH_2D_2/^{12}CH_4$. We also collected natural fluids from the South Chamorro Seamount where AOM is known to substantially consume abiotic source methane (Wheat et al., 2020), in order to examine whether the isotopologue fractionation differs between laboratory incubations and endogenous AOM in natural environments. In combination, our work aims to address how environmental conditions can potentially affect isotopologue fractionation, as well as rates and magnitudes of isotopic bond re-ordering during AOM. This information will improve our ability to distinguish primary signatures of methane formation from biologically-driven overprinting to maximize the utility of $^{13}CH_3D/^{12}CH_4$ and $^{12}CH_2D_2/^{12}CH_4$ as tracers of methane formation and subsequent processing.
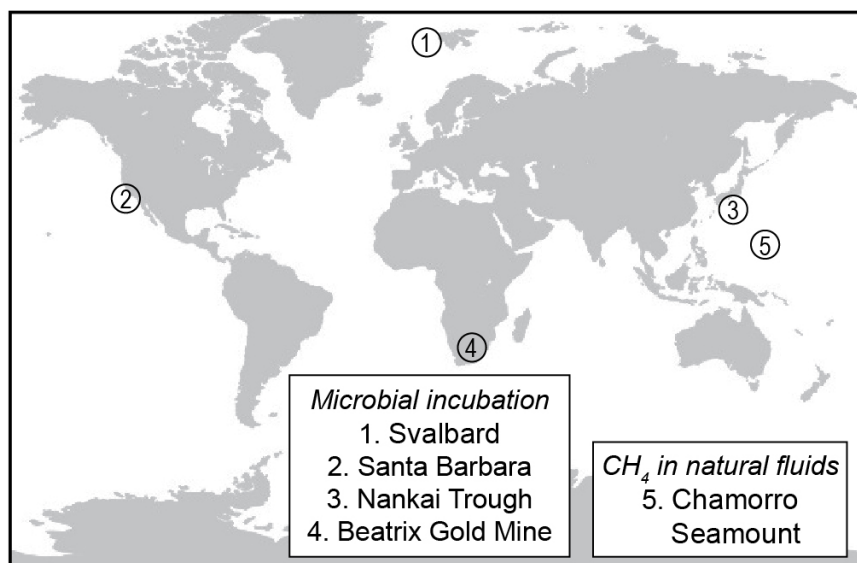

Fig. 5-1 Global map showing sampling sites for this study. Marine sediments or fracture fluids were collected for slurry or fluid incubations at (1) Svalbard methane seeps, (2) Santa Barbara Channel methane seeps, (3) Nankai Trough (International Ocean Discovery Program Hole C0023A), and (4) Beatrix Gold Mine, South Africa. Methane in natural fluids was collected from a sub-seafloor borehole observatory (Ocean Drilling Program Hole 1200C) on (5) South Chamorro Seamount, a serpentinite mud volcano in the Mariana forearc.

2. Materials and methods

2.1. Incubation of methane seep sediment slurry from Svalbard

Marine sediment were collected in summer 2011 with a video-guided multicorer from active methane seeps covered by a dense sulfur-bacteria mat offshore northwestern Svalbard during the R/V *Poseidon* cruise 419 (Site MUC 12; 79°00.417' N, 06°54.131' E, 1235 m water depth). Details of the sampling site, including *ex-situ* activity of AOM (Fig. 2A) and sulfate reduction and geochemical parameters in replicate sediment cores, can be found in Melaniuk et al. (2022). Sediment used for the present study was collected from the top 10 cm of a replicate multicorer core (10 cm inner diameter) and filled headspace-free into 100- and 250-ml borosilicate bottles with butyl stoppers. The sediment was stored anoxically at 4 °C in the dark for 10 years without methane or sulfate addition. The AOM community in the sediment was reactivated in the laboratory at UCLA in April 2020 by mixing with anoxic artificial seawater medium at a ratio of 1:1 (v:v) (Widdel and Bak, 1992; Laso-Pérez et al., 2018) and a methane gas headspace as the sole amended carbon source in a 2-L glass bottle. The cultivation procedures of Laso-Pérez et al. (2018) were followed.
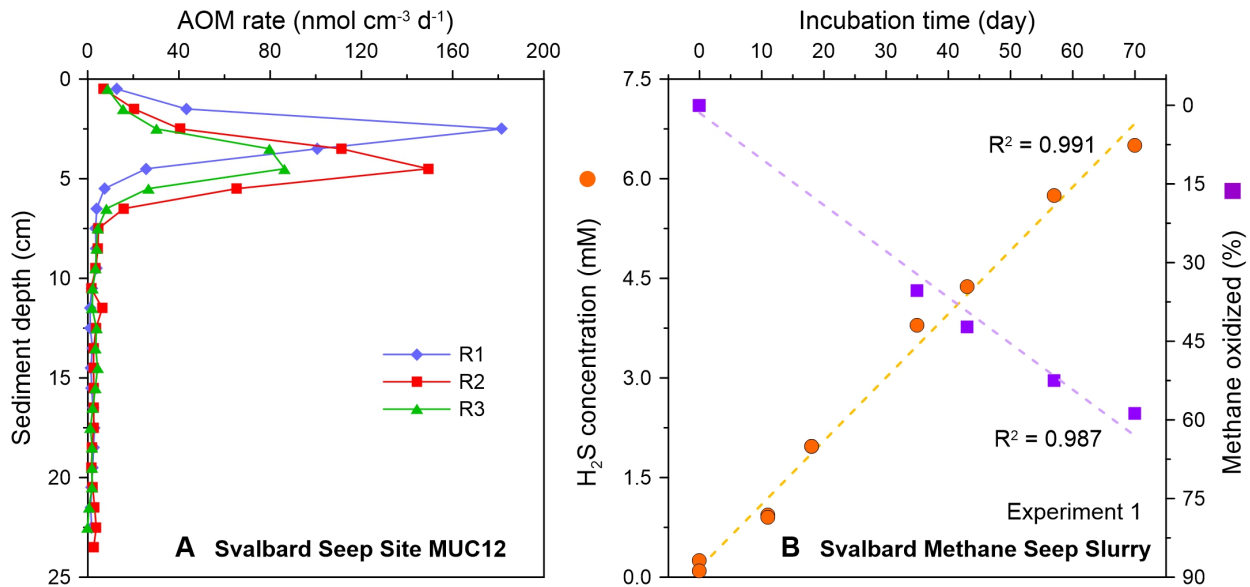
Fig. 5-2 Geochemistry of the Svalbard methane seep sediment and slurry. (A) *Ex-situ* AOM rates determined by $^{14}CH_4$ radiotracer at Site MUC12 offshore Svalbard (Melaniuk et al., 2022). R1–3 represents replicate one through three. (B) Evolution of dissolved sulfide concentration and percentage of methane oxidized in the Svalbard methane seep sediment slurry with high sulfate concentrations. Linear regressions are shown in panel B.

We performed a set of sulfide analyses to confirm the activity of AOM before starting the actual experiments. Sulfide concentration in the supernatant started to increase two months after addition of substrates (sulfate and methane). Further, sulfide concentration increased ca. 0.07 mM per day between the 134th and 205th days since reactivation. The supernatant of the sediment slurry was replaced with fresh anoxic medium when sulfide concentration approached 11 mM. After that, sulfide concentration continued to increase ca. 0.07 mM per day between the 206th and 283rd days since reactivation. The linear increase in sulfide concentration over time indicates that the ANME community was successfully reactivated in the sediment slurry, which is a remarkable finding considering that the sediment was stored for a decade. Thus, the homogenized slurry was equally distributed to two 600-ml culture bottles in replicate and filled up completely with an anoxic artificial seawater medium (Laso-Pérez et al., 2018). Sixty ml of the medium volume was replaced with ca. 200 kPa of methane (Airgas), and both incubations were performed under excess sulfate

(ca. 10 mmol) over methane (5.4 mmol) (cf. Ono et al., 2021). The sediment slurry was then stored horizontally at 4 °C in the dark. Methane isotopologue compositions were analyzed on days 1, 36, 44, 58, and 71 of the incubation. After the first experiment, we reset the slurry for longer incubation through medium replacement and bubbling with N_2/CO_2 gas. Methane isotopologue compositions were analyzed on days 1, 60, 90, and 168 of the incubation.

After the high-sulfate experiment described above, the supernatant in the slurry was replaced with low-sulfate artificial seawater medium (1 mM) multiple times. The sulfate concentration in the slurry decreased over time due to medium replacement and microbial consumption. The produced sulfide was maintained at low concentration (<1 mM) through medium replacement and bubbling with N_2/CO_2 gas. The culture bottle was then filled up completely with the low-sulfate medium, reaching a sulfate concentration of 0.4 mM in the slurry. Sixty ml of the medium volume was replaced with ca. 200 kPa of methane (Airgas), allowing the incubation to be performed under excess methane (5.4 mmol) over sulfate (<0.2 mmol). The low-sulfate experiment was performed identically to the high-sulfate experiment with sulfate concentration as the only variable at the beginning of each incubation. Towards the end of the low-sulfate experiment, sulfate was depleted (0.01 mM) in the slurry. Thus, additional concentrated anoxic sulfate solution (2.5 ml) was added to the culture bottle by a syringe without opening the bottle, reaching a final sulfate concentration of 0.4 mM again in the slurry.

Methane concentration and isotopologue abundance were determined during the incubations on a vacuum line interfaced with a gas chromatograph, and the Panorama mass spectrometer, respectively, as described below in section 2.6. Given the known volume and porosity of the slurry, the amounts of methane that dissolved in the liquid phase were calculated using Henry's law and the Bunsen solubility coefficient (Yamamoto et al., 1976). The total

amounts of methane in the culture bottle were therefore the sum of methane in the headspace and the liquid phase. The liquid phase was also sampled for geochemical analyses. Sulfate concentration was analyzed by ion chromatography (Metrohm 761). Sulfide concentration was measured after Cord-Ruwisch (1985) using a Shimadzu UV-Spectrophotometer (UV-1800). Alkalinity was determined by acid titration with a Metrohm 876 Dosimat Plus (Dale et al., 2015). The relative standard deviation (RSD) of sulfate, sulfide and alkalinity analyses were better than 2%, 5% and 2%, respectively. In addition, pH was determined by a pH meter (VWR sympHony B10P).

A control incubation was set up to assess potential microbial methanogenesis in the same sediment slurry. The control experiment was prepared by replacing the supernatant with a new methane-free anoxic artificial seawater medium and a 60-ml headspace was left to monitor methane concentration. The slurry was then bubbled thoroughly with N_2/CO_2 (90:10) three times (3 hours in total) to get rid of the residual dissolved methane and sulfide from the previous experiments. The slurry was stirred during and between flushing to drive the dissolved methane into the headspace. The control experiment slurry was stored in the dark at 4 °C for three months. The slurry supernatant was collected for sulfide and sulfate concentrations at the start and end of the control incubation. Methane concentration in the gas phase was measured by gas chromatography throughout the three-month period.

2.2. Incubation of methane seep sediment slurries from the Santa Barbara Channel

Marine sediment were collected with four push cores from the Coal Oil Point seep field (Rostocker Seep and Isla Vista Super Seep) in the Santa Barbara Channel in 2017 (Jordan et al., 2020). The top 12.5 cm sediment of the cores was transferred to 300 ml culture bottles at UCLA

following the same procedure as detailed in the Svalbard slurry section above. Low sulfate (< 1 mM) and high sulfate (> 28 mM) concentrations were achieved in the sediment slurry by either dilution steps with anoxic artificial seawater (without sulfate) or additions of concentrated sodium sulfate solution (100 mM). The sediment slurry was incubated in the dark with a 4.4 ml headspace of methane at ca. 100 kPa and 20 °C on a shaker. The methane gas bubble from the sediment slurry was extracted at the end of each experiment and geochemistry analyses were performed as described in the Svalbard slurry section. A similar control experiment followed the Svalbard slurry section with a 4.4 ml Argon headspace.

2.3. Incubations of sediment slurry and fracture fluid from the deep biosphere (Nankai Trough and Beatrix Gold Mine)

Hole C0023A (32°22.0018′ N, 134°57.9844′ E), located in the Nankai Trough on the subduction boundary between the Philippine Sea and Eurasian plates, was drilled during International Ocean Discovery Program (IODP) Expedition 370 in 2016 (Heuer et al., 2017). Marine sediment from 257 m below seafloor (mbsf) were sampled anoxically with rigorous contamination control (see Heuer et al., 2017) and utilized for sediment incubation. In brief, whole-round cores (WRCs) were prepared from recovered sections under super-clean and anoxic conditions onboard the *Chikyu* Drilling Vessel. X-ray computed tomography was performed on all WRCs for lithological identification and to assess core quality on board. Samples without drilling disturbances were designated for incubation and were subjected to secondary scraping to minimize the potential for contamination.

At South Africa's Beatrix Gold Mine (28 ˚14.1′ S, 26˚47.7′ E), fracture fluid was collected in 2016 from the BE326-BH2 borehole, from 1390 m below land surface (mbls) in shaft 3, level

26. A detailed description of the study site and sample collection has been published in Lau et al. (2016). Briefly, fracture fluid was filtered using a 0.2 μm hollow fiber MediaKap®-10 filter (Spectrum Labs, New Brunswick, NJ USA). The microorganisms on the filter were anoxically back-flushed into sterile, capped, N_2-sparged 160-ml borosilicate serum vials to a final cell concentration of ~ 10^7 cells ml^{-1}. Samples were stored at 4 °C upon return to the surface and used for incubation.

Incubations were set up inside a clean anoxic glove bag (Coy Laboratory Products, Grass Lake, MI USA) at Princeton University. Sterile aluminum foil was placed on the working surface of the glove bag and sterile nitrile gloves were used over the glove bag's butyl rubber gloves to minimize potential contamination of low-biomass samples. The surface of C0023A samples was scraped using a sterile scalpel to remove sediment exposed to gas-tight packaging. A total of 10 g (wet weight) of interior sediment was weighed out from sample source core C0023A-5F02 (top depth 257.3 mbsf) and transferred into combusted 160-ml borosilicate serum vials containing 100 ml artificial sulfate-free seawater medium modified from the recipe by Widdel and Bak (1992). For the BE326-BH2 incubation, 10 ml of fracture fluid was added to 90 ml artificial sulfate-free seawater medium. Serum vials were sealed with 0.1 N NaOH-boiled butyl rubber stoppers (Bellco Glass, Inc., Vineland, NJ USA) and aluminum crimps (Supelco Inc., Bellefonte, PA USA), and the headspace was subsequently replaced with 100% methane. Each incubation was supplemented with 10 mM of one of the following electron acceptors: NO_3^-, NO_2^-, SO_4^{2-}, or Fe^{3+} (in the form of hydrous ferric oxide). A control without added electron acceptors was included to assess endogenous microbial activity from remnant electron acceptors available in the inoculum, and an autoclaved sample was included as a killed control. Serum vials containing sediment slurry or fracture fluid were incubated upside-down at an approximate *in-situ* temperature of 40 °C. At

UCLA, the collected residual methane was purified for isotopologue analysis following the method described in section 2.6.

Electron acceptor depletion was monitored using Dionex IC25 ion chromatography coupled to an MSQ-quadruple mass spectrometer (Thermo Scientific, Waltham, MA USA). The sediment slurry or fracture fluid was also subsampled to monitor the $\delta^{13}C$ of dissolved inorganic carbon (DIC). Briefly, 500 µl aliquots were anoxically transferred to combusted, amber borosilicate serum vials treated with saturated $HgCl_2$ and aluminum-crimped sealed with butyl rubber stoppers. Following sample transfer, vials were over-pressurized with ultra-high purity N_2 gas, supplemented with 0.5 N H_3PO_4, and heated overnight in a water bath at 70 °C to extract all DIC out of solution. Isotopic composition of the headspace was analyzed using a Picarro cavity ring-down spectrometer equipped with a G2101-I Isotopic CO_2 analyzer (Picarro, Inc., Sunnyvale, CA USA) in CO_2 focus mode.

2.4. Methyl-coenzyme M reductase (Mcr) experiments

The experiment was performed as described previously with the Mcr enzyme purified from *Methanothermobacter marburgensis* (Mahlert et al., 2002; Scheller et al., 2010) at Pennsylvania State University. Mcr that was used for this assay had absorbance maxima at 387 nm, corresponding to the enzyme's active (Ni^+) form. Coenzyme B (HS-CoB) was prepared from the symmetric disulfide CoB-S-S-CoB by reaction with $NaBH_4$. Methyl-coenzyme M (CH_3-S-CoM) was synthesized from coenzyme M (sodium salt) by methylation with methyl iodide. The complete reaction mixture (4 ml) contained 5 mM CH_3-S-CoM, 2.5 mM HS-CoB and 32.3 mg of Mcr in 50 mM phosphate buffer (pH 7.6). This allowed isotope exchange of the methyl moiety in methyl-coenzyme M and methane to occur. The reaction mixtures were incubated at 20 °C for 48 hours

or 60 ºC for 2–6 hours in a stoppered 10-ml serum vial with a methane headspace of ca. 100 kPa. The difference in incubation times is due to more rapid reaction at 60 ºC. Control reactions contained the complete reaction mixture minus enzyme. At UCLA, the collected gas was purified for isotopologue analysis following the method detailed in section 2.6.

2.5. Methane-bearing natural fluids at the South Chamorro Seamount

South Chamorro Seamount is an active serpentinite mud volcano at ca. 3150 m water depth in the Mariana forearc. In 2001, Hole 1200C was drilled to 266 mbsf and cased during Ocean Drilling Program (ODP) Leg 195 in the summit knoll of South Chamorro Seamount (Fryer and Salisbury, 2006). An oceanic borehole observatory, commonly called a CORK (Circulation Obviation Retrofit Kit), was deployed for subsequent fluid sampling (Wheat et al., 2008). The discharged fluids were largely altered relative to seawater composition, displaying a high pH up to 12.3 with abundant dissolved methane up to 33 mM (Wheat et al., 2008; Wheat et al., 2020). In January 2009, pristine crustal fluids were collected directly as they discharged at Hole 1200C with a remotely operated vehicle (ROV) *HyperDolphin* (HPD Dives 941–947) during Cruise NT09-01 (Wheat et al., 2020). Isobaric gas-tight samplers (Seewald et al., 2002) were used for fluid sampling. Immediately upon recovery of the ROV, fluid samples were subsampled for liquid and gas analyses. Gas extraction from fluid samples was conducted using previously reported techniques (Seewald et al., 2002). At UCLA, the collected gas was purified for isotopologue analysis following the method detailed in the next section.

2.6. Doubly substituted isotopologue measurements and isotope notation

Methane isotopologue abundances of methane gas samples were measured using the Panorama (Nu Instruments) high-mass-resolution gas-source isotope ratio mass spectrometer housed at UCLA. Details surrounding the purification and measurement of methane gas were previously published (Young et al., 2016; Young et al., 2017) and are briefly summarized here. Methane sample gases were purified on a vacuum line interfaced with a gas chromatograph (GC). Samples were delivered to the vacuum line through a septum by a gas-tight syringe and trapped on silica gel at liquid nitrogen temperature. The Helium carrier gas was then used to flush the sample to the GC. Separation was accomplished with a 3-meter 1/8-inch OD stainless steel column packed with 5 Å molecular sieve, followed in series by a 2-meter 1/8-inch OD stainless steel column packed with HayeSep D porous polymer. Peaks were identified using an in-line, passive thermal conductivity detector (TCD). Once methane collection was complete, the sample was transferred to an evacuated sample tube filled with silica gel at liquid nitrogen temperature. Methane in this tube was introduced to the inlet of the mass spectrometer where it was warmed and expanded into the bellow of the instrument.

The Panorama mass spectrometer was set to a mass resolving power of ~40,000 or greater, allowing the measurement of ion currents for resolved $^{12}CH_4^+$, $^{13}CH_4^+$, $^{12}CH_3D^+$, $^{13}CH_3D^+$, and $^{12}CH_2D_2^+$. Isotopologues of masses 16 and 17 were measured using Faraday collectors with amplifier resistors of 10^{11} Ω. Both doubly substituted mass-18 isotopologues, $^{13}CH_3D^+$ and $^{12}CH_2D_2^+$, were measured with an electron multiplier as the axial collector. The measured ratios of these ion currents yield values for bulk $^{13}C/^{12}C$ and D/H as well as for both $\Delta^{13}CH_3D$ and $\Delta^{12}CH_2D_2$. The isotopic compositions of carbon and hydrogen are reported as deviations from the carbon and hydrogen reference materials Vienna Pee Dee Belemnite (VPDB) and Vienna Standard

Mean Ocean Water (VSMOW). Standard delta notation is used to express the fractional differences in per mil units:

$$\delta^{13}C = [(^{13}C/^{12}C)_{sample}/(^{13}C/^{12}C)_{VPDB} - 1] \times 1000 \tag{1}$$

$$\delta D = [(D/H)_{sample}/(D/H)_{VSMOW} - 1] \times 1000 \tag{2}$$

The relative abundances of the two mass-18 isotopologues of methane are reported relative to the stochastic reference frame expressed in per mil using the capital delta notation:

$$\Delta^{13}CH_3D = [(^{13}CH_3D\,/^{12}CH_4)_{sample}/(^{13}CH_3D\,/^{12}CH_4)_{stochastic} - 1] \times 1000 \tag{3}$$

$$\Delta^{12}CH_2D_2 = [(^{12}CH_2D_2/^{12}CH_4)_{sample}/(^{12}CH_2D_2/^{12}CH_4)_{stochastic} - 1] \times 1000 \tag{4}$$

External precision for $\delta^{13}C$, δD, $\Delta^{13}CH_3D$, and $\Delta^{12}CH_2D_2$ is approximately 0.1‰, 0.2‰, 0.2‰ and 0.6‰, respectively (1σ), based on replicate samples. The relationship between temperature and both $\Delta^{13}CH_3D$ and $\Delta^{12}CH_2D_2$ has been predicted through *ab initio* calculations and can be expressed by the following equations (Young et al., 2017):

$$\Delta^{13}CH_3D\,(T) \approx 1000\ln(1 + 0.0355502/T - 433.038/T^2 + 1270210.0/T^3 - 5.94804$$
$$\times\,10^8/T^4 + 1.196630 \times 10^{11}/T^5 - 9.07230 \times 10^{12}/T^6) \tag{5}$$

$$\Delta^{12}CH_2D_2\,(T) \approx 1000\ln(1 + 0.183798/T - 785.483/T^2 + 1056280.0/T^3 + 9.37307$$
$$\times\,10^7/T^4 - 8.919480 \times 10^{10}/T^5 + 9.901730 \times 10^{12}/T^6) \tag{6}$$

where T is in Kelvin. Eqs. (5) and (6) show that $\Delta^{13}CH_3D$ and $\Delta^{12}CH_2D_2$ values are both positive when methane is formed at thermodynamic equilibrium, and approach 0‰ at high temperatures (>1000 K).

2.7. Calculation of isotope fractionation factors using Rayleigh equation

Incubations were performed in glass bottles with frequent shaking and the headspace methane was considered a well-mixed source in a closed system. Although methane in the

headspace was extracted once or twice between the start and end of each experiment, the amount of methane extracted was minor (<3%) compared to the amount of methane in the whole bottle, resulting in a negligible deviation from a strictly closed system. Thus, the Rayleigh fractionation equation (Mariotti et al., 1981) was used to extract fractionation factors for the $^{13}CH_4$, $^{12}CH_3D$, $^{13}CH_3D$, and $^{12}CH_2D_2$ isotopologues relative to $^{12}CH_4$ resulting from anaerobic fractionation:

$$\frac{R}{R^0} = \left(\frac{^{12}CH_4}{^{12}CH_4^{\,0}} \right)^{\alpha-1} \tag{7}$$

where R refers to the ratio of isotopologues of interest in the gas phase (e.g., $^{13}CH_3D$ /$^{12}CH_4$, $^{12}CH_2D_2$/$^{12}CH_4$), the superscript 0 signifies the initial property, and the ratio of methane abundance at time t relative to the initial methane abundance is commonly referred to as F (fraction remaining). The fractionation factor α is the ratio of isotopologue ratios where the numerator ratio refers to the consumed methane and the denominator refers to the reactant methane. For the sake of simplification, the isotopologue fractionation factor for $^{13}CH_3D$ and $^{12}CH_2D_2$ relative to $^{12}CH_4$ are termed $^{13D}\alpha$ and $^{D2}\alpha$, respectively. By convention, $\alpha < 1$ signifies that the reaction favors the isotopically light species, leaving the residue enriched in the heavy isotope or isotopologue. On a plot of $-\ln F$ vs. $\ln(R/R^0)$, the slope (often termed ε) provides the fractionation factor ($^{13}\varepsilon = 1-^{13}\alpha$ or $^{D}\varepsilon = 1-^{D}\alpha$). Fractionations and their uncertainties (95% confidence interval) are calculated by the weighted least square method (York et al., 2004). Errors for methane concentrations are estimated to be 0.4% of the measured value. Note that the F ratio was only measured in the incubation experiment of the Svalbard methane seep sediment.

At zeroth order, the relationship among isotopologue fractionation factors would follow the rule of the geometric mean (Bigeleisen, 1955), in which a stochastic distribution of isotopes occurs among the isotopologues. This would be the case where there is no energetic preference for

forming doubly substituted isotopologues as opposed to randomly distributing isotopes among bonds (e.g., $^{13D}\alpha \approx {}^{13}\alpha \cdot {}^{D}\alpha$). Under these circumstances, the fractionation factors for the doubly substituted species are simply the products of the fractionation factors for the individual isotopes (i.e., the square of the geometric mean of the fractionation factors for doubly substituted species). The deviation from the rule of the geometric mean can be characterized by the kinetic clumped isotopologue fractionation factor, γ, yielding (cf. Wang et al., 2016):

$$^{13D}\alpha = {}^{13D}\gamma \cdot {}^{13}\alpha \cdot {}^{D}\alpha \tag{8}$$

$$^{D2}\alpha = {}^{D2}\gamma \cdot {}^{D}\alpha \cdot {}^{D}\alpha \tag{9}$$

2.8. Open system model — steady-state between transport and oxidation of moving methane

In natural environments, Rayleigh-type methane oxidation is rarely observed because replenishment of methane, facilitated by advection or diffusion, usually applies. We will consider two end-member environmental scenarios: a steady-state open system model presented in this section and a time-dependent closed system model with a methane source and sink in the next section.

In the open system model, methane is transported into and out of the system via advection with concurrent AOM. A steady state between oxidation and supply is considered to have been attained. A mass balance equation at steady state can be expressed as (Hayes, 2001; Wang et al., 2016):

$$R^0 = (1 - \varphi) R_{SS} + R_{SS} \, \varphi \, \alpha \tag{10}$$

where R^0 is the initial isotopologue ratio, R_{SS} is the steady-state value, φ is the fraction of gas affected by oxidation relative to the total flux, and α is the kinetic fractionation factor associated with the oxidation reaction. Such a steady state will occur where the supply and sink occur at

constant rates. Here, advection is assumed to have no isotope effect (Alperin et al., 1988), whereas AOM has associated fractionation factors $^{13}\alpha$, $^{D}\alpha$, $^{13D}\gamma$, and $^{D2}\gamma$. The fractional contribution of AOM to the total sink, φ, is physically related to the Damköhler number, i.e., Da, the ratio of the residence time in the flow system to the characteristic reaction time (i.e., $Da = \tau/(1/k)$ where τ is the residence time and k is the reaction rate constant). The φ values are normalized Da, as in $\varphi = Da/(1+Da)$. Therefore, if k is large in comparison to τ, Da is large and φ approaches 1. At this extreme, a balance between production and oxidation is achieved in a closed system as described in the next section. Conversely, if k is small in comparison to τ, φ approaches 0 and the isotopologue ratio does not change. Values in between these extrema cause the steady-state values to be intermediate between the initial isotopologue ratios and the values at $\varphi = 1$.

2.9. Closed system model — formation of methane balanced against oxidation

In the closed system model, the time-dependent evolution of the moles of an isotopologue of methane can be described in terms of a constant rate of production and a rate of oxidation that behaves as a first-order reaction with an invariable rate constant (Haghnegahdar et al., 2017). In this simplest model, where the balance is only between production and consumption, the system can be described as:

$$\frac{dn_i}{dt} = E_i - k_i n_i,$$ (11)

where n_i is the moles of the isotopic species of interest, E_i is the source term for i (e.g., rate of abiotic or microbial methanogenesis), and k_i is the rate constant for the sink i (i.e., the rate constant for oxidation). The solution to Eq. (11) yields:

$$n_i(t) = n_i^0 e^{-k_i t} + \frac{E_i}{k_i}\left(1 - e^{-k_i t}\right),$$ (12)

where n_i^0 is the initial moles of i. The moles of species i at steady state is obtained by evaluation Eq. (12) where t → ∞, and thus $e^{-k_i t} \to 0$, yielding:

$$n_i(t \sim \infty) = \frac{E_i}{k_i}. \tag{13}$$

Considering i to be the major isotopologue, the steady-state amount of methane is controlled by the ratio of the production rate and the rate constant for oxidation. The steady-state ratio of two isotopologues can therefore be expressed as:

$$\frac{n_j(t \sim \infty)}{n_i(t \sim \infty)} = \frac{E_j}{k_i} \frac{E_i}{k_j} \tag{14}$$

where n is the moles of the two isotopologues i and j. The steady-state isotopologue ratio depends on the isotopologue ratio of the methane produced (E_j/E_i) and the reciprocal of the fractionation due to oxidation (k_i/k_j), independent of the absolute rates.

3. Results

Methane isotopologue data from laboratory experiments and natural fluids are presented in Figure 3. The $\Delta^{13}CH_3D$ and $\Delta^{12}CH_2D_2$ values from the Svalbard sediment slurry incubation and Chamorro Seamount natural fluids are higher than thermodynamic equilibrium values at their ambient temperature (>0 °C; Fig. 3A–C). Other incubations, including the Mcr-catalyzed isotope exchange and incubations of the Santa Barbara Channel sediment, Nankai Trough sediment, and Beatrix Gold Mine fracture fluid, show moderate increases in $\Delta^{13}CH_3D$ but minimal increases in $\Delta^{12}CH_2D_2$ (Fig. 3D–F). Their apparent temperatures based on clumped isotopes are similar to the experimental temperatures, ranging from 20 °C to 60 °C. In the following sections, we first present the laboratory incubation data and then show natural fluid data for comparison.
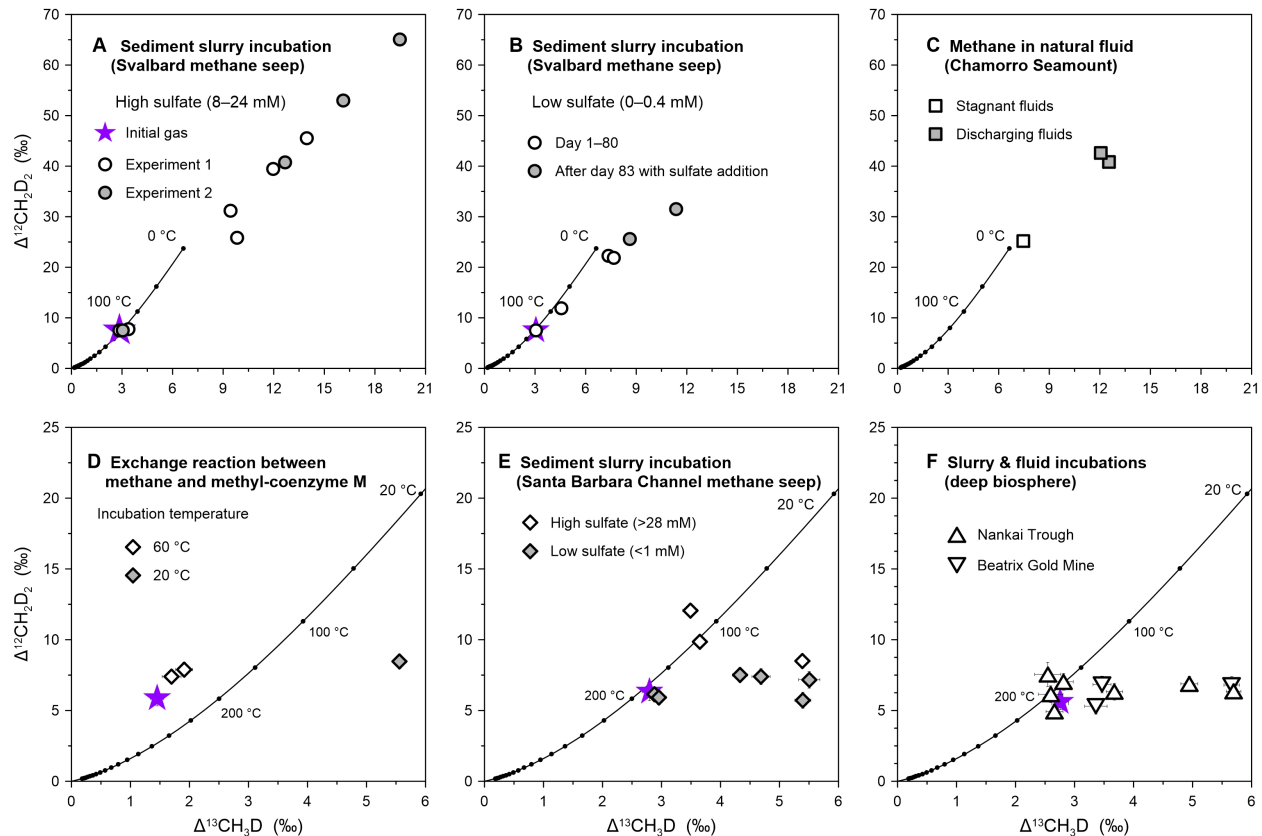
Fig. 5-3 Clumped isotope data of residual methane in AOM incubation experiments and natural fluids. (A–B) Incubation of the Svalbard methane seep sediment slurry with high sulfate concentration (8–24 mM; panel A) and low sulfate concentration (0–0.4 mM; panel B). (C) Methane in natural fluids collected from the South Chamorro Seamount. (D) Exchange reaction between methane and methyl-coenzyme M. (E) Incubation of the Santa Barbara Channel methane seep sediment slurry. (F) Incubations of the Nankai Trough sediment slurry and Beatrix Gold Mine fracture fluid from the deep biosphere. The purple stars represent the initial tank gas. The solid black line depicts theoretical thermodynamic equilibrium abundances of methane isotopologues, along with corresponding temperatures. Error bars are 1σ. Note different scales between panels A–C and D–F.

3.1. Incubation of the Svalbard methane seep sediment slurries

Off-shore methane seep sediment from the Svalbard archipelago host high AOM activity. *Ex-situ* AOM rates determined by ^{14}C-radiotracer techniques peak at 182 nmol cm^{-3} d^{-1} at 2–5 cm below seafloor (Fig. 2A) (Melaniuk et al., 2022). In the reactivated sediment slurry with saturated methane and high sulfate concentrations (8–24 mM), dissolved sulfide concentrations increase linearly as methane is oxidized simultaneously (Fig. 2B), indicating that AOM is active in the sediment slurry and the primary mechanism for methane removal in the experiment. The AOM

rate determined by methane concentrations in the slurry incubation was 90 nmol of methane per cm^3 sediment slurry per day (Fig. 2B), translating into about 180 nmol per cm^3 of undiluted sediment per day. This is consistent with the *ex-situ* AOM rates of the same sediment measured by ^{14}C-radiotracer (Fig. 2A) and other *in vitro* AOM enrichment culture (e.g., Ono et al., 2021; Wegener et al., 2021). No methane was detected and no increase in sulfide concentration was observed in the control experiment containing a headspace gas of N$_2$ and CO$_2$, indicating negligible methanogenesis and organoclastic sulfate reduction, respectively (Fig. S1A).

In two experiments with high sulfate, the bulk δ^{13}C and δD values of residual methane increased by 9.6‰ and 195.4‰, respectively, with declining methane concentrations (Fig. 4A). Based on a Rayleigh distillation model, the respective carbon and hydrogen isotope fractionation factors, expressed in per mil, were found to be 4.9 ± 0.1‰ and 149.0 ± 1.5‰ in the first experiment, and 7.5 ± 0.1‰ and 154.0 ± 1.3‰ in the second experiment (Fig. 5A–B). With progressive methane consumption, Δ^{13}CH$_3$D and Δ^{12}CH$_2$D$_2$ values increased by 16.4‰ and 57.6‰, reaching values of 19.5‰ and 65.1‰, respectively (Figs. 3A, 6A). These values are substantially higher than the values expected for isotopologue equilibrium at the incubation temperature of 4 °C. The kinetic clumped isotopologue fractionations (γ), defined as the ratio of the mass-18 isotopologue fractionation factors to the product of the bulk carbon and hydrogen fractionation factors, describe deviations from the rule of the geometric mean (Bigeleisen, 1955; Wang et al., 2016). The respective γ values for ^{13}CH$_3$D and ^{12}CH$_2$D$_2$ defined by these data were 0.985 ± 0.002 and 0.912 ± 0.006 in the first experiment, and 0.985 ± 0.002 and 0.909 ± 0.005 in the second experiment (Fig. 5C–D).

The same sediment slurry was then incubated with low sulfate concentration (<0.35 mM) under the same conditions (e.g., saturated methane), resulting in a lower thermodynamic driving

force for AOM. Methane isotopologue compositions were analyzed on days 1, 11, 58, and 79 of the incubation. In contrast to the high sulfate experiment, the bulk $\delta^{13}C$ and δD values of residual methane decreased by 10.1‰ and 15.2‰, respectively (Fig. 4B). The $\Delta^{13}CH_3D$ and $\Delta^{12}CH_2D_2$ values, however, increased linearly by 4.6‰ and 14.8‰, respectively (Figs. 3B and 6B). There is no substantial difference in $\Delta^{13}CH_3D$ and $\Delta^{12}CH_2D_2$ values of residual methane taken on days 58 and 79, likely signaling a reduction in the AOM rate due to sulfate limitation (0.01 mM). To examine whether the residual methane will approach isotopologue equilibrium or overshoot it, additional sulfate was added on day 83, to increase the concentration again to 0.39 mM in the slurry. Isotopologue ratios of the residual methane were analyzed on days 91 and 178 of the incubation. Both $\Delta^{13}CH_3D$ and $\Delta^{12}CH_2D_2$ values increased up to 11.4‰ and 31.5‰, respectively (Figs. 3B, 6B). Net isotope fractionation factors are not reported here for low sulfate incubation because of the challenge of accurately quantifying methane consumption, limiting our ability to estimate the fraction of methane remaining in the Rayleigh process, and thus causing large errors, but both $^{13}\alpha$ and $^D\alpha$ are higher than 1.0, in contrast with the high sulfate incubation in which both $^{13}\alpha$ and $^D\alpha$ are lower than 1.0 (Figs. 4A–B, 5).
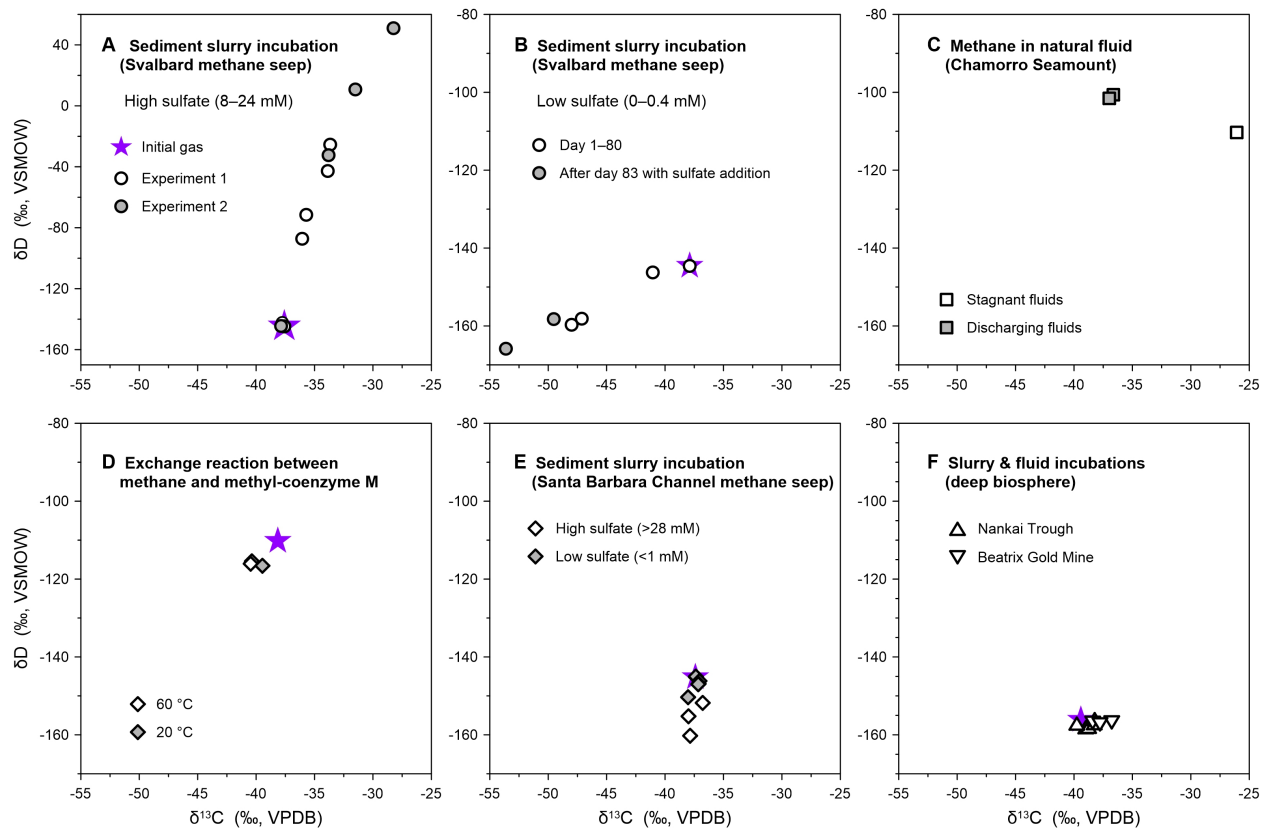
Fig. 5-4 Bulk isotope data of residual methane in AOM incubation experiments and natural fluids. (A–B) Incubation of the Svalbard methane seep sediment slurry with high sulfate concentration (8–24 mM; panel A) and low sulfate concentration (0–0.4 mM; panel B). (C) Methane in natural fluids collected from the South Chamorro Seamount. (D) Exchange reaction between methane and methyl-coenzyme M. (E) Incubation of the Santa Barbara Channel methane seep sediment slurry. (F) Incubations of the Nankai Trough sediment slurry and Beatrix Gold Mine fracture fluid from the deep biosphere. The purple stars represent the initial tank gas. Uncertainties of $\delta^{13}C$ and δD values are encompassed by individual data points.
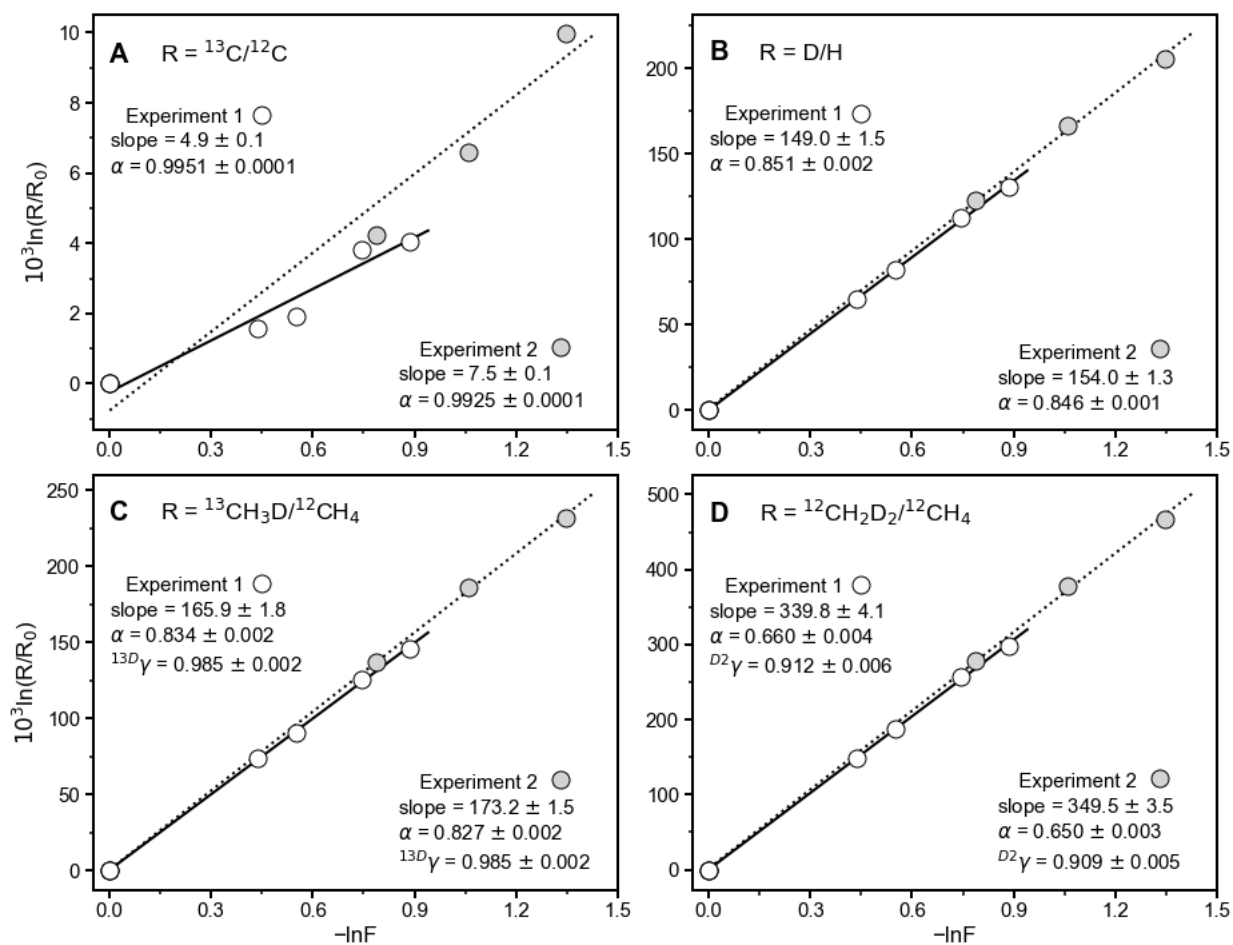
Fig. 5-5 Evolution of methane isotopologue ratios during methane consumption in the incubation of the Svalbard methane seep sediment slurry with high sulfate concentration. Data from experiments 1 and 2 are shown in open and filled circles, respectively. F is the fraction of methane remaining and R is the ratio of isotopologues in the gas phase. α and γ represent the kinetic isotope fractionation factor and clumped isotopologue fractionation factor, respectively. The linear regressions and errors are calculated by the weighted least square method of York et al. (2004).

3.2. Incubation of the Santa Barbara Channel methane seep sediment slurries

Analogous to the incubation of Svalbard sediment slurry, we conducted incubation with Santa Barbara Channel sediment slurries at 20 °C. However, the volume and pressure of headspace methane in the Santa Barbara slurry (4.4 ml under ca. 100 kPa) were much lower than those of the Svalbard slurry (60 ml under ca. 200 kPa), presumably leading to a lower thermodynamic driving force for AOM. An earlier study at the same sites of the Santa Barbara Channel found that the *ex-situ* AOM rates determined by ^{14}C-radiotracer techniques were relatively high, on the order of tens

222

to hundreds of nmol cm^{-3} d^{-1} (Treude and Ziebis, 2010). All incubations with methane headspace showed decreases in sulfate concentration and increases in dissolved sulfide concentration and alkalinity over time. Along with the e*x-situ* AOM rates reported in the earlier study and the control experiment (Fig. S1B), these trends indicate the activity of AOM. Some δD values of residual methane decreased by up to 15.0‰, whereas the δ^{13}C values remained roughly constant over time under both high and low sulfate conditions (Fig. 4E). In the high sulfate slurries (>28 mM), both Δ^{13}CH$_3$D and Δ^{12}CH$_2$D$_2$ of residual methane increased, ranging from 3.5‰ to 5.4‰ for Δ^{13}CH$_3$D and from 8.5‰ to 12.1‰ for Δ^{12}CH$_2$D$_2$ (Fig. 3E). In the low sulfate slurries (<1 mM), the Δ^{12}CH$_2$D$_2$ values remained nearly constant over time (6.7 ± 0.9‰), while the Δ^{13}CH$_3$D increased by 2.7‰, reaching a value of 5.5 ± 0.2‰ relative to stochastic (Fig. 3E). For comparison, when methane molecules are at thermodynamic equilibrium at 20 °C, the respective Δ^{13}CH$_3$D and Δ^{12}CH$_2$D$_2$ values would be 5.9‰ and 20.3‰ (Young et al., 2017).

3.3. Incubation of sediment slurries and fracture fluids from the deep biosphere

Marine sediment and fracture fluids were sampled from the deep subsurface of the Nankai Trough and the Beatrix Gold Mine, respectively. Metagenomics, metatranscriptomics, and fluorescent *in situ* Hybridization (FISH) of the Beatrix Gold Mine fluids were previously published and the results demonstrated that ANMEs are present and active in the incubations (Lau et al., 2016; Harris et al., 2018; Harris et al., 2021). In parallel to the natural abundance incubations described in Section 2.3, long-term (350 day) high-pressure (40 MPa) ^{13}C-CH$_4$ tracer incubations were performed on Nankai Trough sediment slurries (Fig. S2). Based on the production of ^{13}C-DIC (Fig. S3) and δ^{13}C$_{DIC}$ measurements (Fig. S4), trace AOM activity was statistically distinguishable above background, albeit at very low rates (on the order of pmol cm^{-3} day^{-1}). These

findings agree with ^{14}C-CH$_4$ radiotracer experiments reported by Beulig et al. (2022), who found potential AOM activity near detection limits in the Nankai Trough sediment due to a high background of abiotic ^{14}C-CH$_4$ conversion to ^{14}C-CO$_2$ in the medium controls. These results collectively highlight the difficulty in quantifying AOM activity in these oligotrophic, low-biomass, deep biosphere sediment (see Heuer et al., 2020). Thus, only potential AOM activity has been observed and no explicit discussion can be made in this respect.

The bulk isotope data of incubation experiments are consistent with the sluggish nature of microbial activity in the deep subseafloor. Here, nearly all headspace methane showed no substantial changes in δ^{13}C and δD values (<2‰; Fig. 4F). However, substantial changes were found for clumped isotopic ratios. In the Nankai Trough slurries with nitrate or nitrite as the added electron acceptors, only Δ^{13}CH$_3$D increased, reaching a value of 5.7 ± 0.1‰ as incubation time progressed (Figs. 3F, S5C). Similarly, when iron(III) in the form of hydrous ferric oxide was added as the electron acceptor in the Beatrix Gold Mine incubation, Δ^{13}CH$_3$D increased up to 5.7 ± 0.1‰, while there was less increase in Δ^{13}CH$_3$D when sulfate or no electron acceptor was added (Figs. 3F, S5D). Little variation in Δ^{12}CH$_2$D$_2$ values was found in these experiments (Fig. 3F).

3.4. Incubation with methyl-coenzyme M reductase (Mcr) enzyme

We performed experiments with Mcr purified from *Methanothermobacter marburgensis* that catalyzes the exchange of the methyl moiety of methyl-coenzyme M with methane. The δ^{13}C and δD of residual methane decreased by up to 2.3‰ and 6.4‰ in all cases, respectively (Fig. 4D). Both Δ^{13}CH$_3$D and Δ^{12}CH$_2$D$_2$ increased to different degrees relative to the initial methane isotopologue ratios (Fig. 3D). In detail, at 60 °C, the incubations lasted for 2–6 hours in which a small increase of 0.5‰ in Δ^{13}CH$_3$D and 2.0‰ in Δ^{12}CH$_2$D$_2$ were observed. At 20 °C, the

224

incubation lasted for 48 hours and the $\Delta^{13}CH_3D$ of residual methane increased substantially by 4.1‰, reaching a value of 5.6 ± 0.1‰ relative to stochastic while $\Delta^{12}CH_2D_2$ showed a modest increase of only 2.6‰, reaching a value of 8.5 ± 0.5 ‰.

3.5. Natural methane-rich fluids from the South Chamorro Seamount

Three fluid samples were collected from South Chamorro Seamount during *HyperDolphin* Dives 941, 945, and 947 in 2009. The general geochemical data were previously published (Wheat et al., 2020). In brief, the stagnant fluids collected during Dive 941 are rich in sulfate (12 mM) and methane (33 mM), whereas discharging fluids from Dives 945 and 947 have low sulfate concentrations (0.8 mM) and relatively low methane concentrations (23 mM). Further, sulfate and methane concentrations in the fluids were negatively correlated with aqueous sulfide concentration and alkalinity, indicating that the fluids were altered by AOM to different degrees (Wheat et al., 2020). The bulk $\delta^{13}C$ and δD values range from −37.0‰ to −26.1‰ and −110.3‰ to −100.6‰, respectively (Fig. 4C). The respective $\Delta^{13}CH_3D$ and $\Delta^{12}CH_2D_2$ values are 7.5‰ and 25.2‰ in the high-sulfate, high-methane fluid, but increase to 12.6‰ and 42.6‰ in low-sulfate, low-methane fluids (Figs. 3C, 6C). These values are analogous to the results from the Svalbard slurry incubations (Fig. 3A–B).

4. Discussion

4.1. Kinetic fractionations of methane clumped isotopologue during AOM

AOM was highly active in the sediment slurry from the Svalbard methane seep (Fig. 2). The high-sulfate incubation experiment showed progressive enrichment of methane isotopologues containing ^{13}C and D isotopes relative to the initial gas (Figs. 4A and 5), indicating a kinetic isotope

fractionation. Although the kinetic fractionation for D/H ratios is typical, the carbon isotope fractionation is slightly lower than previous studies, which are in the range of 11‰ to 39‰, suggesting differing degrees of reversibility of the carbon network in AOM (Holler et al., 2009; Wegener et al., 2021). The γ value for $^{13}CH_3D$ of 0.985 is lower than those obtained for other methane oxidation reactions such as aerobic oxidation and oxidation by OH and Cl radicals, while the γ values for $^{12}CH_2D_2$ of 0.909–0.912 are similar to those obtained for other methane oxidation reactions (Wang et al., 2016; Haghnegahdar et al., 2017; Whitehill et al., 2017; Ono et al., 2021; Krause et al., 2022). Ono et al. (2021) proposed that the different γ values could be linked to the transition state structure of the reaction. For example, the C–H bond length of methyl-coenzyme M reductase (2.6 Å) and soluble methane monooxygenase (1.3 Å), the key enzymes involved in AOM and aerobic methanotrophy, respectively, are different, necessitating changes in the ^{13}C–D stretching vibrational mode and thus perhaps the difference in kinetic clumped isotopologue effects (Ono et al., 2021).

The extremely high $\Delta^{13}CH_3D$ and $\Delta^{12}CH_2D_2$ values up to 12.6‰ and 42.6‰, respectively, from the Chamorro Seamount, a serpentinite mud volcano in the Mariana forearc (Fig. 6C–F), as well as the high values seen in the Svalbard incubations (Fig. 6A), appear to be signatures of AOM. To date, AOM is the only known process that drives methane isotopologue abundances substantially above equilibrium predictions for both $\Delta^{13}CH_3D$ and $\Delta^{12}CH_2D_2$, as shown in Figure 7. In the laboratory, we treat AOM as a Rayleigh process in which methane is consumed only by AOM in a closed system. This explains the trends in $\Delta^{13}CH_3D$ vs. $\Delta^{12}CH_2D_2$ space for the Svalbard incubations (Fig. 6A–B). For the Chamorro Seamount, an open system that involves flow, is likely to be more suitable as a model for isotopologue fractionation. There, Wheat et al. (2020) demonstrated that methane production was abiotically fueled by hydrogen production from

serpentinization and carbonate dissolution in the deep-sourced fluids, and the fluid compositions were largely altered by AOM as the fluid migrates upwards and encounters deposited pelagic sediment underlying South Chamorro Seamount. Although the pH of the collected fluids is 12, the pH of deep subsurface niches where ANME archaea live and AOM occurs can be lower, as observed in neighboring serpentinite mud volcanoes (Wheat et al., 2020). Earlier studies have shown that microorganisms can tolerate high pH fluids and perform AOM at the Chamorro Seamount (Takai et al., 2005; Curtis et al., 2013; Kawagucci et al., 2018). These AOM-affected fluids make it to the seafloor where they discharge. Therefore, the environment where fluids are traversing through the seamount represents an open system, in which methane is transported into the subduction channel via advection and removed by both advection and AOM, likely resulting in a steady state, or at least a transient steady state. A simple mass balance model can be used to investigate the effects of simultaneous advection and oxidation (see Materials and Methods).
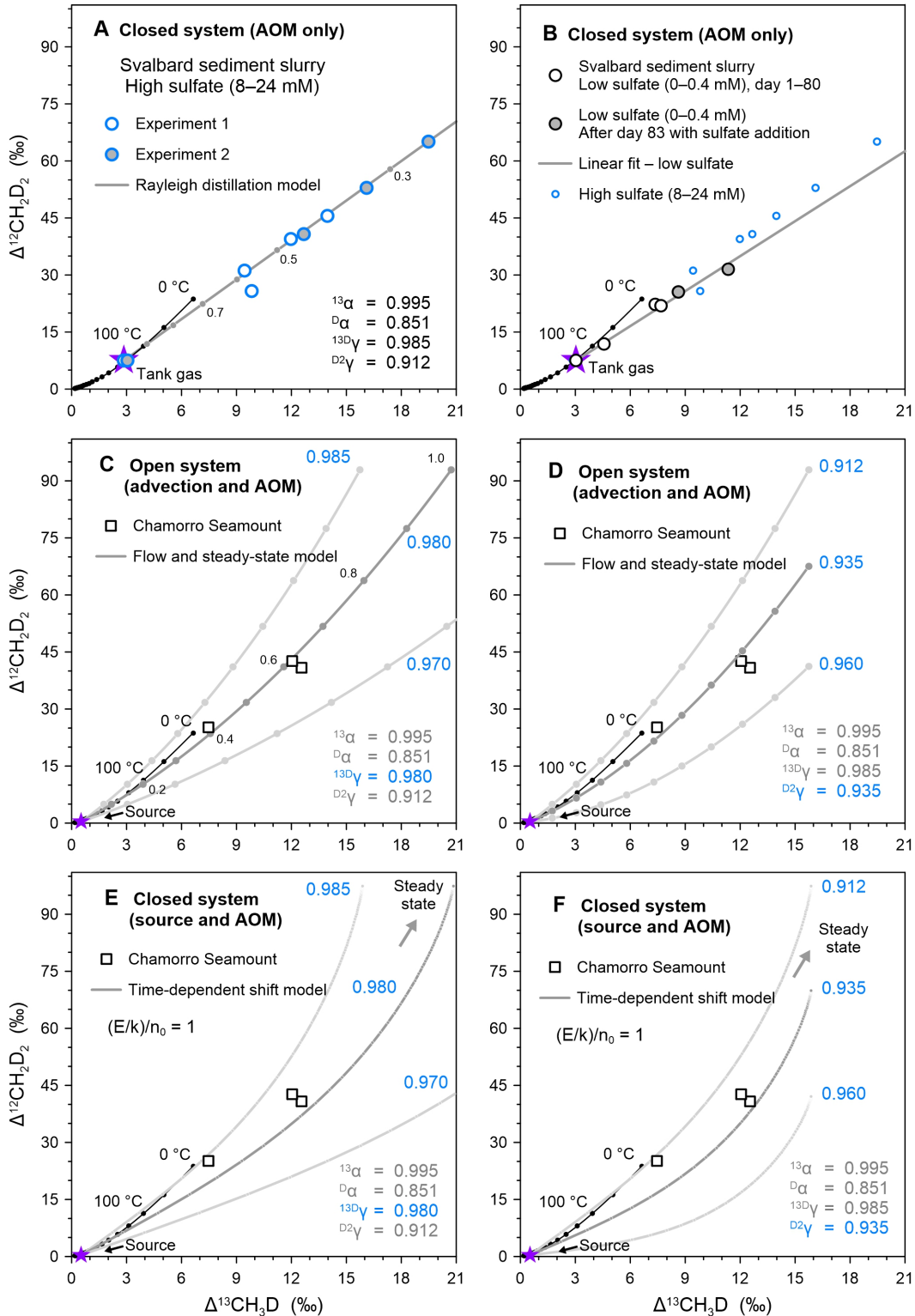
Fig. 5-6 Kinetically-driven methane isotopologue data of residual methane in AOM incubation experiments and methane in natural fluids. (A–B) Residual methane during incubation of the Svalbard methane seep sediment slurry with high sulfate concentration (8–24 mM; panel A) and low sulfate concentration (0–0.4 mM; panel B). (C–F) Methane in natural fluids from the South Chamorro Seamount. Grey lines depict simulation outputs of the Rayleigh fractionation model (A), open-system flow and steady-state model (C–D) and closed-system time-dependent shift

228

model (E–F). The fractionation factors used in each model are shown in each diagram. The purple stars represent the initial tank gas in panel A, and the source methane in panels C–F, respectively. This source methane is adopted from Young et al. (2017), representing abiotic methane gas formed at 500 °C through $Si_5C_{12}H_{36}$ decomposition experiments, which resembles methane production through serpentinization. In panel A, points along the Rayleigh fractionation line are marked at intervals of 0.1 in f, the fraction of initial methane remaining, while in panel C, points along the open-system model are marked at intervals of 0.1 in φ, the fraction of methane removed via oxidation. The modeled trajectories in panels E–F remain largely the same as $(E/k)/n_0$ increase from 10^{-10} to 10^{10} (data not shown), and we use 1 as an arbitrary representation. The solid black line depicts theoretical thermodynamic equilibrium abundances of methane isotopologues, along with corresponding temperatures. Uncertainties of $\Delta^{13}CH_3D$ and $\Delta^{12}CH_2D_2$ values are encompassed by individual data points.

The combined flow and oxidation steady-state models shown in Figure 6C–D largely reproduce the observed large $\Delta^{13}CH_3D$ and $^{12}CH_2D_2$ values at the Chamorro Seamount. Note that to achieve the best fit, a slightly lower γ value for $^{13}CH_3D$ of ~0.980 or a higher γ value for $^{12}CH_2D_2$ of ~0.935 than obtained from the experiments is needed. While the open system model is more suitable to describe these fluids, we also considered the scenario of a closed system in which the formation of methane is balanced against oxidation. In this model, isotopologue abundances vary with time, eventually reaching a steady state that is sensitive to the precise γ values (Fig. 6E–F). We set the ratio of the steady-state moles to initial moles of methane, $(E/k)/n_0$, to 1 since the modeled trajectories remain largely the same as $(E/k)/n_0$ varies. Here, $^{13}CH_3D$ γ values of 0.980–0.985 and $^{12}CH_2D_2$ γ values of 0.912–0.935 are needed to achieve the best fit in the closed system model. These estimated γ values for the Chamorro Seamount fluids from either the open- or closed-system model are largely consistent with those obtained from the Svalbard slurry incubations.

Both open and closed system models display similar positive trajectories in $\Delta^{13}CH_3D$ vs. $\Delta^{12}CH_2D_2$ space, similar to the Rayleigh distillation model (Fig. 6), suggesting that extremely positive $\Delta^{13}CH_3D$ and $\Delta^{12}CH_2D_2$ values are very likely a clumped isotope signature of kinetically-dominated AOM. These positive values are the result of $\gamma < 1$ for both mass-18 isotopologues. Indeed, if $\gamma = 1$ for both rare isotopologues, and all else being equal, $\Delta^{13}CH_3D$ and $\Delta^{12}CH_2D_2$ would both decrease rather than increase with oxidation. We further test the sensitivity of the

models by varying the bulk isotope fractionation factors. The model outputs remain largely the same, though with different curvatures (Fig. S6). The trajectories in $\Delta^{13}CH_3D$ vs. $\Delta^{12}CH_2D_2$ space are much more sensitive to γ values than to $^{13}\alpha$ and $^D\alpha$ values (Figs. 6, S6).

We note that with progressive AOM from the stagnant fluids to the discharging fluids at the Chamorro Seamount as indicated by alkalinity, methane, sulfate, and sulfide concentrations (Wheat et al., 2020), the $\delta^{13}C$ of residual methane decreases by 10.9‰ and δD increases by 9.7‰ in three fluid samples (Fig. 4C), resembling the ANME incubation under low-sulfate conditions (<1 mM) in Wegener et al. (2021). These authors concluded that the net bulk isotope fractionations of AOM reflect a combination of expression of kinetic isotope effects (KIEs) and equilibrium isotope effects (EIEs) (Ono et al., 2021; Wegener et al., 2021). Indeed, when the Svalbard sediment slurry was incubated with even lower sulfate concentrations (<0.35 mM), both $\delta^{13}C$ and δD of residual methane decreased over time (Fig. 4B), suggestive of a greater expression of EIEs in both carbon and hydrogen pathways of AOM due to a lower net thermodynamic drive and thus relatively higher net reversibility of AOM. At inter-species isotope equilibrium at 4 °C, the $\delta^{13}C$ and δD of methane should be around −90‰ and −300‰ based on $\delta^{13}C_{CO2}$ and δD_{H2O} values of ca. −15‰ and −50‰ reported in similar laboratory cultures (e.g., Wegener et al., 2021). Despite the fact that the residual methane in the low-sulfate incubation moves towards isotope equilibrium between both CH_4–CO_2 and CH_4–H_2O molecules (Fig. 4B), $\Delta^{13}CH_3D$ and $\Delta^{12}CH_2D_2$ increase linearly and fall on nearly the same Rayleigh fractionation line in $\Delta^{13}CH_3D$ vs. $\Delta^{12}CH_2D_2$ space as the high-sulfate incubation (Fig. 6B). In particular, the $\Delta^{13}CH_3D$ reaches 7.4‰ when sulfate is depleted (0.01 mM), which is higher than the value expected for intra-species isotope equilibrium at the experimental temperature ($\Delta^{13}CH_3D_{eq.}$ = 6.5‰ at 4 °C). This high $\Delta^{13}CH_3D$ value suggests a kinetic clumped isotopologue fractionation. We surmise that rather than representing

unidirectional consumption of methane, the isotopic effects we observed appear to reflect a convolution of transition-state kinetics and equilibrium isotopic effects. Furthermore, both $\Delta^{13}CH_3D$ and $\Delta^{12}CH_2D_2$ increase linearly again after new sulfate is added to the slurry (0.39 mM), indicating that the final $\Delta^{13}CH_3D$ and $\Delta^{12}CH_2D_2$ values in a methane-rich closed system depend on the electron acceptor concentration and availability. The last measured $\Delta^{13}CH_3D$ and $\Delta^{12}CH_2D_2$ values correspond to apparent temperatures lower than $-34\ °C$ (Fig. 6B), far below the incubation temperature of $4\ °C$. Collectively, our results from the Svalbard sediment slurry and the Chamorro Seamount show clear evidence for kinetic clumped isotopologue fractionation, with the bulk isotope ratios either increasing or decreasing with progressive methane consumption depending upon the availability of the electron acceptor.

4.2. Equilibrium between methane isotopologues during AOM

It has been proposed that AOM drives methane isotopologue abundances to thermodynamic isotopic bond-order equilibrium in a range of marine and continental settings (Ash et al., 2019; Giunta et al., 2019; Tyne et al., 2021; Warr et al., 2021; Ono et al., 2022). The initial step of AOM is Mcr-catalyzed reversal of the final reaction in methanogenic pathways as shown for the enzyme from *M. marburgensis* (Eq. 15):

$$CH_4 + CoM\text{-}S\text{-}S\text{-}CoB \rightleftarrows CH_3\text{-}S\text{-}CoM + HS\text{-}CoB \quad (\Delta G^o = +30\ kJ\ mol^{-1}) \tag{15}$$

where CoM-S-S-CoB is the heterodisulfide of coenzymes M and B, CH₃-S-CoM is methyl-coenzyme M, and HS-CoB is the reduced form of coenzyme B (Scheller et al., 2010). The reversibility of this reaction is evidently central to the mechanism for methane isotopologue equilibration by AOM. The *in vitro* experiments that comprise exchange of methane and the methyl moiety in methyl-coenzyme M (CH₃-S-CoM) characterize the role of the Mcr enzyme in

231

reaction Eq. (15). Decreases in both $\delta^{13}C$ and δD in residual methane are seen in all Mcr experiments (Fig. 4D), which is consistent with an evolution towards equilibrium values. At 60 °C, the optimal temperature for the thermophile-derived enzyme, both $\Delta^{13}CH_3D$ and $\Delta^{12}CH_2D_2$ values of residual methane increase slightly (Fig. 3D). At 20 °C, however, $\Delta^{13}CH_3D$ approaches the equilibrium value, while there is little change in $\Delta^{12}CH_2D_2$. This implies that carbon plays a larger role than hydrogen in the isotopologue selectivity for reaction with the Mcr enzyme at a temperature below optimal.

Incubations of slurry from the Santa Barbara Channel, with a lower amount of methane further inform the assessment of the role of thermodynamic driving forces in determining the isotopologue signatures of AOM. There is a trend towards $\Delta^{13}CH_3D$ and/or $\Delta^{12}CH_2D_2$ values expected for isotopologue equilibrium at experimental temperature (Fig. 3E). Two of the high-sulfate incubations of the Santa Barbara sediment resemble the high-temperature Mcr experiments under the optimal condition, whereas the low-sulfate incubations resemble the low-temperature Mcr experiments (Fig. 3D–E). Importantly, the amounts of methane injected into the Santa Barbara slurry (0.5 mmol) are much lower than those into the Svalbard slurry (5.4 mmol), leading to a much lower thermodynamic drive for AOM for the former and an overall lower rate of reaction. Thus, the net reversibility and isotope exchange during AOM in the Santa Barbara slurry may be much higher than that in the Svalbard slurry under either high- or low-sulfate conditions. This sluggish exchange ultimately allows methane isotopologues to react with Mcr reversibly, achieving partial intra-species equilibrium in the Santa Barbara slurry incubations. The low rate of exchange may be exacerbated by the fact that the ANME community in coastal sandy Santa Barbara sediment with high depositional rates is less active with less biomass compared to that from the deep-sea fine-grained Svalbard methane seep sediment. The lower sedimentation rates at

the Svalbard seep focus AOM in the same sediment for an extended period, allowing the ANME community to grow and enrich.

All experiments of the deep biosphere sediment and fluid incubations suggest that there is a trend toward equilibrium values for $\Delta^{13}CH_3D$ but little change in $\Delta^{12}CH_2D_2$ within experimental timescales, regardless of which electron acceptor is present (Fig. 3F). In detail, a positive correlation between incubation time (up to 500 days) and increase in $\Delta^{13}CH_3D$ values is found in incubation experiments of the Nankai Trough sediment (Fig. S5C), consistent with the well documented sluggish nature of microbial activity in the deep subseafloor (Hoehler and Jørgensen, 2013; Heuer et al., 2020).

One may postulate that the $\Delta^{13}CH_3D$ values in our incubations that appear to approach equilibrium values would in fact continue to increase beyond the equilibrium value given sufficient time. However, this is probably not the case. The respective maximum observed for $\Delta^{13}CH_3D$ values is 5.56‰ (2 days), 5.50‰ (3 days), 5.70‰ (500 days), and 5.66‰ (350 days) in the Mcr experiment, and the incubations of the Santa Barbara Channel sediment, the Nankai Trough sediment, and the Beatrix Gold Mine fracture fluid (Fig. 3D–F). The apparent temperatures based on $\Delta^{13}CH_3D$ are 32 °C, 33 °C, 27 °C, and 28 °C, respectively (30 ± 3 °C, n = 4). These are all close to the ambient temperature under which these different incubations took place. Although it cannot be categorically ruled out that these $\Delta^{13}CH_3D$ values reflected ambient temperatures by happenstance during an ongoing kinetically driven trend, it would be fortuitous that this would occur four times in independent experimentation. Therefore, we conclude that the $\Delta^{13}CH_3D$ values increase over time towards equilibrium and indeed remain at thermodynamic equilibrium despite a large range of incubation times of 2 to 500 days in the above four experiments.

4.3. Kinetically-driven AOM *versus* equilibrium-driven AOM

Taking all of our results together, we find that the $\Delta^{13}CH_3D$ and $\Delta^{12}CH_2D_2$ signatures of AOM can be understood in terms of reversibility at the Mcr step. The degree of reversibility is presumably controlled by the tenets of disequilibrium thermodynamics in which rates of reaction are proportional to reaction affinity (deviations in chemical potentials from equilibrium). Kinetic clumped isotope fractionation is found in the Svalbard slurry in which large amounts of methane are provided to the active ANME community. This kinetic signature is also seen in natural fluids from the South Chamorro Seamount, indicating that the kinetic isotopologue fractionation does not differ substantially between laboratory incubations and natural environments (Fig. 6). When less methane is provided, $\Delta^{13}CH_3D$ tends to increase towards thermodynamic near-equilibrium values with minimal increases in $\Delta^{12}CH_2D_2$ (Fig. 3E). For example, there is a striking difference in the isotopologue evolution of residual methane between the Svalbard slurry, in which kinetics drives $\Delta^{13}CH_3D$ and $\Delta^{12}CH_2D_2$ to extreme values, and the Santa Barbara slurry incubations in which changes occur mainly in $\Delta^{13}CH_3D$ and appear to approach equilibrium, even though the sediments are both from methane seeps (Fig. 3). Another reason for this discrepancy is the biomass of ANME archaea under different conditions, such that in slurry that experienced high methane concentrations over a longer period of time, the biomass may be higher and vice-versa. We therefore infer that AOM with high sulfate concentrations may show either kinetic or equilibrium behavior depending on the local ANME community, the availability of methane, and thus the overall thermodynamic drive.

We conclude that both $\Delta^{13}CH_3D$ and $\Delta^{12}CH_2D_2$ values reflect kinetic isotope fractionation and increase beyond intra-methane thermodynamic equilibrium when the net AOM reaction has low reversibility due to high rates, whereas largely reversible exchange between methane

isotopologues facilitated by the Mcr enzyme under a lower thermodynamic drive leads to methane isotopic bond re-ordering, driving the abundances of methane isotopologues ultimately to thermodynamic quasi-equilibrium values. This observation is consistent with reaction affinity as a primary determinant for the behavior of the system. These departures from equilibrium, or reaction affinities, are controlled by environmental factors, including but not limited to, temperature, concentrations of methane and electron acceptors, and perhaps the type of electron acceptors. Although it seems that $^{13}CH_3D$ and $^{12}CH_2D_2$ equilibration are ultimately controlled by the reversibility of AOM, the driver for different trajectories in $\Delta^{13}CH_3D$ vs. $\Delta^{12}CH_2D_2$ space is still elusive. Future efforts should explicitly focus on the environmental controls of the enzymatic activity of intracellular pathways and the reversibility of AOM, and their intrinsic link to methane isotopologue ratios.

5. Summary and implications

A schematic representation of methane clumped isotope signatures of diverse methane sources, as well as kinetically- and equilibrium-driven AOM, is shown in Figure 8. Extremely low $\Delta^{12}CH_2D_2$ values down to ca. −40‰ have been observed for microbial methane under experimental and natural conditions, as well as thermogenic and abiotic methane generated by laboratory experiments (e.g., Young et al., 2017; Young, 2019; Dong et al., 2021). Besides equilibrium-driven AOM, isotopologue data near thermodynamic equilibrium have been attributed to high-maturity thermogenic or high-temperature abiotic methane, as well as low-rate methanogenesis (Stolper et al., 2015; Wang et al., 2015; Young et al., 2017; Ash et al., 2019; Giunta et al., 2019; Taenzer et al., 2020; Warr et al., 2021; Xie et al., 2021; Gropp et al., 2022; Ono et al., 2022). Recently, Ono et al. (2022) demonstrated that methanogenesis does not occur or

only proceeds at extremely slow rates at low pH$_2$ in energy-limiting deep sedimentary environments using an isotopologue flow network model, and therefore inferred that near-equilibrium methane isotopologue signals in deep marine sediment are produced by the catalytic reversibility of the Mcr enzyme, likely from ANME archaea performing either AOM or net methanogenesis. This inference is consistent with our incubation experiments in which Mcr-catalyzed isotope exchange occurs.
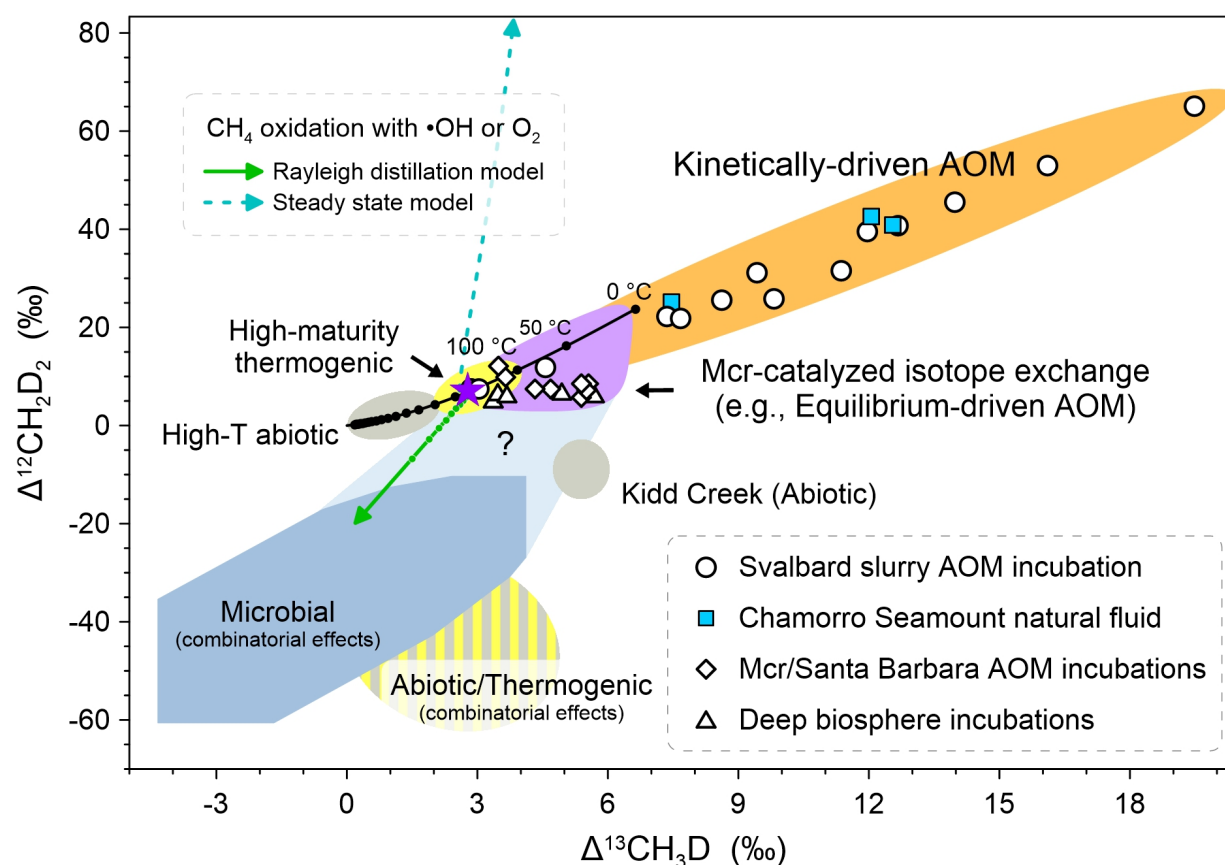

Fig. 5-7 A schematic representation of methane clumped isotope signatures of diverse methane sources, as well as kinetically- and equilibrium-driven AOM. Circle symbols depict residual methane during incubation of the Svalbard methane seep sediment slurry, while methane data of natural fluids from the South Chamorro Seamount are shown as square symbols. Rhombus symbols illustrate residual methane from the Mcr exchange experiment and incubations of the Santa Barbara Channel sediment slurry. Deep biosphere incubations are shown as triangle symbols. The solid black line depicts theoretical thermodynamic equilibrium abundances of methane isotopologues, along with corresponding temperatures. The purple star represents the tank gas used in the slurry incubation experiments, and the zone of equilibrium-driven AOM is based on an initial gas of thermogenic origin. For comparison, two modeled trajectories for methane oxidation with OH radical (γ for $^{13}CH_3D = 0.999$, γ for $^{12}CH_2D_2 = 0.907$; Haghnegahdar et al., 2017), the major methane sink in air, are shown: the solid line is the Rayleigh distillation model (cf. Fig. 6A), the dashed line is the steady-state closed-system model (($E/k)/n_0 = 1$; cf. Fig. 6E). The trajectories for aerobic oxidation of methane are similar to those of CH$_4$ + OH reaction (Krause et al., 2022).

The zonation of methane sources is adopted from Young et al. (2017), Young (2019) and Dong et al. (2021). Isotopologue data right below the thermodynamic equilibrium curve can reflects diverse methane sources and sinks as indicated by the question mark, representing equilibrium-driven AOM and the early stage of kinetically-driven AOM (this study; Ash et al., 2019; Ono et al., 2021), low-rate methanogenesis (e.g., Stolper et al., 2015; Wang et al., 2015), low-maturity thermogenic gas (Xie et al., 2021), Kidd Creek abiotic gas (Young et al., 2017), etc. All the plotted data are from this study. The reader is referred to the text for interpretation of the figure.

To date, extremely positive $\Delta^{13}CH_3D$ and $\Delta^{12}CH_2D_2$ values have been observed, as demonstrated here, only under conditions where AOM occurs with a low degree of reversibility. This observation raises an intriguing question whether methane clumped isotope signature of AOM could have the potential to be diagnostic of AOM on Earth and perhaps throughout the solar system where methane has been detected (Webster et al., 2015; Waite et al., 2017; Yung et al., 2018; Thompson et al., 2022). For example, the *in-situ* discovery of isotopically depleted methane gas on Mars by Curiosity (Webster et al., 2015; House et al., 2022) indicates that methane is produced either biogenically or abiogenically (Atreya et al., 2007; Yung et al., 2018), and its emission results in the presence of methane in the atmosphere of Mars (Formisano et al., 2004). On the other hand, although the atmospheric methane sink on Mars has been quantified (Atreya et al., 2007; Yung et al., 2018), abiotic loss mechanisms would suggest a mean atmospheric residence time of ~300 years – substantially longer than observed methane lifetimes on the order of months to years (Lefèvre, 2019). The conditions for a subsurface microbial sink on Mars are still elusive. Nevertheless, the reaction transport model by Marlow et al. (2014) demonstrated that AOM could be a feasible metabolism on ancient Mars, for example, in sulfate-rich groundwater with methane from serpentinization by-products, and acid-sulfate fluids with methane produced from basalt alteration. The surface of Mars also includes deposits of iron oxides and manganese oxides, Fe- and Mn-dependent AOM therefore has also been proposed as a possible metabolism for recent and ancient Mars (House et al., 2011). Applying these inferences to our understanding of methane cycling on Mars is speculative. Nonetheless, a robust *in-situ* approach is needed to trace processes

of methane cycling on future missions such as Mars Life Explorer (National Academies of Sciences, Engineering, and Medicine, 2022).

Mars is one of the most promising candidates for the application of methane isotope clumping. The reason is that doubly substituted isotopologues of methane remove the difficulties associated with using bulk $^{13}C/^{12}C$ and D/H elsewhere in the solar system, where the geochemical context necessary for interpreting these ratios are hampered by incompletely characterized chemical cycles (Lefèvre, 2019; Young, 2019; House et al., 2022). In $\Delta^{13}CH_3D$ vs. $\Delta^{12}CH_2D_2$ space, microbial, thermogenic, and abiotic methane gases are either below or near the thermodynamic equilibrium predictions (Fig. 7). Once formed, methane could be oxidized photochemically or by microbial oxidation. These sinks have different $\Delta^{13}CH_3D$ vs. $\Delta^{12}CH_2D_2$ signatures, depending upon whether a steady state is achieved or not. The details depend on the precise γ values, but in general, by analogy with Earth's atmosphere, oxidation in the atmosphere (e.g., by OH radicals) should ultimately lead to either high $\Delta^{12}CH_2D_2$ of order tens to hundreds of per mil at less variable $\Delta^{13}CH_3D$ values in residual methane at steady state, or extremely low values for both where a steady state between methane formation and oxidation has not been achieved (Fig. 7) (Haghnegahdar et al., 2017). The trajectories for microbial aerobic oxidation of methane are like those of the CH_4 + OH reaction (Krause et al., 2022). AOM, on the other hand, can lead to extremely high $\Delta^{12}CH_2D_2$ and $\Delta^{13}CH_3D$ values up to 65.1‰ and 19.5‰, respectively, as shown here. Indeed, these signatures are essentially orthogonal. Although mixing scenarios could mimic the extreme signatures from AOM, those mixing scenarios require extremely large differences in bulk carbon and hydrogen isotopic values of the two endmembers of methane (e.g., hundreds of per mil difference in endmember δD values), possibly allowing kinetically-driven AOM to be distinguished from mixing with concurrent measurement of bulk isotopes.

While intriguing, we presently point out that clumped isotopes for methane would be an approach with a high potential for false negatives, as only anaerobic oxidation of methane, and only under conditions of low reversibility, would reasonably produce a sufficiently diagnostic signal. Another caveat here is that significant technical development would be necessary to measure methane that has an atmospheric mixing ratio on the order of a few ppb. Nonetheless, along with previous isotopologue studies on microbial methanogenesis (Stolper et al., 2015; Wang et al., 2015; Young et al., 2017; Taenzer et al., 2020), our work on the effects of AOM on doubly substituted isotopologues of methane suggests that future missions could benefit from additional research and technique development for *in-situ* mission measurements of methane clumped isotopes on Mars, Enceladus, and other solar system bodies where the methane cycling is a key (bio)geochemical tracer.

Declaration of Competing Interest

The authors declare that they have no known competing financial interests or personal relationships that could have appeared to influence the work reported in this paper.

Appendix A. Supplementary Material

Supplementary figures associated with this article are included in the supplementary material.

References

Alperin M.J., Reeburgh W.S. and Whiticar M.J. (1988) Carbon and hydrogen isotope fractionation resulting from anaerobic methane oxidation. *Global Biogeochem. Cycles* **2**, 279-288.

Ash J.L., Egger M., Treude T., Kohl I., Cragg B., Parkes R.J., Slomp C.P., Sherwood Lollar B. and Young E.D. (2019) Exchange catalysis during anaerobic methanotrophy revealed by 12CH2D2 and 13CH3D in methane. *Geochem. Persp. Let.* **10**, 26-30.

Atreya S.K., Mahaffy P.R. and Wong A.-S. (2007) Methane and related trace species on Mars: Origin, loss, implications for life, and habitability. *Planetary and Space Science* **55**, 358-369.

Beulig F., Røy H., McGlynn S.E. and Jørgensen B.B. (2019) Cryptic CH4 cycling in the sulfate–methane transition of marine sediments apparently mediated by ANME-1 archaea. *The ISME Journal* **13**, 250-262.

Beulig F., Schubert F., Adhikari R.R., Glombitza C., Heuer V.B., Hinrichs K.U., Homola K.L., Inagaki F., Jørgensen B.B., Kallmeyer J., Krause S.J.E., Morono Y., Sauvage J., Spivack A.J. and Treude T. (2022) Rapid metabolism fosters microbial survival in the deep, hot subseafloor biosphere. *Nat. commun.* **13**, 312.

Bigeleisen J. (1955) Statistical Mechanics of Isotopic Systems with Small Quantum Corrections. I. General Considerations and the Rule of the Geometric Mean. *The Journal of Chemical Physics* **23**, 2264-2267.

Cao X., Bao H. and Peng Y. (2019) A kinetic model for isotopologue signatures of methane generated by biotic and abiotic CO2 methanation. *Geochim. Cosmochim. Acta* **249**, 59-75.

Chuang P.-C., Yang T.F., Wallmann K., Matsumoto R., Hu C.-Y., Chen H.-W., Lin S., Sun C.-H., Li H.-C., Wang Y. and Dale A.W. (2019) Carbon isotope exchange during anaerobic oxidation of methane (AOM) in sediments of the northeastern South China Sea. *Geochim. Cosmochim. Acta* **246**, 138-155.

Cord-Ruwisch R. (1985) A quick method for the determination of dissolved and precipitated sulfides in cultures of sulfate-reducing bacteria. *J. Microbiol. Methods* **4**, 33-36.

Curtis A.C., Wheat C.G., Fryer P. and Moyer C.L. (2013) Mariana Forearc Serpentinite Mud Volcanoes Harbor Novel Communities of Extremophilic Archaea. *Geomicrobiol. J.* **30**, 430-441.

Dale A.W., Sommer S., Lomnitz U., Montes I., Treude T., Liebetrau V., Gier J., Hensen C., Dengler M., Stolpovsky K., Bryant L.D. and Wallmann K. (2015) Organic carbon production, mineralisation and preservation on the Peruvian margin. *Biogeosciences* **12**, 1537-1559.

Dong G., Xie H., Formolo M., Lawson M., Sessions A. and Eiler J. (2021) Clumped isotope effects of thermogenic methane formation: Insights from pyrolysis of hydrocarbons. *Geochim. Cosmochim. Acta* **303**, 159-183.

Douglas P.M.J., Stolper D.A., Eiler J.M., Sessions A.L., Lawson M., Shuai Y., Bishop A., Podlaha O.G., Ferreira A.A., Santos Neto E.V., Niemann M., Steen A.S., Huang L., Chimiak L., Valentine D.L., Fiebig J., Luhmann A.J., Seyfried W.E., Etiope G., Schoell M., Inskeep W.P., Moran J.J. and Kitchen N. (2017) Methane clumped isotopes: Progress and potential for a new isotopic tracer. *Org. Geochem.* **113**, 262-282.

Etiope G. and Sherwood Lollar B. (2013) ABIOTIC METHANE ON EARTH. *Rev. Geophys.* **51**, 276-299.

Formisano V., Atreya S., Encrenaz T., Ignatiev N. and Giuranna M. (2004) Detection of Methane in the Atmosphere of Mars. *Science* **306**, 1758-1761.

Fryer P.B. and Salisbury M.H. (2006) Leg 195 synthesis: Site 1200-Serpentinite seamounts of the Izu-Bonin/Mariana convergent plate margin (ODP Leg 125 and 195 drilling results). *Proc. ODP Sci. Res.* **195**, 1-30.

Giunta T., Young E.D., Warr O., Kohl I., Ash J.L., Martini A., Mundle S.O.C., Rumble D., Pérez-Rodríguez I., Wasley M., LaRowe D.E., Gilbert A. and Sherwood Lollar B. (2019) Methane sources and sinks in continental sedimentary systems: New insights from paired clumped isotopologues 13CH3D and 12CH2D2. *Geochim. Cosmochim. Acta* **245**, 327-351.

Gropp J., Iron M.A. and Halevy I. (2021) Theoretical estimates of equilibrium carbon and hydrogen isotope effects in microbial methane production and anaerobic oxidation of methane. *Geochim. Cosmochim. Acta* **295**, 237-264.

Gropp J., Jin Q. and Halevy I. (2022) Controls on the isotopic composition of microbial methane. *Sci. Adv.* **8**, eabm5713.

Haghnegahdar M.A., Schauble E.A. and Young E.D. (2017) A model for 12CH2D2 and 13CH3D as complementary tracers for the budget of atmospheric CH4. *Global Biogeochem. Cycles* **31**, 1387-1407.

Harris R.L., Lau M.C.Y., Cadar A., Bartlett D.H., Cason E., Heerden E.v., Onstott T.C. and Hotopp J.C.D. (2018) Draft Genome Sequence of "Candidatus Bathyarchaeota" Archaeon BE326-BA-RLH, an Uncultured Denitrifier and Putative Anaerobic Methanotroph from South Africa's Deep Continental Biosphere. *Microbiology Resource Announcements* **7**, e01295-01218.

Harris R.L., Vetter M.C.Y.L., van Heerden E., Cason E., Vermeulen J.-G., Taneja A., Kieft T.L., DeCoste C.J., Laevsky G.S. and Onstott T.C. (2021) FISH-TAMB, a Fixation-Free mRNA Fluorescent Labeling Technique to Target Transcriptionally Active Members in Microbial Communities. *Microb. Ecol.*

Hayes J.M. (2001) Fractionation of Carbon and Hydrogen Isotopes in Biosynthetic Processes. *Rev. Mineral Geochem.* **43**, 225-277.

Heuer V.B., Inagaki F., Morono Y., Kubo Y., Maeda L. and the Expedition 370 Scientists (2017) Temperature Limit of the Deep Biosphere off Muroto. *Proceedings of the International Ocean Discovery Program*, Volume 370.

Heuer V.B., Inagaki F., Morono Y., Kubo Y., Spivack A.J., Viehweger B., Treude T., Beulig F., Schubotz F., Tonai S., Bowden S.A., Cramm M., Henkel S., Hirose T., Homola K., Hoshino T., Ijiri A., Imachi H., Kamiya N., Kaneko M., Lagostina L., Manners H., McClelland H.-L., Metcalfe K., Okutsu N., Pan D., Raudsepp M.J., Sauvage J., Tsang M.-Y., Wang D.T., Whitaker E., Yamamoto Y., Yang K., Maeda L., Adhikari R.R., Glombitza C., Hamada Y., Kallmeyer J., Wendt J., Wörmer L., Yamada Y., Kinoshita M. and Hinrichs K.-U. (2020) Temperature limits to deep subseafloor life in the Nankai Trough subduction zone. *Science* **370**, 1230-1234.

Hoehler T.M., Borowski W.S., Alperin M.J., Rodriguez N.M. and Paull C.K. (2000) Model, stable isotope, and radiotracer characterization of anaerobic methane oxidation in gas hydrate-bearing sediments of the Blake Ridge. *Proceedings of the Ocean Drilling Program, Scientific Results* **164**, 79-85.

Hoehler T.M. and Jørgensen B.B. (2013) Microbial life under extreme energy limitation. *Nature Reviews Microbiology* **11**, 83-94.

Holler T., Wegener G., Knittel K., Boetius A., Brunner B., Kuypers M.M.M. and Widdel F. (2009) Substantial 13C/12C and D/H fractionation during anaerobic oxidation of methane by marine consortia enriched in vitro. *Environmental Microbiology Reports* **1**, 370-376.

Holler T., Wegener G., Niemann H., Deusner C., Ferdelman T.G., Boetius A., Brunner B. and Widdel F. (2011) Carbon and sulfur back flux during anaerobic microbial oxidation of methane and coupled sulfate reduction. *P. Natl. Acad. Sci. USA* **108**, E1484-E1490.

House C.H., Beal E.J. and Orphan V.J. (2011) The Apparent Involvement of ANMEs in Mineral Dependent Methane Oxidation, as an Analog for Possible Martian Methanotrophy. *Life* **1**, 19-33.

House C.H., Wong G.M., Webster C.R., Flesch G.J., Franz H.B., Stern J.C., Pavlov A., Atreya S.K., Eigenbrode J.L., Gilbert A., Hofmann A.E., Millan M., Steele A., Glavin D.P., Malespin C.A. and Mahaffy P.R. (2022) Depleted carbon isotope compositions observed at Gale crater, Mars. *P. Natl. Acad. Sci. USA* **119**, e2115651119.

IPCC (2021) Climate Change 2021: The Physical Science Basis. Contribution of Working Group I to the Sixth Assessment Report of the Intergovernmental Panel on Climate Change. IPCC, Geneva, Switzerland.

Jordan S.F.A., Treude T., Leifer I., Janßen R., Werner J., Schulz-Vogt H. and Schmale O. (2020) Bubble-mediated transport of benthic microorganisms into the water column: Identification of methanotrophs and implication of seepage intensity on transport efficiency. *Scientific Reports* **10**, 4682.

Kawagucci S., Miyazaki J., Morono Y., Seewald J.S., Wheat C.G. and Takai K. (2018) Cool, alkaline serpentinite formation fluid regime with scarce microbial habitability and

possible abiotic synthesis beneath the South Chamorro Seamount. *Progress in Earth and Planetary Science* **5**, 74.

Kevorkian R.T., Callahan S., Winstead R. and Lloyd K.G. (2021) ANME-1 archaea may drive methane accumulation and removal in estuarine sediments. *Environmental Microbiology Reports* **13**, 185-194.

Krause S.J.E., Liu J., Young E.D. and Treude T. (2022) Δ13CH3D and Δ12CH2D2 signatures of methane aerobically oxidized by Methylosinus trichosporium with implications for deciphering the provenance of methane gases. *Earth Planet. Sci. Lett.* **593**, 117681.

Krause S.J.E. and Treude T. (2021) Deciphering cryptic methane cycling: Coupling of methylotrophic methanogenesis and anaerobic oxidation of methane in hypersaline coastal wetland sediment. *Geochim. Cosmochim. Acta* **302**, 160-174.

Laso-Pérez R., Krukenberg V., Musat F. and Wegener G. (2018) Establishing anaerobic hydrocarbon-degrading enrichment cultures of microorganisms under strictly anoxic conditions. *Nature Protocols* **13**, 1310-1330.

Lau M.C.Y., Kieft T.L., Kuloyo O., Linage-Alvarez B., van Heerden E., Lindsay M.R., Magnabosco C., Wang W., Wiggins J.B., Guo L., Perlman D.H., Kyin S., Shwe H.H., Harris R.L., Oh Y., Yi M.J., Purtschert R., Slater G.F., Ono S., Wei S., Li L., Sherwood Lollar B. and Onstott T.C. (2016) An oligotrophic deep-subsurface community dependent on syntrophy is dominated by sulfur-driven autotrophic denitrifiers. *P. Natl. Acad. Sci. USA* **113**, E7927-E7936.

Lefèvre F. (2019) The Enigma of Methane on Mars, in: Cavalazzi B., Westall F. (Eds.), Biosignatures for Astrobiology. Springer International Publishing, Cham, pp. 253-266.

Liu Q. and Liu Y. (2016) Clumped-isotope signatures at equilibrium of CH4, NH3, H2O, H2S and SO2. *Geochim. Cosmochim. Acta* **175**, 252-270.

Ma Q., Wu S. and Tang Y. (2008) Formation and abundance of doubly-substituted methane isotopologues (13CH3D) in natural gas systems. *Geochim. Cosmochim. Acta* **72**, 5446-5456.

Mahlert F., Grabarse W., Kahnt J., Thauer R.K. and Duin E.C. (2002) The nickel enzyme methyl-coenzyme M reductase from methanogenic archaea: in vitro interconversions among the EPR detectable MCR-red1 and MCR-red2 states. *JBIC Journal of Biological Inorganic Chemistry* **7**, 101-112.

Mariotti A., Germon J.C., Hubert P., Kaiser P., Letolle R., Tardieux A. and Tardieux P. (1981) Experimental determination of nitrogen kinetic isotope fractionation: Some principles; illustration for the denitrification and nitrification processes. *Plant Soil* **62**, 413-430.

Marlow J.J., LaRowe D.E., Ehlmann B.L., Amend J.P. and Orphan V.J. (2014) The Potential for Biologically Catalyzed Anaerobic Methane Oxidation on Ancient Mars. *Astrobiology* **14**, 292-307.

Melaniuk K., Sztybor K., Treude T., Sommer S. and Rasmussen T.L. (2022) Influence of methane seepage on isotopic signatures in living deep-sea benthic foraminifera, 79° N. *Scientific Reports* **12**, 1169.

National Academies of Sciences, Engineering, and Medicine (2022) Origins, Worlds, and Life: A Decadal Strategy for Planetary Science and Astrobiology 2023-2032. The National Academies Press, Washington, DC.

Ono S., Rhim J.H., Gruen D.S., Taubner H., Kölling M. and Wegener G. (2021) Clumped isotopologue fractionation by microbial cultures performing the anaerobic oxidation of methane. *Geochim. Cosmochim. Acta* **293**, 70-85.

Ono S., Rhim J.H. and Ryberg E.C. (2022) Rate limits and isotopologue fractionations for microbial methanogenesis examined with combined pathway protein cost and isotopologue flow network models. *Geochim. Cosmochim. Acta* **325**, 296-315.

Ono S., Wang D.T., Gruen D.S., Sherwood Lollar B., Zahniser M.S., McManus B.J. and Nelson D.D. (2014) Measurement of a Doubly Substituted Methane Isotopologue, 13CH3D, by Tunable Infrared Laser Direct Absorption Spectroscopy. *Anal. Chem.* **86**, 6487-6494.

Reeburgh W.S. (2003) Global Methane Biogeochemistry. *Treatise on Geochemistry* **4**, 347.

Repeta D.J., Ferrón S., Sosa O.A., Johnson C.G., Repeta L.D., Acker M., DeLong E.F. and Karl D.M. (2016) Marine methane paradox explained by bacterial degradation of dissolved organic matter. *Nat. Geosci.* **9**, 884-887.

Röckmann T., Popa M.E., Krol M.C. and Hofmann M.E.G. (2016) Statistical clumped isotope signatures. *Scientific Reports* **6**, 31947.

Scheller S., Goenrich M., Boecher R., Thauer R.K. and Jaun B. (2010) The key nickel enzyme of methanogenesis catalyses the anaerobic oxidation of methane. *Nature* **465**, 606-608.

Schoell M. (1988) Multiple origins of methane in the Earth. *Chem. Geol.* **71**, 1-10.

Seewald J.S., Doherty K.W., Hammar T.R. and Liberatore S.P. (2002) A new gas-tight isobaric sampler for hydrothermal fluids. *Deep-Sea Res. Pt. I* **49**, 189-196.

Sherwood Lollar B., Lacrampe-Couloume G., Slater G.F., Ward J., Moser D.P., Gihring T.M., Lin L.H. and Onstott T.C. (2006) Unravelling abiogenic and biogenic sources of methane in the Earth's deep subsurface. *Chem. Geol.* **226**, 328-339.

Stolper D.A., Lawson M., Davis C.L., Ferreira A.A., Neto E.V.S., Ellis G.S., Lewan M.D., Martini A.M., Tang Y., Schoell M., Sessions A.L. and Eiler J.M. (2014a) Formation temperatures of thermogenic and biogenic methane. *Science* **344**, 1500-1503.

Stolper D.A., Martini A.M., Clog M., Douglas P.M., Shusta S.S., Valentine D.L., Sessions A.L. and Eiler J.M. (2015) Distinguishing and understanding thermogenic and biogenic sources of methane using multiply substituted isotopologues. *Geochim. Cosmochim. Acta* **161**, 219-247.

Stolper D.A., Sessions A.L., Ferreira A.A., Santos Neto E.V., Schimmelmann A., Shusta S.S., Valentine D.L. and Eiler J.M. (2014b) Combined 13C–D and D–D clumping in methane: Methods and preliminary results. *Geochim. Cosmochim. Acta* **126**, 169-191.

Taenzer L., Labidi J., Masterson A.L., Feng X., Rumble D., Young E.D. and Leavitt W.D. (2020) Low Δ12CH2D2 values in microbialgenic methane result from combinatorial isotope effects. *Geochim. Cosmochim. Acta* **285**, 225-236.

Takai K., Moyer C.L., Miyazaki M., Nogi Y., Hirayama H., Nealson K.H. and Horikoshi K. (2005) Marinobacter alkaliphilus sp. nov., a novel alkaliphilic bacterium isolated from subseafloor alkaline serpentine mud from Ocean Drilling Program Site 1200 at South Chamorro Seamount, Mariana Forearc. *Extremophiles* **9**, 17-27.

Thompson M.A., Krissansen-Totton J., Wogan N., Telus M. and Fortney J.J. (2022) The case and context for atmospheric methane as an exoplanet biosignature. *P. Natl. Acad. Sci. USA* **119**, e2117933119.

Timmers P.H.A., Welte C.U., Koehorst J.J., Plugge C.M., Jetten M.S.M. and Stams A.J.M. (2017) Reverse Methanogenesis and Respiration in Methanotrophic Archaea. *Archaea* **2017**, 22.

Treude T., Orphan V., Knittel K., Gieseke A., House C.H. and Boetius A. (2007) Consumption of Methane and CO2 by Methanotrophic Microbial Mats from Gas Seeps of the Anoxic Black Sea. *Appl. Environ. Microbiol.* **73**, 2271-2283.

Treude T. and Ziebis W. (2010) Methane oxidation in permeable sediments at hydrocarbon seeps in the Santa Barbara Channel, California. *Biogeosciences* **7**, 3095-3108.

Tyne R.L., Barry P.H., Lawson M., Byrne D.J., Warr O., Xie H., Hillegonds D.J., Formolo M., Summers Z.M., Skinner B., Eiler J.M. and Ballentine C.J. (2021) Rapid microbial methanogenesis during CO2 storage in hydrocarbon reservoirs. *Nature* **600**, 670-674.

Waite J.H., Glein C.R., Perryman R.S., Teolis B.D., Magee B.A., Miller G., Grimes J., Perry M.E., Miller K.E., Bouquet A., Lunine J.I., Brockwell T. and Bolton S.J. (2017) Cassini finds molecular hydrogen in the Enceladus plume: Evidence for hydrothermal processes. *Science* **356**, 155-159.

Wang D.T., Gruen D.S., Lollar B.S., Hinrichs K.-U., Stewart L.C., Holden J.F., Hristov A.N., Pohlman J.W., Morrill P.L., Könneke M., Delwiche K.B., Reeves E.P., Sutcliffe C.N., Ritter D.J., Seewald J.S., McIntosh J.C., Hemond H.F., Kubo M.D., Cardace D., Hoehler T.M. and Ono S. (2015) Nonequilibrium clumped isotope signals in microbial methane. *Science* **348**, 428-431.

Wang D.T., Welander P.V. and Ono S. (2016) Fractionation of the methane isotopologues 13CH4, 12CH3D, and 13CH3D during aerobic oxidation of methane by Methylococcus capsulatus (Bath). *Geochim. Cosmochim. Acta* **192**, 186-202.

Warr O., Young E.D., Giunta T., Kohl I.E., Ash J.L. and Sherwood Lollar B. (2021) High-resolution, long-term isotopic and isotopologue variation identifies the sources and sinks of methane in a deep subsurface carbon cycle. *Geochim. Cosmochim. Acta* **294**, 315-334.

Webb M.A. and Miller T.F. (2014) Position-Specific and Clumped Stable Isotope Studies: Comparison of the Urey and Path-Integral Approaches for Carbon Dioxide, Nitrous Oxide, Methane, and Propane. *The Journal of Physical Chemistry A* **118**, 467-474.

Webster C.R., Mahaffy P.R., Atreya S.K., Flesch G.J., Mischna M.A., Meslin P.-Y., Farley K.A., Conrad P.G., Christensen L.E., Pavlov A.A., Martín-Torres J., Zorzano M.-P., McConnochie T.H., Owen T., Eigenbrode J.L., Glavin D.P., Steele A., Malespin C.A., Archer P.D., Sutter B., Coll P., Freissinet C., McKay C.P., Moores J.E., Schwenzer S.P., Bridges J.C., Navarro-Gonzalez R., Gellert R. and Lemmon M.T. (2015) Mars methane detection and variability at Gale crater. *Science* **347**, 415-417.

Wegener G., Gropp J., Taubner H., Halevy I. and Elvert M. (2021) Sulfate-dependent reversibility of intracellular reactions explains the opposing isotope effects in the anaerobic oxidation of methane. *Sci. Adv.* **7**, eabe4939.

Wheat C.G., Fryer P., Fisher A.T., Hulme S., Jannasch H., Mottl M.J. and Becker K. (2008) Borehole observations of fluid flow from South Chamorro Seamount, an active serpentinite mud volcano in the Mariana forearc. *Earth Planet. Sci. Lett.* **267**, 401-409.

Wheat C.G., Seewald J.S. and Takai K. (2020) Fluid transport and reaction processes within a serpentinite mud volcano: South Chamorro Seamount. *Geochim. Cosmochim. Acta* **269**, 413-428.

Whitehill A.R., Joelsson L.M.T., Schmidt J.A., Wang D.T., Johnson M.S. and Ono S. (2017) Clumped isotope effects during OH and Cl oxidation of methane. *Geochim. Cosmochim. Acta* **196**, 307-325.

Whiticar M.J. (1999) Carbon and hydrogen isotope systematics of bacterial formation and oxidation of methane. *Chem. Geol.* **161**, 291-314.

Widdel F. and Bak F. (1992) Gram-Negative Mesophilic Sulfate-Reducing Bacteria, in: Balows A., Trüper H.G., Dworkin M., Harder W., Schleifer K.-H. (Eds.), The Prokaryotes: A Handbook on the Biology of Bacteria: Ecophysiology, Isolation, Identification, Applications. Springer New York, New York, NY, pp. 3352-3378.

Xiao K.-Q., Beulig F., Kjeldsen K.U., Jørgensen B.B. and Risgaard-Petersen N. (2017) Concurrent Methane Production and Oxidation in Surface Sediment from Aarhus Bay, Denmark. *Front. Microbiol.* **8**.

Xie H., Dong G., Formolo M., Lawson M., Liu J., Cong F., Mangenot X., Shuai Y., Ponton C. and Eiler J. (2021) The evolution of intra- and inter-molecular isotope equilibria in natural gases with thermal maturation. *Geochim. Cosmochim. Acta* **307**, 22-41.

Yamamoto S., Alcauskas J.B. and Crozier T.E. (1976) Solubility of methane in distilled water and seawater. *Journal of Chemical & Engineering Data* **21**, 78-80.

Yan Z., Joshi P., Gorski C.A. and Ferry J.G. (2018) A biochemical framework for anaerobic oxidation of methane driven by Fe (III)-dependent respiration. *Nat. commun.* **9**.

Yeung L.Y. (2016) Combinatorial effects on clumped isotopes and their significance in biogeochemistry. *Geochim. Cosmochim. Acta* **172**, 22-38.

York D., Evensen N.M., Martínez M.L. and Delgado J.D.B. (2004) Unified equations for the slope, intercept, and standard errors of the best straight line. *American Journal of Physics* **72**, 367-375.

Yoshinaga M.Y., Holler T., Goldhammer T., Wegener G., Pohlman J.W., Brunner B., Kuypers M.M.M., Hinrichs K.-U. and Elvert M. (2014) Carbon isotope equilibration during sulphate-limited anaerobic oxidation of methane. *Nat. Geosci.* **7**, 190-194.

Young E.D. (2019) A Two-Dimensional Perspective on CH4 Isotope Clumping: Distinguishing Process from Source, in: Orcutt B.N., Daniel I., Dasgupta R. (Eds.), Deep Carbon: Past to Present. Cambridge University Press, Cambridge, pp. 388-414.

Young E.D., Kohl I.E., Lollar B.S., Etiope G., Rumble D., Li S., Haghnegahdar M.A., Schauble E.A., McCain K.A., Foustoukos D.I., Sutclife C., Warr O., Ballentine C.J., Onstott T.C., Hosgormez H., Neubeck A., Marques J.M., Pérez-Rodríguez I., Rowe A.R., LaRowe D.E., Magnabosco C., Yeung L.Y., Ash J.L. and Bryndzia L.T. (2017) The relative abundances of resolved l2CH2D2 and 13CH3D and mechanisms controlling isotopic bond ordering in abiotic and biotic methane gases. *Geochim. Cosmochim. Acta* **203**, 235-264.

Young E.D., Rumble D., Freedman P. and Mills M. (2016) A large-radius high-mass-resolution multiple-collector isotope ratio mass spectrometer for analysis of rare isotopologues of O2, N2, CH4 and other gases. *Int. J. Mass spectrom.* **401**, 1-10.

Yu L., He D., Yang L., Rensing C., Zeng R.J. and Zhou S. (2022) Anaerobic methane oxidation coupled to ferrihydrite reduction by Methanosarcina barkeri. *Sci. Total Environ.* **844**, 157235.

Yung Y.L., Chen P., Nealson K., Atreya S., Beckett P., Blank J.G., Ehlmann B., Eiler J., Etiope G., Ferry J.G., Forget F., Gao P., Hu R., Kleinböhl A., Klusman R., Lefèvre F., Miller C., Mischna M., Mumma M., Newman S., Oehler D., Okumura M., Oremland R., Orphan V., Popa R., Russell M., Shen L., Sherwood Lollar B., Staehle R., Stamenković V., Stolper D., Templeton A., Vandaele A.C., Viscardy S., Webster C.R., Wennberg P.O., Wong M.L. and Worden J. (2018) Methane on Mars and Habitability: Challenges and Responses. *Astrobiology* **18**, 1221-1242.
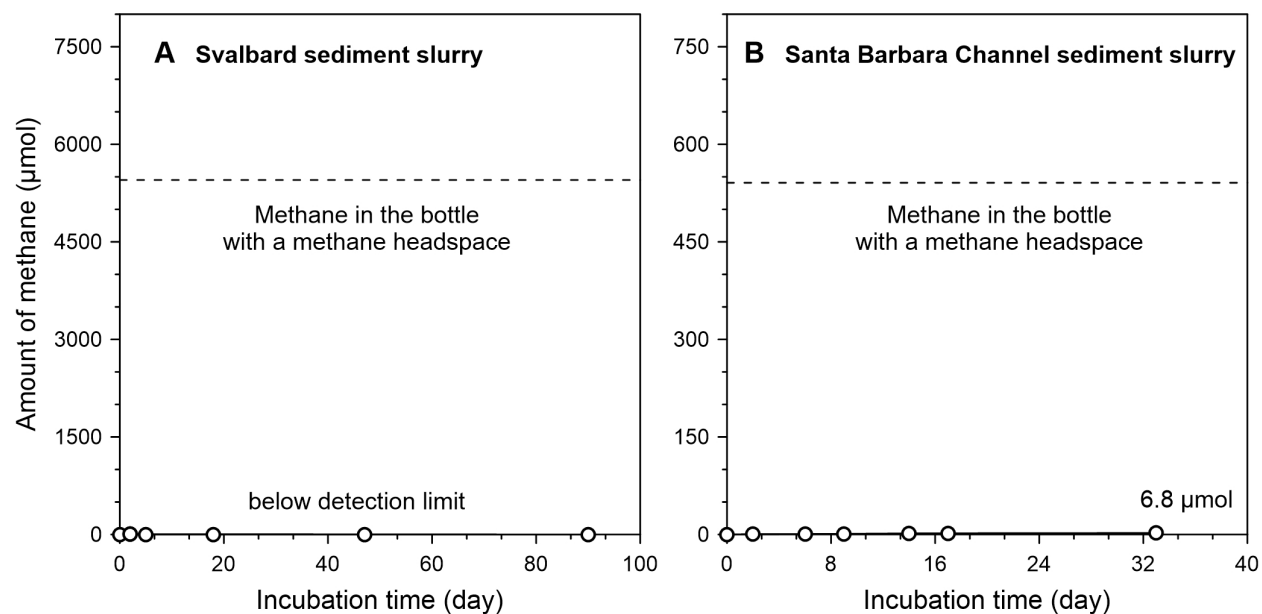
Fig. 1 Methane production (amount of methane over time) in the methane-free control experiment: (A) Svalbard sediment slurry, (B) Santa Barbara Channel sediment slurry. For reference, dashed lines represent the amount of methane in the bottle with a pure methane headspace. The control incubation of Santa Barbara slurry showed a small amount of methane build-up in the headspace of the sediment slurry over the 33 days. We interpret this methane increase as the result of equilibration between the slurry and gaseous phases rather than microbial methanogenesis, because unlike the Svalbard sediment slurry (flushed three times), the Santa Barbara Channel sediment slurry was flushed only one time following previous experiments with a pure methane headspace. However, if the methane build-up was the result of microbial methanogenesis, it would represent a very small fraction (ca. 1%) of the methane that is normally added during our experiments, resulting in a negligible isotope effect.
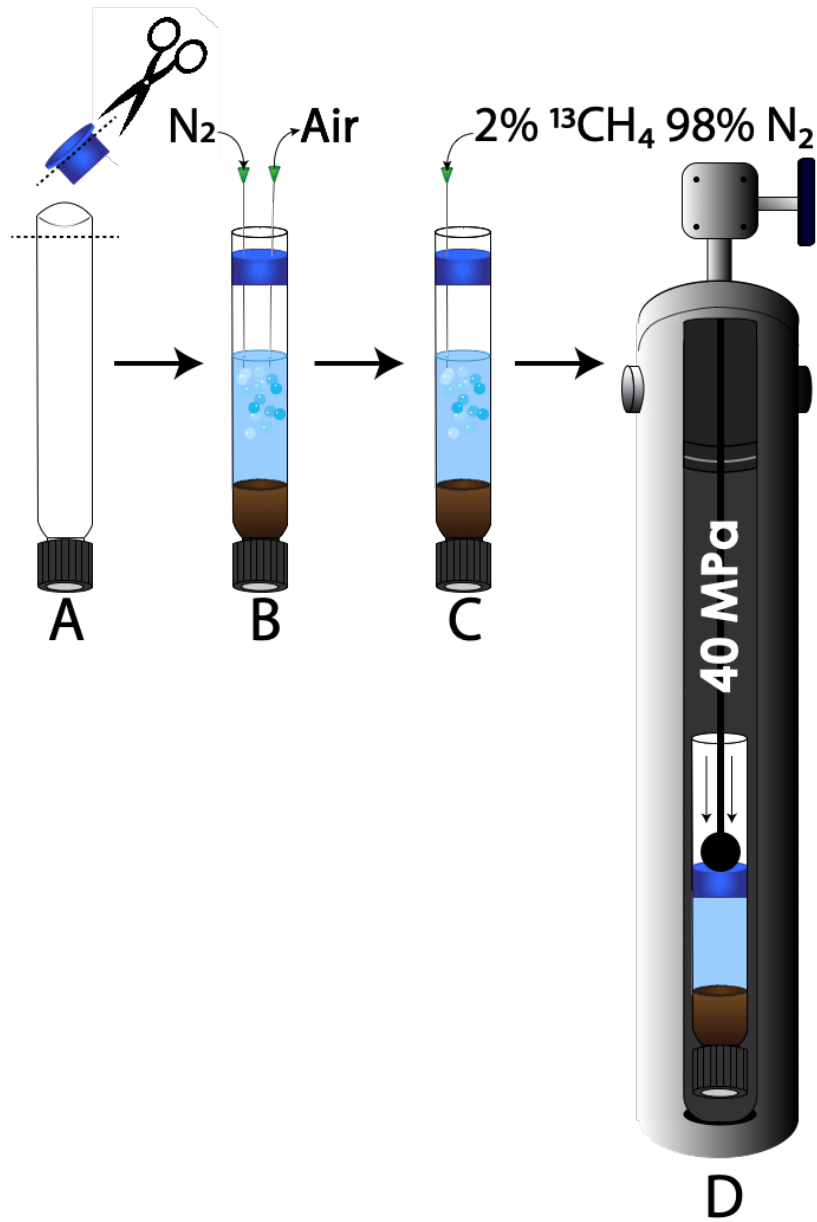
Fig. 2 High pressure cultivation scheme. (A) The bottoms of Hungate tubes are removed using a glass cutter and replaced with a hand-made piston prepared from a butyl rubber stopper. (B) Headspace is sparged with N_2 gas to remove lab air following anaerobic addition of sediment and media. (C) Headspace is replaced with N_2 atmosphere with ^{13}C-labeled CH_4. (D) Cross-section of stainless-steel hydrostatic pressure vessel containing inverted Hungate tubes. Pressurization to 40 MPa pushes the $^{13}CH_4$ headspace into solution by way of the butyl rubber piston.
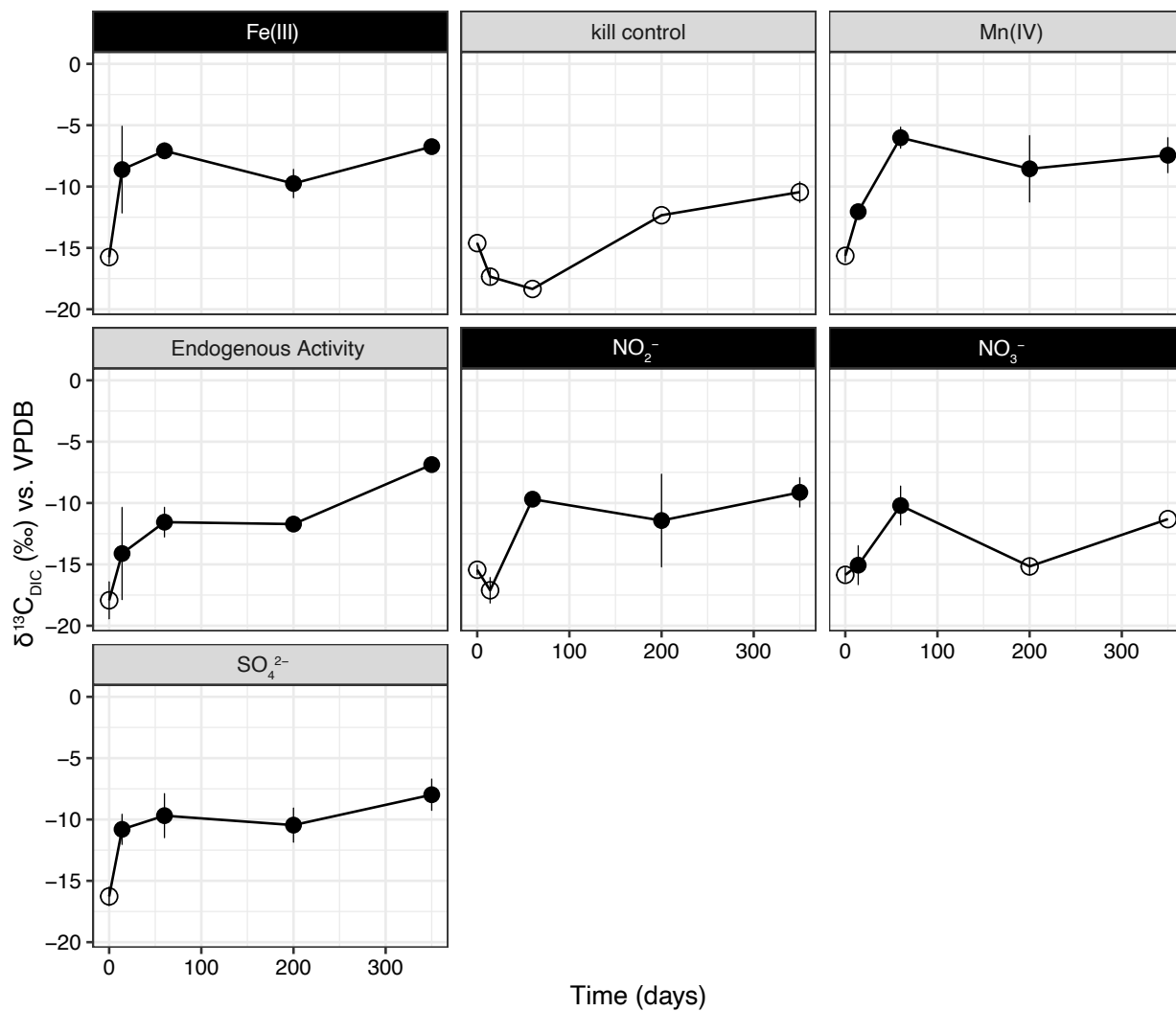
Fig. 3 $\delta^{13}C_{DIC}$ in high pressure (40 MPa) Nankai deep biosphere sediment incubated with $^{13}CH_4$. Rates were calculated relative to an autoclaved kill control according to Equation S1. Black facets indicate electron acceptor conditions where $\Delta^{13}CH_3D$ and $\Delta^{12}CH_2D_2$ were measured in parallel experiments incubated at ambient pressure (ca. 150 kPa) and with 100% natural abundance methane. Significance (closed circles) was determined at each time point if $\delta^{13}C_{DIC\_sample} > (\delta^{13}C_{DIC\_kill} + 3*SD_{kill})$. $\delta^{13}C_{DIC}$ was calculated according to Eq. S1.
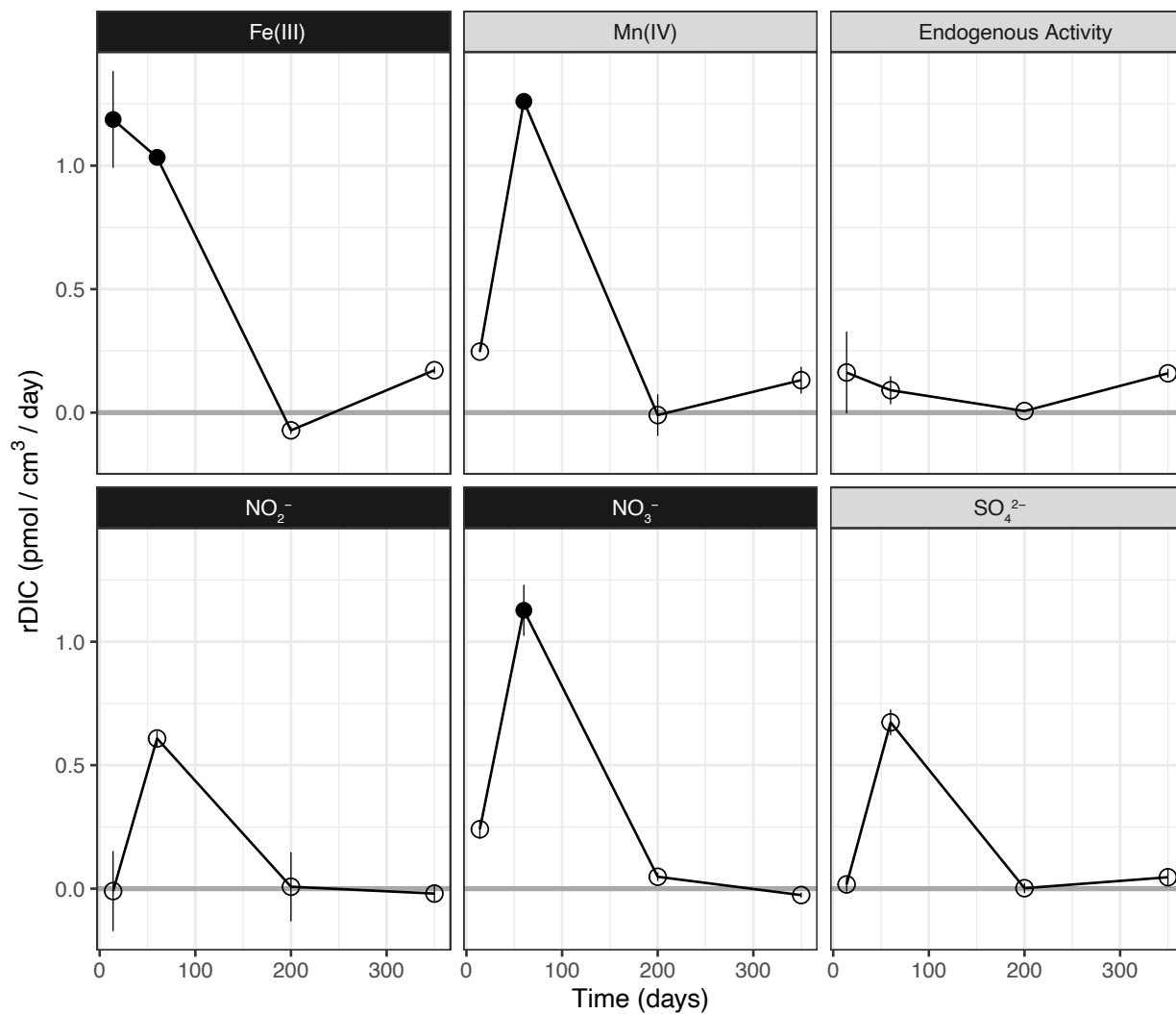
Fig. 4 Rates of AOM $^{13}C_{DIC}$ production (r_{DIC}) in high pressure (40 MPa) Nankai deep biosphere sediment incubated with $^{13}CH_4$. Rates were calculated relative to an autoclaved kill control (normalized here as $r_{DIC} = 0$) according to Eq. S2. Black facets indicate electron acceptor conditions where $\Delta^{12}CH_2D_2$ and $\Delta^{13}CH_3D$ were measured in parallel experiments incubated at ambient pressure (ca. 150 kPa) and with 100% natural abundance methane. Closed circles indicate statistically significant r_{DIC} relative to the kill control (one-tailed test, $P < 0.05$).
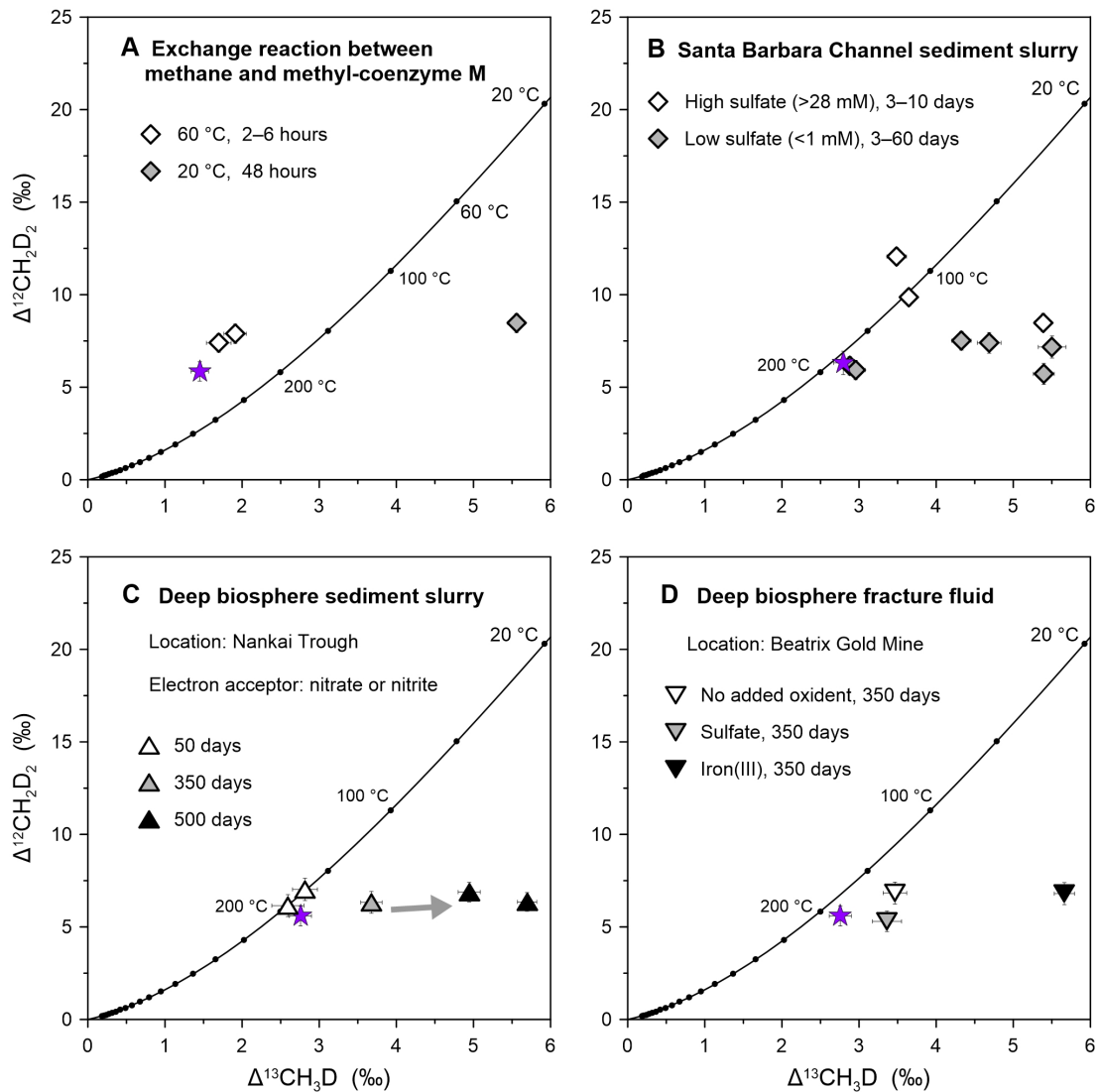
Fig. 5 Equilibrium-driven methane isotopologue data with detailed description for residual methane in incubation experiments. (A) Exchange reaction between methane and methyl-coenzyme M. (B) Santa Barbara Channel sediment incubation with sulfate. (C) Nankai Trough sediment incubation with nitrate or nitrite. (D) Beatrix Gold Mine fracture fluid incubation with sulfate or iron (III). Electron acceptor, incubation time and temperature are shown in the legend of each panel. The purple stars represent the initial tank gas. The solid black line depicts theoretical thermodynamic equilibrium abundances of methane isotopologues, along with corresponding temperatures. Error bars are 1σ.
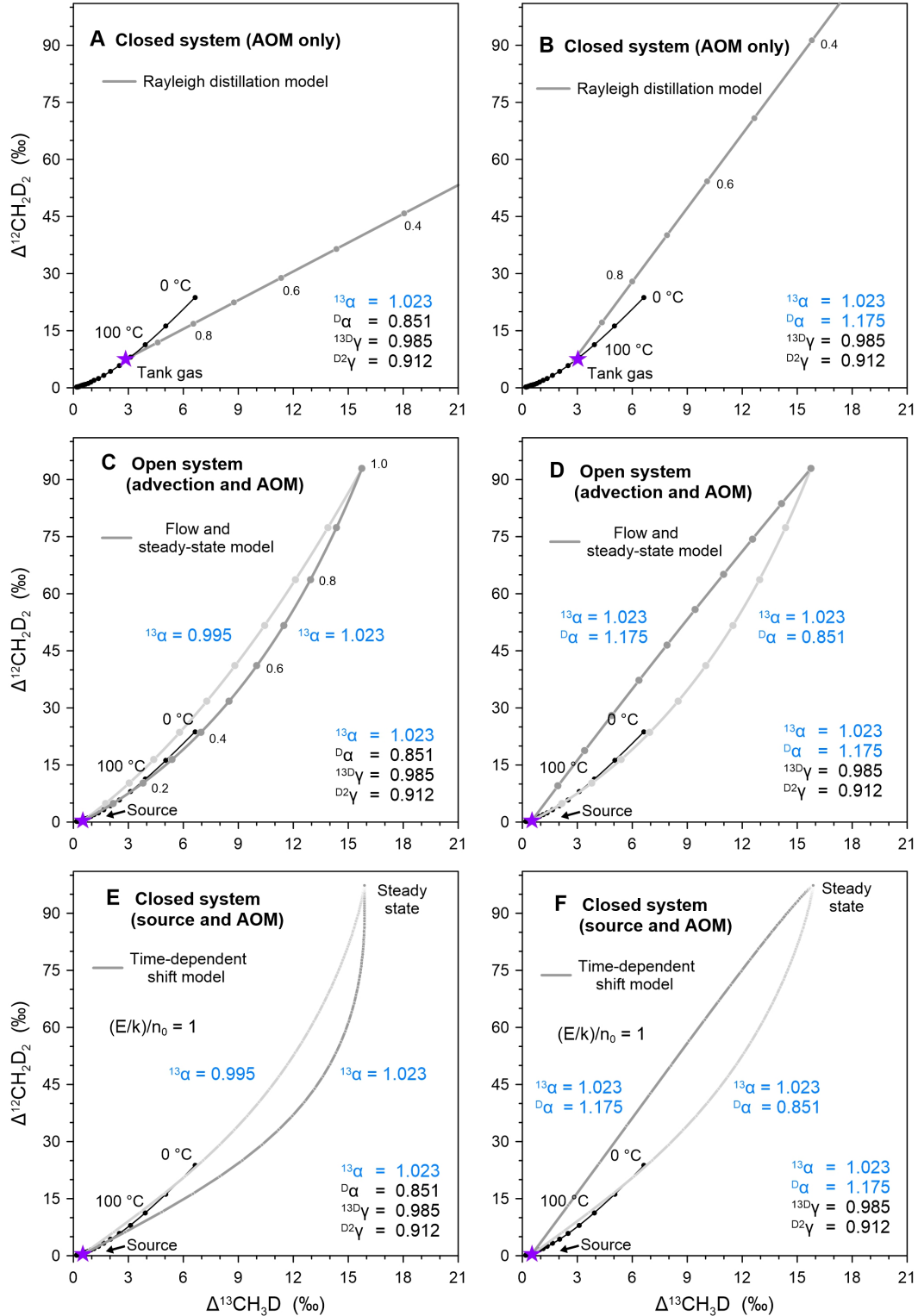
Fig. 6 Sensitivity test of the Rayleigh fractionation model (A–B), open-system flow and steady-state model (C–D) and closed-system time-dependent shift model (E–F). Bulk isotope fractionation factors in blue are changed from the original values shown in Fig. 6. The carbon isotope fractionation factor (1.023) is adopted from the low sulfate experiment of Wegener et al. (2021). A higher hydrogen isotope fractionation factor of 1.175 is used here as a maximum estimation. Lines and markers follow Fig. 6.

Chapter 5 supplementary methods

$^{13}CH_4$ tracer microcosm experiment at high hydrostatic pressure – Nankai Trough

Microcosms were set up inside an anaerobic glove bag (Coy Laboratory Products, Grass Lake, MI USA) under a 5:95 H_2:N_2 atmosphere. Fresh aluminum foil was placed on the working surface of the glove bag and ethanol-sterilized nitrile gloves were worn over the glove bag's neoprene gloves to minimize potential contamination of low-biomass samples. The surface of each C0023A whole round core (WRC) was scraped using an ethanol-sterilized scalpel to remove sediment exposed to Kochi Core Center's anaerobic packaging. For each WCR, ~ 1 g (wet weight) of freshly exhumed interior sediment was transferred into high-pressure modified Hungate tubes (Fig. S2; Bowles et al., 2011) containing 5 mL anoxic sulfate-free artificial seawater medium at pH 8.0 (Widdel and Bak, 1992; Holler et al., 2011) and supplemented with 10 mM (final concentration) of one of the following electron acceptors: SO_4^{2-}, NO_2^-, NO_3^- , Mn^{4+} (in the form of MnO_2), or Fe^{3+} (in the form of $Fe_2O_3 \bullet H_2O$), in addition to a no-added oxidant control (i.e., "endogenous activity). $Fe_2O_3 \bullet H_2O$ and MnO_2 were synthesized as previously described (Cornell and Schwertmann, 2003; Händel et al., 2013). The headspace of each microcosm was replaced with 2:98 $^{13}CH_4$:N_2 (100 kPa), prepared by mixing via gas-tight syringes (Trajan Scientific and Medical, Melbourne, Australia) in sealed Tedlar® bags (DuPont, Wilmington, DE USA). An autoclaved kill control was included as a reference for determining significant biological AOM. All treatments were assessed in biological triplicate.

Microcosms were inverted and placed inside stainless-steel hydrostatic vessels with a pin-retained piston closure pre-heated in gravity ovens to an approximate *in-situ* temperature of 40˚C (Fig. S2). Vessels were sealed and pressurized to 40 ± 0.5 MPa using a hydrostatic pump as previously described (Yayanos, 1995) and subsequently returned to gravity ovens for incubation.

Subsamples of the enrichments were collected at 0, 14, 60, 200, and 350 days to monitor CH_4 concentrations and the evolution of $\delta^{13}C_{DIC}$. Briefly, hydrostatic vessels were removed from ovens and depressurized for retrieval of Hungate tube microcosms. From each sample, a 500 µl aliquot of the slurry was anaerobically transferred using Ar-sparged syringes and needles into combusted borosilicate serum vials pre-treated with saturated $HgCl_2$ to kill any microbes contained in the sample (Sherwood Lollar et al., 1993a; Sherwood Lollar et al., 1993b). Vials were sealed under a 100% N_2 atmosphere with crimped 0.1 NaOH-treated butyl rubber stoppers (Bellco Glass, Inc., Vineland, NJ USA). Following sample transfer, serum vials were over-pressurized with N_2 gas to minimize the risk of mixing with atmospheric CO_2. To exsolve all DIC out of solution, vials were supplemented with 100 µL of 0.5 N H_3PO_4, and heated overnight in a water bath at 70˚C. CH_4 concentrations and $\delta^{13}C_{DIC}$ were analyzed from the headspace using a Picarro cavity ringdown spectrometer equipped with a G2101-I Isotopic CO_2 analyzer (Picarro, Inc., Sunnyvale, CA USA). Resulting isotopic values were calculated according to

$$\delta^{13}C_{DIC} = \left(\frac{\left(\frac{^{13}C_{DIC}}{^{12}C_{DIC}}\right)_{sample}}{\left(\frac{^{13}C_{DIC}}{^{12}C_{DIC}}\right)_{standard}} - 1 \right) \times 1000 \text{ ‰} \tag{S1}$$

with respect to the $[^{13}C/^{12}C]$ ratio of the Vienna Pee Dee Belemnite standard. AOM was determined to have a significant influence on $\delta^{13}C_{DIC}$ if its average $\delta^{13}C_{DIC} \pm$ standard deviation (SD) was greater than the average $\delta^{13}C_{DIC} + 3 \times$ SD of the kill control ($\delta^{13}C_{DIC_{d.kill}}$) (Fig. S3).

DIC production rates (r_{DIC}) for each sample are shown in Figure S4 and were calculated according to

$$r_{DIC} \left(\text{pmol cm}^{-3}\text{day}^{-1} \right) = \frac{\left(\frac{\delta^{13}C_{DIC_d} - \delta^{13}C_{DIC_{d.kill}}}{\delta^{13}C_{13CH_4} - \delta^{13}C_{DIC_{d.kill}}} \right) DIC_d \left(\frac{\rho_d}{g_d} \right)}{t} \tag{S2}$$

where DIC_d is the sum of $^{13}C_{DIC}$ and $^{12}C_{DIC}$ in pmol at depth d, ρ_d is the bulk density of the sediment

at depth d in grams cm^{-3} (http://sio7.jamstec.go.jp/j-cores.data/370/C0023A/), and g_d is the grams

of sediment incubated from depth d, and t is the number of days of incubation. Data were assumed

to follow a normal distribution and r_{DIC} values were assigned z-scores according to

$$z = (r_{DIC\_sample} - \mu_{kill})/\sigma_{kill} \tag{S3}$$

from which P values were subsequently calculated using a 1-tailed test.

Chapter 5 supplementary references

Bowles M. W., Samarkin V. A. and Joye S. B. (2011) Improved measurement of microbial activity in deep-sea sediments at in situ pressure and methane concentration. *Limnol. Oceanogr. Methods* **9**, 499–506.

Cornell R. M. and Schwertmann U. (2003) Introduction to the Iron Oxides. In *The Iron Oxides* Wiley. pp. 1–7.

Händel M., Rennert T. and Totsche K. U. (2013) A simple method to synthesize birnessite at ambient pressure and temperature. *Geoderma* **193**–**194**, 117–121.

Holler T., Widdel F., Knittel K., Amann R., Kellermann M. Y., Hinrichs K.-U., Teske A., Boetius A. and Wegener G. (2011) Thermophilic anaerobic oxidation of methane by marine microbial consortia. *ISME J.* **5**, 1946–1956.

Sherwood Lollar B., Frape S. K., Fritz P., Macko S. A., Welhan J. A., Blomqvist R. and Lahermo P. W. (1993a) Evidence for bacterially generated hydrocarbon gas in Canadian shield and fennoscandian shield rocks. *Geochim. Cosmochim. Acta* **57**, 5073–5085.

Sherwood Lollar B., Frape S. K., Weise S. M., Fritz P., Macko S. A. and Welhan J. A. (1993b) Abiogenic methanogenesis in crystalline rocks. *Geochim. Cosmochim. Acta* **57**, 5087–5097.

Wegener G., Gropp J., Taubner H., Halevy I. and Elvert M. (2021) Sulfate-dependent reversibility of intracellular reactions explains the opposing isotope effects in the anaerobic oxidation of methane. *Sci. Adv.* **7**, eabe4939.

Widdel F. and Bak F. (1992) *The Prokaryotes*. eds. A. Balows, H. G. Trüper, M. Dworkin, W. Harder, and K.-H. Schleifer, Springer New York, New York, NY.

Yayanos A. A. (1995) Microbiology to 10,500 Meters in the Deep Sea. *Annu. Rev. Microbiol.* **49**, 777–805.

Chapter 6

Conclusions and Future Directions

It is my hope that the original research presented in this dissertation is a valuable resource to current and future scientists and students in Earth and planetary sciences. Collectively, the studies that comprise this dissertation advance and improve the understanding of methane-related biogeochemistry, geomicrobiology, stable isotope geochemistry and astrobiology with new knowledge.

The adapted radiotracer method developed in Chapter 2, and applied to field samples in chapters 2 and 3, was successful at following ^{14}C-labeled carbon from mono-methylamine to methane via methylotrophic methanogenesis, followed by conversion to inorganic carbon by AOM. The method allowed for a new understanding of how methanogenesis is coupled to AOM within the sulfate-reducing zone. It will therefore be a useful tool for future investigations that aim at elucidating cryptic methane cycling activity in natural settings.

Previous research on methanogenesis in aquatic realms focused mostly on hydrogenotrophic and acetoclastic methanogenesis below the SMTZ, however, the work presented here suggest that methylotrophic methanogenesis plays a much larger role in the coastal marine environment than was previously understood (Conrad, 2020). Work presented herein further demonstrates that cryptic methane cycling occurs within multiple sedimentary environments. This finding strongly suggests that cryptic methane cycling could be an important process in other wetland and coastal marine environments globally, keeping atmospheric methane emissions at bay. The cryptic methane cycle may also be implicated in sustaining methanogenic and methanotrophic microbial communities at a level that keeps sediment primed to consume methane, even when

265

critical environmental conditions may change (e.g., changes in methane efflux, enhance eutrophication, electron acceptor availability and oxygen flushing).

The findings in Chapter 3 point to a non-methanogenic biological process that consumes methylamine, which appears to be concurrently active with cryptic methane cycling. This finding suggests that non-competitive substrates like methylamine, may not be as non-competitive as previously understood. The observations described in Chapter 3 underline the metabolic complexity of the microbial communities within their host sediment.

Chapters 4 and 5 improve the current, conventional understanding of how $\Delta^{13}CH_3D$ and $\Delta^{12}CH_2D_2$ shift with progressive methane oxidation by microbial activity. We can conclude from the findings in these two chapters that $\Delta^{13}CH_3D$ and $\Delta^{12}CH_2D_2$ signatures of aerobic and anaerobic oxidation of methane are distinguishable from $\Delta^{13}CH_3D$ and $\Delta^{12}CH_2D_2$ from microbial methanogenesis. Moreover, we conclude the $\Delta^{13}CH_3D$ and $\Delta^{12}CH_2D_2$ aerobic and anaerobic oxidation of methane are distinguishable from each other. Thus the findings in these chapters also reveal the potential utility of $\Delta^{13}CH_3D$ and $\Delta^{12}CH_2D_2$ to distinguish processes, in this case microbial oxidation of methane sources

Moving forward, new questions and hypothesis will undoubtedly arise as cryptic methane cycling, and methane clumped isotopologue signatures continue to be investigated. Therefore, it is important to present here considerations for future investigations. While developing and testing the adapted radiotracer method (Chapter 2) in the laboratory, there was no observable abiotic turnover of the ^{14}C-labeled mono-methylamine to ^{14}C-labeled total inorganic carbon (Krause and Treude, 2021). However, when the method was applied to actual environmental samples, a considerable amount of radioactivity was detected in the ^{14}C-labeled TIC fraction of control sediment samples that were halted of any biological activity prior to the addition of ^{14}C-labeled

mono-methylamine. This means that a portion of the ^{14}C-labeled mono-methylamine was turned over to ^{14}C-labeled TIC through an abiotic mechanism, that has yet to be identified. Although our analysis does reveal cryptic methane cycling activity, the abiotic turnover of the ^{14}C-labled mono-methylamine affects the ability to calculate accurate methylotrophic methanogenesis rates. Future investigations that employ the adapted radiotracer method should investigate the cause and mechanism for this abiotic turnover. Properly identifying the anomaly and providing a pragmatic solution, will allow for significantly improved and more accurate calculations of the methanogenesis rate within the cryptic methane cycle. Future investigations would also benefit from methods that can detect low porewater methylamine concentrations (< 3 μM), as well as, determine the absolute concentration of methylamines in the solid phase and whether or not it is bioavailable (Xiao et al., 2022). Such investigations would further improve calculating methylotrophic methanogenesis rates.

The adapted radiotracer method does not elucidate the key microbial players involved in the cryptic methane cycle. Methanogens and ANMEs are closely related and use the same enzymatic pathways in different directions (Hallam et al., 2004; Knittel and Boetius, 2009; Timmers et al., 2017). This enzymatic capability means that the cryptic methane cycle could potentially be mediated by a single organism or by multiple organisms working together. Future work should focus on combining geochemical with genomic analysis to elucidate key players involved in the cryptic methane cycle.

Zhuang et al. (2019a) discovered that methylamine utilization by either purely methanogenesis or other heterotrophic metabolisms, varies between sampling locations of marine sediment. In other words, at some sampling locations methylamine was shuttled to methanogenesis, whereas at other locations methylamines were consumed via heterotrophic

metabolisms. This lateral heterogeneity could mean that although the cryptic methane cycle could be found in coastal marine and wetland environments globally, the extent in which methylamine is shuttled to methanogenesis versus other heterotrophic bacteria is dependent on the microbial community composition. Future work should combine geochemical and genomic analysis to investigate how methylamine is metabolized by different microbial communities in a variety of locations.

The studies presented on cryptic methane cycling in this dissertation did not consider seasonality, since samples at each location were only collected and analyzed in one season. In many coastal environments, seasonality is an important parameter to consider. For example, along Eastern continental boundaries, coastal upwelling occurs seasonally, leading to natural eutrophication events and ultimately the loading of the coastal marine sediment with organic matter (Kessouri et al., 2021). Future work should evaluate the effects of seasonal changes on the cryptic methane cycle activity.

Using methane clumped isotopologues as a tool for determining methane production and consumption processes is still in its early stages. And yet this tool already exhibits very promising signs for becoming the robust gold standard for determining sources and alterations of methane. The studies presented in this dissertation are the first to determine $\Delta^{13}CH_3D$ and $\Delta^{12}CH_2D_2$ isotopologue behavior together in methane altered by microbial methane oxidation. However, future laboratory-based investigations should repeat incubations with pure oxidation in a closed system and with varying conditions (e.g., growth rates, incubation temperatures and trace metal concentrations). In addition, future investigations should attempt to replicate in the laboratory closed system steady-state conditions (simultaneous methane production and consumption) or open system flow-through systems (i.e., chemostat) to compare with the theoretical findings in this

dissertation. Moreover, methane clumped isotopologue signatures have been determined in a variety of environmental samples from different locations, which have been plotted in $\Delta^{13}CH_3D$ and $\Delta^{12}CH_2D_2$ space (Giunta et al., 2019; Young et al., 2017). Using the findings of this dissertation in hand, future investigations should diagnose whether any of these previous $\Delta^{13}CH_3D$ and $\Delta^{12}CH_2D_2$ signatures from methane collected from the environment have been altered by methane oxidation.

The findings within Chapters 4 and 5 have implications to astrobiological questions as well. Methane is typically thought to be a signature of biological activity in exoplanet sciences (Thompson et al., 2022). For example methane has been detected in the atmosphere of Mars (Webster et al., 2018) and of the Saturn moons Titan and Enceladus (Bouquet et al., 2015; Lunine and Atreya, 2008). Methane clumped isotopologues have been proposed to be potential powerful tool to determine the process of methane formation on other planets and moons in our solar system (Young, 2019). Even if the methane detected in any exoplanet setting is not generated by biological activity, the findings in this dissertation provide a new understanding elucidating a biological process that takes methane out of the system. Future investigations should consider the data in this dissertation when determining the process and source of methane within other planetary and moon bodies.

In conclusion, while pursuing my research objectives for this dissertation I found the science of methane a hugely stimulating subject matter. Participating in fieldwork in the form of oceanographic expeditions and day field trips and conducting experiments in the laboratory all allowed me to develop a deep appreciation for the complexity of the geomicrobiology, the biogeochemical footprints in the sedimentary environment and the geochemical impacts on the local and regional water environments, which appear to contribute mightily to the accelerated

changes in the global atmospheric climate. Clearly, much more innovative work can and needs to be done to better understand methane as a fundamental compound making up and influencing the fate of Earth as well as other planetary bodies in our solar system. Exciting research opportunities exist to help answer burning questions and resolve problems facing society nationally and internationally, which I look forward to being a part of.

References

Bouquet A., Mousis O., Waite J. H. and Picaud S. (2015) Possible evidence for a methane source in Enceladus' ocean. *Geophysical Research Letters* **42**, 1334-1339.

Conrad R. (2020) Importance of hydrogenotrophic, aceticlastic and methylotrophic methanogenesis for methane production in terrestrial, aquatic and other anoxic environments: a mini review. *Pedosphere* **30**, 25-39.

Giunta T., Young E. D., Warr O., Kohl I., Ash J. L., Martini A., Mundle S. O., Rumble D., Pérez-Rodríguez I. and Wasley M. (2019) Methane sources and sinks in continental sedimentary systems: New insights from paired clumped isotopologues 13CH3D and 12CH2D2. *Geochimica et Cosmochimica Acta* **245**, 327-351.

Hallam S. J., Putnam N., Preston C. M., Detter J. C., Rokhsar D., Richardson P. M. and DeLong E. F. (2004) Reverse methanognesis: testing the hypothesis with environmental genomics. *Science* **305**, 1457-1462.

Kessouri F., McWilliams J. C., Bianchi D., Sutula M., Renault L., Deutsch C., Feely R. A., McLaughlin K., Ho M. and Howard E. M. (2021) Coastal eutrophication drives acidification, oxygen loss, and ecosystem change in a major oceanic upwelling system. *Proceedings of the National Academy of Sciences* **118**, e2018856118.

Knittel K. and Boetius A. (2009) Anaerobic oxidation of methane: progress with an unknown process. *Annu. Rev. Microbiol.* **63**, 311-334.

Krause S. J. and Treude T. (2021) Deciphering cryptic methane cycling: Coupling of methylotrophic methanogenesis and anaerobic oxidation of methane in hypersaline coastal wetland sediment. *Geochimica et Cosmochimica Acta* **302**, 160-174.

Lunine J. I. and Atreya S. K. (2008) The methane cycle on Titan. *Nature Geoscience* **1**, 159-164.

Thompson M. A., Krissansen-Totton J., Wogan N., Telus M. and Fortney J. J. (2022) The case and context for atmospheric methane as an exoplanet biosignature. *Proceedings of the National Academy of Sciences* **119**, e2117933119.

Timmers P. H. A., Welte C. U., Koehorst J. J., Plugge C. M., Jetten M. S. M. and Stams A. J. M. (2017) Reverse methanogenesis and respiration in methanotrophic archaea. *Archaea* **Article ID 1654237**.

Webster C. R., Mahaffy P. R., Atreya S. K., Moores J. E., Flesch G. J., Malespin C., McKay C. P., Martinez G., Smith C. L. and Martin-Torres J. (2018) Background levels of methane in Mars' atmosphere show strong seasonal variations. *Science* **360**, 1093-1096.

Xiao K.-Q., Moore O. W., Babakhani P., Curti L. and Peacock C. L. (2022) Mineralogical control on methylotrophic methanogenesis and implications for cryptic methane cycling in marine surface sediment. *Nature Communications* **13**, 1-9.

Young E., Kohl I., Lollar B. S., Etiope G., Rumble D., Li S., Haghnegahdar M., Schauble E., McCain K. and Foustoukos D. (2017) The relative abundances of resolved l2 CH 2 D 2 and 13 CH 3 D and mechanisms controlling isotopic bond ordering in abiotic and biotic methane gases. *Geochimica et Cosmochimica Acta* **203**, 235-264.

Young E.D. (2019) A Two-Dimensional Perspective on CH4 Isotope Clumping: Distinguishing Process from Source, in: Orcutt B.N., Daniel I., Dasgupta R. (Eds.), Deep Carbon: Past to Present. Cambridge University Press, Cambridge, pp. 388-414.

Zhuang G.-C., Montgomery A. and Joye S. B. (2019) Heterotrophic metabolism of C1 and C2 low molecular weight compounds in northern Gulf of Mexico sediments: Controlling factors and implications for organic carbon degradation. *Geochimica et Cosmochimica Acta* **247**, 243-260.